JYU DISSERTATIONS 819

Shreya Mahajan

Exploring the Applicability of Amine-Containing Metal–Organic Frameworks on Direct Air Capture of Carbon Dioxide

UNIVERSITY OF JYVÄSKYLÄ
FACULTY OF MATHEMATICS
AND SCIENCE

JYU DISSERTATIONS 819

Shreya Mahajan

Exploring the Applicability of Amine-Containing Metal–Organic Frameworks on Direct Air Capture of Carbon Dioxide

Esitetään Jyväskylän yliopiston matemaattis-luonnontieteellisen tiedekunnan suostumuksella
julkisesti tarkastettavaksi Ylistönrinteen auditoriossa Kem4
syyskuun 13. päivänä 2024 kello 12.

Academic dissertation to be publicly discussed, by permission of
the Faculty of Mathematics and Science of the University of Jyväskylä,
in Ylistönrinne, auditorium Kem4, on September 13, 2024, at 12 o'clock.

JYVÄSKYLÄN YLIOPISTO
UNIVERSITY OF JYVÄSKYLÄ

JYVÄSKYLÄ 2024

Editors
Manu Lahtinen
Department of Chemistry, University of Jyväskylä
Päivi Vuorio
Open Science Centre, University of Jyväskylä

ISBN 978-952-86-0280-4
ISSN 2489-9003

Permanent link to this publication: http://urn.fi/URN:ISBN:978-952-86-0280-4

ABSTRACT

Mahajan, Shreya
Exploring the Applicability of Amine-Containing Metal–Organic Frameworks on Direct Air Capture of Carbon Dioxide
Jyväskylä: University of Jyväskylä, 2024, 69 p. + original articles
(JYU Dissertations
ISSN 2489-9003; 819)
ISBN 978-952-86-0280-4 (PDF)

Negative emission technologies (NETs), such as direct air capture (DAC), hold substantial potential in limiting planetary warming. Among the various CO_2-capturing materials being explored, a promising class of porous crystalline materials, such as metal–organic frameworks (MOFs), have come out ahead as potentially customizable materials for selectively capturing atmospheric CO_2. The thesis's first section covers the most recent achievements made in developing MOFs for DAC potential. It provides a detailed account of structural approaches, examines MOFs' DAC performance under different conditions, and discusses the CO_2 adsorption pathways. The second section of the thesis encapsulates the key results published in three journal articles related to this work.

The results and discussion section detail the preparation of an amino-triazole-based *N*-rich bent ligand and the structural determination of its sixteen new molecular salts, each assisted by different anions. Several characterization techniques were employed to fully understand these anion-templated supramolecular assemblies, which are self-assembled by a combination of noncovalent interactions, constituting different protonation sites and a versatile spectrum of conformations of the bent ligand. The amino-triazole-based ligand was further utilized in constructing a series of MOFs, namely, MOF-**1**-Zn, MOF-**2**-Zn, and MOF-**3**-Zn. This was achieved using the mixed-linker strategy, combining the selected ligand with a carboxylate linker to introduce basic functionalities ($–NH_2$) and polarizable sulfur atoms onto the MOF pores. In addition to examining the CO_2 capture capabilities of the MOFs, we systematically investigated the dynamic behavior of the pillared-layer MOF, MOF-**2**-Zn, in a single-crystal-to-single-crystal (SC-to-SC) manner during solvent exchange and removal processes. The latter part of the thesis focuses on utilizing amine-tethered MOF for capturing CO_2, aiming to understand long-term material behavior and performance when employed under realistic DAC working conditions. The results presented in this study highlight various obstacles facing the practical implementation of studied amine-tethered MOF for DAC. These challenges include kinetic limitations and inadequate hydrolytic stability, emphasizing that these critical aspects should be focused more on developing practical DAC materials.

Keywords: noncovalent interactions, metal–organic frameworks, single-crystal-to-single-crystal transformation, direct air capture, CO_2 adsorption

TIIVISTELMÄ

Mahajan, Shreya
Amiineja sisältävien metalliorgaanisten verkkorakenteiden soveltuvuus hiilidioksidin talteenottoon suoraan ilmasta
Jyväskylä: Jyväskylän yliopisto, 2024, 69 s. + alkuperäiset artikkelit
(JYU Dissertations
ISSN 2489-9003; 819)
ISBN 978-952-86-0280-4 (PDF)

Negatiivisiin hiilipäästöihin tavoiteltavilla tekniikoilla, kuten suoraan ilmasta talteenotolla (Direct Air Capture, DAC) on merkittävä potentiaali planeettojen lämpenemisen rajoittamisessa. Erilaisten hiilidioksidia sitovien kiinteiden huokosmateriaalien joukossa lupaaviksi materiaaleiksi ovat nousseet rakenteeltaan kiteiset metalliorgaaniset verkkorakenteet (Metal Organic Frameworks, MOFs), joiden eduksi voidaan lukea mm. niiden suuri kemiallinen muokattavuus, suuri huokospinta-ala sekä selektiivisyys hiilidioksidia kohtaan. Väitöskirjatyön ensimmäisessä osassa käydään kirjallisuuden kautta läpi viimeisimpiä tieteellisiä saavutuksia MOF-materiaalien soveltuvuudesta CO_2:n talteenottoon DAC-olosuhteissa, tarkastellen yksityiskohtaisesti MOF:ien rakenteellisia ominaisuuksia ja muokkausmahdollisuuksia, MOF:ien DAC-suorituskykyä eri sorptio-olosuhteissa sekä lopuksi CO_2:n erilaisia adsorptiomekanismeja. Työn toisessa osiossa on käyty läpi tiivistetysti väitöskirjatyöhön liittyvien kolmen tieteellisissä aikakausilehdissä julkaistujen artikkelien tärkeimpiä tuloksia.

Artikkelissa I tutkittiin yksityiskohtaisesti typpirikkaan sekä geometrialtaan taivutetun 4-amino-3,5-bis(4-pyridyyli)-1,2,4-triatsoli ligandin valmistusmenetelmiä sekä siitä valmistettuja 16:sta derivaattasuolaa erilaisten mineraalihappojen avustuksella. Suolojen yksikideröntgendiffraktiolla määritettyjen kiderakenteiden avulla tutkittiin suolojen kationi-anioni vuorovaikutuksia, anionitemplaattiefektiä, ligandien geometrioita ja protonoitumisasteita sekä monimuotoisia supramolekulaarisia kokoonpanoja, jotka muodostuivat kiderakenteissa ei-kovalenttisten heikkojen vuorovaikutuksien välityksellä. Artikkelissa II hyödynnettiin edellä mainittua aminobispyridyylitriatsoli ligandia, josta valmistettiin uudenlaisia kahteen erilaiseen ligandiin perustuvia ja Zn-noodimetallista rakentuvia MOF-yhdisteitä: nimettyinä MOF-**1**-Zn, MOF-**2**-Zn ja MOF-**3**-Zn. Kahden ligandin valmistustekniikassa triatsoli-pohjainen ligandi seostettiin tiofeenidikarboksyyli-happo ligandin kanssa tavoitellen aminoryhmien ja polarisoituvien rikkiatomien yhteisvaikutusta MOF-huokosrakenteessa. Valmistettujen ns. pilarirakenteisten MOF-yhdisteiden (p**2**-Zn) hiilidioksidin talteenottokyky testien (DAC-olosuhteissa) ohella, yhdisteille havaittiin kiderakenteiden dynaamista käyttäytymistä kiinteän tilan liuottimen vaihto- ja poistoprosesseissa ns. yksikiteestä-yksikiteeseen mekanismeina (Single-Crystal-to-Single-Crystal, SC-to-SC). Artikkelissa III tutkittiin amiinifunktionalisoidun etyleenidiamiini-Mg-MOF-74 adsorbentin soveltuvuutta CO_2:n talteenotossa, tavoitteena karakterisoida materiaalin pitkäaikaista käyttäytymistä ja suorituskykyä realistisissa DAC-olosuhteissa. Tulokset tuovat esille lukuisia ongelmakohtia, jotka liittyvät testatun MOF-adsorbentin soveltuvuudesta CO_2-sorptioon DAC-tekniikalla. Erityisiksi haasteiksi osoittautuivat adsorbentin kineettiset rajoitteet sekä riittämätön hydrolyyttinen stabiilius, näin ollen korostaen, että edellä mainittuihin ominaisuuksiin tulee tulevaisuudessa keskittyä entistäkin enemmän käytännön DAC-olosuhteisiin soveltuvia adsorbentteja kehitettäessä.

Avainsanat: ei-kovalenttiset vuorovaikutukset, metalliorgaaniset verkkorakenteet, yksikiteestä-yksikiteeseen rakennemuutos, suoraan ilmasta talteenotto, CO_2 sorptio

Author
Shreya Mahajan
Department of Chemistry
P.O. Box 35
FI-40014 University of Jyväskylä
Finland
shreya.s.mahajan@jyu.fi

Supervisors
Adjunct Professor Manu Lahtinen
Department of Chemistry
P.O. Box 35
FI-40014 University of Jyväskylä
Finland

Reviewers
Professor Anna Lähde
Department of Environmental and Biological Sciences
University of Eastern Finland
Finland

Professor Antonio Frontera
Department of Chemistry
Universitat de les Illes Balears
Spain

Opponent
Professor Len Barbour
Department of Chemistry and Polymer Science
Stellenbosch University
South Africa

FOREWORD

The research included in this doctoral thesis was conducted at the Department of Chemistry at the University of Jyväskylä from 2020 to 2024. I am grateful for the financial support from the Academy of Finland, the University of Jyväskylä, and the Finnish Cultural Foundation.

I would like to express my immense gratitude to my supervisor, Adjunct Professor Manu Lahtinen, for giving me the opportunity to work under his guidance and for introducing me to the fascinating field of MOFs. His consistent support, encouragement, and mentorship have significantly contributed to my growth as a researcher over the years. I am grateful for his kindness, understanding, open-mindedness, positivity, and motivation throughout the course of my journey. I am deeply thankful for the flexibility extended to me, which allowed me to advance as a researcher and cultivate my own ideas. Last but not least, I am sincerely grateful for his profound knowledge in the field, from which I have learned immensely.

I want to express my sincere gratitude to Senior Scientist Jere Elfving, with whom I had the privilege of collaborating and working during my Ph.D. Thank you for your invaluable contributions and insightful discussions, and for helping me enrich my work through our fruitful collaboration. I would also like to thank my reviewers, Professor Anna Lähde and Professor Antonio Frontera, for evaluating my thesis and offering constructive feedback.

I want to express my gratitude to all current and former members of the Lahtinen research group and other colleagues in the Department of Chemistry. I would like to extend my special thanks to Dr. Samu Forsblom and Antti Marttinen for their engaging scientific discussions, support, and availability.

I owe a great deal of gratitude to my incredible parents, Kapil and Richa, for being my unwavering pillars of strength. The education, encouragement, and motivation they have provided have been instrumental in my journey. Dad, your unwavering belief in me has instilled the confidence that nothing is unattainable if I dare to dream. My sister Manisha and niece Delisha have been constant sources of joy, and our conversations during my commutes to university have been incredibly uplifting. To my brother, Shubham, I am grateful for your consistent support and understanding. My family's ongoing support remains my foundation, and I cannot express enough gratitude for everything they have done and continue to do for me.

I must acknowledge the immense support and encouragement from my friends Yamini and Rajanish throughout my Ph.D. journey. Yamini, my true friend of thirteen years, encouraged me to leave India and pursue my Ph.D., offering unwavering support and checking on me during tough times. Rajanish, I am grateful for your generosity and unwavering support. You are a truly unique individual, and I couldn’t have imagined my time in Jyväskylä without you. Your presence has been invaluable to me during challenging times, and I consider you part of my family. Thank you for being such an amazing friend.

To my fiancé, Sachin, thank you for your unwavering support over the past four years. Your inspiration and motivation have been invaluable, consistently reminding me of my aspirations and encouraging me when I doubted myself. Your steadfast presence has been my rock, and I eagerly anticipate our future together. Thank you for being an incredible support system; I look forward to embarking on our next adventures together.

To all my colleagues, friends, and family, thank you so much!

LIST OF INCLUDED PUBLICATIONS

(I) Mahajan, S.; Marttinen, A.; Forsblom, S. and Lahtinen, M., Inorganic Anion-Mediated Supramolecular Entities of 4-Amino-3,5-Bis(4-Pyridyl)-1,2,4-Triazole Salts Assisted by the Interplay of Noncovalent Interactions, *Cryst. Growth Des.*, **2023**, *23*, 5144–5162.

(II) Mahajan, S. and Lahtinen, M., 3D Zinc–Organic Frameworks Based on Mixed Thiophene Dicarboxylate and 4-Amino-3,5-bis(4-pyridyl)-1,2,4-triazole Linkers: Syntheses, Structural Diversity, and Single-Crystal-to-Single-Crystal Transformations, *Cryst. Growth Des.*, **2024**, *24*, 747–762.

(III) Mahajan, S.; Elfving, J. and Lahtinen, M., Evaluating the viability of ethylenediamine-functionalized Mg-MOF-74 in direct air capture: The challenges of stability and slow adsorption rate, *J. Environ. Chem. Eng.*, **2024**, *12*, 112193.

Author´s contribution

The author of the present dissertation performed all the syntheses, characterization, X-ray structural analysis, PXRD analysis, and thermal data presented in publications **I-III**, excluding crystallization experiments and PXRD measurements in publications **I**. For CO_2 adsorption studies, the author participated in making the experiments and the analyses jointly with coauthor Elfving J. in the case of **II-III**. The author wrote the initial draft of Publications **I-II**, and associated supporting information, wrote Publication **III** together with the coauthor (Elfving, J.), and contributed significantly to the revision process in all the Publications.

CONTENTS

ABBREVIATIONS, ACRONYMS AND DEFINITIONS

(1°,2°)	*primary, secondary*
°	degree
3-4-3	*N,N′*-bis(3-aminopropyl)-1,4-diaminobutane
ABDC	2-aminobenzene-1,4-dicarboxylic acid
AC	activated carbon
ad	adenine
ads	adsorption
AEEA	*N*-(2-aminoethyl)ethanolamine
Ar	argon
Atz	3-amino-1,2,4-triazole
AU	asymmetric unit
BC	biochar
BECCS	bioenergy carbon capture and storage
bpt	4-amino-3,5-bis(4-pyridyl)-1,2,4-triazole
C	concentration
CCS	carbon capture and storage
CCU	carbon capture and utilization
CH_4	methane
$CHCl_3$	chloroform
CNTs	carbon nanotubes
CO_2	carbon dioxide
CUSs	coordinately unsaturated sites
DAC	direct air capture
des	desorption
DFT	density functional theory
dmf	*N,N′*-dimethylformamide
dmpn	2,2-dimethyl-1,3-diaminopropane
EA	elemental analysis
ED	ethylenediamine
EtOH	ethanol
FT-IR	fourier-transform infrared spectroscopy
gf	guest-freed
GHGs	greenhouse gases
H_2BDC	1,4-benzenedicarboxylic acid
H_2O	water
H_2tdc	thiophene-2,5-dicarboxylic acid
H_3btc	1,3,5-benzenetricarboxylic acid
H_4DH3PhDC	2′,5′-dimethyl-3,3″-dihydroxy-[1,1′:4′,1″-terphenyl]-4,4″-dicarboxylic acid
H_4dobdc	2,5-dihydroxyterephthalic acid
H_4dobpdc	4,4′-dioxido-3,3′-biphenyldicarboxylic acid
H_4dotpdc	4,4″-dihydroxy-[1,1′:4′,1″-terphenyl]-3,3″-

	dicarboxylic acid
HDatz	3,5-diamino-1H-1,2,4-triazole
HUMs	hybrid ultramicroporous materials
i-PrOH	isopropyl alcohol
MEA	monoethanolamine
MeCN	acetonitrile
MeOH	methanol
mmen	*N,N′*-dimethylethylenediamine
MOFs	metal–organic frameworks
MSA	moisture-swing adsorption
N_2	dinitrogen
NETs	negative emissions technologies
NH_2-BDC	2-amino-terephthalic acid
NMR	nuclear magnetic resonance
OMSs	open metal sites
ox	oxalic acid
P/VSA	pressure/vacuum swing adsorption
PCC	postcombustion capture
pc-H_4dobpdc	3,3′-dihydroxybiphenyl-4,4′-dicarboxylic acid
PEI	poly(ethyleneimine)
PXRD	powder X-ray diffraction
q	sorption capacity
Q_{st}	isosteric heat of adsorption
RH	relative humidity
SBUs	secondary building units
SC-to-SC	single-crystal-to-single-crystal
SCXRD	single-crystal X-ray Diffraction
sql	square lattice
T	temperature
t	time
TCSA	temperature-concentration swing adsorption
TEPA	tetraethylenepentamine
THF	tetrahydrofuran
TREN	tris(2-aminoethyl)amine
TSA	temperature swing adsorption
TVCSA	temperature-vacuum-concentration swing adsorption
Vol	volume

1 INTRODUCTION

Greenhouse gases (GHGs), including CO_2 and CH_4, among others, are critical contributors to global climate change. Hence, curbing the ever-increasing GHG emissions is vital. Unfortunately, global CO_2 emissions have already surpassed 410 ppm, far higher than before the industrial age (~280 ppm CO_2).[1] These alarming levels of CO_2 in the atmosphere have already resulted in the rise of the planet's temperature by more than 1 °C. These warming levels pose an existential challenge to human society, evidenced by rising sea levels, melting polar ice caps, substantial alterations in weather events, and subsequent harmful impacts on various ecosystems. To counteract the planet's temperature rise and accompanying climate change events, the goal has been set to limit the global average temperature rise to "<2 °C" and focus on endeavoring to hold it within 1.5 °C, as laid out in the Paris Agreement.[2]

To hit the target of 1.5 or 2 °C warming limit set worldwide, it is essential to attain net-zero CO_2 emissions by 2050 or 2070, respectively.[3] This is a humongous task, not solely because it calls for drastic and immediate cuts of substantial emissions but also because they are distributed across diverse sectors. The majority (roughly 75%) of global greenhouse gas emissions are from energy-related applications in specific sectors such as residential settings, industrial activities, and transportation. Meanwhile, sectors like waste, agriculture, forestry, the chemical industry, and cement production primarily produced the remaining emissions.[4]

Thus, getting to net zero CO_2 emissions necessitates a diverse mix of mitigation strategies in addition to natural pathways. Rapid decarbonization of power and transportation sectors will be pivotal for net zero emission pathways. Displacing nonrenewable energy sources with representative renewable energy sources such as solar, wind, and other alternative technologies can reduce the devastating effects of rising temperatures. The reduction of emissions in the transportation sector can be achieved by deploying electric vehicles and promoting the use of biofuels and hydrogen. Alongside curtailing fossil fuel emissions and removing excess CO_2 from the atmosphere—a process known as "negative emissions" is expected to play an instrumental role in restoring climate stability.[5]

1.1 CO_2 capture, storage and utilization

Carbon capture and storage, or CCS, is a group of promising technologies that proposes to minimize the rate of CO_2 emission by removing carbon dioxide generated from a large stationary source before it can enter the Earth's atmosphere. As such, CCS enables the mitigation of CO_2 produced by energy-intensive sectors like power generation, steel plants, and cement production. Typically, CCS comprises three subsequent stages, i.e., capturing CO_2 at an emitting source, transporting the extracted CO_2 through gas pipelines or ships to a storage location, and permanently storing or burying it back into the ground.[6,7]

Three main carbon capture methods for manufacturing facilities and power plants include precombustion capture, postcombustion capture (PCC), and oxy-fuel combustion capture (Figure 1).[7–9] The precombustion capture method involves the production of synthetic gas (or syngas). The syngas is then reacted with water to produce CO_2 and H_2. The CO_2 is easily separated, while the high-purity hydrogen is utilized for electricity production. The PCC method recovers CO_2 from flue gas streams exiting from the combustion process of primary fuel (typically coal or natural gas) with the air. This technology has wide applicability because it can be retrofitted to older CO_2 point sources. The CO_2 composition in the gas streams can typically range from ~3 vol-%, e.g., natural gas-fired power plants, to ~15 vol-%, e.g., coal-fired power plants. The CO_2 is diluted primarily by nitrogen, the major component, along with water vapor, oxygen, and other trace impurities. Another potential technology designed for collecting CO_2 is performing oxy-fuel combustion. This technology requires a pure oxygen environment (not regular air) to burn fuel, producing byproducts such as water and CO_2. PCC is currently the most appealing and widely implemented CCS application among all these existing methods.[10] A promising tool complementary to CCS for climate change abatement is carbon capture and utilization (CCU), which involves the recycling of carbon. CCU mainly allows the utilization of captured CO_2 by turning it into useful commodities, such as chemicals and fuels.[11]

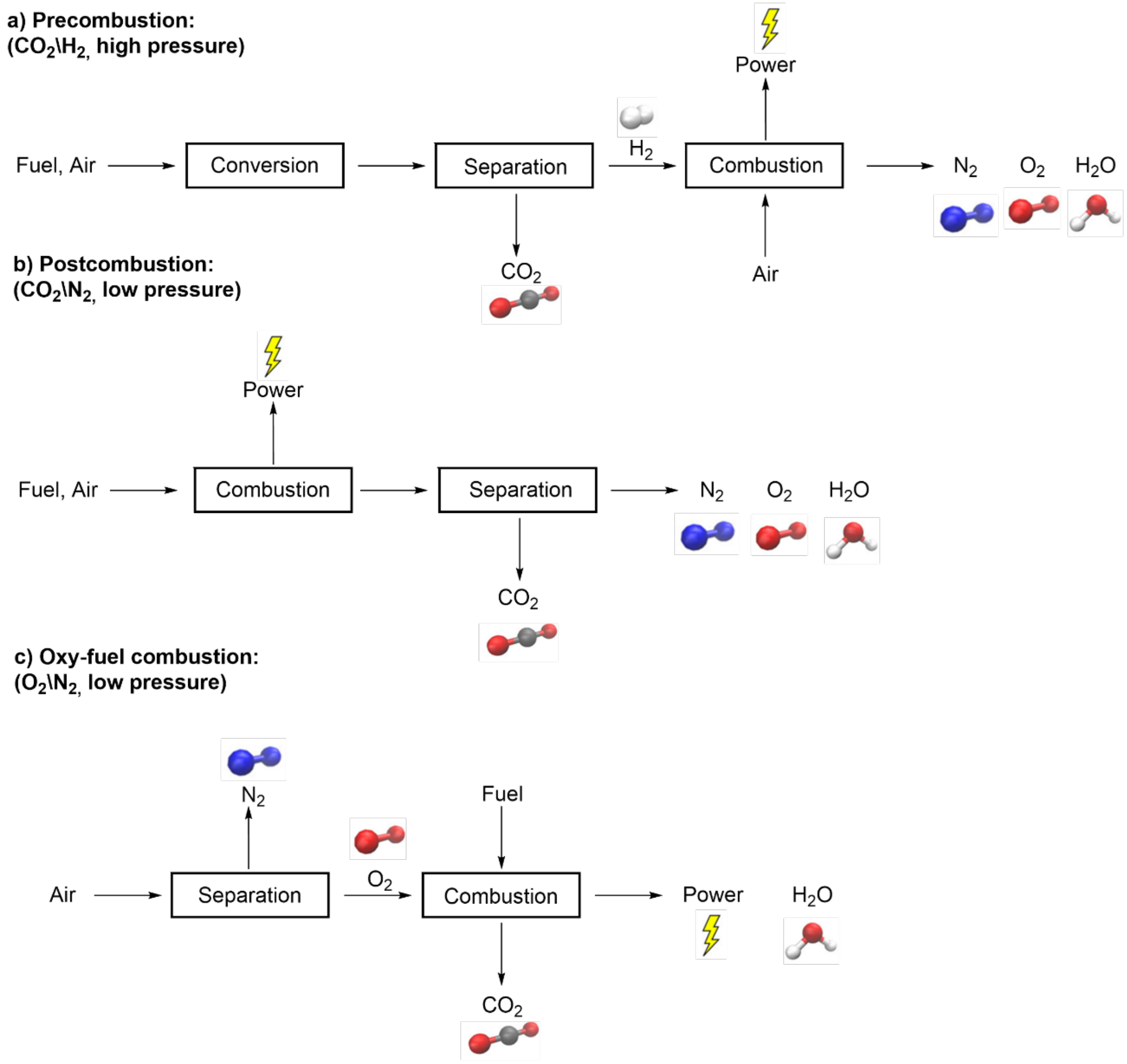

a) Precombustion:
(CO_2\H_2, high pressure)

b) Postcombustion:
(CO_2\N_2, low pressure)

c) Oxy-fuel combustion:
(O_2\N_2, low pressure)

Figure 1: Three different types of methods for CO_2 capture: (a) precombustion, (b) postcombustion, and (c) oxy-fuel combustion.[8]

While the technologies mentioned above reduce emissions by capturing CO_2 at the source of origin, negative emissions technologies (NETs) aim to address existing CO_2 in the atmosphere. Thus, these NETs also play a key role in achieving the set climate goals by capturing additional CO_2 and lowering the climate-harming CO_2 levels. Some methods of achieving negative emissions include biochar (BC), afforestation, bioenergy carbon capture and storage (BECCS), and direct air capture (DAC).[12] Among various approaches, DAC stands out mainly because of its siting flexibility and minimum space requirement, albeit it still faces technological barriers.

1.2 Direct air capture (DAC)

Direct air capture (DAC) is a method that withdraws CO_2 straight from the air around us through physicochemical means. DAC is versatile in its ability to offset CO_2 emissions originating from mobile and distributed sources, alongside addressing emissions from the past. Certainly, one of the attractive aspects of this technology is that DAC plants can be built in ideal locations. This prominently includes, for instance, spots near storage infrastructures or at industrial sites where CO_2 is reused, thereby obviating the requirement for long-distance transportation of massive amounts of CO_2. Moreover, the low or nonexistent level of harmful contaminants (such as SOx and NOx), which can negatively impact the performance of CO_2 sorbents, is further beneficial for the DAC process.[13,14] Although DAC technology is not extensively employed yet, it holds great potential to become an indispensable tool of climate solution strategies. The downside, of course, is that DAC still needs further exploration of certain technological factors, especially the cost and energy requirements. Therefore, considerable technological innovation and carefully targeted research are necessary to fully maximize the potential of this technology to halt climate change.[14–16]

DAC operates through exothermic sorption of atmospheric CO_2 by a CO_2-capture agent (solid adsorbent), followed by its endothermic desorption phase. Essentially, the initial step involves drawing the atmospheric air into a contactor containing the CO_2-capture agent, which selectively grabs CO_2 molecules from the air. Subsequently, e.g., heat and/or pressure swing is applied to the CO_2-saturated adsorbent to drive off the captured CO_2. In doing so, the CO_2-capturing material is regenerated and is ready for a new adsorption-desorption cycle. The extracted concentrated CO_2 can then either be converted, stored, reused, or permanently deposited.[17–19]

From an economical and environmental perspective, the CO_2-capturing adsorbent must be reused repetitively over numerous adsorption/desorption cycles. There are different approaches for the cyclic capture regeneration process, such as pressure/vacuum swing adsorption (P/VSA) or temperature swing adsorption (TSA). The P/VSA approach regenerates the adsorbents by lowering the pressure, while TSA accomplishes it using high-temperature heat.[20] Another method includes moisture-swing adsorption (MSA), which relies on a change in moisture/humidity levels to release CO_2.[21] These modes can be used independently or, in some instances, combined to attain better regeneration efficiency.

Markedly, two prominent technologies for filtering CO_2 molecules out of the air are solvent- and solid-based systems.[18,22] Both technologies showcase great potential for practical scalability, although adsorption-based technologies demonstrate lower operational costs as they require less energy for the cyclic capture regeneration process.[17,23] In the past decades, various solid sorbents, including silica, alumina, zeolites, amine-based materials, metal oxides, polymers, and carbon-based materials, such as activated carbon (AC), graphite, graphene, fullerene, carbon nanotubes (CNTs), and biochar, etc. have been employed for CO_2 capture technologies.[10,24] In particular, a noteworthy class of compounds called metal–organic frameworks (MOFs)[9,25–27] has been recognized as potentially customizable adsorbents, making them appealing contenders for CO_2 capture technologies among a range of solid materials.

1.3 Metal–Organic Frameworks (MOFs) for CO_2 capture

Advanced porous materials such as MOFs are built up by binding inorganic clusters (such as metallic species) with multidentate organic ligands or linkers *via* metal-ligand coordination bonds (dative bonds) to yield multidimensional crystalline materials (Figure 2). Promisingly, by altering the combination of its constituents, MOFs can be customized to have a vast range of functionalities, pore sizes, and structural geometries.[28] In principle, the flexibility with which metal nodes and organic units can be varied leads to the opportunity to envisage the boundless number of chemically and structurally varying frameworks. Undoubtedly, relative to classical porous materials, MOFs offer unparalleled structural advantages, including enormous accessible surface areas, exceptionally high pore volumes, modifiable structures, and tailorable pore size. Indeed, these notable features endow MOFs with incredibly versatile capabilities and underpin them for a broad range of applications, including but not limited to chemical sensing, molecular adsorption, drug delivery, catalysis, and purification.[29–33]

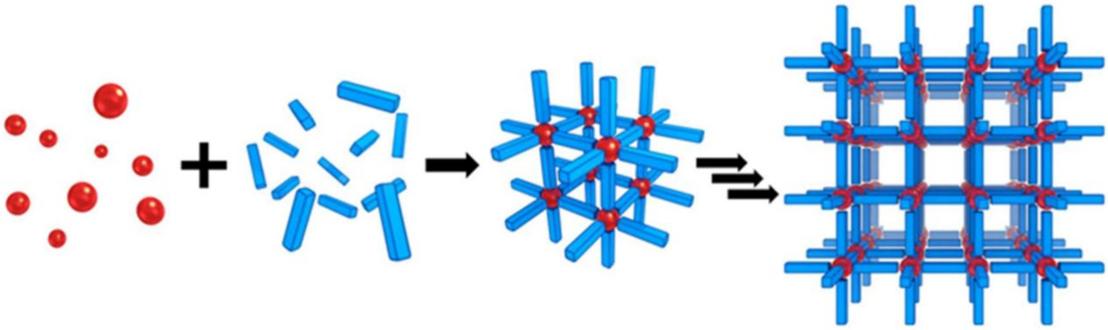

Figure 2: Schematic representation of MOF constituent's self-assembly process: metal nodes (red spheres) and organic units (blue struts).[34]

When building MOFs for DAC applications, it is imperative to consider at least two key aspects. Firstly, the high selectivity and reversible capture of CO_2 from ultra-dilute conditions (~420 ppm), and secondly, its performance under realistic working conditions.[22,25,26,35–38] To this end, MOFs that display CO_2-binding functionalities are reaching the required efficiency for selectively binding CO_2 over other abundant components in the air. Moreover, the reversible CO_2

binding/release process ensures that the MOF can readily be recovered and reused for multiple cycles.[25,37] In contrast, liquid absorbents, such as aqueous monoethanolamine (MEA) solution, exhibit a strong affinity for CO_2 but need energy-intensive regeneration.[25,36,38] The sorbent stability under realistic process conditions, most importantly its resistance to water vapor and heat, is another benchmark factor that needs to be considered when MOFs are screened for industrial separations.

Over the years, several approaches have been proposed and explored to optimize adsorbents for efficient CO_2 capture under ultra-dilute concentrations. The following sections highlight the most prevalent structural designs that endow MOFs with the ability to adsorb CO_2 under DAC conditions. It is worth mentioning that although many adsorbents are available in the literature, this discussion focuses on some of the most notable CO_2-selective MOFs. The sections below provide a brief overview of the progress made in developing MOFs for having DAC potential. The overview outlines fundamental structural approaches, an examination of the DAC performance of MOFs under different conditions, material longevity, and the underlying CO_2 adsorption pathways.

1.3.1 MOFs with exposed metal cations

MOFs encompassing exposed metal cations, also known as coordinately unsaturated sites (CUSs) or open metal sites (OMSs), have demonstrated remarkable potential for CO_2 capture.[25] In principle, these CUSs in MOFs have a great affinity for CO_2, given that the partial positive charges on the metal sites typically work as Lewis acid centers, thus leading to a stronger interaction with quadrupolar CO_2 molecules over dinitrogen (N_2). Accordingly, a higher concentration of accessible OMSs within MOFs affords reasonable isosteric heat of adsorption (Q_{st}) for CO_2, enabling more selective CO_2 adsorption than other small non-polar components (e.g., N_2) in the atmosphere. Distinct exposed metal centers were observed in dinuclear paddlewheel (open Cu^{2+} sites) and trinuclear secondary building units (SBUs) (open Fe^{3+} sites), as exemplified by $Cu_3(btc)_2$ (H_3btc = 1,3,5-benzenetricarboxylic acid; HKUST-1)[39], and $Fe_3OX(btc)_2$ (X= OH or F; MIL-100(Fe))[40], respectively.

Besides these, the most prominent examples of OMS-MOFs, illustrating outperforming CO_2 adsorption capabilities, are termed as M-MOF-74 family (M is a divalent cation, e.g., Mg^{2+}, Ni^{2+}, Co^{2+}, Zn^{2+}), commonly referred to as CPO-27-M, or $M_2(dobdc)$ (derived from H_4dobdc= 2,5-dihydroxyterephthalic acid).[41-43] Interestingly, the isoreticular expansion analogs of MOF-74 are realized from elongated organic linkers with lengths varying from one to eleven phenylene units (7 to 50 Å), affording a series of derivative frameworks known as IRMOF-74-I to XI.[44] A key MOF in the MOF-74 family, Mg-MOF-74, is known so far as the best-performing MOF at elevated temperatures for higher concentrations of CO_2 (10-15%), adsorbing 5.28 $mmol_{CO2}/g_{sorbent}$, at 40 °C and 0.15 bar, respectively.[45]

The Mg-MOF-74 structure comprises infinite rod-like SBUs and exhibits robust ~11 Å hexagonal one-dimensional channels. Each metal ion in this three-dimensional hexagonal framework is penta-coordinated with dobdc^{4-} ligand bound by three carboxylate groups and two phenolates. The one weakly bound solvent molecule (e.g., water or dmf, depending on the synthetic conditions) fills the sixth coordination site, completing the octahedral coordination environment around the metal core. To access abundant open Mg^{2+} sites, the dangling solvent molecules can be evacuated by activating the framework with the application of heat and vacuum treatment. In the activated form (guest-free state), the magnesium cation possesses a square pyramidal coordination geometry (Figure 3), thereby resulting in an unshielded positive charge pointing inwards to the MOF-74 channels and allowing favorable interactions with CO_2 guest molecules inside the pore systems.

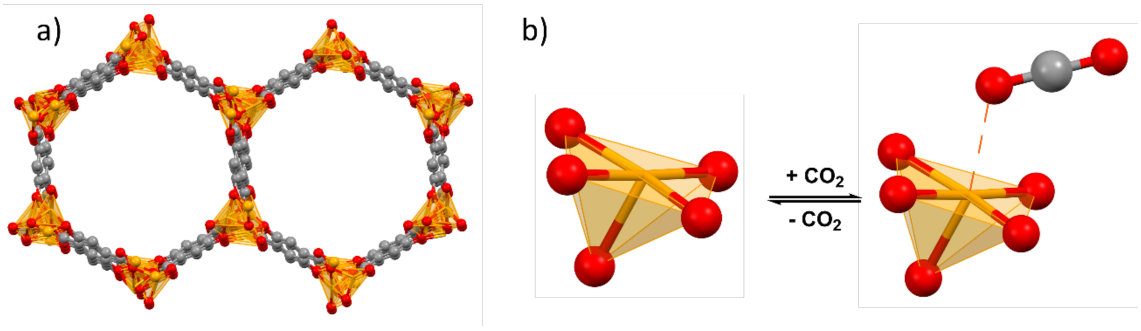

Figure 3: Illustration of (a) Mg_2(dobdc), and (b) CO_2 insertion into a row of Mg^{II}–sites. Only relevant atoms are shown; spheres represent Mg (orange), oxygen (red), and carbon (grey); redrawn from CSD entry: QOQXUS.[46]

For M-MOF-74, a combination of experimental studies and theoretical calculations have revealed that CO_2 typically binds to square pyramidal M^{2+} cation in an end-on coordination fashion.[25,47–49] Notably, it has been shown that the CO_2 adsorption properties can be tuned by substituting different metallic centers in the isostructural M-MOF-74 series.[42] The strong affinity of the Mg-MOF-74 for CO_2 adsorbate is noted by the high Q_{st} value (43 kJ/mol). However, as a structure analogous to Mg-MOF-74, Zn-MOF-74 displayed the weakest interactions (Q_{st} = 26 kJ/mol), whereas Ni-MOF-74 and Co-MOF-74 displayed moderate affinities of 38 and 33 kJ/mol, respectively.[50] Typically, the high CO_2 affinity displayed by Mg-MOF-74 has been explained by the dominant ionic character of the Mg–O bond, originating from the Lewis acidic nature of the coordinatively unsaturated Mg sites. Owing to the metal center's electron-deficient nature, it demonstrates a partial positive charge, which results in the attraction of electron-rich O atoms of CO_2 (Figure 3). Thus, contributing to effective charge-quadrupole forces between free metal sites and the CO_2 molecules.[35,42]

While MOFs with such structural features demonstrate a very good CO_2 uptake under dry conditions, they face key challenges when deployed under moisturized gas streams. More specifically, these highly reactive OMSs remain unprotected from the attack of strongly polar water molecules, resulting in favoring high water adsorption rather than CO_2.[51] For instance, Mg-MOF-74 displays a high CO_2 adsorption capacity of 6.1 $mmol_{CO2}/g_{sorbent}$ at 0.15 bar CO_2 and 25 °C under dry conditions.[42] However, when Mg-MOF-74 is exposed to a humid environment, H_2O has been shown to out-compete CO_2 for exposed metal cation adsorption sites, revealing only 16% of the original capacity for flue gas capture under 70% relative humidity (RH).[52] Thus, the reactivity of OMSs with moisture forbids CO_2 adsorption by rapidly diminishing the reactive sites and making such structural features unsatisfactory for realistic DAC applications. However, as summarized in the following sections, these OMSs can be exploited to incorporate chemisorption sites in the interior of MOFs, which often allows selective CO_2 adsorption in the presence of water.

1.3.2 Amine-appended MOFs

In general, capturing CO_2 effectively from typical atmospheric conditions requires sorbents that offer optimum CO_2 capacity along with preferential adsorption of CO_2 against N_2 and H_2O. Although solvent-based systems demonstrate fast and selective adsorption of CO_2 even in the presence of moisture, the regeneration following this chemically driven CO_2 separation is energy intensive and, therefore, cost prohibitive.[53] As an alternative, supported amine adsorbents have been widely acknowledged as the most promising solutions for low-pressure CO_2 adsorption.[25,27] By confining amines into the pores of the porous support material, the resulting chemical adsorbents impart chemisorptive interactions and feature considerably lower energy requirements.[53]

Typically, the CO_2 capture pathway for immobilized amine groups (primary or secondary) onto solid supports proceeds *via* a two-step reversible mechanism comprising the reaction of CO_2 with an active amine group to form zwitterion species, followed by its deprotonation by a free amine group to produce ammonium carbamate ion pairs.[51,54] In humidified gas streams, H_2O can take part in the reaction of CO_2 with an amine group to afford ammonium bicarbonate (Scheme 1).[51,55,56]

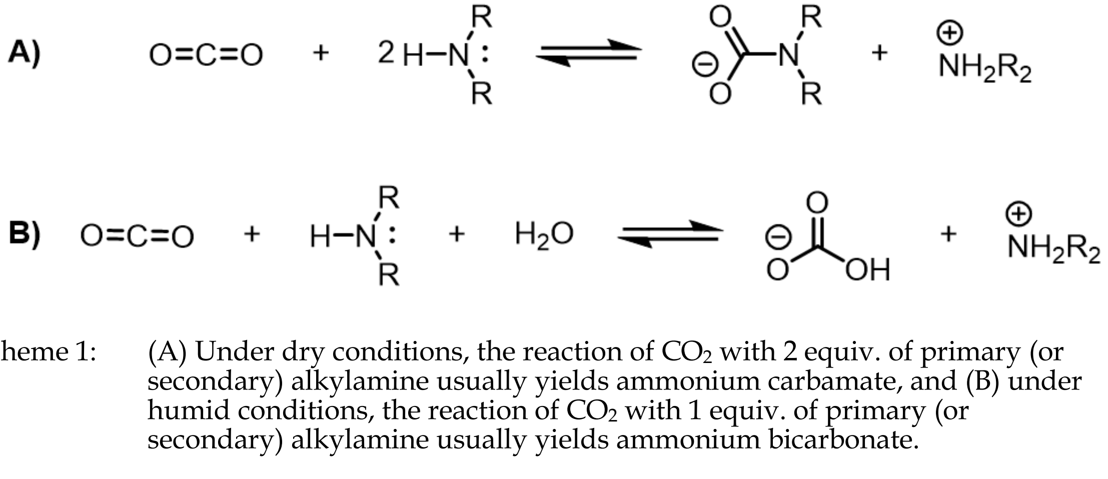

Scheme 1: (A) Under dry conditions, the reaction of CO_2 with 2 equiv. of primary (or secondary) alkylamine usually yields ammonium carbamate, and (B) under humid conditions, the reaction of CO_2 with 1 equiv. of primary (or secondary) alkylamine usually yields ammonium bicarbonate.

It can be noted that the CO_2 adsorption over supported amines is not only limited to the formation of carbamate or bicarbonate moieties. The nature of CO_2 adducts formed may vary depending on the support material, adsorption conditions, and amine loading; for example, the reaction of CO_2 with supported amines may also give rise to carbamic acid under dry or humid conditions.[57–60]

The porous materials extensively used to produce amine-based adsorbents include porous silica, mesoporous alumina, mesoporous carbon, porous polymers, and nanofibrillated cellulose-based supports.[56,61–66] Beyond these, by borrowing advantages from MOF support and amine sites, high-performing materials suitable for DAC can be prepared by incorporating amine functionalities within a MOF. So far, two straightforward strategies have been used to decorate the framework pores with Lewis basic functionalities. First, employing amine functionality within the linker. Second, post-synthetic modification of frameworks with highly basic amines appended to OMSs.

1.3.2.1 MOFs with amine-functionalized ligands

The inclusion of amine-functionalized ligands in MOF synthesis is one of the strategies to functionalize MOF pore walls with amines and by that, boost the binding affinity for CO_2 gas molecules. An early example of *N*-rich MOF is bio-MOF-11 [$Co_2(ad)_2(CO_2CH_3)_2 \cdot 2DMF \cdot 0.5H_2O$], derived from the assembly of adenine and cobalt acetate tetrahydrate. Owing to the adenine's Lewis basic adsorption sites, both aromatic amine and pyrimidine groups decorate the pore's surface, resulting in moderate CO_2 uptake (~1.30 $\text{mmol}_{CO2}/\text{g}_{\text{sorbent}}$ at 0.15 bar CO_2, 25 °C) with relatively a low Q_{st} value of ~45 kJ/mol.[67]

Aromatic amine-containing ligands, particularly 2-amino-terephthalic acid (NH_2-BDC), have been extensively explored to construct aromatic amine-based frameworks for effective CO_2 adsorption.[9] For instance, amine-bearing IRMOF-3 [$Zn_4O(NH_2\text{-BDC})_3$] had slightly higher CO_2 adsorption than the parent, nonfunctionalized IRMOF-1 [$Zn_4O(BDC)_3$].[68] Similar enhancements were seen in different amine-bearing MOFs, namely NH_2-MIL-53 [$Al(OH)(NH_2\text{-BDC})$], NH_2-UiO-66 [$Zr_6O_4(OH)_4(NH_2\text{-BDC})_6$], and NH_2-MIL-125 [$Ti_8O_8(OH)_4(NH_2\text{-BDC})_6$].[69–71] Besides, MOFs constructed from amine ligands with a combination of carboxylate linkers have also demonstrated improved CO_2 adsorption and superior N_2/CO_2 selectivity. For example, the CO_2 uptake in amino triazolate-based MOF $Zn_2(Atz)_2(ox)$ (where Atz = 3-amino-1,2,4-triazole and ox = oxalic acid) was observed to be around 3.78 $\text{mmol}_{CO2}/\text{g}_{\text{sorbent}}$ (at 1.2 bar and 20 °C) and negligible for N_2, H_2, and Ar.[72] The CO_2 molecules were observed to primarily interact with amine moieties *via* H-bonding ($N-H\cdots O$) and electrostatic interactions, as reflected in a low Q_{st} value of ~40.8 kJ/mol.[72,73]

It should be noted that in the context of low-concentration CO_2, MOFs that involve aromatic amines tend to bind CO_2 less strongly than post-synthetically modified MOFs. This is attributed to the difference in basicity between alkyl amines and aromatic amines. Because of the delocalization of the lone pair onto the aromatic amine linker, the nature of CO_2 binding in such aromatic amine-based frameworks might not be the same as it would be with alkyl amines. This is also reflected by the observed modest heat of adsorption (30-50 kJ/mol), emphasizing that only physisorption is taking place over these materials, and therefore, stronger basic functionality in the organic backbone will be needed to afford chemisorption.[9,35,74]

For example, in an attempt to improve CO_2 capture performance under humid streams, a terphenylene linker of the expanded version of parent MOF-74 termed IRMOF-74-III (Mg_2(DH3PhDC), where H_4DH3PhDC = 2′,5′-dimethyl-3,3″-dihydroxy-[1,1′:4′,1″-terphenyl]-4,4″-dicarboxylic acid), was decorated with highly reactive alkylamine groups.[75] The presence of dangling amine groups onto an organic linker in the pores of IRMOF-74-III-CH_2NH_2 enabled identical CO_2 uptake under both dry and moist conditions. The dynamic breakthrough experiment demonstrated CO_2 uptake of 0.8 $\mathrm{mmol_{CO2}/g_{sorbent}}$ using a mixed gas containing 16/84% of CO_2/N_2, respectively, at 25 °C under dry and moist conditions (65% RH).[75] Thus, this highlights that CO_2 adsorption was hardly impacted by water vapor, and the selective CO_2 capture over water is associated with the presence of primary alkylamine functionalities that served as adsorption sites for CO_2 instead of OMSs. Conversely, under similar humid conditions, IRMOF-74-III-CH_3 without amine-functionalization displayed an 80% loss in material performance compared to dry conditions. It was assumed that IRMOF-74-III-CH_3 relied on OMSs for CO_2 adsorption. However, under wet conditions, the water molecules readily outcompete CO_2 for occupying these OMSs, thereby inhibiting access to CO_2.

Notably, this strategy has been extended further by increasing the primary alkylamine functionalities in the same framework.[58] Two primary amine groups were covalently anchored onto each organic linker of IRMOF-74-III, yielding IRMOF-74-III-$(CH_2NH_2)_2$. In comparison to IRMOF-74-III-CH_2NH_2, the resulting MOF displayed a 34% increase (1.2 $\mathrm{mmol_{CO2}/g_{sorbent}}$) in its dynamic CO_2 uptake, indicative of CO_2 capacity dependence on the density of amino groups within framework pores. Importantly, it was found that under dry conditions, IRMOF-74-III-$(CH_2NH_2)_2$ predominantly chemisorbs CO_2 by forming carbamic acid species instead of ammonium carbamates. However, with increased humidity, the reaction between adsorbed CO_2 and linker amine sites favored the formation of ammonium carbamate species (Figure 4).[58]

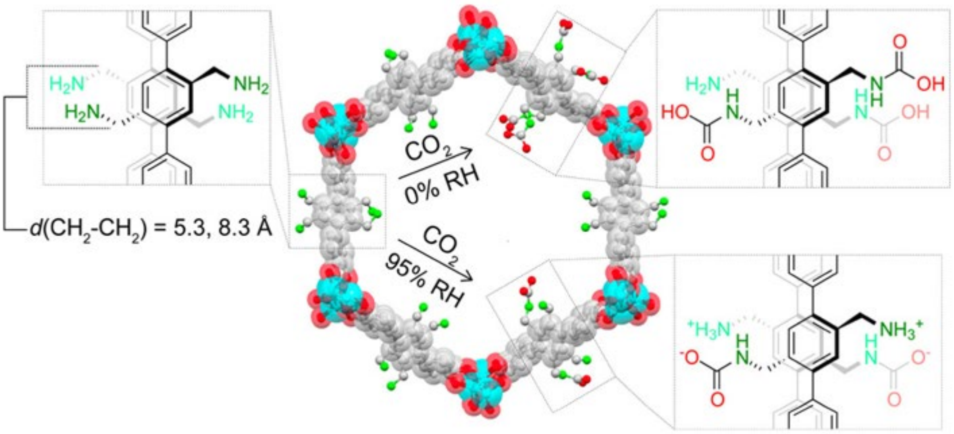

Figure 4: Carbon dioxide chemisorption products, carbamic acid, and ammonium carbamates in IRMOF-74-III-$(CH_2NH_2)_2$.[58]

Evidently, the concept of installing Lewis basic amine moieties within the linker backbone seems to be attractive for superior CO_2/H_2O selectivity, but the overall CO_2 adsorption capacities achieved have not reached the level to compete with post-synthetically amine-grafted frameworks (Section 1.3.2.2). Thus, maximizing the density of alkylamines within the framework and increasing the adsorption capacity, particularly around ultra-diluted CO_2 pressures, would be expected to unlock the full potential of this class of material for practical DAC application.[25,37]

1.3.2.2 MOFs with post-synthetic amine functionalization

The post-synthetic pathway involves anchoring highly basic diamines onto the CUSs of the MOF, where only one end of diamine is tied down, and the other amine end is exposed in the channel to bind CO_2 through chemisorption. For instance, open Mg^{2+} sites of Mg-MOF-74 have been exploited to tether shorter diamines, including ethylenediamine (ED)[76] and hydrazine[77]. Choi *et al.*[76] reported that ED-appended Mg-MOF-74 produced a 12% increase in CO_2 uptake (1.51 $mmol_{CO2}/g_{sorbent}$) in the presence of dry simulated air streams (400 ppm CO_2/Ar) compared to the parent framework. Furthermore, under dry TSA cycling, aminated-MOF was found to retain its original uptake over four cycles, as opposed to unmodified MOF, which lost at least 20% of its CO_2 capacity, from 1.35 to 1.06 $mmol_{CO2}/g_{sorbent}$. In a follow-up study, both aminated-MOF and unmodified Mg_2(dobdc) were subjected to steam treatment (110 °C in steam/N_2, 48 h) in an autoclave.[78] The TGA adsorption experiment (pure CO_2 at 25 °C) revealed that CO_2 capacity for the aminated-MOF did not change much (4.66 to 4.47 $mmol_{CO2}/g_{sorbent}$), while plain unfunctionalized Mg_2(dobdc) uptake faded by 60%, dropping from 4.27 to 1.71 $mmol_{CO2}/g_{sorbent}$. Although this study showed that the CO_2 uptake is hardly affected by water presence, little was known about the repeated use of the ED-grafted Mg_2(dobdc).

Later, Liao *et al.*[77] demonstrated that hydrazine-modified Mg-MOF-74 could achieve CO_2 capacity as high as 3.89 $mmol_{CO2}/g_{sorbent}$ under atmospheric CO_2 concentrations (400 ppm and 25 °C). The observed high CO_2 capacity is attributed to the high density of amine groups in the framework and their capability to capture CO_2 by forming highly desirable carbamic acid. This is manifested by a much higher Q_{st} value (90 kJ/mol) obtained at near-zero coverage. Nonetheless, the high toxicity of hydrazine represents a challenge to the material's usefulness in real DAC applications.

The isoreticular pore-expanded variant of Mg-MOF-74, named Mg_2(dobpdc), was synthesized using an extended linker [H_4dobpdc = 4,4′-dioxido-3,3′-biphenyldicarboxylic acid]. The sufficiently enlarged channels (18.4 Å) obtained allowed the successful attachment of *N*,*N*′-dimethylethylenediamine (mmen) into the Mg_2(dobpdc). The resulting mmen-appended Mg_2(dobpdc) displayed a CO_2 uptake of 2.00 $mmol_{CO2}/g_{sorbent}$ at atmospheric CO_2 levels and a high Q_{st} value of 71 kJ/mol, indicating a clear dependency on chemisorptive interactions. Additionally, the material was observed to maintain its adsorption capacity throughout ten cyclic runs in dry air.[79]

The mmen-appended M_2(dobpdc) (M = Mg, Mn, Fe, Co, Zn) are identified as "phase-change" adsorbents with nonclassical, single-step-shape isotherms. The step-like CO_2 adsorption profile arises from a cooperative mechanism wherein both ends of mmen species serve to participate in binding CO_2 (Figure 5). Particularly, a proton is transferred from a metal-bound amine to an adjacent uncoordinated amine end as an incoming CO_2 molecule concurrently gets inserted into the dative metal-nitrogen bond. Hence, this results in the disruption of M–N bonds followed by the formation of M–O bonds, which in turn leads to metal-bound carbamate species charge-balanced by neighboring ammonium counter cations that line the pore surfaces of the framework entirely.[80]

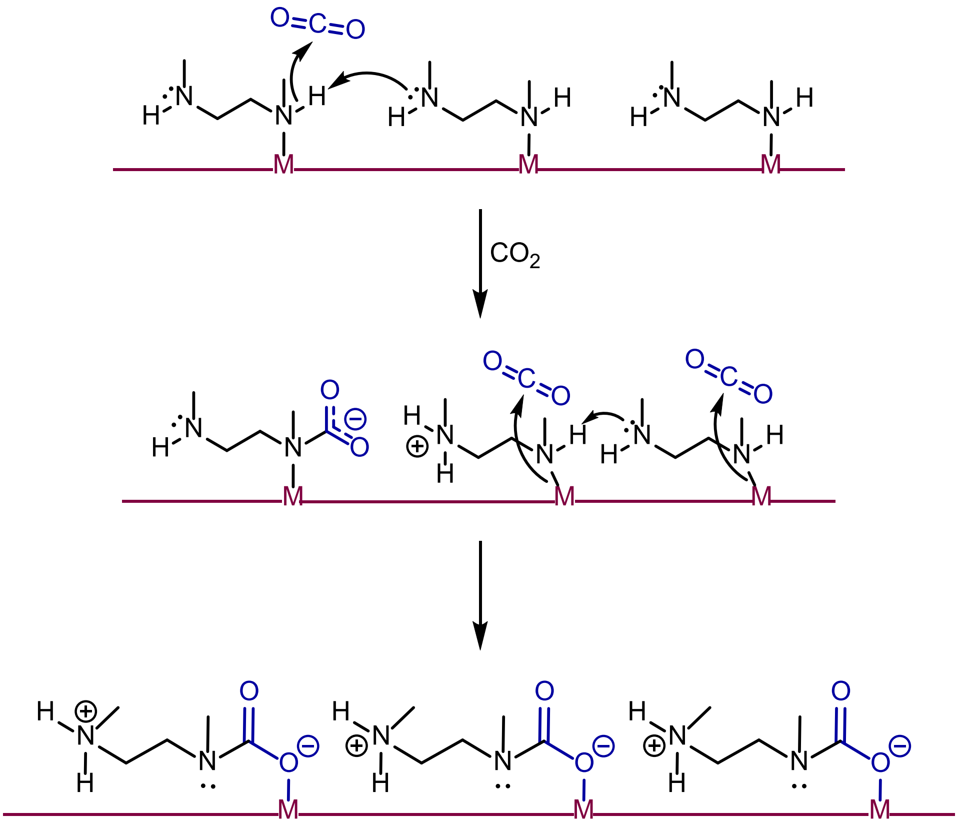

Figure 5: Illustration of cooperative CO_2 insertion mechanism. Reproduced (modified) from ref.[80]

Intriguingly, after exposure to a humid gas mixture (14% CO_2/N_2 up to 32% RH conditions), CO_2 adsorption on mmen-appended Mg_2(dobpdc) was found to be 14% higher (nearly 4.2 $mmol_{CO2}/g_{sorbent}$) compared to dry conditions. Infrared spectroscopy measurements provided no evidence of bicarbonate species and corroborated the cooperative CO_2 insertion mechanism even in the presence of water. Notably, for mmen-appended Ni_2(dobpdc), the difference in CO_2 adsorption was more pronounced, with approximately a 3-fold increase compared to dry conditions. This is because an exceptionally stable Ni–N bond makes CO_2 insertion into the Ni–N bond difficult, thus leading to a typical Langmuir-type isotherm. Hence, it was inferred that water's promoting effect could be related to the formation of bicarbonate species or the formation of additional ammonium carbamate pairs.[51]

The utility of ED-functionalized Mg_2(dobpdc) for CO_2 capture from air has also been tested.[81] The aminated MOF exhibited an excellent uptake of 2.83 $mmol_{CO2}/g_{sorbent}$ at 390 ppm dry CO_2 and T = 25 °C, with a relatively lower Q_{st} range of 49–51 kJ/mol. Notably, compared to the modified version of mmen, this material´s uptake is about 1.4 times higher. It has much sharper CO_2 isotherms, presumably because of the increased accessibility of CO_2 onto primary amines compared to the secondary amine groups. Based on *in situ* IR measurements, CO_2 chemisorption was found to be associated with the formation of the carbamic acid mechanism. This study also suggested that aminated material is not greatly impacted by humidity. However, during the TSA cycling, the material demonstrated a 6% capacity fade after five cycles in simulated air.

In addition to mmen and ED, Mg_2(dobpdc) has been tethered with a wide range of organic diamine species, resulting in a series of diamine appended Mg_2(dobpdc) variants with different CO_2 adsorption products (Figure 6). For example, Forse *et al.*[82] conducted a systematic survey of thirteen different diamine-appended Mg_2(dobpdc) variants. They demonstrated that the use of the multinuclear nuclear magnetic resonance (NMR) spectroscopy combined with van-der-Waals-corrected density functional theory (DFT) calculations can enable the identification of canonical CO_2 adsorption adducts, for example, carbamic acid pairs and ammonium carbamate chains. The formation of ammonium carbamate chains was determined to be the predominant pathway for a range of diamine-appended Mg_2(dobpdc) variants. Interestingly, the exploration of dmpn-Mg_2(dobpdc) material (dmpn = 2,2-dimethyl-1,3-diaminopropane) revealed a new mixed chemisorption mode involving the formation of both carbamic acid species and ammonium carbamates (Figure 6).

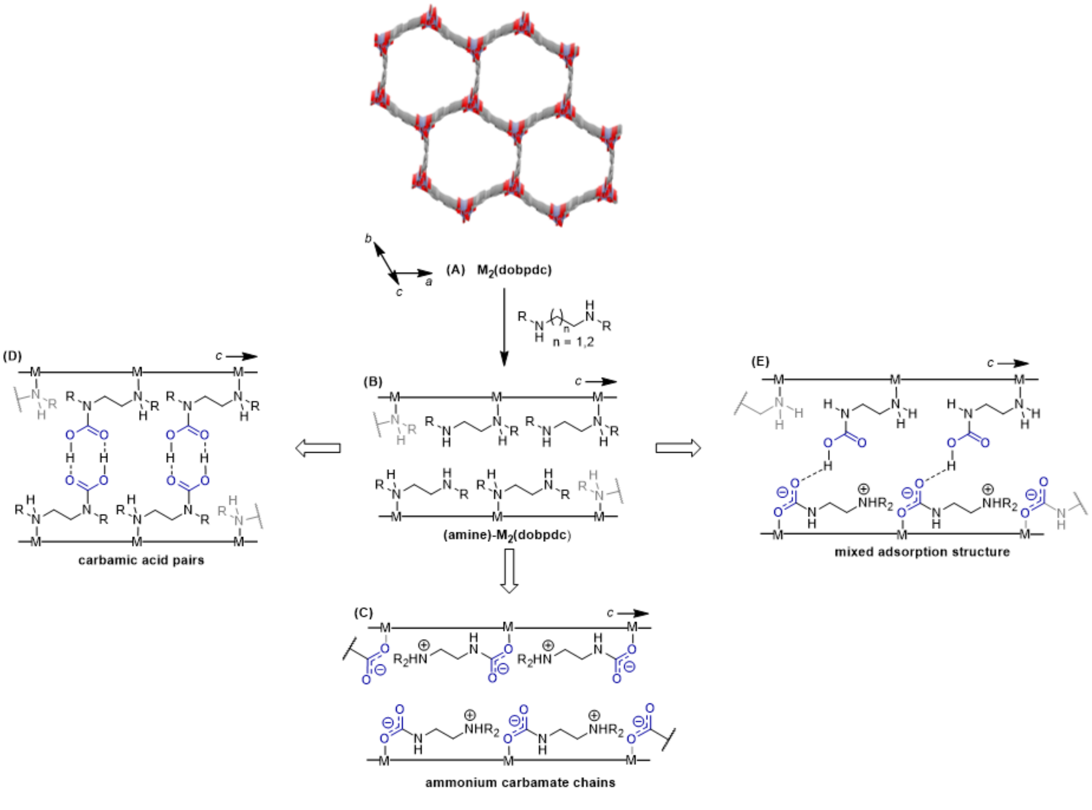

Figure 6: Illustration of different CO_2 adsorption modes in amine appended M_2(dobpdc) variants. (a) M_2(dobpdc), (b) amine-appended M_2(dobpdc), (c) ammonium carbamate chains, (d) carbamic acid pairs, and (e) mixed ammonium carbamate-carbamic acid. Redrawn from CSD entry: JETVOW[83]; reproduced (modified) from ref.[84]

To date, variants of Mg_2(dobpdc) grafted with *primary, secondary* (1°,2°) diamines are notable for their low CO_2 step pressures and thermal stabilities. It has been shown that increasing the alkyl group size on the secondary amine endows (1°,2°) alkylethylenediamine-Mg_2(dobpdc) variants with more resistance against diamine volatilization. Nevertheless, these frameworks displayed double-step CO_2 adsorption behavior rather than one-step, which has been ascribed to steric conflict between neighboring ammonium carbamate chains within an asymmetrical pore structure. Thus, this phenomenon leads to increased H_2O co-adsorption under wet conditions and limits the CO_2 working capacities. It was found that these undesirable steric conflicts between neighboring diamines could be lessened by placing the neighboring metal centers farther apart from each other. This was achieved by switching the base framework from Mg_2(dobpdc) to either a framework that possesses uniform hexagonal channels, like in Mg_2(pc-dobpdc) (pc-H_4dobpdc = 3,3′-dihydroxybiphenyl-4,4′-dicarboxylic acid) or an extended organic ligand, like Mg_2(dotpdc) (H_4dotpdc = 4,4″-dihydroxy-[1,1′:4′,1″-terphenyl]-3,3″-dicarboxylic acid). As a result, reduced steric conflict afforded materials that displayed single-step CO_2 adsorption behavior, minimal co-adsorption of water vapor, and no noticeable diamine loss.[85]

Efforts have been devoted to replacing diamines with high molecular weight tetraamine chains to overcome the shortcoming of diamine severing upon CO_2 capture/release cycles. For example, Kim *et al.*[86] reported robust (3-4-3)-appended Mg_2(dobpdc) [3-4-3 = *N*,*N*′-bis(3-aminopropyl)-1,4-diaminobutane] exhibits cooperativity achieved through double-step ammonium carbamate chains mechanism. Unlike singly tethered diamines, these tetramines are strongly tied down at both ends by coordinative interactions, which in turn stabilizes the amines by locking them within the chemical framework and serves to enhance thermal and hydrolytic stability under harsh conditions.

While numerous studies dealing with alkylamine-appended Mg-MOF-74 variants have appeared, only a handful of studies have quantified the adsorption behavior of other MOFs for DAC. Among these, the MIL-101 family and Zr-based UiO-66 MOFs are the most commonly assessed support materials for amine loadings in CO_2 DAC applications.[87–92] For example, Darunte *et al.*[87] investigated the DAC performance of supported tris(2-aminoethyl)amine (TREN) and branched poly(ethyleneimine) (PEI) in MIL-101(Cr) under ambient conditions. The TREN-loaded MIL-101(Cr) showed an impressive CO_2 capacity of 2.8 $mmol_{CO2}/g_{sorbent}$ under DAC conditions. However, the long-term stability of the modified material remained a concern since a considerable loss from its initial capacity was observed only after three continuous cycles due to the amine volatilization in cycling experiments. Nonetheless, PEI-loaded MIL-101(Cr) featured fairly good cyclic stability with a modest CO_2 uptake of 1.35 $mmol_{CO2}/g_{sorbent}$ in 400 ppm CO_2.

To boost the CO_2 capture performance, Li *et al.*[88] exploited a new approach based on the Brønsted acid-base reaction, wherein alkylamine molecules were integrated into sulfonated Cr-MIL-101-SO_3H MOF. The tris(2-aminoethyl)amine (TAEA) modified Cr-MIL-101-SO_3H exhibited a CO_2 cyclic uptake capacities of 2.28 and 1.12 $mmol_{CO2}/g_{sorbent}$ in the presence of 150 mbar CO_2, 40 °C and 0.4

mbar CO_2, 20 °C, respectively. Additionally, the material was observed to maintain its adsorption capacity throughout 15 continuous cyclic runs.

Another notable example is the work of Rim *et al.*[89], in which 30 wt. % of tetraethylenepentamine (TEPA) was successfully loaded into MIL-101(Cr) to achieve CO_2 uptakes of 1.12 and 0.39 $mmol_{CO2}/g_{sorbent}$ at DAC sub-ambient (-20 °C) and ambient conditions (25 °C), respectively. Interestingly, this material showed a stable working capacity of 0.73 $mmol_{CO2}/g_{sorbent}$ (dry CO_2) and 0.82 $mmol_{CO2}/g_{sorbent}$ (humid, 70% RH) upon 15 and 5 small temperature swings, respectively, requiring much lower regeneration energy (e.g., adsorption at -20 °C and desorption at 25 °C). In the further studies of Rim *et al.*[59], *in situ* FT-IR was utilized to identify the nature of the CO_2 capture behavior for MIL-101(Cr)-supported TEPA (30 wt. %). It was postulated that amines-CO_2 interaction was dominated by both physisorption, as well as the formation of carbamic acid species that were stabilized by surface hydroxyl groups or water molecules, eventually accounting for notable CO_2 uptake.

In a recent contribution, Liu *et al.*[90] presented evaluation of *N*-(2-aminoethyl) ethanolamine (AEEA) functionalized MOFs, namely MIL-100(Cr) (referred to as MF-Cr-AEEA), MIL-100(Fe) (MF-Fe-AEEA), and UiO-66(Zr) (MF-Zr-AEEA) for CO_2 capture in DAC conditions. This study outlined that AEEA bound CUS sites exclusively through a secondary amine, and the primary amine end, exposed into the channel, served as a CO_2 adsorptive site. Notably, the studied sorbents showed varying CO_2 capture capacities, with MF-Cr-AEEA yielding the highest uptake capacity of 2.05 $mmol_{CO2}/g_{sorbent}$ at humid DAC conditions (water vapor concentration 1%). On the contrary, other modified sorbents demonstrated rather negligible capacities. The higher performance of MF-Cr-AEEA was attributed to the high abundance of exposed Cr^{3+} cations in MIL-100(Cr) by offering better amine grafting without impairing active sites because of the framework's higher surface area, pore volume, and low acidity. However, during cycling experiments, the CO_2 capture capacity of MF-Cr-AEEA was found to drop down to around 1.86 $mmol_{CO2}/g_{sorbent}$ only after seven adsorption-desorption cycles. In another study, monoethanolamine (MEA) impregnated MIL-101(Cr) was assessed for its potential for a DAC process. The modified material attained a DAC pseudo-equilibrium capacity of 1.50 $mmol_{CO2}/g_{sorbent}$ under dry conditions, which was further elevated to 2.15 $mmol_{CO2}/g_{sorbent}$ under humid conditions (~80% RH). However, detailed stability tests have not been reported over repetitive adsorption-desorption cycles for this sorbent type nor under humid or dry conditions.[91]

More recently, Dong *et al.*[92] prepared a series of Quasi-X-UIO-66 (X= 1, 2, 3) using varying amounts of *p*-aminobenzoic acid in place of 1,4-benzene dicarboxylic acid. When tested under DAC conditions, the CO_2 adsorption properties of these pristine MOFs were found to be negligible. To improve their performance, post-synthetic modification methods were utilized to prepare a class of ethylenediamine-modified quasi-MOF (X-UIO-EDA). Exposure of 2-UIO-EDA at 25 °C, both to dry air streams (400 ppm CO_2/Ar) and humid atmosphere led to CO_2 adsorption of 0.04 and 0.44 $mmol_{CO2}/g_{sorbent}$, respectively.

Thus, this suggests that 2-UIO-EDA not only copes with water presence but also demonstrates the beneficial impact of water on CO_2 uptake with an impressive 10-fold increase at 30% RH. The large CO_2 capacity under moist conditions was attributed to the generation of CO_2 adducts, such as bicarbonate and hydronium carbamate species, combined with H-bonding interactions between the adsorption products within the microporous confinement of the framework.

1.3.3 MOFs with exposed anions

Another route to enhance CO_2 adsorption under DAC conditions is developing hybrid ultramicroporous materials (HUMs), which are narrow-pored (<7 Å diameter) three-dimensional frameworks with polarizable inorganic anion lining the pore walls. These materials do not have exposed metal cations that show CO_2-CUS interactions. Instead, they possess exposed negative charges (high-density fluorinated sites) that can capture CO_2 by attracting electropositive C atoms ($C^{\delta+}\cdots F^{\delta-}$). Thus, these HUMs offer strong binding sites with the added benefit of lower CO_2 Q_{st} (~40-55 kJ/mol) compared to solid amine-functionalized materials.

Typically, these HUMs are composed of 2D square lattice (sql) sheets pillared by inorganic anions (e.g., SiF_6^{2-}, SIFSIX; TiF_6^{2-}, TIFSIX; $NbOF_5^{2-}$, NbOFFIVE).[93–96] For instance, SIFSIX-3-Zn (where 3 = pyrazine) comprises Zn-pyrazine square grids pillared using SiF_6^{2-} moieties (Figure 7). At 25 °C and 0.4 mbar CO_2, the CO_2 capacity and Q_{st} for SIFSIX-3-Zn were 0.13 $mmol_{CO2}/g_{sorbent}$ and 45 kJ/mol, respectively.[94] Notably, the Jahn-Teller distortion of the six-coordinated Cu^{2+} nodes in the isostructural variant of SIFSIX-3-Cu reduces the pore size dimensions to 3.5 Å, which is 0.3 Å less than the parent Zn^{2+} derivative. This, in turn, serves to maximize physisorption. The uptake of SIFSIX-3-Cu under DAC conditions and the isosteric heat of CO_2 adsorption was found to be 1.24 $mmol_{CO2}/g_{sorbent}$ and 54 kJ/mol, respectively, which is significantly higher than that on the OMS-MOFs, such as Mg-MOF-74 (e.g., 0.08 $mmol_{CO2}/g_{sorbent}$ and 47 kJ/mol, respectively). Noticeably, the improved CO_2 capture performance resulted from stronger electrostatic forces between SIFSIX pillars and CO_2. Additionally, tight-fitting pores of SIFSIX-3-Cu perfectly coincide with the CO_2 (kinetic diameter 3.3 Å), allowing a tailored fit for CO_2.[94] Although SIFSIX-3-Cu demonstrated notable DAC performance under dry conditions, it was observed to be structurally unstable when exposed to high humidity and moderate temperature (75% RH, 40°C).[97]

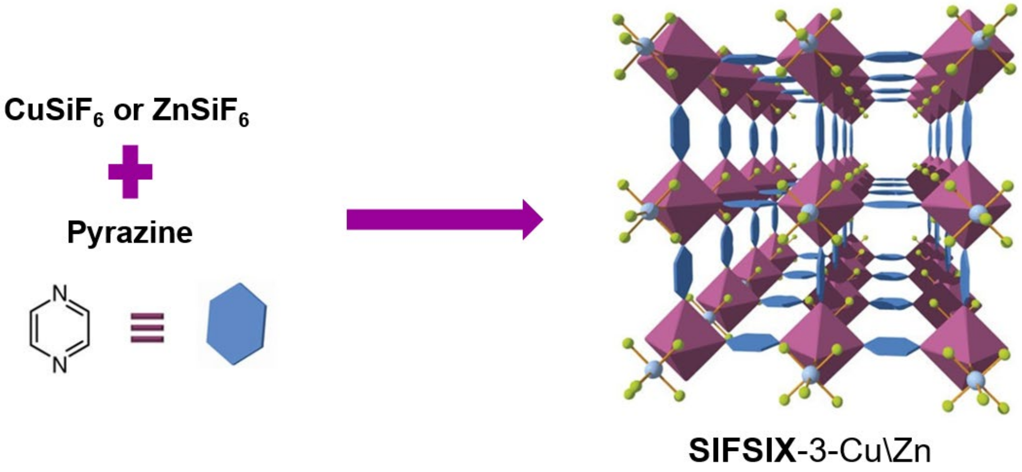

Figure 7: Illustration of SIFSIX-3-Cu/Zn; pore size 3.50/3.84 Å. Reproduced (modified) from ref.[94]

An effective way to maximize physisorption in HUMs is by altering the pillaring anion from SiF_6^{2-} to $NbOF_5^{2-}$.[95] This substitution results in an increased M–F bonding distance (d(Nb–F) =1.899(1)Å versus d(Si–F) = 1.681(1)Å), as Nb^{5+} is a bigger cation compared to Si^{4+}. Consequently, this shortens the d(F···F), which further contracts the pore size to 3.210(8) Å, thereby generating a tighter binding site for CO_2. Amongst the pyrazine-linked HUMs, the perfectly matched pore in NbOFFIVE-1-Ni (pore environment and size) afforded the most promising CO_2 performance under DAC concentrations with the uptake of 1.3 $mmol_{CO2}/g_{sorbent}$ at 25 °C and 0.4 mbar CO_2 partial pressure.[95] Hydrolytically stable TIFSIX-3-Ni was also developed using TiF_6^{2-} pillars. Markedly, TIFSIX-3-Ni yielded a CO_2 uptake capacity of ~1.1 $mmol_{CO2}/g_{sorbent}$ at 25 °C and 0.4 mbar CO_2 and a high Q_{st} of 50kJ/mol.[96]

After further optimization of the SIFSIX series, hydrophobic HUM, denoted as SIFSIX-18-Ni-β, was fabricated by pillaring 2D layers of Ni(II) nodes and organic linkers (3,3′,5,5′-tetramethyl-1H,1′H-4,4′-bipyrazole) using SIFSIX pillars, featuring methyl-decorated pores.[98] In the presence of dry 500 ppm CO_2, the capture capacity of SIFSIX-18-Ni-β was observed to be 0.4 $mmol_{CO2}/g_{sorbent}$. Interestingly, molecular simulations demonstrated that SIFSIX-18-Ni-β interacts with CO_2 through multiple interactions like an enzyme. Specifically, CO_2 molecules form interactions with SIFSIX units and methyl groups *via* C···F and CH···O interactions, respectively, thus simultaneously providing substantially stronger binding for CO_2 and enhancing surface hydrophobicity.[98]

The impact of water co-adsorption during CO_2 capture was also quantified using SIFSIX-18-Ni-β and other high-performing HUMs. The results displayed that at low concentrations of CO_2 (1000 ppm), the CO_2 capture capacity was only slightly reduced when switching from dry to high moisture content (0.7 $mmol_{CO2}/g_{sorbent}$ at 0% RH versus 0.3 $mmol_{CO2}/g_{sorbent}$ at 74% RH). Besides, the material exhibited a low water uptake of 1.64 mmol g^{-1} (at 95% RH), while the other high-performing HUMs, including NbOFFIVE-1-Ni, TIFSIX-3-Ni, and SIFSIX-3-Ni, demonstrated high water uptake of 10.09, 7.46, and 8.8 mmol g^{-1}, respectively. The enhanced moisture stability of SIFSIX-18-Ni-β in comparison to other HUMs is attributed to the presence of hydrophobic CO_2 binding sites (methyl-decorated pores) and, therefore, demonstrates the potential of capturing trace CO_2 in both dry and moist conditions.[98]

1.3.4 Flexible MOFs

Materials demonstrating robust adsorbate-adsorbent interactions (e.g., higher Q_{st} values) have greater CO_2 uptake capacities at low pressures, but they require higher temperatures for CO_2 desorption. In this regard, MOFs that feature structural responsiveness, such as flexible MOFs, may prove beneficial.[25] These MOFs can pack CO_2 molecules effectively by adjusting their pore size under gas pressure, allowing CO_2 capture and release reversibly. These materials undergo structural transformations through various dynamic modes, often termed breathing, swelling, ligand rotation, and subnet displacement[99], in response to some kind of external stimuli such as guest molecules, pressure, or temperature variation. Since the flexible MOFs exhibit guest-assisted phase transition (e.g., upon CO_2 adsorption), their adsorption profile displays stepped-shape isotherms and, therefore, enables greater working capacity and milder regeneration conditions.[99]

One of the best representative examples of "breathing" MOFs is water-stable Cr-based MIL-53 [Cr(OH)(bdc)].[100] Breathing behavior is often reflected by a structural transition from a closed-pore structure (or narrow pore) to an open-pore structure (or large pore) and back. For example, in the presence of CO_2, MIL-53(Cr), when fully dehydrated, undergoes a structural change, transforming from a large to a close-pore structure (Figure 8). At a pressure below 1 bar, it exhibited a CO_2 uptake of nearly 2 $\mathrm{mmol_{CO2}/g_{sorbent}}$. Upon further pressure increase (above 5 bar), the pore structure reopens, thereby resulting in a stepwise adsorption. This allows for an appreciable amount of CO_2 to be adsorbed, with an impressive uptake of approximately 9-10 $\mathrm{mmol_{CO2}/g_{sorbent}}$ (at 20 bar).[101] Similarly, at higher pressure (above 11 bar), the narrow pore configuration of hydrated MIL-53(Cr) evolves to an open-pore phase, leading to a notable CO_2 uptake. Remarkably, in the presence of CH_4, hydrated MIL-53(Cr) showed extremely low uptake, only ~0.2 mmol/g at 20 bar, presumably because of the repulsive interactions of pre-adsorbed H_2O towards non-polar CH_4.[102] Thus, the breathing nature of MIL-53(Cr) demonstrates ultrahigh adsorptive selectivity for CO_2 over CH_4 *via* the quadrupolar interaction of CO_2 with the hydroxyl groups that line the pore surface of MIL-53.

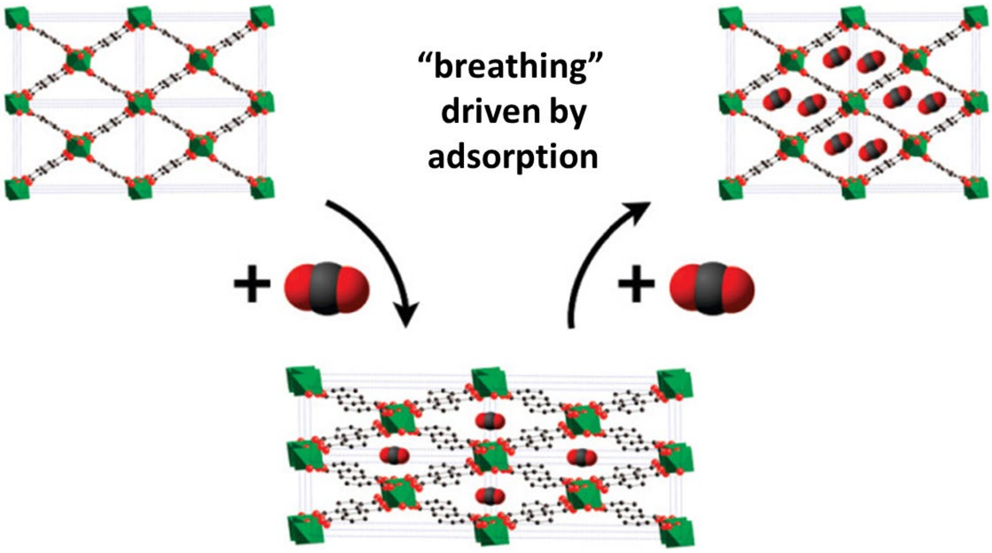

Figure 8: Schematic representation of MIL-53 "breathing" induced by CO_2 adsorption at increasing pressure. Reproduced (modified) from ref.[103]

Sometimes, the interaction between CO_2 and sorbent is not robust enough to evoke the pore-opening of a flexible framework. In such scenarios, flexing can be induced by an alternative route. For example, Carrington *et al.*[104] reported an SHF-61 MOF ($(Me_2NH_2)[In(ABDC)_2]$, ABDC = 2-aminobenzene-1,4-dicarboxylic acid), a flexible framework that exhibited solvent-induced breathing behavior. Particularly, a closed phase was generated upon removing dmf from a solvated form of SHF-61-DMF. However, a wide-pore structure was obtained from chloroform-exchanged SHF-61 due to the much weaker interactions between MOF and $CHCl_3$ in contrast to highly interacting dmf. Markedly, this leads to lower CO_2 adsorption capacity (2.43 $mmol_{CO2}/g_{sorbent}$ at 18 bar) in the narrow-pore structure, while the open phase structure form resulted in a greater CO_2 uptake at higher pressure conditions (6.25 $mmol_{CO2}/g_{sorbent}$ at 19.5 bar).

Alternatively, pronounced flexing was also observed for a Zn-based pillared-layer framework named ZnDatzBdc (HDatz = 3,5-diamino-1*H*-1,2,4-triazole, H_2Bdc = 1,4-benzenedicarboxylic acid).[105] Upon exposure to certain gases, such as CO_2, N_2, and CH_4, only CO_2 was discovered to be capable of inducing a structural transformation. This transition reversibly causes the fully desolvated ZnDatzBdc to switch from a close-phase to an open-phase configuration. This was ascribed to the combined effect of H-bonding disruption/re-formation and the rotation of phenyl units. As a result, ZnDatzBdc displayed a stepped isotherm arising from the adsorption of an appreciable amount of CO_2 through a gate-opening behavior (Figure 9). Notably, ZnDatzBdc exhibited a low CO_2 uptake of 0.38 $mmol_{CO2}/g_{sorbent}$ before the gate-opening phenomenon but increased abruptly above the gating pressure of 0.25 and 0.83 bar, revealing CO_2 capacities of 2.89 and 2.05 $mmol_{CO2}/g_{sorbent}$ at 1 bar, 0 and 25 °C, respectively. Remarkably, the adsorption isotherms were determined to be fully reproducible over five CO_2 capture−release cycles. Moreover, the breakthrough experiments indicated that ZnDatzBdc could efficiently separate CO_2 from

CO_2/N_2 and CO_2/CH_4 mixtures, showing CO_2 working capacities of 2.25 and 1.95 mmol/g, respectively. Overall, the outlook of flexible MOFs for the carbon capture process appears promising. Indeed, further detailed research on such responsive behavior, focusing on vital aspects, such as excellent separation performance and hydrolytic stability, could potentially offer new directions for CO_2 capture in DAC conditions.

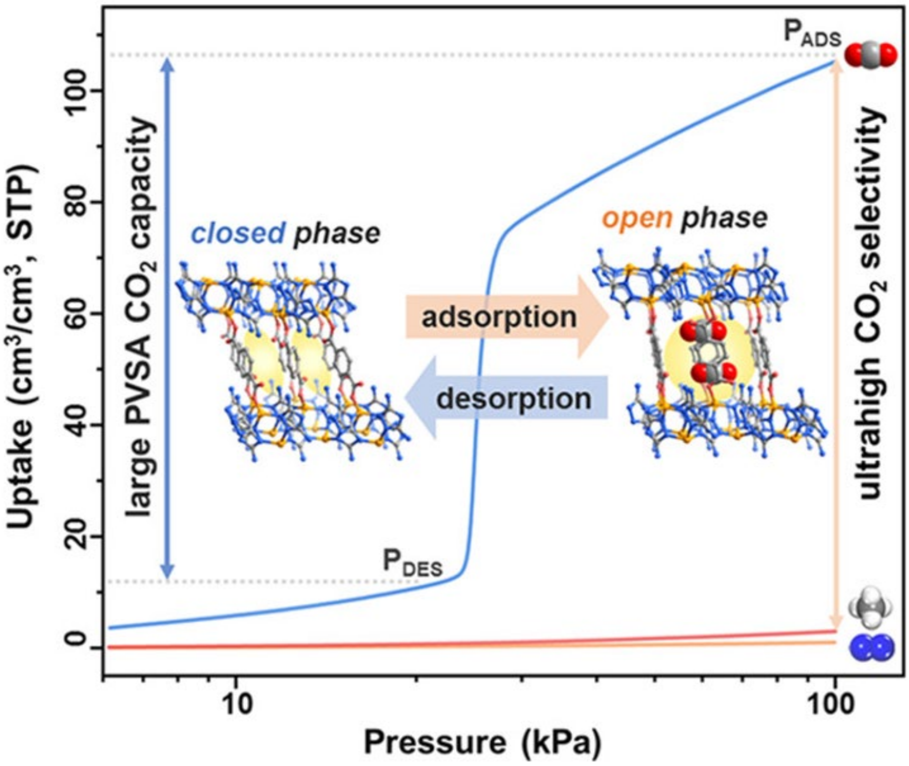

Figure 9: Representation of CO_2, N_2 and CH_4 adsorption isotherm (0 °C) recorded for ZnDatzBdc.[105]

2 RESULTS AND DISCUSSION

2.1 Aim of the work

This work aimed to synthesize and characterize amine-functionalized MOFs for interest in CO_2 DAC applications. To accomplish this, we first focused on synthesizing a ligand with a 4-amino-1,2,4-triazole backbone that seemed highly attractive because of its flexible conformation and the presence of a combination of the functionalities. We then conducted a systemic analysis of diverse supramolecular entities formed by this ligand in the presence of different types of anions. This involved an exploration of different molecular conformations and diverse noncovalent interactions that can be leveraged for the formation of MOFs. Next, we turned our efforts toward synthesizing MOFs with amine functionality installed into the linker backbone. Employing the mixed-linker approach, we combined the selected ligand with a carboxylate linker to decorate the MOF pores with basic functionalities ($–NH_2$) and polarizable sulfur atoms. Meanwhile, in parallel, we evaluated a post-synthetically amine functionalized MOF, aiming to understand the material behavior and performance when employed under realistic DAC working conditions. Accordingly, the content of this thesis is a compendium of the three research publications, the objectives for which are as follows:

Paper **I** centered around establishing new anion-assisted supramolecular entities of bent 4-amino-3,5-bis(4-pyridyl)-1,2,4-triazole (bpt) ligand encompassing basic functional sites ($–NH_2$). This work has been particularly interested in the geometric analysis, protonation states of the ligand, and the range of noncovalent interactions influencing these supramolecular systems. This work assessed different molecular conformations of the ligand and molecular packing of a series of supramolecular extended architectures. With a particular focus on anion chemistry, we also provided insights into anion cluster assembly and a diverse range of intriguing anion-water clusters.

Paper **II** focused on the preparation and characterization of three Zn-based mixed-ligand frameworks, $\{[Zn(bpt)(tdc)]\cdot dmf\}_n$ (denoted MOF-**1**-Zn), $\{[Zn_2(bpt)(tdc)_2]\cdot 2(dmf)\}_n$ (MOF-**2**-Zn), and $\{[Zn(bpt)(tdc)(H_2O)]\cdot dmf\}_n$ (MOF-**3**-Zn) built *via* a combination of sulfur-based heterocyclic ligand (H_2tdc = thiophene-2,5-dicarboxylic acid) and –NH_2 group-bearing linker (bpt) under different crystallization conditions. Furthermore, the dynamic behavior, *via* single-crystal-to-single-crystal (SC-to-SC) transformations induced by solvent exchange and removal on a pillared-layer MOF was examined by soaking the crystals of MOF-**2**-Zn into nine different solvents ranging from polar protic to polar aprotic and nonpolar solvents. Different conformation modes of pillar-ligand were assessed, with attention to understanding the host–guest interactions for different SC-to-SC guest-exchange complexes. In addition, we also evaluated the potential application of synthesized Zn-based mixed-linker MOFs in CO_2 adsorption studies.

Paper **III** aimed to explore the behavior and effectiveness of ethylenediamine-appended Mg-MOF-74 (ED@MOF-74) in capturing CO_2 from air under real-world operating environments. The performance of amine-appended MOF was examined in temperature-concentration swing adsorption (TCSA) mode using a fixed-bed adsorption-desorption setup supplemented with a series of systematic experiments, including structural characterization. More specifically, the central aspects of real-life applications of MOFs in DAC, CO_2 adsorption rate, and repetitive adsorption-desorption cycles under a range of operating conditions, including temperature and humidity, were quantified. A summary of the experimental procedures and the most important results published in Papers **I-III** are presented and discussed below.

2.2 Syntheses

2.2.1 General notes for 4-amino-3,5-bis(4-pyridyl)-1,2,4-triazole (bpt) and salts syntheses[I]

Synthesis of bpt: The ligand synthesis was adapted and modified from the reference (Scheme 2).[106] Specifically, a mixture of 4-cyanopyridine, hydrazine monohydrate, water, and ethanol was sealed in a Teflon-lined steel-made autoclave and heated at 120 °C for three days. After cooling to 22 °C and washing with water and acetone, pale brown-orange crystals were obtained.

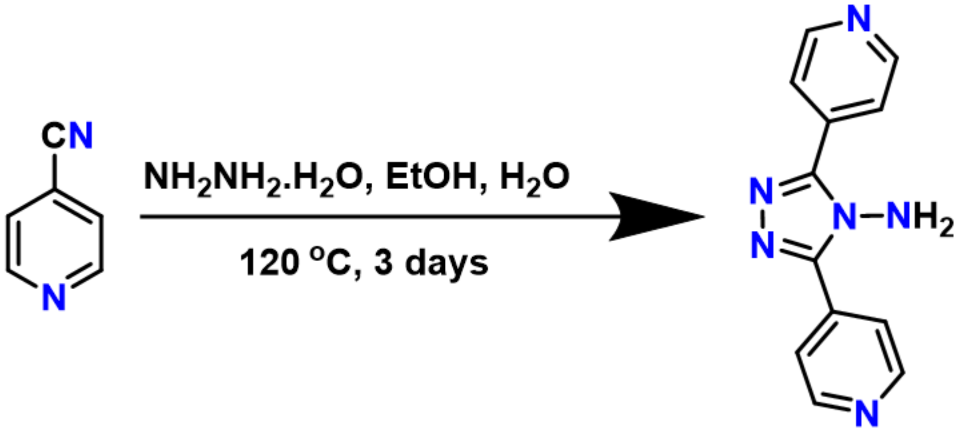

Scheme 2: Synthetic route for the preparation of 4-amino-3,5-bis(4-pyridyl)-1,2,4-triazole (bpt).[I]

Crystallization methods: The complexes reported in this study were prepared from bulk powders, using H_2O/acetone (or dioxane) vapor diffusion or evaporation methods (Scheme 3).

Preparation of H_2LCl_2 (**1**), H_2LBr_2 (**2**), $H_2L(NO_3)_2$ (**3**), $HL(H_2PO_4)$ (**4**), $H_2L(H_2PO_4)_2$ (**5**), $H_2L(SO_4)\cdot H_2O$ (**8**), H_2LSiF_6 (**9**) and $H_2LSiF_6\cdot 2H_2O$ (**10**): Typically, to a 5 M acid solution, L (bpt) was added and shaken thoroughly and was left undisturbed for one day (4 days for salt **9**). The faint-yellow crystals grown in the case of a HNO_3 solution (**3**) were collected and rinsed with water and acetone. To the remaining vials, H_2O (except salt **9**) and acetone (dioxane for salt **5**) were added to precipitate crystals per appropriate LHx salt (fine powder for salt **9**). The resulting crystals were filtered off, washed with acetone, and dried in air. The complex (**9**) was obtained as single crystals suitable for analysis upon slow evaporation of bulk powder containing water solution.

Preparation of $H_2L(NO_3)_2$ (**7**): The single crystals of salt (**3**) were dissolved in a methanol/water mixture. Upon slow evaporation, the crystals grew within a few days.

Preparation of $[H_2L]_2I_4$ (**6**), $H_2L(HF_2)_2$ (**11**), H_3LI_3 (**12**), $H_3L(BF_4)_3$ (**13**), $H_3L(ClO_4)_3$ (**14**), $H_3L(ClO_4)_3\cdot 2H_2O$ (**15**) and $H_3L(H_3O)(SiF_6)_2\cdot 2H_2O$ (**16**): To a 5 M acid solution (2 mL), 150 mg of L (bpt) was added and shaken thoroughly and was left undisturbed for one day. In the case of HI solution (**6**), H_2O was added. The crystals suitable for characterization were obtained by allowing the solutions to slowly evaporate in open or closed (pin-holed) vials.

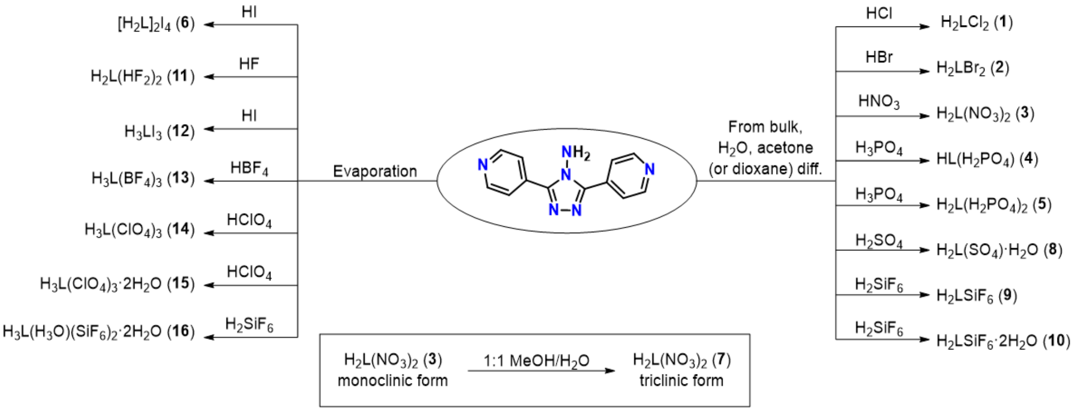

Scheme 3: Representation of different LHx salts synthesized in this work.[I]

2.2.2 Syntheses of MOF-1-Zn, MOF-2-Zn and MOF-3-Zn[II]

Crystallization was attempted using solvothermal or slow evaporation techniques. MOF experiments conducted in this work typically involved combining divalent zinc ions with H_2tdc and bpt in a given stoichiometric ratio in dmf, or in solvent combinations, including dmf, ethanol, and water.

Preparation of MOF-**1**-Zn: Compound was produced by mixing 1.48:1:1 $Zn(NO_3)_2\cdot 6H_2O$:bpt:H_2tdc and adding dmf as solvent. In a Teflon-lined steel-made autoclave, $Zn(NO_3)_2\cdot 6H_2O$, bpt, and H_2tdc, along with dmf, were added. The solvothermal reaction was carried out at 120 °C for 72 hours and cooled to room temperature within 24 hours. The crystals were recovered by filtration, washed with dmf, and briefly air-dried.

Preparation of MOF-**2**-Zn: Compound was made with the above said reaction conditions but using a 1:1:1 ratio of $Zn(NO_3)_2\cdot 6H_2O$:bpt:H_2tdc. MOF-**1**-Zn and MOF-**2**-Zn as plate- and block-like colorless single crystals were obtained as a mixture, which was washed with dmf and briefly air-dried.

Preparation of MOF-**3**-Zn: Briefly, to a 100 mL round-bottomed flask charged with a magnetic stirrer and a solution of $Zn(NO_3)_2\cdot 6H_2O$ in water and bpt in hot ethanol, a solution of H_2tdc in dmf was added to it dropwise at 80 °C. After one hour, the solution was filtered to eliminate the possible residues. Then, the solution was allowed to evaporate slowly for one week. The resultant rod-shaped crystals were subsequently collected and placed in fresh dmf over several hours. Afterward, the crystals were dried in the air.

2.2.2.1 Solvent exchange and removal general procedure

The native mixture was first rinsed thoroughly with dmf, and then the crystals were immersed in 10 mL of chloroform and methanol for two and three days, respectively. During this time, the solvents were replaced at 12- and 24-hour intervals, respectively. The chloroform and methanol exchanged MOF-**2**-Zn were referred to as **2**-$CHCl_3$ and **2**-MeOH, respectively.

Similarly, the single crystals of **2**-EtOH, **2**-*i*-PrOH, **2**-MeCN, **2**-acetone, **2**-THF, **2**-dioxane, and **2**-cyclohexane were prepared by soaking the MOF-**2**-Zn crystals in 10 mL of ethanol, isopropyl alcohol, acetonitrile, acetone, tetrahydrofuran, 1,4-dioxane, and cyclohexane, respectively for seven days, which were replaced at 24-hour intervals for three days. Additionally, single crystals of **2**-gf (solvent-free version of the product) were prepared by desolvation of **2**-EtOH under *vacuo* at 110 °C for 5 hours.

2.2.3 Synthesis of ED@MOF-74^{III}

The Mg-MOF-74 was synthesized at room temperature following the published method with slight modification.[107] Before the amine functionalization, Mg-MOF-74 was subjected to heating at 200 °C for 2 hours under *vacuo* and then reacted with ED in anhydrous toluene *via* refluxing under inert conditions for one day. The resulting dark yellowish powder was recovered *via* filtration, washed extensively with toluene and hexane, and dried at 120 °C by applying *vacuo* for 4 hours.

2.3 Structural descriptions^{I,II}

2.3.1 Ligand conformation analysis

The conformation of a ligand plays a significant role in determining the nature of supramolecular entities. The cationic L displayed varying conformations for different natures of anions (e.g., spherical or polyhedron), resulting in a series of H-bonding geometry patterns and wide-ranging supramolecular assemblies. The structural elucidation of all the studied salts reveals that the bpt practically assumes three different orientations, which facilitates its categorization into three distinct Groups, as exemplified in Figure 10. Group I encompasses mono- and di-protonated salts, namely H_2LCl_2 (**1**), H_2LBr_2 (**2**), $H_2L(NO_3)_2$ (**3**), $HL(H_2PO_4)$ (**4**), $H_2L(H_2PO_4)_2$ (**5**), and $[H_2L]_2I_4$ (**6**). The six molecular salts crystallized in an anhydrous form, and bpt acquired an almost flattened conformation supported by modest dihedral angles, as shown in Table 1. In the Group I, the highest dihedral angle between the pyridyl and middle triazole core was measured to be less than ±17°.

Group II consists of diprotonated salts such as $H_2L(NO_3)_2$ (**7**), $H_2L(SO_4)\cdot H_2O$ (**8**), H_2LSiF_6 (**9**), $H_2LSiF_6\cdot 2H_2O$ (**10**), and $H_2L(HF_2)_2$ (**11**). The structures of salts (**8**, **10**) feature water molecules inclusion into their crystal system. Typically, in this Group, the bpt adopts a moderately twisted geometry, with pyridyl groups tilting at comparable angles ranging from 16 to 27° with respect to the triazole ring. On the other hand, the Group III comprises all triprotonated salts, including H_3LI_3 (**12**), $H_3L(BF_4)_3$ (**13**), $H_3L(ClO_4)_3$ (**14**), $H_3L(ClO_4)_3\cdot 2H_2O$ (**15**), and $H_3L(H_3O)(SiF_6)_2\cdot 2H_2O$ (**16**). In this Group, one of the pyridyl units aligns with the central triazole motif, while the second pyridyl ring is significantly tilted. Alternatively, both pyridyl units are markedly tilted in the same or opposite directions, resulting in dihedral angles of up to 43° with the triazole ring. Notably, in the most tilted arrangements, such as those found in iodide and tetrafluoroborate complexes (**12**, **13**), the pyridyl units are almost perpendicularly oriented with respect to each other (Figure 10). Diagrams of the asymmetric unit (AU) with atom numberings for all the conformation groups are provided in Paper **I**.

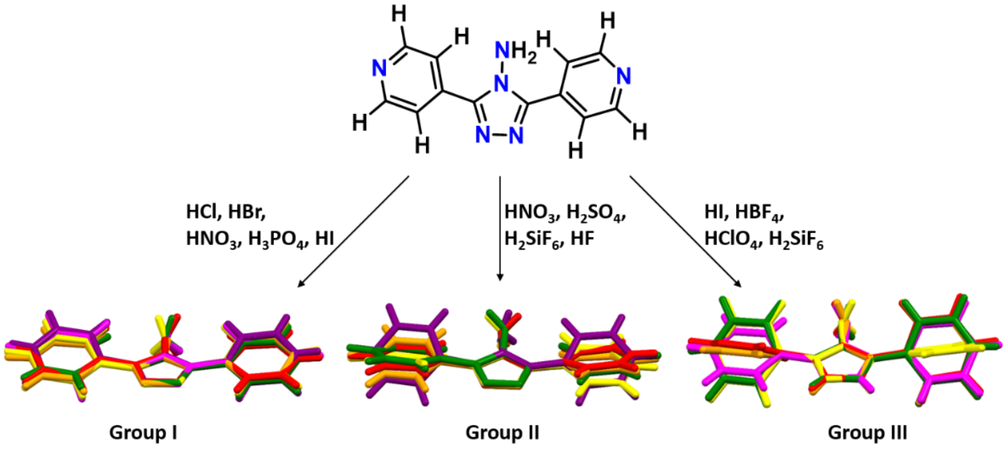

Figure 10: L (bpt) conformations are grouped based on their similarity. Group I: (**1**) H_2LCl_2 (red), (**2**) H_2LBr_2 (orange), (**3**) $H_2L(NO_3)_2$ in monoclinic form (yellow), (**4**) $HL(H_2PO_4)$ (green), (**5**) $H_2L(H_2PO_4)_2$ (magenta), (**6**) $[H_2L]_2I_4$ (purple); Group II: (**7**) $H_2L(NO_3)_2$ in triclinic form (red), (**8**) $H_2L(SO_4)\cdot H_2O$ (orange), (**9**) H_2LSiF_6 (purple), (**10**) $H_2LSiF_6\cdot 2H_2O$ (yellow), (**11**) $H_2L(HF_2)_2$ (green); Group III: (**12**) H_3LI_3 (red), (**13**) $H_3L(BF_4)_3$ (orange), (**14**) $H_3L(ClO_4)_3$ (yellow), (**15**) $H_3L(ClO_4)_3\cdot 2H_2O$ (green), and (**16**) $H_3L(H_3O)(SiF_6)_2\cdot 2H_2O$ (magenta).[I]

Table 1 Dihedral angles between pyridyl units and middle triazole core on L (bpt) in complexes (**1**) – (**16**).[I]

Group I			Group II			Group III		
salt	**angle 1[a] (deg)**	**angle 2[b] (deg)**	**salt**	**angle 1[a] (deg)**	**angle 2[b] (deg)**	**salt**	**angle 1[a] (deg)**	**angle 2[b] (deg)**
1	1.8(2)	-7.3(2)	**7**	16.0(2)	-18.3(2)	**12**	31.4(9)	42.5(9)
2	9.5(3)	-5.2(3)	**8**	-22.22 (19)	0.97(18)	**13**	34.08(18)	36.92(18)
3	-11.24 (18)	11.44 (18)	**9**	26.9(6)	-13.4(5)	**14**	-35.1(2)	-35.8(2)
4	-0.5(3)	10.8(3)	**10**	27.8(2)	0.4(3)	**15**	37.7(6)	-36.5(6)
5	13.0(2)	-16.1(2)	**11**	22.7(2)	-14.9(2)	**16**	23.9 (2)	-3.4(2)
6	15.5(6) 13.7(6)[c]	-15.5(6) -17.7(6)[d]						

[a] Atoms for the dihedral angles: N3–C2–C7–C12.

[b] Atoms for the dihedral angles: N4–C5–C13–C14.

[c] Atoms for the dihedral angles: N21–C20–C25–C30 for the 2nd ligand in the asymmetric unit for salt (**6**).

[d] Atoms for the dihedral angles: N22–C23–C31–C36 for the 2nd ligand in the asymmetric unit for salt (**6**).

2.3.2 Hydrogen bonding and packing modes

Salts (**1**, **2**), which crystallized in the triclinic space group *P*-1, exhibited a packing arrangement in a bricklayer fashion (Figure 11). Analysis of H-bond motifs (Graphs sets)[108] revealed linear $\mathrm{C}_2^1(14)$ chains made of $\mathrm{pyNH^+\cdots X}$ interactions, further forming larger $\mathrm{R}_4^2(20)$ motifs. Besides H-bonding, aromatic π–π stacking (face-to-face) further supports the bricklayer packing. Unlike salts (**1**, **2**), the diprotonated ligands in salt (**6**) assemble in columns (Figure 11), which are stabilized by relatively weak π–π interactions, presumably influenced by the larger size of the iodide anion ($\mathrm{Cl^-} < \mathrm{Br^-} < \mathrm{I^-}$). Salt (**3**) crystallized in monoclinic space group $P2_1/c$, displaying a zig-zag pattern stabilized by a group of noncovalent interactions. These include several types of H-bond motifs (e.g., $\mathrm{C}_2^2(12)$, $\mathrm{C}_2^1(10)$, $\mathrm{C}_2^2(6)$), weak dimer associations ($[\mathrm{NO_3}]^- \cdots [\mathrm{NO_3}]^-$ contacts)[109,110], and anion–π interaction (*d*(O–centroid) estimated to be 3.0680(11) Å) (Figure 11). Notably, the anion's steric effects played a crucial role in determining the spatial arrangement of the molecules. Thus, compared to other salts (**1**, **2**), a slightly longer distance between the aromatic rings and a slight tilt between the pyridyl rings offer relatively weaker π–π interactions in salt (**3**), possibly due to the steric effects of the nitrate anions.[111]

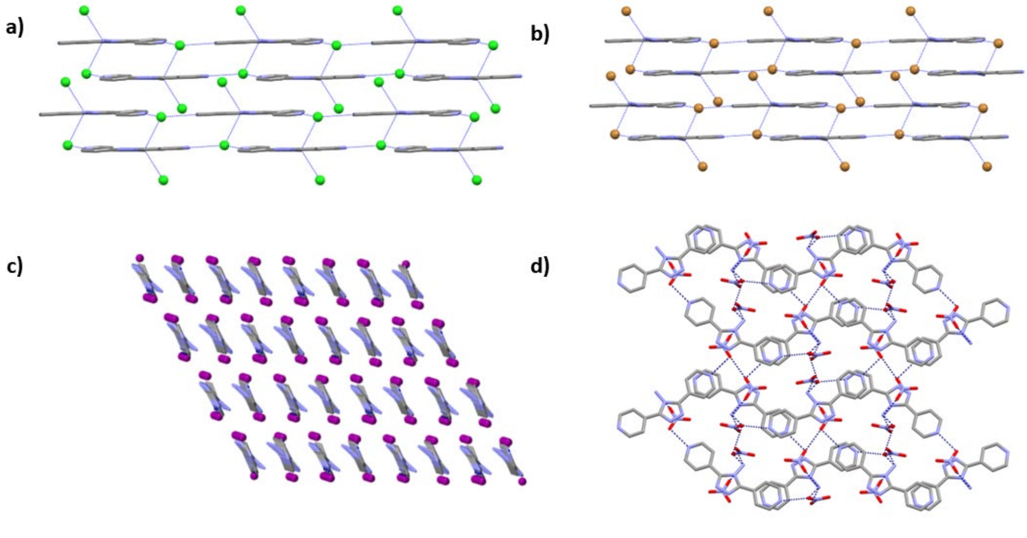

Figure 11: Molecular packing of (a) salt (**1**), (b) salt (**2**), (c) salt (**6**), and (d) salt (**3**), along *b*-, *b*-, *c*-, and *a*-axes, respectively. Only relevant atoms are shown; hydrogen atoms are omitted for clarity; H-bonds are exemplified by blue dashed lines (applies to all figures).[I]

Salts (**4**, **5**) crystallized in a monoclinic system with $P2_1/c$ or $I2/a$ symmetries, respectively. Salts (**4**, **5**) form layered structures with distinct H-bond directed patterns, each containing mono- or diprotonated ligand interacting with $[\mathrm{H_2PO_4}]^-$anions (Figure 12). The monoprotonated salt (**4**) features an infinite helical chain of dihydrogen phosphate through O–H···O hydrogen bonds (*d*(O–O) = 2.5417(18) Å) around a 2-fold screw axis. The ligands interconnect the chains in a “stair-steps” pattern. This arrangement features intersecting H-bond chains with H-bonded geometry patterns, including $R_4^2(20)$ and $R_4^4(24)$ structural motifs (Figure 13). The salt (**5**) comprises two crystallographically distinct $[H_2PO_4]^-$ anions featuring different coordination environments (Figure 12). Infinite zig-zag chains sustained by O–H⋯O bonds ($O \cdots O = {\sim}2.5$ Å) are interlinked by a second type of $[H_2PO_4]^-$ anion, thereby forming a hexameric cluster $(H_2PO_4^-)_6$ with $R_6^6(24)$ motif (Figure 13). The interlinked pattern of unique hydrogen bonds results in geometry types, such as $R_2^2(8)$ and $R_4^4(28)$ (Figure 13).

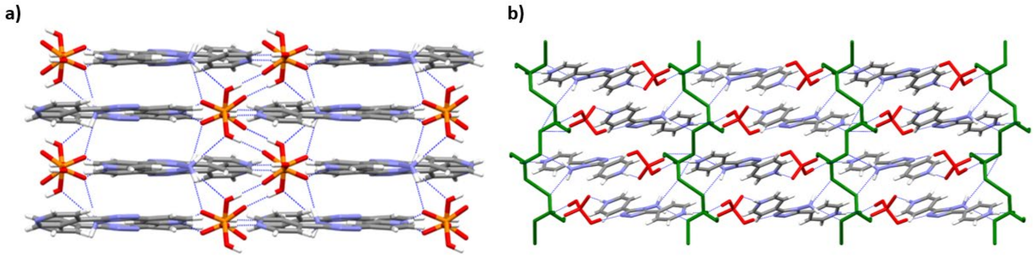

Figure 12: Molecular packing of (a) salt (**4**), (b) salt (**5**), along *c*-, and *b*-axes, respectively.[I]

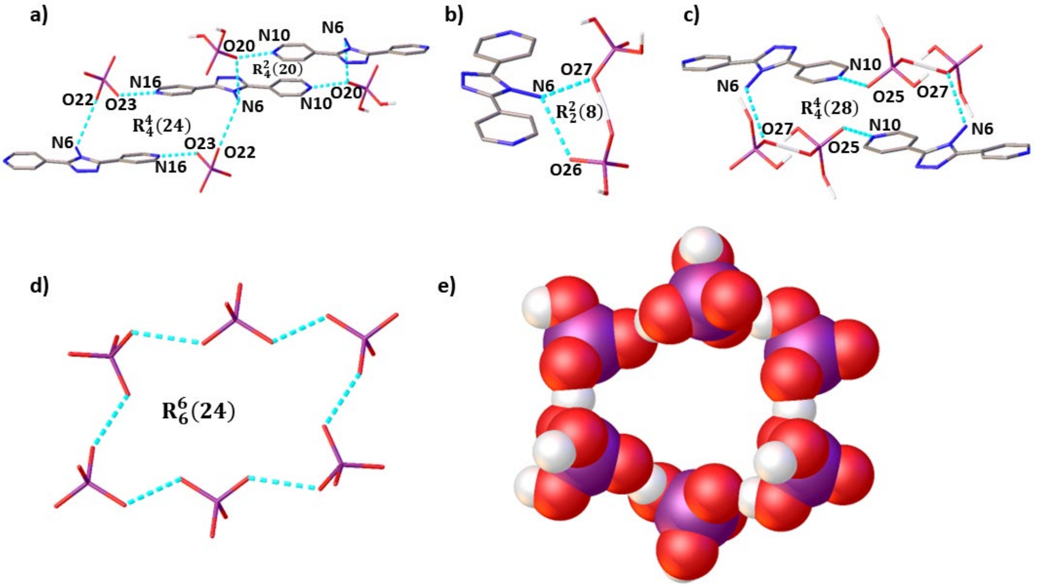

Figure 13: Examples of hydrogen-bonded motifs found (a) in the salt (**4**), (b, c) in the salt (**5**), (d) $(H_2PO_4^-)_6$ aggregate, and (e) anion cluster illustrated in space-fill.[I]

Group II salts (**7-11**) feature H-bonding-driven layered architectures composed of cationic ligands in partnership with different anions. These salts are distinguished by their recurring cyclic ring motifs, notably $R_4^2(20)$ and $R_4^4(24)$, that connect the cationic ligands and different anions, as illustrated in Figure 14.

Nevertheless, the inclusion of water in some salts, for instance, salts (**8**) and (**10**), further creates complex H-bond patterns and offers a range of structural features.

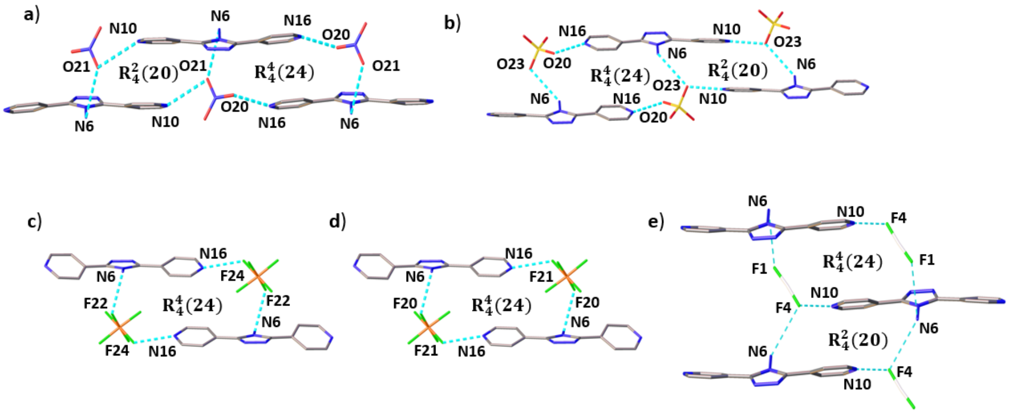

Figure 14: Examples of hydrogen-bonded motifs found (a) in salt (**7**), (b) in salt (**8**), (c) in salt (**9**), (d) in salt (**10**), and (e) in salt (**11**).[I]

For instance, in salt (**8**), tetrahedral $[SO_4]^{2-}$ connects with water *via* an O–H···O hydrogen bond to form a cyclic tetramer $[(SO_4)_2-(H_2O)_2]^{4-}$ cluster[112] exhibiting a structural motif $R_4^4(12)$ (Figure 15). The packing diagram along the *b*-axis reveals a distinctive layered arrangement that includes a cyclic tetramer inserted between cationic ligands. Salt (**10**), another hydrated salt, showcases interesting cyclic octameric clusters $[(SiF_6)_4-(H_2O)_4]_{\infty}^{8-}$ being part of $R_8^8(24)$ structural motif that extends in an undulated sheet *via* O–H···F H-bonds, facilitating the generation of a wave-like layered structure (Figure 15). Apart from multiple H-bond interactions, including N–H···O, O–H···F, and N–H···F, the additional stabilization is further provided by anion–π interactions.

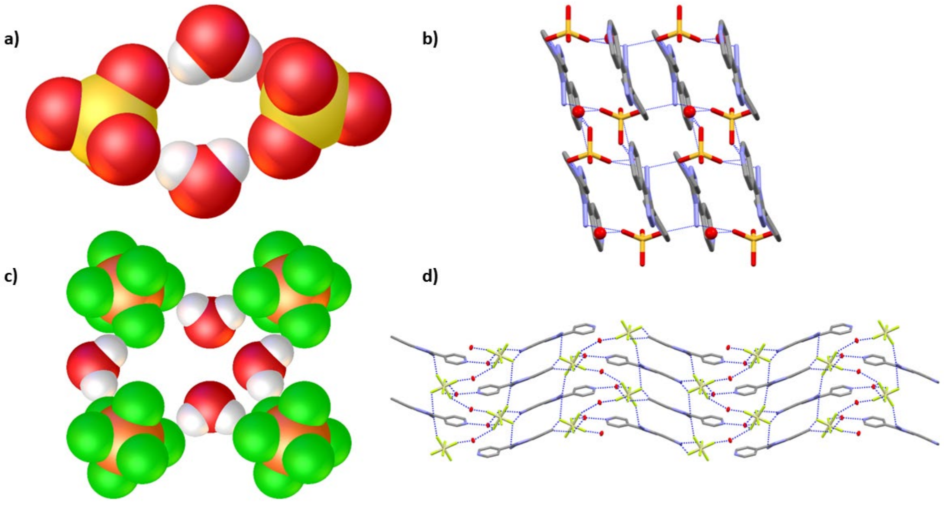

Figure 15: Salt (**8**) (a) cyclic tetramer cluster, (b) molecular packing along the *c*-axis, salt (**10**) (c) cyclic octameric cluster, and (d) molecular packing along the *a*-axis.[I]

An important aspect of Group III salts (**12**-**16**) is the prevalence of anion–π interactions alongside the establishment of multisite and/or bifurcated H-bond patterns (e.g., N–H⋯F, N–H⋯O, C–H⋯O, O–H⋯O, N–H⋯N, and O–H⋯F), which ultimately drive the formation of a wide array of structural arrangements (Figure 16). Salts (**12**, **13**) showcased iodide and fluorine atoms establishing anion–π interactions with a triazole ring with an anion⋯ring–centroid distance of 3.495(2) and 3.3691(14) Å, respectively. The partial view of the molecular packing of salts (**12**, **13**) is illustrated in Figure 16, highlighting anion–π interactions.

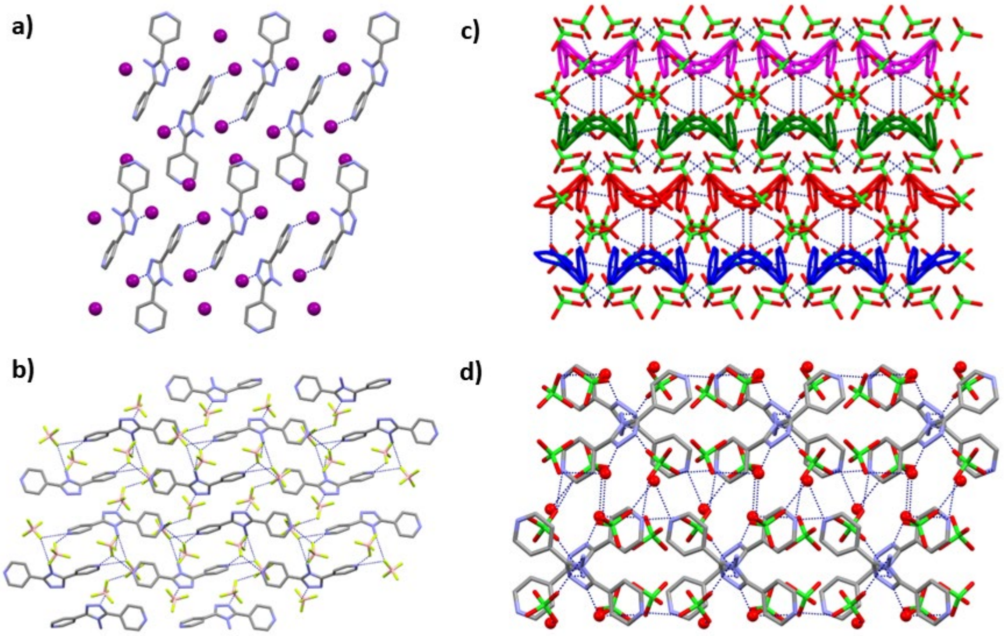

Figure 16: Molecular packing of (a) salt (**12**), (b) salt (**13**), (c) salt (**14**), and (d) salt (**15**), along *a*-, *b*-, *a*-, and *c*-axes, respectively.[I]

An observation of the water-free crystal structure (**14**) revealed a tri-protonated ligand interacting with three $[ClO_4]^-$ anions, forming infinite zig-zag chains *via* N–H⋯O interactions with $C_2^1(14)$ motif. Moreover, anion-anion interactions were identified between ClO_4^- anions[113], while the oxygen atom of $[ClO_4]^-$ was also noted at close proximity from the triazole ring with *d*(O–centroid) of 3.0468(17) Å. By contrast, salt (**15**) incorporates water molecules, forming an acyclic perchlorate-water-perchlorate-water cluster $(ClO_4^-)_2(H_2O)_2$ surrounded by cationic ligands. The H-bonding network is diversified, involving perchlorate anion interactions with water molecules and cationic ligands *via* O–H⋯O, N–H⋯O, and C–H⋯O H-bonds, respectively. Meanwhile, water molecules interact with protonated pyridyl and triazole moieties of bpt *via* N–H⋯O H-bonds. Interestingly, direct interactions between two cationic ligands mediated *via* amino N–H donor group and triazole nitrogen acceptor with a distance between N–N estimated to be 2.981(5) Å were also identified. When viewed along the *c*-axis, the cationic ligands appear to form a criss-cross orientation (Figure 16). Salt

(**16**) displays infinite H-bonded sheets comprising intricate cyclic motifs, particularly tetrameric and 16-membered cyclic motifs involving water molecules, hydronium ions, and hexafluorosilicate anions (Figure 17). The cyclic motifs are interconnected throughout *via* O–H···F and N–H···F H-bonds, sustaining a bilayer arrangement along the *b*-axis (Figure 17).

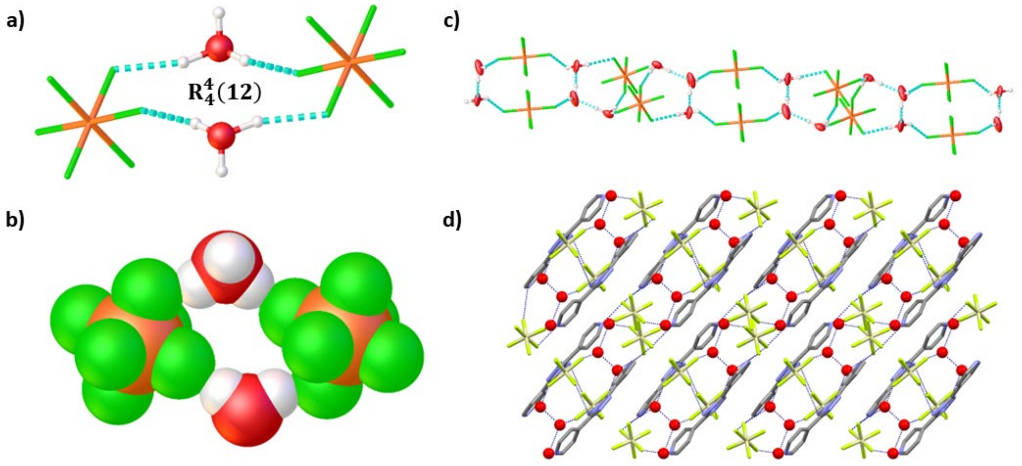

Figure 17: Illustration of the salt (**16**) (a, b) hydrogen-bonding motif found in a cyclic tetrameric cluster and its space-fill illustration, (c) a side view of the hydrogen-bonded sheet of water molecules, hexafluorosilicate anions, and hydronium ions, and (d) molecular packing along the *b*-axis.I

Powder X-ray diffraction (PXRD) data collected for the investigated salts indicated that based on Pawley whole-pattern unit cell indexing fits, bulk samples of studied salts are almost consistent (except **11**) with the corresponding single-crystal structures. For the salt (**11**), based on the Pawley fit, it was validated that the produced bulk powder contained only the neutral bpt, consistent with the elemental analysis (EA) results. Moreover, it is worth noting that all complexes studied, displayed good thermal stability attributable to the extensive H-bonding and attractive interactions between cations and anions. Notably, the decomposition temperatures for salts (**1**-**16**) fall within the range of 150-240 °C. Paper **I** provides extensive descriptions of molecular packings and detailed characterization of all studied salts.

2.3.3 Structural details of MOF-1-Zn, MOF-2-Zn and MOF-3-Zn

The MOFs, MOF-**1**-Zn and MOF-**2**-Zn were synthesized *via* the solvothermal method as detailed in the synthesis section by combing Zn^{II}, $(tdc)^{2-}$, and a pillaring co-ligand (bpt). MOF-**1**-Zn and MOF-**2**-Zn crystallizes in orthorhombic *Pcca* and monoclinic *I*2/*a* space groups with a formula of $\{[Zn(bpt)(tdc)]\cdot dmf\}_n$ and $\{[Zn_2(bpt)(tdc)_2]\cdot 2(dmf)\}_n$, respectively. Both structures exhibit a double-interpenetrated 3D framework. In MOF-**1**-Zn, each Zn^{II} center is coordinated with three oxygen atoms from three different $(tdc)^{2-}$ ligands and two nitrogen atoms from two bpt ligands. The ligand (tdc)$^{2-}$ exhibits binding mode 1 (Scheme 4), which allows it to link to three Zn^{II} atoms through monodentate and bridging fashion, eventually forming a perfectly planar metal-carboxylate two-dimensional layer lying in the crystallographic *ac*-plane (Figure 18). Each 2D layer connects to the bpt ligand through its pyridyl units to establish a 3D pillared-layer network (Figure 18).

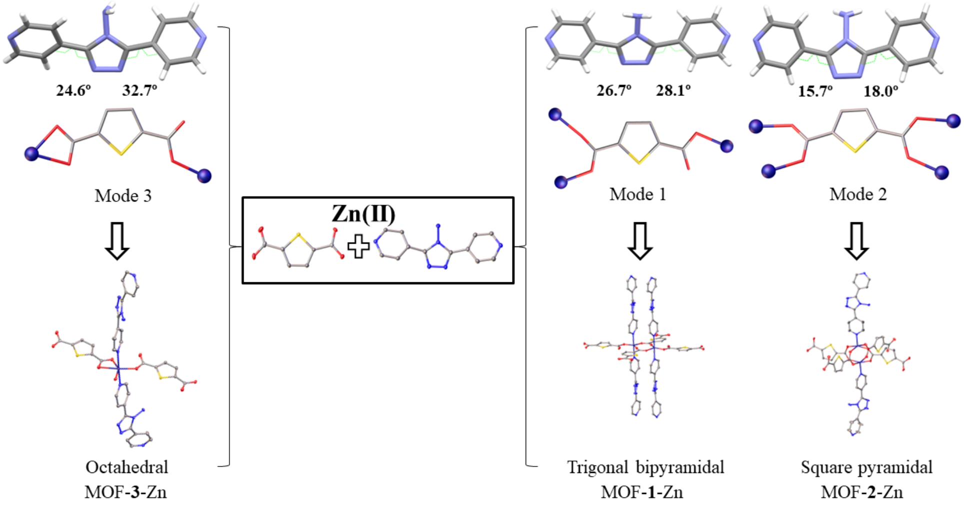

Scheme 4: Illustration of (tdc)$^{2-}$ binding modes, molecular confirmation of bpt, and the coordination geometry of Zn^{II} ion in MOF-**1**-Zn, MOF-**2**-Zn, and MOF-**3**-Zn, respectively.[II]

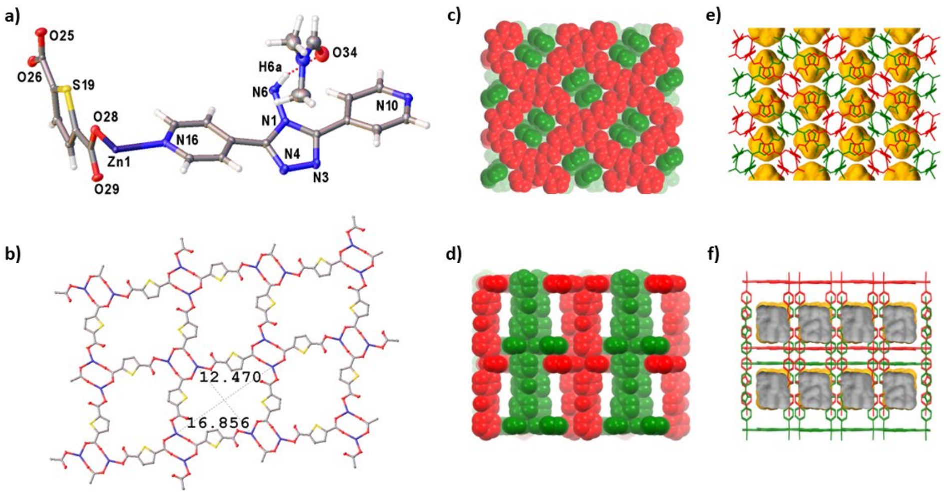

Figure 18: Structural description of MOF-**1**-Zn. (a) asymmetric unit, (b) 2D network, (c, d) double-interpenetrated 3D framework along the *b*- and *c*-axes, respectively, and (e, f) potential void space visualized by yellow/gray (outer/inner) colors (applies to all figures).[II]

MOF-**2**-Zn is based on dinuclear paddlewheel nodes $[Zn_2(O_2C)_4]$ linked equatorially by $(tdc)^{2-}$ ligands to generate corrugated two-dimensional layers (Figure 19). The bpt ligands further coordinate to the axial sites of the Zn-paddlewheel (Scheme 4), thereby expanding the structure in three dimensions and furnishing a pillared paddlewheel MOF (Figure 19).

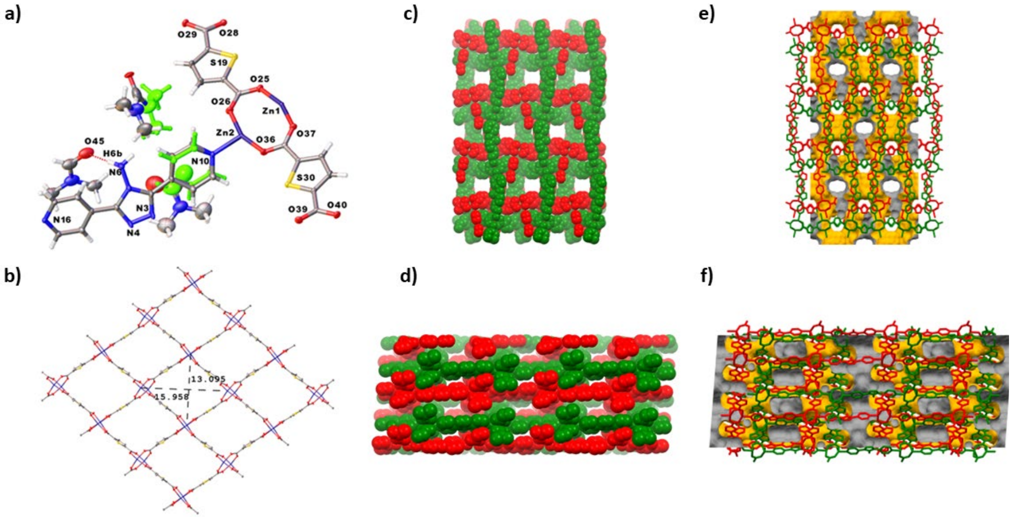

Figure 19: Structural description of MOF-**2**-Zn. (a) asymmetric unit, (b) 2D network, (c, d) double-interpenetrating 3D framework along the *a*- and *b*-axes, respectively, and (e, f) potential void space visualized by yellow/gray colors.[II]

There are notable differences in the arrangement of bpt in MOF-**2**-Zn compared with that of MOF-**1**-Zn. In MOF-**1**-Zn, two pyridyl rings are equally highly tilted and are in parallel directions with respect to the middle triazole ring, while in MOF-**2**-Zn, they show modest tilting. The crystal packing of MOF-**1**-Zn shows robust π–contacts between parallel pillaring struts, where the face-to-face $d(\pi\text{–}\pi)$ is measured at 3.710(2)-3.856(2) Å. However, this type of arrangement is absent in MOF-**2**-Zn. Additionally, as mentioned before, the 2D layer in MOF-**2**-Zn is not planar but is a corrugated two-dimensional layer, whereas in MOF-**1**-Zn, the two-dimensional layer is nearly flat. Overall, the free volume of MOF-**1**-Zn and MOF-**2**-Zn without considering solvents is 23.4% and 35.3%, respectively, as estimated by contact surface calculations (Figure 19).

The self-assembly of Zn^{II} ions with $(tdc)^{2-}$ and bpt ligands in H_2O/dmf/EtOH solvent mixture leads to the crystallization of $\{[Zn(bpt)(tdc)(H_2O)]\cdot dmf\}_n$, hereafter MOF-**3**-Zn, in the hexagonal symmetry (space group $P6_1$), as deduced by SCXRD studies. Within MOF-**3**-Zn, the coordination sphere of Zn^{II} is of distorted octahedral geometry, with one monodentate and one chelating $(tdc)^{2-}$, one water molecule, and two nitrogen atoms from two bpt ligands (Scheme 4). The two pyridyl rings are highly tilted in the opposite direction with a dihedral angle of 56.61(10)° between them. MOF-**3**-Zn is constructed from infinite wavy 3_1-helices delimited *via* Zn-bpt bridging extending along the *c*-axis (Figure 20). These parallel helices are interlinked to each other *via* (tdc)$^{2-}$ chains that possess three different orientations while passing from one to the next layer, thereby propagating the structure in three dimensions. When viewed along the *b*- and *c*-axes, the guest molecules (dmf) occupy the structural voids in a row formation and hexagonal helical chains, respectively. The packing of the guest-freed MOF-**3**-Zn reveals a free volume of about 22.9%. The general feature of the pillared-layer frameworks is the coexistence of network interpenetration; likewise, MOF-**3**-Zn also possesses a double-interpenetrated 3D framework (Figure 20). Paper **II** comprehensively examines all studied MOFs, featuring a detailed structural analysis of crystal structures and thorough structural characterization.

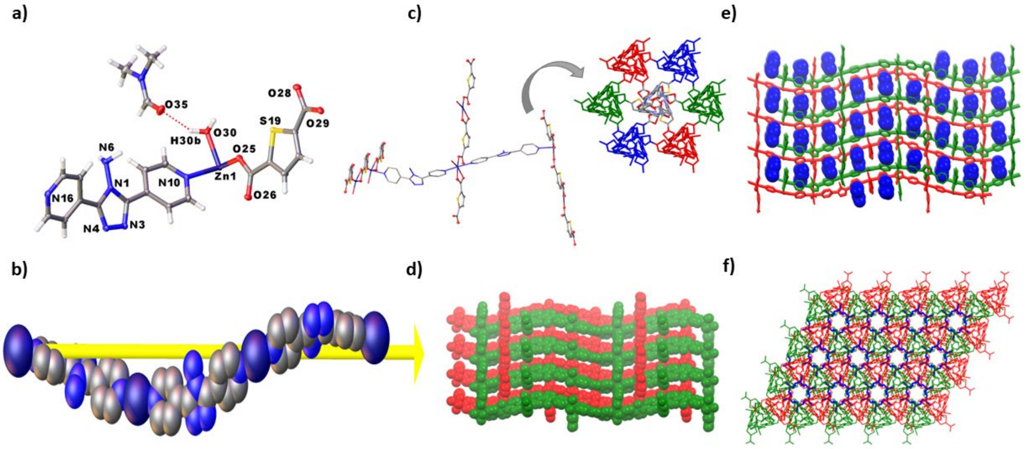

Figure 20: Structural description of MOF-**3**-Zn. (a) asymmetric unit, (b) 3_1-helix along the *b*-axis illustrated in space fill, (c) three different orientations of (tdc)$^{2-}$ linkers (A: blue, B: red, and C: green), (d) double-interpenetrated 3D framework along the *b*-axis, and (e, f) guest (dmf in blue) filled channels viewed along the *b*- and *c*-axes, respectively.[II]

2.3.4 Single-crystal-to-single-crystal (SC-to-SC) guest exchange

It is well-documented that paddlewheel SBUs are commonly found in flexible MOFs within zinc- and copper-based systems. Specifically, zinc-based paddlewheel MOFs are generally characterized by lower stability and higher flexibility when compared to copper-based systems. The pillared-layer MOFs are characterized by their ability to exhibit intrinsic framework flexibility, owing to the presence of elastic paddlewheel nodes.[114] Our study revealed that MOF-**2**-Zn (**2**) underwent an SC-to-SC transformation by the dmf to chloroform exchange, to form **2**-CHCl$_3$. The structural characterization of the exchanged **2**-CHCl$_3$ compound revealed a change in the space group: $I2/a$ space group of **2** was transformed into $P2_1/c$ for **2**-CHCl$_3$. In particular, as exemplified by frameworks overlay (Figure 21), structural transformation primarily arose from the bpt conformational variations and subtle alterations in the metal-ligand junction. Thus, in **2**-CHCl$_3$, both pyridyls of bpt show the tilted conformation [dihedral angle ~60.6(3)°] relative to each other, while pyridyls display coplanar characteristics [5.8(2)°] in **2**.

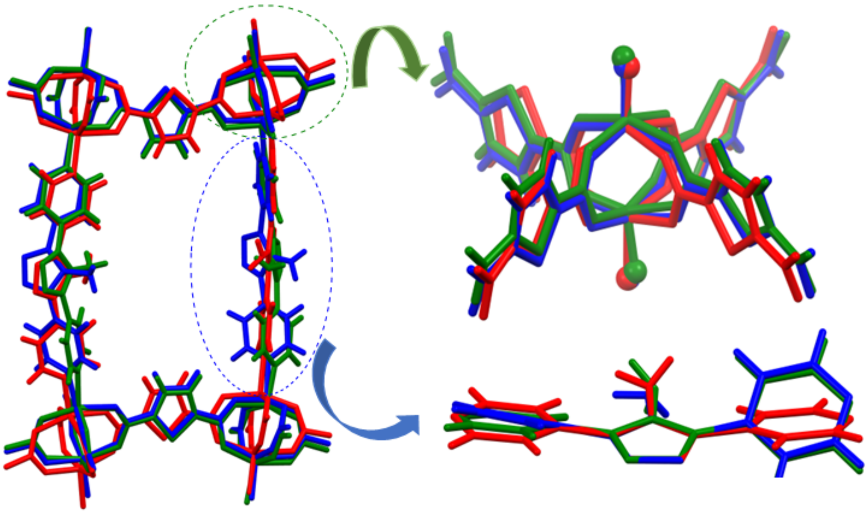

Figure 21: Superimposition of the nets of **2** (red) and **2**-$CHCl_3$ (green and blue). Only relevant atoms are shown.[II]

Apart from its notable tilting, the bpt pillar can also adjust its NH_2-triazole core in response to the guest solvent. In this study, we defined the structural transformation changes using two parameters: “$\emptyset$” and “δ”. The former represents the orientation of the NH_2-triazole core unit, while the latter represents the dihedral angles between two adjacent thiophene rings. From **2** to **2**-$CHCl_3$, the $\emptyset$- and δ- angles evolve from 45.9(3)° to 37.7(5)/40.0(4)°, and 69.5(17)° to 78.5(2)° respectively, demonstrating the capability of the host framework to adapt towards the included guest. Aside from these variations, the **2** and **2**-$CHCl_3$ are different in terms of the shape of the channels and guest-accessible voids, as manifested in Figure 22. Thus, the adaptive behavior of the pore structure towards incoming guest contents is characterized by adequate structural rearrangement, as previously observed.[114–117]

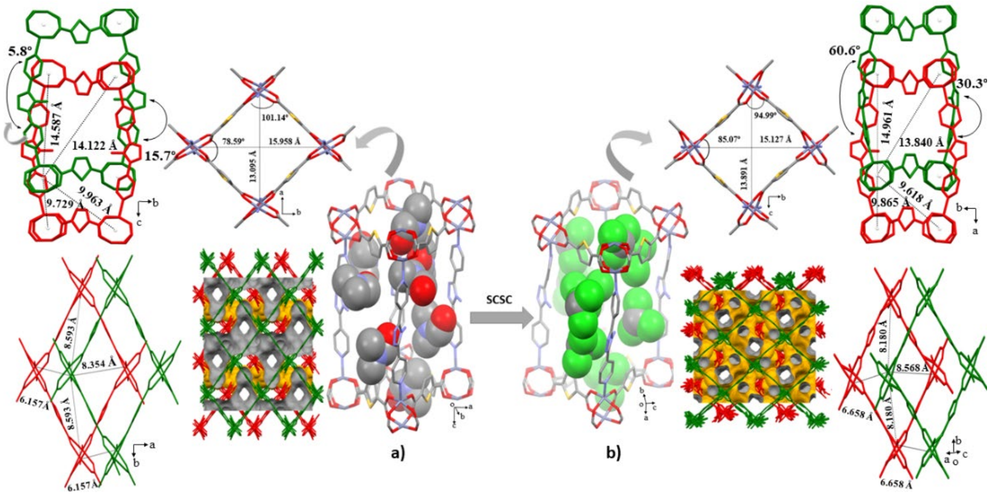

Figure 22: SC-to-SC structural transformation: from (a) **2** (with dmf) to (b) **2**-$CHCl_3$.[II]

2.3.5 Structural details of different solvates

Intrigued by the framework responsiveness, we further aimed to expand the study on how the exchange of dmf with other solvents, each with a different molecular dimension and polarity ((E_N^T))[118,119] impacts the structural characteristics of the framework. The study involved the solvent-exchange processes of **2** with three distinct classes of organic solvents, namely polar protic, polar aprotic, and nonpolar solvents, during which a series of SC-to-SC transformations were observed (Figure 23). The primary objectives of these experiments were to examine each solvent's ability to replace dmf completely, monitor the framework distortions, and identify some general correlations.

It was observed that polar and polar aprotic solvents could fully replace dmf trapped inside the pores of pristine MOF-**2**-Zn, while solely nonpolar cyclohexane fell short of complete replacement. This could be attributed to the incapacity of non-interactive cyclohexane to establish any H-bond interactions with the framework. Therefore, as in the case of **2**-cyclohexane, one independent dmf molecule binding the framework through N–H···O interaction per AU is retained, while the remaining void is filled with cyclohexane (Figure 23).

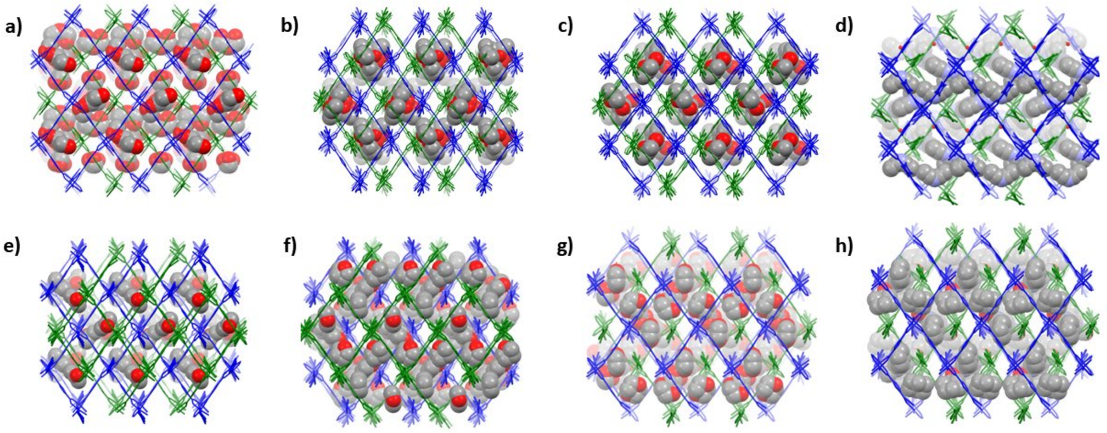

Figure 23: Representation of solvent molecules (a) methanol, (b) ethanol, (c) isopropyl alcohol, (d) acetonitrile, (e) acetone, (f) tetrahydrofuran, (g) 1,4 dioxane, and (h) cyclohexane/dimethylformamide mixture filling the voids along the *c*-axis.[II]

In all the instances, the SC-to-SC transformation was not accompanied by the change in the space group (all remained as $I2/a$). Indeed, the most notable changes derived from the solvent exchange process regard the molecular conformation of the bpt, where the guest solvent molecular size plays a crucial role. For example, the smaller solvent molecules (e.g., MeCN and MeOH) drive the pyridyl units to adopt a near-planar orientation relative to each other, with dihedral angles ranging from ~2-8°. However, the presence of larger solvents induces a twist between pyridyl rings, characterized by the dihedral range of ~32 to 46°, as can be inferred from Figure 24.

The orientation of the amino-triazole ring was observed to be markedly influenced by its ability to form host–guest interactions. Among various solvents, the most polar and the smallest solvent, methanol, induces a distinctive orientation of the amino-triazole ring (69.6°), while the other guest-exchanged frameworks demonstrated a range of ~47-55°. The MeOH accommodates perfectly inside the pores and interacts prominently with the framework backbone (MeOH–host contacts), enabling the amino and triazole functionalities to form H-bonds with MeOH. Meanwhile, these H-bond active solvents are also involved in intermolecular H-bonding with other MeOH molecules and with the carboxylic oxygen atoms. Detailed comparison and structural variations, including metal-ligand linkages and potential void distribution for all the solvated structures, are provided in Paper **II**.

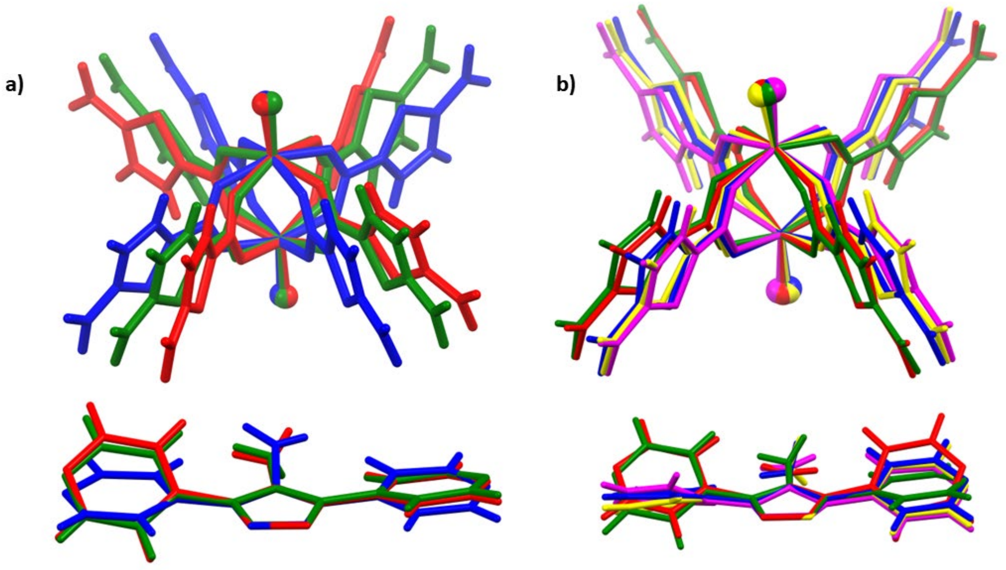

Figure 24: (a) Superimposition of the nets: polar protic solvents (a) **2**-MeOH (blue), **2**-EtOH (red), **2**-*i*-PrOH (green) and polar aprotic and nonpolar solvents: (b) **2**-MeCN (red), **2**-acetone (blue), **2**-THF (green), **2**-dioxane (magenta), and **2**-cyclohexane (yellow).[II]

2.3.6 SC-to-SC guest removal

The guest-freed **2**-gf was obtained by thermal-*vacuo* treatment of **2**-EtOH crystals. The crystal system transformed from monoclinic to triclinic along with space group change from $I2/a$ to P-1. Compared to that of **2** (or **2**-EtOH), the guest-freed **2**-gf displays a shrinkage in the unit-cell volume of ~80 % and a much lower void space (4.0 %). The dihedral angle between the pyridyl and triazole plane increases from 12.5° (**2**-EtOH) to 20°, and the δ-angle decreases from 65.6° (**2**-EtOH) to 36.7° (Figure 25). The guest-freed **2**-gf underwent changes in the coordination sphere of one zinc center, from five-coordinated square pyramidal to four-coordinated distorted tetrahedral geometry (Figure 25), with d(Zn–Zn) measured at 3.374(3) Å, which is drastically longer than the "classical" paddlewheel unit.[120,121] Overall, as depicted in Figure 25, the transformation from

2-EtOH to **2**-gf led to the movement of doubly interpenetrated nets and the motion of the bpt and $(tdc)^{2-}$ linkers without disturbing the framework integrity.

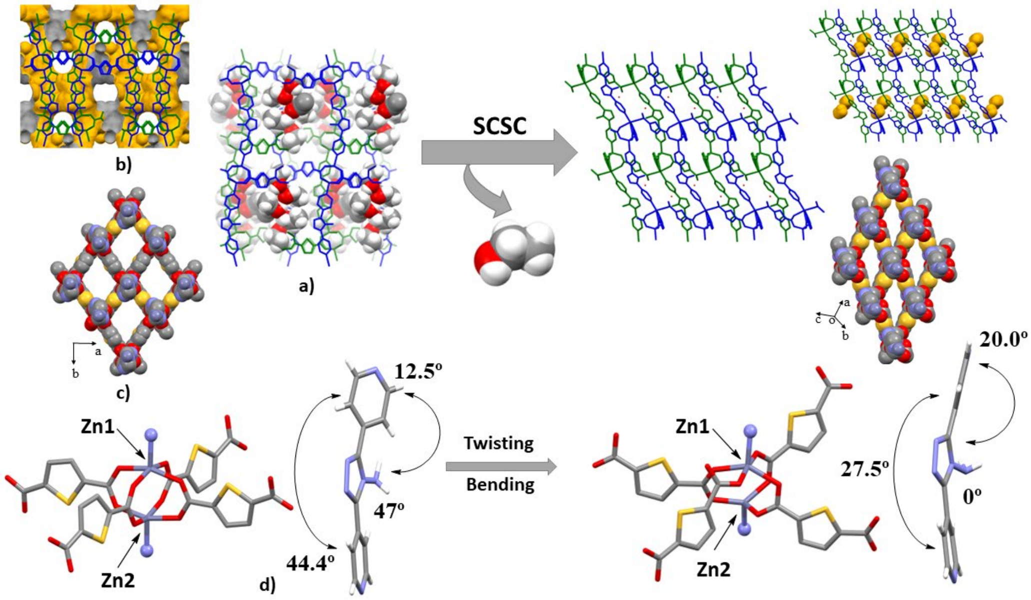

Figure 25: SC-to-SC structural transformation from **2**-EtOH to **2**-gf. (a) along the *a*-axis, (b) potential void space visualized by yellow/gray colors, (c) a view indicating structural transformation along the (bpt)-axis, and (d) changes in the coordination geometry of Zn^{II} nodes and bpt angles.[II]

2.4 CO_2 adsorption studies[II,III]

The CO_2 adsorption study investigated the adsorption properties of pillared-layer MOFs incorporating thiophene moieties and $-NH_2$ functional group, hypothesizing framework-CO_2 interactions *via* induced dipole and quadrupolar interactions. The CO_2 adsorption tests were conducted under varying dry CO_2 streams (400 ppm, 4000 ppm, and 15% CO_2) using a fixed-bed adsorption device (more details are provided in Paper **II**). Results showed negligible CO_2 adsorption for MOF-**1**-Zn at 400 ppm and 4000 ppm and nearly 0.2 $mmol_{CO2}/g_{MOF}$ at 15% CO_2 (Table 2). The phase mixture samples (MOF-**1**-Zn and MOF-**2**-Zn) demonstrated a CO_2 uptake capacity of up to 0.9 $mmol_{CO2}/g_{MOF}$ at 15% CO_2. The low CO_2 capture performance could potentially be explained by the framework shrinkage post thermal-*vacuo* treatment, hindering CO_2 diffusion.

Table 2 Summary of experimental conditions and CO_2 adsorption-desorption uptake capacities.[II]

Experiment	C_{CO2} (vol %)	T_{ads} (°C)	T_{des} (°C)	$q_{CO2,ads}$ (mmol$_{CO2}$/g)	$q_{CO2,des}$ (mmol$_{CO2}$/g)
MOF-1-Zn	0.04	12	100	0.01 ± 0.00	0.00 ± 0.00
MOF-1-Zn	0.4	12	100	0.04 ± 0.00	0.05 ± 0.00
MOF-1-Zn	15	12	100	0.18 ± 0.11	0.16 ± 0.01
Phase mixture, cycle 1	15	12	100	0.24 ± 0.14	0.13 ± 0.00
Phase mixture, cycle 2	15	12	100	0.33 ± 0.19	0.17 ± 0.01
Phase mixture, cycle 3	15	12	100	0.88 ± 0.52	0.17 ± 0.01

While the pillared-layer MOFs take up considerably lower amounts of CO_2 gas, the subsequent evaluation of ethylenediamine-appended Mg-MOF-74 (ED@MOF-74) demonstrated promising advancements in CO_2 uptake capacity, especially in the DAC applications. Therefore, in parallel, a series of adsorption experiments were carried out under varying process parameters to investigate the practical applicability of ED@MOF-74 in DAC conditions (400 ppm CO_2 balanced with N_2) using the same fixed-bed adsorption device. Table 3 summarizes the measured capacities from various experiments performed in this study. As such, the initial tests involved pristine Mg-MOF-74 using the temperature-vacuum-concentration swing adsorption (TVCSA) scheme, yielding an adsorption capacity of nearly 0.03 mmol$_{CO2}$/g$_{sorbent}$ at 25 °C. Vacuuming was omitted in the subsequent runs to prevent adsorbent loss. The following experiment involved ED@MOF-74, which was regenerated at 100 °C and exposed to dry conditions (400 ppm CO_2) for 12 hours. This resulted in a dramatic increase in CO_2 adsorption capacity to approximately 0.4 mmol$_{CO2}$/g$_{sorbent}$, surpassing that of pristine MOF. In subsequent experiments, the desorption temperature was increased to 120 °C to achieve effective thermal regeneration, resulting in enhanced CO_2 capacities (Table 3). The following sections provide brief insights into the impact of adsorption temperature and humidity on CO_2 adsorption and the outcomes of cyclic CO_2 capacity. A more in-depth analysis is available in Paper **III**.

Table 3 Summary of adsorption-desorption uptake capacities obtained in different experiments under humid and dry conditions.[III]

Experiment	C_{H2O} (vol %)	t_{ads} (h)	T_{ads} (^{o}C)	T_{des} (^{o}C)	$q_{CO2,ads}$ (mmol$_{CO2}$/g)	$q_{CO2,des}$ (mmol$_{CO2}$/g)	$q_{H2O,ads}$ (mmol$_{H2O}$/g)	$q_{H2O,des}$ (mmol$_{H2O}$/g)
1	0	12	25	100	0.42 ± 0.05	0.36 ± 0.03		
2	0	16	26	120	0.67 ± 0.08	0.77 ± 0.06		
3	1.6	16	25	120	1.79 ± 0.22	1.68 ± 0.14	11.60 ± 0.81	11.76 ± 0.42
4	1.6	16	35	120	0.66 ± 0.08	0.77 ± 0.06	8.42 ± 0.59	9.44 ± 0.33
5	0	16	35	120	1.14 ± 0.14	0.98 ± 0.08		
6	0	16	25	120	0.98 ± 0.12	0.87 ± 0.07		
7	0	16	25	120	0.90 ± 0.11	0.84 ± 0.07		
Dry cyclic	0	5	25	120	0.82 ± 0.10	0.75 ± 0.06		
Humid cyclic	1.9	5	25	120	1.07 ± 0.13	0.90 ± 0.07	10.08 ± 0.7	10.95 ± 0.39
Long cyclic	0	12	25	120	0.91 ± 0.11	0.94 ± 0.08		
Long cyclic	0	12	35	120	0.95 ± 0.12	0.89 ± 0.07		

2.4.1 Impact of adsorption temperature

To examine the impact of temperature on the CO_2 adsorption behavior of ED@MOF-74, breakthrough experiments were conducted at different adsorption temperatures (12, 25, 35, 52, 77, and 102 °C) under dry 400 ppm CO_2/N_2 and regeneration step under pure N_2 feed at 120 °C. The 400 ppm CO_2 capacity of ED@MOF-74 faded progressively at elevated temperatures, specifically higher than 35 °C. At temperatures, such as 25 °C and 35 °C, ED@MOF-74 showed similar adsorption/desorption capacities, approximately 0.9 mmol$_{CO2}$/g$_{sorbent}$. On the other hand, lower temperatures, notably 12 °C, exhibited a lowered CO_2 uptake, roughly 0.7 mmol$_{CO2}$/g$_{sorbent}$ (Figure 26). At 12 °C, the adsorption rate was notably lower compared to higher temperatures, with a gradual slowdown observed after an initial rapid increase in the CO_2 concentration. As such, the CO_2 concentration continued to rise over the 12-hour adsorption phase, indicating ED@MOF-74 did not attain saturation at the end of the 12 °C adsorption experiment. At 12 °C, the adsorption rate remains relatively high during the 5–10 hours, gradually decreasing from 0.032 to 0.017 mmol$_{CO2}$/(g$_{sorbent}$·h), contrasting with a drop from 0.035 to nearly 0.008 mmol$_{CO2}$/(g$_{sorbent}$·h) at 25 °C. Thus, this emphasizes that ED@MOF-74 suffers from a limited adsorption rate when capturing CO_2 from atmospheric conditions, particularly at temperatures below 25 °C.

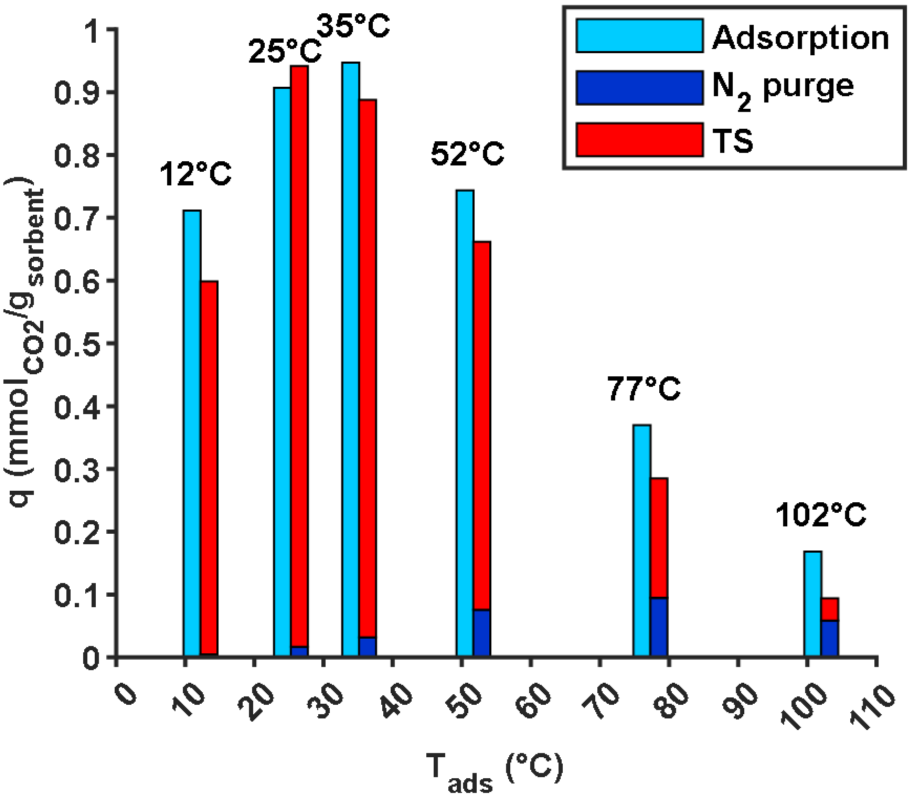

Figure 26: CO_2 adsorption and desorption uptake capacities at 12, 25, 35, 52, 77, and 102 °C adsorption temperatures. Adsorption- 400 ppm dry CO_2 (12h) and temperature swing (TS) at 120 °C.[III]

2.4.2 Impact of humidity

In the study of ED@MOF-74, it was observed that the adsorption capacity of CO_2 improved upon introducing water. At 25 °C and 400 ppm CO_2 with 2 vol-% humidity, the remarkable adsorption capacity of ~1.8 $mmol_{CO2}/g_{sorbent}$ was achieved, compared to ~0.7 $mmol_{CO2}/g_{sorbent}$ at 35 °C. This marks a notable 60% capacity fade with just a minor temperature swing (10 °C). Nevertheless, no drop in capacity was observed between 25 °C and 35 °C under dry conditions, as discussed previously. Notably, a similar observation was made for aminopolymer-impregnated silica under DAC settings; a study inferred that the presence of humidity mitigates kinetic limitations.[122]

The comparison of adsorption breakthrough data revealed that in the wet 25 °C experiment, the CO_2 concentration increased markedly slower towards the feed compared to both dry and wet 35 °C conditions (Figure 27). As a result, during the initial two hours of adsorption, the rate was dramatically higher in the wet 25 °C experiment. Specifically, the adsorption rate at the start was 1.34 $mmol_{CO2}/(g_{sorbent}\cdot h)$ and lowered to approximately 1.06 $mmol_{CO2}/(g_{sorbent}\cdot h)$ after 30 min of adsorption under moist conditions at 25 °C, representing a 21% drop. Conversely, under a dry 25 °C experiment, the values were 0.82 and 0.55 $mmol_{CO2}/(g_{sorbent}\cdot h)$, showing a 33% drop.

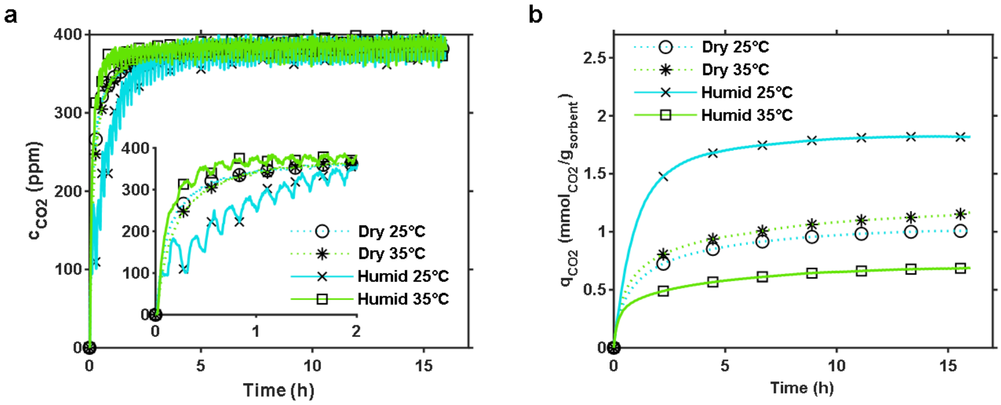

Figure 27: Experimental (a) CO_2 concentration, and (b) CO_2 uptake profiles in dry and wet conditions at 25 °C and 35 °C.[III]

Noteworthily, ED@MOF-74 displayed a pronounced affinity for water adsorption, reaching approximately 10-11 $mmol_{H2O}/g_{sorbent}$, considerably higher than the corresponding CO_2 capacities (Table 3). The high H_2O uptake can have the following possible implications when employing this material for DAC. Firstly, the substantial amount of adsorbed H_2O can escalate the energy demand of the process. Secondly, temperature increase caused by H_2O adsorption leads to a reduced adsorption rate and can affect the productivity of CO_2. In addition, the most important implication of moisture is its influence on long-term sorbent stability.

2.4.3 Cyclic CO_2 capacity

Examining CO_2 adsorption over multiple consecutive adsorption cycles is critical to determining the material's tolerance to varying process parameters. The CO_2 capture/release cycle experiments on ED@MOF-74 revealed distinct behaviors under dry and wet conditions. In dry cycling, the adsorption and desorption capacities initially stabilized after the fourth cycle, with a marginal decrease from ~0.85 to 0.79 $mmol_{CO2}/g_{sorbent}$ for adsorption and ~0.75 to 0.73 $mmol_{CO2}/g_{sorbent}$ for desorption over 18 cycles, corresponding to nearly 2.7% drop (~0.2% per cycle), see Figure 28.

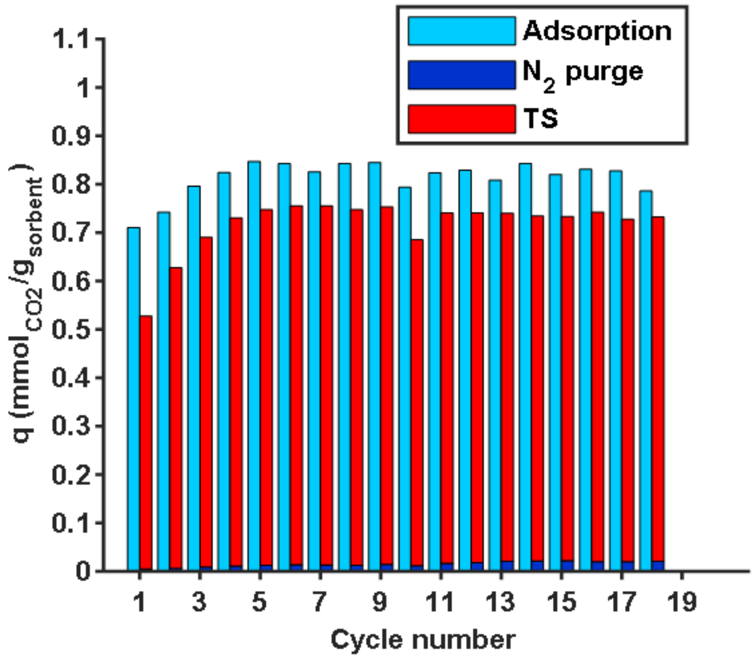

Figure 28: CO_2 adsorption and desorption uptake capacities in the repeated cycles of dry TCSA mode. Adsorption- 400 ppm CO_2 at 25 °C and desorption- pure N_2 feed at 120 °C.[III]

Notably, a considerable decrease in capacity was observed during the cyclic studies under humid conditions (Figure 29). The humid CO_2 desorption capacity dropped sharply from ~0.90 to 0.44 mmol$_{CO2}$/g$_{sorbent}$ in the first seven cycles (nearly 50% drop, ~7% per cycle) and furthered to ~0.23 mmol$_{CO2}$/g$_{sorbent}$ by the 18th cycle, amounting to ~74% decrease. On the other hand, desorption H_2O capacity displayed a somewhat constant decline from ~11 to 8.5 mmol$_{H2O}$/g$_{sorbent}$, with a decrease of nearly 1.3% per cycle (over a 23% drop). The notable performance decline is likely ensued from the structural changes in the underlying MOF or the loss of active amine sites upon subsequent adsorption-desorption cycles.[123–126] Altogether, the characterization of ED@MOF-74 samples post-cycling using PXRD, EA, and FT-IR studies corroborated a dramatic decrease in crystallinity, nitrogen content, and spectral band intensity assigned to amine modes (details in Paper **III**). Hence, these results suggest that the overall lowered CO_2 capacities observed for ED@MOF-74 may be due to amine degradation after successive TCSA cycles.

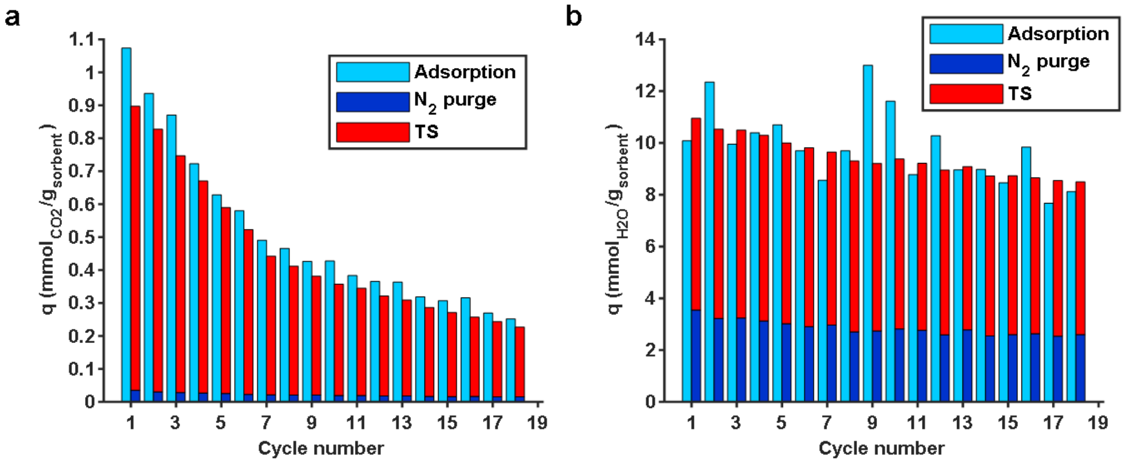

Figure 29: Adsorption and desorption uptake capacities in the repeated cycles of wet TCSA of (a) CO_2 and (b) H_2O. Adsorption- 400 ppm CO_2 at 25 °C with 2 vol-% H_2O in N_2 and desorption- pure N_2 feed at 120 °C.III

SUMMARY

In this work, we focused on two primary areas of investigation. The first area involved preparing an amino-triazole-based *N*-rich bent ligand and designing and discovering its molecular salts assisted by different anions. The second area delved into syntheses and characterization of amine-containing MOFs, focusing on exploiting their potential applications in CO_2 DAC. The investigation into anion-mediated supramolecular entities of bpt revealed how fine-tuning the experimental conditions led to the creation of a vast array of molecular salts, including both anhydrous and hydrated forms with different protonation states. Different orientations of bpt were differentiated, ranging from flattened conformation to perpendicularly tilted pyridyl units. The molecular salts obtained from different geometries of inorganic anions (e.g., linear, spherical, trigonal planar, tetrahedral, and octahedral) assembled into diverse supramolecular architectures, manifested by a group of promising noncovalent interactions, including H-bonding, π–π interactions, anion–π interactions, and anion–anion interactions. The resulting wide variety of supramolecular extended architectures included bricklayer, columns, stair-steps, zig-zag, helical, double chains, wave-like, and criss-cross orientations.

Subsequently, we diverged from bpt salts to constructing a series of double-interpenetrated mixed-ligand MOFs by varying the crystallization conditions and aimed to investigate the structural properties and CO_2 adsorption capabilities of amine-containing MOFs. Particular interest in our study has been drawn towards pillared-layer MOF, MOF-**2**-Zn, which was found to exhibit remarkable flexibility, undergoing SC-to-SC transformations upon the exchange and removal of guest solvents. This adaptability was elucidated by the framework's ability to undergo structural alterations arising from the subtle alterations in the metal-ligand junction, the orientation of the NH_2-triazole core, and pyridyl moieties, depending on the guest solvent type. The integration of distinct classes of solvents impacted the molecular conformations within the framework, featuring specific host–guest and guest–guest interactions. Notably, the evacuated $\{Zn_2\}$-“paddlewheel”-based framework maintained its crystallinity and 3D networked structure. The preliminary results of the CO_2 adsorption study revealed that the pillared-layer MOFs take up considerably lower amounts of CO_2 gas. However, much more work must be done at various temperatures and higher partial pressure ranges for precise characterization, particularly important for pressure-swing adsorption applications involving flexible adsorbents.

Our study was extended to exploring amine-tethered MOF for capturing CO_2, aiming to understand the material long-term behavior and performance when employed in a real-world DAC environment. This study on ED@MOF-74 for DAC revealed significant challenges, providing a valuable guide for future research and optimization. Key findings include the material's high regeneration temperatures, kinetic limitations, high affinity towards water, and vulnerability to humid regeneration cycles, making it less ideal for practical DAC applications without further optimization. The performance of ED@MOF-74 is susceptible to

operational conditions, particularly temperature and water activity, with significant stability issues over the course of extensive humid cycling. In future work, additional CO_2 studies under diverse relative humidity and temperature conditions, coupled with TVSA cycling, would enhance our understanding of amine-containing MOFs. Overall, the key insights gained from this contribution point out more broadly towards the necessity for comprehensive CO_2 adsorption testing under different scenarios relevant to DAC, including extended cycling experiments. Addressing the identified issues could lead to developing efficient and durable amine-containing adsorbents suitable for real-world DAC applicability, ultimately contributing to efforts to capture GHG emissions and solve environmental challenges.

REFERENCES

1. Stein, T., Carbon dioxide now more than 50% higher than pre-industrial levels _ National Oceanic and Atmospheric Administration, https://www.noaa.gov/news-release/carbon-dioxide-now-more-than-50-higher-than-pre-industrial-levels (11.12.2023).
2. United Nations Framework Convention on Climate Change, Adoption of the Paris Agreement, Paris, 2015.
3. Luz, S., The evidence is clear: the time for action is now. We can halve emissions by 2030,IPCC, https://www.ipcc.ch/2022/04/04/ipcc-ar6-wgiii-pressrelease/ (12.12.2023).
4. Ritchie, H.; Rosado, P. ja Roxer, M., CO_2 and Greenhouse Gas Emissions, https://ourworldindata.org/co2-and-greenhouse-gas-emissions (13.12.2023).
5. Fawzy, S.; Osman, A. I.; Doran, J. ja Rooney, D. W., Strategies for mitigation of climate change: a review, *Environ. Chem. Lett.*, **2020**, *18*, 2069–2094.
6. Boot-Handford, M. E.; Abanades, J. C.; Anthony, E. J.; Blunt, M. J.; Brandani, S.; Mac Dowell, N.; Fernández, J. R.; Ferrari, M.-C.; Gross, R.; Hallett, J. P.; Haszeldine, R. S.; Heptonstall, P.; Lyngfelt, A.; Makuch, Z.; Mangano, E.; Porter, R. T. J.; Pourkashanian, M.; Rochelle, G. T.; Shah, N.; Yao, J. G. ja Fennell, P. S., Carbon capture and storage update, *Energy Environ. Sci.*, **2014**, *7*, 130–189.
7. Olajire, A. A., CO_2 capture and separation technologies for end-of-pipe applications – A review, *Energy*, **2010**, *35*, 2610–2628.
8. Kupgan, G.; Abbott, L. J.; Hart, K. E. ja Colina, C. M., Modeling Amorphous Microporous Polymers for CO_2 Capture and Separations, *Chem. Rev.*, **2018**, *118*, 5488–5538.
9. Sumida, K.; Rogow, D. L.; Mason, J. A.; McDonald, T. M.; Bloch, E. D.; Herm, Z. R.; Bae, T.-H. ja Long, J. R., Carbon Dioxide Capture in Metal–Organic Frameworks, *Chem. Rev.*, **2012**, *112*, 724–781.
10. Soo, X. Y. D.; Lee, J. J. C.; Wu, W.-Y.; Tao, L.; Wang, C.; Zhu, Q. ja Bu, J., Advancements in CO_2 capture by absorption and adsorption: A comprehensive review, *J. CO_2 Util.*, **2024**, *81*, 102727.
11. Kaliyaperumal, A.; Gupta, P.; Prasad, Y. S. S.; Chandiran, A. K. ja Chetty, R., Recent Progress and Perspective of the Electrochemical Conversion of Carbon Dioxide to Alcohols, *ACS Eng. Au*, **2023**, *3*, 403–425.
12. Smith, P.; Davis, S. J.; Creutzig, F.; Fuss, S.; Minx, J.; Gabrielle, B.; Kato, E.; Jackson, R. B.; Cowie, A.; Kriegler, E.; van Vuuren, D. P.; Rogelj, J.; Ciais, P.; Milne, J.; Canadell, J. G.; McCollum, D.; Peters, G.; Andrew, R.; Krey, V.; Shrestha, G.; Friedlingstein, P.; Gasser, T.; Grübler, A.; Heidug, W. K.; Jonas, M.; Jones, C. D.; Kraxner, F.; Littleton, E.; Lowe, J.; Moreira, J. R.; Nakicenovic, N.; Obersteiner, M.; Patwardhan, A.; Rogner, M.; Rubin, E.; Sharifi, A.; Torvanger, A.; Yamagata, Y.; Edmonds, J. ja Yongsung, C., Biophysical and economic limits to negative CO_2 emissions, *Nat. Clim. Chang.*, **2016**, *6*, 42–50.

13. Erans, M.; Sanz-Pérez, E. S.; Hanak, D. P.; Clulow, Z.; Reiner, D. M. ja Mutch, G. A., Direct air capture: process technology, techno-economic and socio-political challenges, *Energy Environ. Sci.*, **2022**, *15*, 1360–1405.
14. Sanz-Pérez, E. S.; Murdock, C. R.; Didas, S. A. ja Jones, C. W., Direct Capture of CO_2 from Ambient Air, *Chem. Rev.*, **2016**, *116*, 11840–11876.
15. Fuss, S.; Lamb, W. F.; Callaghan, M. W.; Hilaire, J.; Creutzig, F.; Amann, T.; Beringer, T.; de Oliveira Garcia, W.; Hartmann, J.; Khanna, T.; Luderer, G.; Nemet, G. F.; Rogelj, J.; Smith, P.; Vicente, J. L. V.; Wilcox, J.; del Mar Zamora Dominguez, M. ja Minx, J. C., Negative emissions—Part 2: Costs, potentials and side effects, *Environ. Res. Lett.*, **2018**, *13*, 063002.
16. Gonzalez Sanchez, R.; Chatzipanagi, A.; Kakoulaki, G.; Buffi, M. ja Szabo, S., The Role of Direct Air Capture in EU's Decarbonisation and Associated Carbon Intensity for Synthetic Fuels Production, *Energies*, **2023**, *16*, 3881.
17. E. Bajamundi, C. J.; Koponen, J.; Ruuskanen, V.; Elfving, J.; Kosonen, A.; Kauppinen, J. ja Ahola, J., Capturing CO_2 from air: Technical performance and process control improvement, *J. CO_2 Util.*, **2019**, *30*, 232–239.
18. Keith, D. W.; Holmes, G.; St. Angelo, D. ja Heidel, K., A Process for Capturing CO_2 from the Atmosphere, *Joule*, **2018**, *2*, 1573–1594.
19. Climeworks, subsite: "direct air capture," (2023), https://www.climeworks.com (22.3.2024).
20. Taddei, M. ja Petit, C., Engineering metal–organic frameworks for adsorption-based gas separations: from process to atomic scale, *Mol. Syst. Des. Eng.*, **2021**, *6*, 841–875.
21. Lackner, K. S., Capture of carbon dioxide from ambient air, *Eur. Phys. J. Spec. Top.*, **2009**, *176*, 93–106.
22. Piscopo, C. G. ja Loebbecke, S., Strategies to Enhance Carbon Dioxide Capture in Metal-Organic Frameworks, *Chempluschem*, **2020**, *85*, 538–547.
23. Fasihi, M.; Efimova, O. ja Breyer, C., Techno-economic assessment of CO_2 direct air capture plants, *J. Clean. Prod.*, **2019**, *224*, 957–980.
24. Dziejarski, B.; Serafin, J.; Andersson, K. ja Krzyżyńska, R., CO_2 capture materials: a review of current trends and future challenges, *Mater. Today Sustain.*, **2023**, *24*, 100483.
25. Bose, S.; Sengupta, D.; Rayder, T. M.; Wang, X.; Kirlikovali, K. O.; Sekizkardes, A. K.; Islamoglu, T. ja Farha, O. K., Challenges and Opportunities: Metal–Organic Frameworks for Direct Air Capture, *Adv. Funct. Mater.*, **2023**.
26. Liu, J.; Wei, Y. ja Zhao, Y., Trace Carbon Dioxide Capture by Metal–Organic Frameworks, *ACS Sustain. Chem. Eng.*, **2019**, *7*, 82–93.
27. Mahajan, S. ja Lahtinen, M., Recent progress in metal-organic frameworks (MOFs) for CO_2 capture at different pressures, *J. Environ. Chem. Eng.*, **2022**, *10*, 108930.
28. Furukawa, H.; Cordova, K. E.; O'Keeffe, M. ja Yaghi, O. M., The Chemistry and Applications of Metal-Organic Frameworks, *Science*, **2013**, *341*,1230444.
29. Li, J.; Wang, X.; Zhao, G.; Chen, C.; Chai, Z.; Alsaedi, A.; Hayat, T. ja Wang, X., Metal–organic framework-based materials: superior adsorbents for the

capture of toxic and radioactive metal ions, *Chem. Soc. Rev.*, **2018**, *47*, 2322–2356.

30. Olorunyomi, J. F.; Geh, S. T.; Caruso, R. A. ja Doherty, C. M., Metal–organic frameworks for chemical sensing devices, *Mater. Horiz.*, **2021**, *8*, 2387–2419.
31. Lawson, H. D.; Walton, S. P. ja Chan, C., Metal–Organic Frameworks for Drug Delivery: A Design Perspective, *ACS Appl. Mater. Interfaces*, **2021**, *13*, 7004–7020.
32. Yang, D. ja Gates, B. C., Catalysis by Metal Organic Frameworks: Perspective and Suggestions for Future Research, *ACS Catal.*, **2019**, *9*, 1779–1798.
33. Zhang, Y.; Cui, X. ja Xing, H., Recent advances in the capture and abatement of toxic gases and vapors by metal–organic frameworks, *Mater. Chem. Front.*, **2021**, *5*, 5970–6013.
34. Moghadam, P. Z.; Li, A.; Wiggin, S. B.; Tao, A.; Maloney, A. G. P.; Wood, P. A.; Ward, S. C. ja Fairen-Jimenez, D., Development of a Cambridge Structural Database Subset: A Collection of Metal–Organic Frameworks for Past, Present, and Future, *Chem. Mater.*, **2017**, *29*, 2618–2625.
35. Ding, M.; Flaig, R. W.; Jiang, H.-L. ja Yaghi, O. M., Carbon capture and conversion using metal–organic frameworks and MOF-based materials, *Chem. Soc. Rev.*, **2019**, *48*, 2783–2828.
36. Patel, H. A.; Byun, J. ja Yavuz, C. T., Carbon Dioxide Capture Adsorbents: Chemistry and Methods, *ChemSusChem*, **2017**, *10*, 1303–1317.
37. Trickett, C. A.; Helal, A.; Al-Maythalony, B. A.; Yamani, Z. H.; Cordova, K. E. ja Yaghi, O. M., The chemistry of metal–organic frameworks for CO_2 capture, regeneration and conversion, *Nat. Rev. Mater.*, **2017**, *2*, 17045.
38. Liu, Y.; Wang, Z. U. ja Zhou, H., Recent advances in carbon dioxide capture with metal-organic frameworks, *Greenhouse Gases: Sci. and Technol.*, **2012**, *2*, 239–259.
39. Chui, S. S.-Y.; Lo, S. M.-F.; Charmant, J. P. H.; Orpen, A. G. ja Williams, I. D., A Chemically Functionalizable Nanoporous Material $[Cu_3(TMA)_2(H_2O)_3]_n$, *Science*, **1999**, *283*, 1148–1150.
40. Horcajada, P.; Surblé, S.; Serre, C.; Hong, D.-Y.; Seo, Y.-K.; Chang, J.-S.; Grenèche, J.-M.; Margiolaki, I. ja Férey, G., Synthesis and catalytic properties of MIL-100(Fe), an iron(III) carboxylate with large pores, *Chem. Commun.*, **2007**, 2820–2822.
41. Rosi, N. L.; Kim, J.; Eddaoudi, M.; Chen, B.; O'Keeffe, M. ja Yaghi, O. M., Rod Packings and Metal−Organic Frameworks Constructed from Rod-Shaped Secondary Building Units, *J. Am. Chem. Soc.*, **2005**, *127*, 1504–1518.
42. Caskey, S. R.; Wong-Foy, A. G. ja Matzger, A. J., Dramatic Tuning of Carbon Dioxide Uptake via Metal Substitution in a Coordination Polymer with Cylindrical Pores, *J. Am. Chem. Soc.*, **2008**, *130*, 10870–10871.
43. Dietzel, P. D. C.; Blom, R. ja Fjellvåg, H., Base-induced formation of two magnesium metal-organic framework compounds with a bifunctional tetratopic ligand, *Eur. J. Inorg. Chem.*, **2008**, 3624–3632.

44. Deng, H.; Grunder, S.; Cordova, K. E.; Valente, C.; Furukawa, H.; Hmadeh, M.; Gándara, F.; Whalley, A. C.; Liu, Z.; Asahina, S.; Kazumori, H.; O'Keeffe, M.; Terasaki, O.; Stoddart, J. F. ja Yaghi, O. M., Large-Pore Apertures in a Series of Metal-Organic Frameworks, *Science*, **2012**, *336*, 1018–1023.
45. Mason, J. A.; Sumida, K.; Herm, Z. R.; Krishna, R. ja Long, Jeffrey. R., Evaluating metal–organic frameworks for post-combustion carbon dioxide capture via temperature swing adsorption, *Energy Environ. Sci.*, **2011**, *4*, 3030.
46. Pato-Doldán, B.; Rosnes, M. H. ja Dietzel, P. D. C., An In-Depth Structural Study of the Carbon Dioxide Adsorption Process in the Porous Metal–Organic Frameworks CPO-27-M, *ChemSusChem*, **2017**, *10*, 1710–1719.
47. Hou, X.-J.; He, P.; Li, H. ja Wang, X., Understanding the Adsorption Mechanism of C_2H_2, CO_2, and CH_4 in Isostructural Metal–Organic Frameworks with Coordinatively Unsaturated Metal Sites, *J. Phys. Chem. C*, **2013**, *117*, 2824–2834.
48. Kong, X.; Scott, E.; Ding, W.; Mason, J. A.; Long, J. R. ja Reimer, J. A., CO_2 Dynamics in a Metal–Organic Framework with Open Metal Sites, *J. Am. Chem. Soc.*, **2012**, *134*, 14341–14344.
49. Queen, W. L.; Brown, C. M.; Britt, D. K.; Zajdel, P.; Hudson, M. R. ja Yaghi, O. M., Site-Specific CO_2 Adsorption and Zero Thermal Expansion in an Anisotropic Pore Network, *J. Phys. Chem. C*, **2011**, *115*, 24915–24919.
50. Queen, W. L.; Hudson, M. R.; Bloch, E. D.; Mason, J. A.; Gonzalez, M. I.; Lee, J. S.; Gygi, D.; Howe, J. D.; Lee, K.; Darwish, T. A.; James, M.; Peterson, V. K.; Teat, S. J.; Smit, B.; Neaton, J. B.; Long, J. R. ja Brown, C. M., Comprehensive study of carbon dioxide adsorption in the metal–organic frameworks M_2(dobdc) (M = Mg, Mn, Fe, Co, Ni, Cu, Zn), *Chem. Sci.*, **2014**, *5*, 4569–4581.
51. Mason, J. A.; McDonald, T. M.; Bae, T.-H.; Bachman, J. E.; Sumida, K.; Dutton, J. J.; Kaye, S. S. ja Long, J. R., Application of a High-Throughput Analyzer in Evaluating Solid Adsorbents for Post-Combustion Carbon Capture via Multicomponent Adsorption of CO_2, N_2, and H_2O, *J. Am. Chem. Soc.*, **2015**, *137*, 4787–4803.
52. Kizzie, A. C.; Wong-Foy, A. G. ja Matzger, A. J., Effect of Humidity on the Performance of Microporous Coordination Polymers as Adsorbents for CO_2 Capture, *Langmuir*, **2011**, *27*, 6368–6373.
53. Abdullatif, Y.; Sodiq, A.; Mir, N.; Bicer, Y.; Al-Ansari, T.; El-Naas, M. H. ja Amhamed, A. I., Emerging trends in direct air capture of CO_2: a review of technology options targeting net-zero emissions, *RSC Adv.*, **2023**, *13*, 5687–5722.
54. Didas, S. A.; Kulkarni, A. R.; Sholl, D. S. ja Jones, C. W., Role of Amine Structure on Carbon Dioxide Adsorption from Ultradilute Gas Streams such as Ambient Air, *ChemSusChem*, **2012**, *5*, 2058–2064.
55. Didas, S. A.; Sakwa-Novak, M. A.; Foo, G. S.; Sievers, C. ja Jones, C. W., Effect of Amine Surface Coverage on the Co-Adsorption of CO_2 and Water:

Spectral Deconvolution of Adsorbed Species, *J. Phys. Chem. Lett.*, **2014**, *5*, 4194–4200.

56. Panda, D.; Kulkarni, V. ja Singh, S. K., Evaluation of amine-based solid adsorbents for direct air capture: a critical review, *React. Chem. Eng.*, **2023**, *8*, 10–40.
57. Yu, J. ja Chuang, S. S. C., The Role of Water in CO_2 Capture by Amine, *Ind. Eng. Chem. Res.*, **2017**, *56*, 6337–6347.
58. Flaig, R. W.; Osborn Popp, T. M.; Fracaroli, A. M.; Kapustin, E. A.; Kalmutzki, M. J.; Altamimi, R. M.; Fathieh, F.; Reimer, J. A. ja Yaghi, O. M., The Chemistry of CO_2 Capture in an Amine-Functionalized Metal-Organic Framework under Dry and Humid Conditions, *J. Am. Chem. Soc.*, **2017**, *139*, 12125–12128.
59. Rim, G.; Priyadarshini, P.; Song, M.; Wang, Y.; Bai, A.; Realff, M. J.; Lively, R. P. ja Jones, C. W., Support Pore Structure and Composition Strongly Influence the Direct Air Capture of CO_2 on Supported Amines, *J. Am. Chem. Soc.*, **2023**, *145*, 7190–7204.
60. Wilfong, W. C.; Srikanth, C. S. ja Chuang, S. S. C., In Situ ATR and DRIFTS Studies of the Nature of Adsorbed CO_2 on Tetraethylenepentamine Films, *ACS Appl. Mater. Interfaces*, **2014**, *6*, 13617–13626.
61. Lu, W.; Sculley, J. P.; Yuan, D.; Krishna, R. ja Zhou, H.-C., Carbon Dioxide Capture from Air Using Amine-Grafted Porous Polymer Networks, *J. Phys. Chem. C*, **2013**, *117*, 4057–4061.
62. Wang, J.; Huang, H.; Wang, M.; Yao, L.; Qiao, W.; Long, D. ja Ling, L., Direct Capture of Low-Concentration CO_2 on Mesoporous Carbon-Supported Solid Amine Adsorbents at Ambient Temperature, *Ind. Eng. Chem. Res.*, **2015**, *54*, 5319–5327.
63. Chaikittisilp, W.; Kim, H.-J. ja Jones, C. W., Mesoporous Alumina-Supported Amines as Potential Steam-Stable Adsorbents for Capturing CO_2 from Simulated Flue Gas and Ambient Air, *Energy Fuels*, **2011**, *25*, 5528–5537.
64. Sayari, A.; Liu, Q. ja Mishra, P., Enhanced Adsorption Efficiency through Materials Design for Direct Air Capture over Supported Polyethylenimine, *ChemSusChem*, **2016**, *9*, 2796–2803.
65. Zhou, W.; Wu, H. ja Yildirim, T., Enhanced H_2 Adsorption in Isostructural Metal−Organic Frameworks with Open Metal Sites: Strong Dependence of the Binding Strength on Metal Ions, *J. Am. Chem. Soc.*, **2008**, *130*, 15268–15269.
66. Sehaqui, H.; Gálvez, M. E.; Becatinni, V.; cheng Ng, Y.; Steinfeld, A.; Zimmermann, T. ja Tingaut, P., Fast and Reversible Direct CO_2 Capture from Air onto All-Polymer Nanofibrillated Cellulose—Polyethylenimine Foams, *Environ. Sci. Technol.*, **2015**, *49*, 3167–3174.
67. An, J.; Geib, S. J. ja Rosi, N. L., High and Selective CO_2 Uptake in a Cobalt Adeninate Metal−Organic Framework Exhibiting Pyrimidine- and Amino-Decorated Pores, *J. Am. Chem. Soc.*, **2010**, *132*, 38–39.

68. Millward, A. R. ja Yaghi, O. M., Metal−Organic Frameworks with Exceptionally High Capacity for Storage of Carbon Dioxide at Room Temperature, *J. Am. Chem. Soc.*, **2005**, *127*, 17998–17999.
69. Couck, S.; Denayer, J. F. M.; Baron, G. V.; Rémy, T.; Gascon, J. ja Kapteijn, F., An Amine-Functionalized MIL-53 Metal−Organic Framework with Large Separation Power for CO_2 and CH_4, *J. Am. Chem. Soc.*, **2009**, *131*, 6326–6327.
70. Yang, Q.; Wiersum, A. D.; Llewellyn, P. L.; Guillerm, V.; Serre, C. ja Maurin, G., Functionalizing porous zirconium terephthalate UiO-66(Zr) for natural gas upgrading: a computational exploration, *Chem. Commun.*, **2011**, *47*, 9603.
71. Kim, S.-N.; Kim, J.; Kim, H.-Y.; Cho, H.-Y. ja Ahn, W.-S., Adsorption/catalytic properties of MIL-125 and NH_2-MIL-125, *Catal. Today*, **2013**, *204*, 85–93.
72. Vaidhyanathan, R.; Iremonger, S. S.; Dawson, K. W. ja Shimizu, G. K. H., An amine-functionalized metal organic framework for preferential CO_2 adsorption at low pressures, *Chem. Commun.*, **2009**, 5230.
73. Vaidhyanathan, R.; Iremonger, S. S.; Shimizu, G. K. H.; Boyd, P. G.; Alavi, S. ja Woo, T. K., Direct Observation and Quantification of CO_2 Binding Within an Amine-Functionalized Nanoporous Solid, *Science*, **2010**, *330*, 650–653.
74. Ali Akbar Razavi, S. ja Morsali, A., Linker functionalized metal-organic frameworks, *Coord. Chem. Rev.*, **2019**, *399*, 213023.
75. Fracaroli, A. M.; Furukawa, H.; Suzuki, M.; Dodd, M.; Okajima, S.; Gándara, F.; Reimer, J. A. ja Yaghi, O. M., Metal–Organic Frameworks with Precisely Designed Interior for Carbon Dioxide Capture in the Presence of Water, *J. Am. Chem. Soc.*, **2014**, *136*, 8863–8866.
76. Choi, S.; Watanabe, T.; Bae, T.-H.; Sholl, D. S. ja Jones, C. W., Modification of the Mg/DOBDC MOF with Amines to Enhance CO_2 Adsorption from Ultradilute Gases, *J. Phys. Chem. Lett.*, **2012**, *3*, 1136–1141.
77. Liao, P. Q.; Chen, X. W.; Liu, S. Y.; Li, X. Y.; Xu, Y. T.; Tang, M.; Rui, Z.; Ji, H.; Zhang, J. P. ja Chen, X. M., Putting an ultrahigh concentration of amine groups into a metal-organic framework for CO_2 capture at low pressures, *Chem. Sci*, **2016**, *7*, 6528–6533.
78. Andirova, D.; Lei, Y.; Zhao, X. ja Choi, S., Functionalization of Metal–Organic Frameworks for Enhanced Stability under Humid Carbon Dioxide Capture Conditions, *ChemSusChem*, **2015**, *8*, 3405–3409.
79. McDonald, T. M.; Lee, W. R.; Mason, J. A.; Wiers, B. M.; Hong, C. S. ja Long, J. R., Capture of Carbon Dioxide from Air and Flue Gas in the Alkylamine-Appended Metal–Organic Framework mmen-Mg_2(dobpdc), *J. Am. Chem. Soc.*, **2012**, *134*, 7056–7065.
80. McDonald, T. M.; Mason, J. A.; Kong, X.; Bloch, E. D.; Gygi, D.; Dani, A.; Crocellà, V.; Giordanino, F.; Odoh, S. O.; Drisdell, W. S.; Vlaisavljevich, B.; Dzubak, A. L.; Poloni, R.; Schnell, S. K.; Planas, N.; Lee, K.; Pascal, T.; Wan, L. F.; Prendergast, D.; Neaton, J. B.; Smit, B.; Kortright, J. B.; Gagliardi, L.;

Bordiga, S.; Reimer, J. A. ja Long, J. R., Cooperative insertion of CO_2 in diamine-appended metal-organic frameworks, *Nature*, **2015**, *519*, 303–308.

81. Lee, W. R.; Hwang, S. Y.; Ryu, D. W.; Lim, K. S.; Han, S. S.; Moon, D.; Choi, J. ja Hong, C. S., Diamine-functionalized metal–organic framework: exceptionally high CO_2 capacities from ambient air and flue gas, ultrafast CO_2 uptake rate, and adsorption mechanism, *Energy Environ. Sci.*, **2014**, *7*, 744–751.
82. Forse, A. C.; Milner, P. J.; Lee, J.-H.; Redfearn, H. N.; Oktawiec, J.; Siegelman, R. L.; Martell, J. D.; Dinakar, B.; Zasada, L. B.; Gonzalez, M. I.; Neaton, J. B.; Long, J. R. ja Reimer, J. A., Elucidating CO_2 Chemisorption in Diamine-Appended Metal–Organic Frameworks, *J. Am. Chem. Soc.*, **2018**, *140*, 18016–18031.
83. Forse, A. C.; Gonzalez, M. I.; Siegelman, R. L.; Witherspoon, V. J.; Jawahery, S.; Mercado, R.; Milner, P. J.; Martell, J. D.; Smit, B.; Blümich, B.; Long, J. R. ja Reimer, J. A., Unexpected Diffusion Anisotropy of Carbon Dioxide in the Metal–Organic Framework Zn_2(dobpdc), *J. Am. Chem. Soc.*, **2018**, *140*, 1663–1673.
84. Berge, A. H.; Pugh, S. M.; Short, M. I. M.; Kaur, C.; Lu, Z.; Lee, J.-H.; Pickard, C. J.; Sayari, A. ja Forse, A. C., Revealing carbon capture chemistry with 17-oxygen NMR spectroscopy, *Nat. Commun.*, **2022**, *13*, 7763.
85. Milner, P. J.; Martell, J. D.; Siegelman, R. L.; Gygi, D.; Weston, S. C. ja Long, J. R., Overcoming double-step CO_2 adsorption and minimizing water co-adsorption in bulky diamine-appended variants of Mg_2(dobpdc), *Chem. Sci.*, **2018**, *9*, 160–174.
86. Kim, E. J.; Siegelman, R. L.; Jiang, H. Z. H.; Forse, A. C.; Lee, J.-H.; Martell, J. D.; Milner, P. J.; Falkowski, J. M.; Neaton, J. B.; Reimer, J. A.; Weston, S. C. ja Long, J. R., Cooperative carbon capture and steam regeneration with tetraamine-appended metal–organic frameworks, *Science*, **2020**, *369*, 392–396.
87. Darunte, L. A.; Oetomo, A. D.; Walton, K. S.; Sholl, D. S. ja Jones, C. W., Direct Air Capture of CO_2 Using Amine Functionalized MIL-101(Cr), *ACS Sustain. Chem. Eng.*, **2016**, *4*, 5761–5768.
88. Li, H.; Wang, K.; Feng, D.; Chen, Y.; Verdegaal, W. ja Zhou, H., Incorporation of Alkylamine into Metal–Organic Frameworks through a Brønsted Acid–Base Reaction for CO_2 Capture, *ChemSusChem*, **2016**, *9*, 2832–2840.
89. Rim, G.; Kong, F.; Song, M.; Rosu, C.; Priyadarshini, P.; Lively, R. P. ja Jones, C. W., Sub-Ambient Temperature Direct Air Capture of CO_2 using Amine-Impregnated MIL-101(Cr) Enables Ambient Temperature CO_2 Recovery, *JACS Au*, **2022**, *2*, 380–393.
90. Liu, F.; Wang, T.; Dong, H. ja Liu, W., Modified metal–organic framework by a novel coordinatively unsaturated amine grafting mechanism for direct air capture of CO_2, *Chem. Eng. J.*, **2023**, *454*, 140431.

91. Jiang, K.; Yang, J.; Zhou, Y. ja Gu, J., Synergetic enhancement of CO_2 direct air capture with monoethanolamine-impregnated MIL-101(Cr) MOFs, *Microporous Mesoporous Mater.*, **2024**, *366*, 112920.
92. Dong, H.; Li, L.-H.; Feng, Z.; Wang, Q.-N.; Luan, P.; Li, J. ja Li, C., Amine-Functionalized Quasi-MOF for Direct Air Capture of CO_2, *ACS Mater. Lett.*, **2023**, *5*, 2656–2664.
93. Nugent, P.; Giannopoulou, E. G.; Burd, S. D.; Elemento, O.; Giannopoulou, E. G.; Forrest, K.; Pham, T.; Ma, S.; Space, B.; Wojtas, L.; Eddaoudi, M. ja Zaworotko, M. J., Porous materials with optimal adsorption thermodynamics and kinetics for CO_2 separation, *Nature*, **2013**, *495*, 80–84.
94. Shekhah, O.; Belmabkhout, Y.; Chen, Z.; Guillerm, V.; Cairns, A.; Adil, K. ja Eddaoudi, M., Made-to-order metal-organic frameworks for trace carbon dioxide removal and air capture, *Nat. Commun.*, **2014**, *5*, 4228.
95. Bhatt, P. M.; Belmabkhout, Y.; Cadiau, A.; Adil, K.; Shekhah, O.; Shkurenko, A.; Barbour, L. J. ja Eddaoudi, M., A Fine-Tuned Fluorinated MOF Addresses the Needs for Trace CO_2 Removal and Air Capture Using Physisorption, *J. Am. Chem. Soc.*, **2016**, *138*, 9301–9307.
96. Kumar, A.; Hua, C.; Madden, D. G.; O'Nolan, D.; Chen, K.-J.; Keane, L.-A. J.; Perry, J. J. ja Zaworotko, M. J., Hybrid ultramicroporous materials (HUMs) with enhanced stability and trace carbon capture performance, *Chem. Commun.*, **2017**, *53*, 5946–5949.
97. Madden, D. G.; Scott, H. S.; Kumar, A.; Chen, K.-J.; Sanii, R.; Bajpai, A.; Lusi, M.; Curtin, T.; Perry, J. J. ja Zaworotko, M. J., Flue-gas and direct-air capture of CO_2 by porous metal–organic materials, *Philos. Trans. R. Soc. A: Mathe. Phys. Eng. Sci.*, **2017**, *375*, 20160025.
98. Mukherjee, S.; Sikdar, N.; O'Nolan, D.; Franz, D. M.; Gascón, V.; Kumar, A.; Kumar, N.; Scott, H. S.; Madden, D. G.; Kruger, P. E.; Space, B. ja Zaworotko, M. J., Trace CO_2 capture by an ultramicroporous physisorbent with low water affinity, *Sci. Adv.*, **2019**, *5*, 1–8.
99. Zhao, P.; Tsang, S. C. E. ja Fairen-Jimenez, D., Structural heterogeneity and dynamics in flexible metal-organic frameworks, *Cell Rep. Phys. Sci.*, **2021**, *2*, 100544.
100. Serre, C.; Millange, F.; Thouvenot, C.; Noguès, M.; Marsolier, G.; Louër, D. ja Férey, G., Very Large Breathing Effect in the First Nanoporous Chromium(III)-Based Solids: MIL-53 or $Cr^{III}(OH)\cdot\{O_2C{-}C_6H_4{-}CO_2\}\cdot\{HO_2C{-}C_6H_4{-}CO_2H\}_x\cdot H_2O_y$, *J. Am. Chem. Soc.*, **2002**, *124*, 13519–13526.
101. Serre, C.; Bourrelly, S.; Vimont, A.; Ramsahye, N. A.; Maurin, G.; Llewellyn, P. L.; Daturi, M.; Filinchuk, Y.; Leynaud, O.; Barnes, P. ja Férey, G., An Explanation for the Very Large Breathing Effect of a Metal–Organic Framework during CO_2 Adsorption, *Adv. Mater.*, **2007**, *19*, 2246–2251.
102. Llewellyn, P. L.; Bourrelly, S.; Serre, C.; Filinchuk, Y. ja Férey, G., How Hydration Drastically Improves Adsorption Selectivity for CO_2 over CH_4 in the Flexible Chromium Terephthalate MIL-53, *Angew. Chem. Int. Ed.*, **2006**, *45*, 7751–7754.

103. Neimark, A. V.; Coudert, F.-X.; Triguero, C.; Boutin, A.; Fuchs, A. H.; Beurroies, I. ja Denoyel, R., Structural Transitions in MIL-53 (Cr): View from Outside and Inside, *Langmuir*, **2011**, *27*, 4734–4741.
104. Carrington, E. J.; McAnally, C. A.; Fletcher, A. J.; Thompson, S. P.; Warren, M. ja Brammer, L., Solvent-switchable continuous-breathing behaviour in a diamondoid metal–organic framework and its influence on CO$_2$ versus CH$_4$ selectivity, *Nat Chem.*, **2017**, *9*, 882–889.
105. Peng, J.; Liu, Z.; Wu, Y.; Xian, S. ja Li, Z., High-Performance Selective CO$_2$ Capture on a Stable and Flexible Metal–Organic Framework via Discriminatory Gate-Opening Effect, *ACS Appl. Mater. Interfaces*, **2022**, *14*, 21089–21097.
106. Bentiss, F.; Lagrenée, M.; Traisnel, M.; Mernari, B. ja Elattari, H., A simple one step synthesis of new 3,5-disubstituted-4-amino-1,2,4-triazoles, *J Heterocycl. Chem.*, **1999**, *36*, 149–152.
107. Vornholt, S. M.; Henkelis, S. E. ja Morris, R. E., Low temperature synthesis study of metal–organic framework CPO-27: investigating metal, solvent and base effects down to −78 °C, *Dalton Trans.*, **2017**, *46*, 8298–8303.
108. Etter, M. C.; MacDonald, J. C. ja Bernstein, J., Graph-set analysis of hydrogen-bond patterns in organic crystals, *Acta Crystallogr. sect. B*, **1990**, *46*, 256–262.
109. Kim, H.-J., Assembly of Sn(IV)-Porphyrin Cation Exhibiting Supramolecular Interactions of Anion···Anion and Anion··π Systems, *Molbank*, **2022**, *2022*, M1454.
110. Hursthouse, M. B.; Montis, R.; Niitsoo, L.; Sarson, J.; Threlfall, T. L.; Asiri, A. M.; Khan, S. A.; Obaid, A. Y. ja Al-Harbi, L. M., Anhydrates and/or hydrates in nitrate, sulphate and phosphate salts of 4-aminopyridine, (4-AP) and 3,4-diaminopyridine (3,4-DAP): The role of the water molecules in the hydrates, *CrystEngComm*, **2014**, *16*, 2205–2219.
111. Zhang, G.; Zhang, X.; Kong, L.; Wang, S.; Tian, Y.; Tao, X. ja Yang, J., Anion-controlled dimer distance induced unique solid-state fluorescence of cyano substituted styrene pyridinium, *Sci. Rep.*, **2016**, *6*, 37609.
112. Hoque, Md. N. ja Das, G., Cationic Tripodal Receptor Assisted Formation of Anion and Anion–Water Clusters: Structural Interpretation of Dihydrogen Phosphate Cluster and Sulfate–Water Tetramer [(SO$_4$)$_2$–(H$_2$O)$_2$]$^{4-}$, *Cryst. Growth Des.*, **2014**, *14*, 2962–2971.
113. Hoque, N.; Manna, U. ja Das, G., Discrepancy in anion coordination directed by isomeric pyridine – urea receptors : Solid state recognition of hydrated anions, *Polyhedron*, **2016**, *119*, 307–316.
114. Senkovska, I.; Bon, V.; Abylgazina, L.; Mendt, M.; Berger, J.; Kieslich, G.; Petkov, P.; Luiz Fiorio, J.; Joswig, J.; Heine, T.; Schaper, L.; Bachetzky, C.; Schmid, R.; Fischer, R. A.; Pöppl, A.; Brunner, E. ja Kaskel, S., Understanding MOF Flexibility: An Analysis Focused on Pillared Layer MOFs as a Model System, *Angew. Chem. Int. Ed.*, **2023**, *62,* e202218076.
115. Wang, S.-Q.; Mukherjee, S. ja Zaworotko, M. J., Spiers Memorial Lecture: Coordination networks that switch between nonporous and porous

structures: an emerging class of soft porous crystals., *Faraday Discuss.*, **2021**, *231*, 9–50.

116. Giovanardi, D.; Mazzeo, P. P.; Pelagatti, P. ja Bacchi, A., Guest Molecules Play Tug of War in a Breathing MOF: The Stepwise Monitoring of an Elastic Framework Deformation via SC-SC Transformations, *Cryst. Growth Des.*, **2023**, *23*, 8726–8734.
117. Zhu, A.; Yang, Q.; Mukherjee, S.; Kumar, A.; Deng, C.; Bezrukov, A. A.; Shivanna, M. ja Zaworotko, M. J., Tuning the Gate-Opening Pressure in a Switching pcu Coordination Network, X-pcu-5-Zn, by Pillar-Ligand Substitution, *Angew. Chem.*, **2019**, *131*, 18380–18385.
118. Reichardt, C., Solvatochromic Dyes as Solvent Polarity Indicators, *Chem. Rev.*, **1994**, *94*, 2319–2358.
119. de J. Velásquez-Hernández, M.; López-Cervantes, V. B.; Martínez-Ahumada, E.; Tu, M.; Hernández-Balderas, U.; Martínez-Otero, D.; Williams, D. R.; Martis, V.; Sánchez-González, E.; Chang, J.-S.; Lee, J. S.; Balmaseda, J.; Ameloot, R.; Ibarra, I. A. ja Jancik, V., CCIQS-1: A Dynamic Metal–Organic Framework with Selective Guest-Triggered Porosity Switching, *Chem. Mater.*, **2022**, *34*, 669–677.
120. Seo, J.; Bonneau, C.; Matsuda, R.; Takata, M. ja Kitagawa, S., Soft secondary building unit: Dynamic bond rearrangement on multinuclear core of porous coordination polymers in gas media, *J. Am. Chem. Soc.*, **2011**, *133*, 9005–9013.
121. Bon, V.; Senkovska, I.; Wallacher, D.; Többens, D. M.; Zizak, I.; Feyerherm, R.; Mueller, U. ja Kaskel, S., In Situ Observation of Gating Phenomena in the Flexible Porous Coordination Polymer $Zn_2(BPnDC)_2(bpy)$(SNU-9) in a Combined Diffraction and Gas Adsorption Experiment, *Inorg. Chem.*, **2014**, *53*, 1513–1520.
122. Kwon, H. T.; Sakwa-Novak, M. A.; Pang, S. H.; Sujan, A. R.; Ping, E. W. ja Jones, C. W., Aminopolymer-Impregnated Hierarchical Silica Structures: Unexpected Equivalent CO_2 Uptake under Simulated Air Capture and Flue Gas Capture Conditions, *Chem. Mater.*, **2019**, *31*, 5229–5237.
123. Kumar, A.; Madden, D. G.; Lusi, M.; Chen, K.; Daniels, E. A.; Curtin, T.; Perry, J. J. ja Zaworotko, M. J., Direct Air Capture of CO_2 by Physisorbent Materials, *Angew. Chem. Int. Ed.*, **2015**, *54*, 14372–14377.
124. Voskanyan, A. A.; Goncharov, V. G.; Novendra, N.; Guo, X. ja Navrotsky, A., Thermodynamics Drives the Stability of the MOF-74 Family in Water, *ACS Omega*, **2020**, *5*, 13158–13163.
125. Adil, K.; Bhatt, P. M.; Belmabkhout, Y.; Abtab, S. M. T.; Jiang, H.; Assen, A. H.; Mallick, A.; Cadiau, A.; Aqil, J. ja Eddaoudi, M., Valuing Metal–Organic Frameworks for Postcombustion Carbon Capture: A Benchmark Study for Evaluating Physical Adsorbents, *Adv. Mater.*, **2017**, *29*, 1702953.
126. Choe, J. H.; Kim, H.; Kang, M.; Yun, H.; Kim, S. Y.; Lee, S. M. ja Hong, C. S., Functionalization of Diamine-Appended MOF-Based Adsorbents by Ring Opening of Epoxide: Long-Term Stability and CO_2 Recyclability under Humid Conditions, *J. Am. Chem. Soc.*, **2022**, *144*, 10309–10319.

ORIGINAL PAPERS

I

INORGANIC ANION-MEDIATED SUPRAMOLECULAR ENTITIES OF 4-AMINO-3,5-BIS(4-PYRIDYL)-1,2,4-TRIAZOLE SALTS ASSISTED BY THE INTERPLAY OF NONCOVALENT INTERACTIONS

by

Mahajan, S.; Marttinen, A.; Forsblom, S.; Lahtinen, M. 2023

Crystal Growth & Design, 23(7), 5144-5162

https://doi.org/10.1021/acs.cgd.3c00393

CRYSTAL
GROWTH
&DESIGN

pubs.acs.org/crystal

Article

Inorganic Anion-Mediated Supramolecular Entities of 4-Amino-3,5-Bis(4-Pyridyl)-1,2,4-Triazole Salts Assisted by the Interplay of Noncovalent Interactions

Shreya Mahajan, Antti Marttinen, Samu Forsblom, and Manu Lahtinen*

Cite This: *Cryst. Growth Des.* 2023, 23, 5144−5162

Read Online

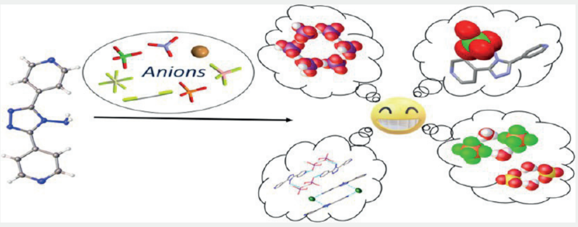

ABSTRACT: The development of new families of synthetic molecular systems projecting neutral, bi-, or multi-H-bonding donor units is significant to acquire the desired selectivity within the fascinating area of anion recognition. Here, we illustrate the reaction between a neutral 4-amino-3,5-bis(4-pyridyl)-1,2,4-triazole ligand (**L**) with acidic solutions containing either chloride, bromide, nitrate, phosphate, iodide, sulfate, hexafluorosilicate, fluoride, tetrafluoroborate or perchlorate anions, yielding 16 new anion-mediated supramolecular entities, H_2LCl_2 (**1**), H_2LBr_2 (**2**), $H_2L(NO_3)_2$ (**3**), $HL(H_2PO_4)$ (**4**), $H_2L(H_2PO_4)_2$ (**5**), $[H_2L]_2I_4$ (**6**), $H_2L(NO_3)_2$ (**7**), $H_2L(SO_4)\cdot H_2O$ (**8**), H_2LSiF_6 (**9**), $H_2LSiF_6\cdot 2H_2O$ (**10**), $H_2L(HF_2)_2$ (**11**), H_3LI_3 (**12**), $H_3L(BF_4)_3$ (**13**), $H_3L(ClO_4)_3$ (**14**), $H_3L(ClO_4)_3\cdot 2H_2O$ (**15**), and $H_3LH_3O(SiF_6)_2\cdot 2H_2O$ (**16**), thoroughly examined by elemental analyses, Fourier transform-attenuated total reflectance-infrared (FT-ATR-IR), thermal analysis, powder diffraction, and single-crystal X-ray diffraction. We identified the propensity of $H_2PO_4^-$ into a cyclic hexameric cluster $(H_2PO_4^-)_6$ stabilized by a bent ligand **L** via a combination of functionalities such as an amino group, pyridyl terminals, and a triazolyl core. Additionally, we also found the anion−water clusters ranging from a cyclic tetramer $[(SO_4)_2-(H_2O)_2]^{4-}$ and an octameric cluster $[(SiF_6)_4-(H_2O)_4]^{8-}_{\infty}$ to an acyclic tetramer $[(ClO_4^-)_2(H_2O)_2]$. As shown by the study, subtle modulation in the crystallization environment offers the possibility to yield entirely distinctive forms of molecular salts comprising both anhydrous and a few hydrates with different protonated numbers (mono-, di- or triprotonated). A systematic study indicates that the molecular salts obtained from different anions construct diverse supramolecular extended architectures (e.g., bricklayer, columns, zig-zag, stair-steps, wave-like, helical, double chain, and criss-cross orientation) self-assembled by a combination of noncovalent interactions, constituting distinct H-bonded geometry patterns, essentially depending on the molecular conformation of the bent ligand and the type of the anion utilized (linear, spherical, triangular, tetrahedral, and octahedral) in the preparation of salts.

1. INTRODUCTION

The importance of noncovalent interactions in supramolecular assemblies has been well acknowledged and widely demonstrated in the elaboration of supramolecular entities in many scientific disciplines, such as environmental, biological, chemical, and materials sciences to name a few.[1−5] Under noncovalent interactions, hydrogen bonding remains famous and the most reliable, together with other weak forces such as cation−π,[6] anion−π,[7] π−π stacking interactions,[8] and halogen bonding,[9] which have procured augmented consideration in the field of supramolecular chemistry.

The coexistence of such noncovalent interactions plays a vital role in anion-binding properties and the construction of supramolecular assemblies. Anion binding has attracted continued interest because of the pertinent role performed by anions in biological, chemical, and environmental processes.[10−12] From a structural perspective, it is well known that anions may perform diverse roles during crystallization processes, which include anions acting as a building unit, a secondary building unit (SBU) component, a templating agent, or as a spectator solely for charge balance.[13] The resulting assemblies can essentially be governed by the nature and a wide spectrum of geometries available for inorganic anions ranging from linear ($[HF_2]^-$), spherical (Cl^-, Br^-, I^-), trigonal planar ($[NO_3]^-$), and tetrahedral ($[ClO_4]^-$, $[SO_4]^{2-}$, $[H_2PO_4]^-$, $[BF_4]^-$) to octahedral ($[SiF_6]^{2-}$) geometries.

Within the intrinsic anion chemistry in aqueous media, anion−water clusters hold special interest, as a wide array of structures encompassing a cyclic tetramer, a pentamer, a hexamer, and an octamer can be generated, which are

Received: March 31, 2023
Revised: May 26, 2023
Published: June 23, 2023

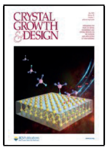

predominantly controlled by noncovalent interactions being regulated from the surrounding ligand.[14] Likewise, of all of the oxyanion species, phosphates especially possess a natural propensity to undergo self-aggregation to form anion assemblies, i.e., "anion clusters", as reported in the literature.[15−17] Indeed, phosphate recognition by receptors has received tremendous attention owing to its substantial influence on biological and physiological systems.[18] Hence, understanding such interanionic interactions is an interesting challenge and is now considered a critical area of supramolecular focus.[19−21] Nevertheless, supramolecular chemists have devoted tremendous efforts toward understanding and recognizing the serious concerns induced by anions, and substantial development have been accomplished in the range of fields as distinct as anion transport, sensing, extraction, organocatalysts, and so forth.[22−24] Subsequently, new families of synthetic molecular systems projecting neutral, bi-, or multi-H-bonding donor units have emerged in the literature to acquire the desired selectivity within the fascinating area of anion recognition.[4,12,25,26]

Alongside these well-preorganized synthetic receptors outspread in the field of supramolecular chemistry, the chemistry of bis(pyridyl)-based molecules has been the subject of intensive study and has brought new avenues in the construction of elegant supramolecular entities, as aromatic N-comprising supramolecular synthons offer a promising platform to study the interplay of varied noncovalent interactions employed in crystal engineering.[27,28] Ding and coworkers[29] reported anion-assisted supramolecular entities of 2,5-bis(4-pyridyl)-1,3,4-oxadiazole (**4-bpo**), showing structural insights into wide-ranging supramolecular networks manifested by different noncovalent interactions and nature of inorganic anions. To this purpose, we envisioned that the incorporation of a 4-amino-1,2,4-triazole moiety between the two pyridyl groups would be meaningful, as the amino group could serve additional H-bonding sites or feature potential coordination in controlling the formation of final higher-dimensional supramolecular assemblies. With this in mind, we turned our attention to the ligand (**L**, Figure 1), whose capabilities for spin crossover properties[30−32] and anion−π interactions[33] have been well known. Besides, this bent ligand has been exploited for the construction and design of novel metal−organic frameworks (MOF$_S$)[34−37] and documented independently by the group Du et al.[38] as cocrystals with a series of organic carboxylic acids.

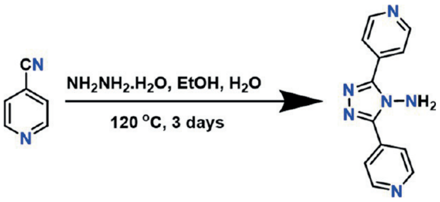

Figure 1. General synthesis route for 4-amino-3,5-bis(4-pyridyl)-1,2,4-triazole (**L**).

Surprisingly, the research on anion-templated supramolecular assemblies of this ligand remains underexplored. This motivated us in this study to highlight some interesting structural insights into new diverse supramolecular networks constructed by the bent ligand. Examination of **L** encouraged us to ponder over a few points: Will anion's steric effects influence the molecular conformation of **L**? What will be the role of counteranion geometry on H-bonding patterns? Can we attempt to produce salts with mono-, di-, or triprotonated ligands via tuning the acid in different crystallization conditions? Formation of anion or anion−water clusters? Which panel of noncovalent interactions will mediate the molecular packing of the complexes? To address these questions, we launched a systematic analysis on 16 new supramolecular assemblies induced by inorganic anionic species, implying how subtle modulation of distinct noncovalent forces and their dependence on geometries features of anions drive the final formation of supramolecular architectures, the studies of which are submitted in this article.

2. EXPERIMENTAL PROCEDURES

2.1. Materials and Physical Measurements. All of the reagents and solvents were obtained from standard commercial suppliers and utilized as received unless otherwise specified.

2.1.1. Single-Crystal X-ray Diffraction (SCXRD). The diffraction data for the single-crystal structure determination were collected on a Rigaku SuperNova dual-source (Cu and Mo micro-sources) X-ray diffractometer equipped with an Atlas CCD detector and multilayer optics producing monochromatized Cu K_α (1.54187 Å) radiation. The data collection, reduction of datasets, and analytical face-index-based absorption correction methods were carried out using the CrysAlisPRO[39] program. All structures were solved by intrinsic phasing (ShelXT)[40,41] and refined on F^2 by full-matrix least-squares techniques with the ShelXL program in the Olex^2 (v. 1.3 and 1.5) program[42] that utilizes the SHELXL-2013 module.[43] All C−H hydrogen atoms were calculated to their optimal positions and treated as riding atoms using isotropic displacement parameters of 1.2 (sp^2 group) larger than that of the host atom, whereas N−H hydrogen atoms indicating protonation of the ligand or hydrogens of acid groups (e.g., sulfate, phosphate) were primarily found from the electron density maps and were refined freely.

2.1.2. Powder X-ray Diffraction (PXRD). PXRD data were measured using a Panalytical X'Pert PRO diffractometer with Cu K_α radiation (λ = 1.54187 Å; Ni β-filter; 45 kV, 40 mA). Each powder sample was attached to a silicon-made "zero-background signal generating" plate using petrolatum jelly as an adhesive. Diffraction intensities were recorded by an X'Celerator detector at room temperature with a 2θ range of 4−60°, a step size of 0.017°, and a counting time of 70 s per step. Data processing, search-match phase analyses, and Pawley fits were carried out by the program X'pert HighScore Plus (v. 4.9). Search-match phase identification analyses were made against the ICDD-PDF4+ database (version 2020) implemented in the HighScore.[44,45] In the Pawley fits, the unit-cell parameters of the PXRD patterns were refined by using the corresponding single-crystal structure parameters as the basis of least-squares refinement. Variables for the fits were as follows: zero-offset, polynomial background, sample height displacement, unit-cell parameters, and peak profile parameters (peak width, shape, and asymmetry).

2.1.3. Thermal Analysis. The thermal properties of the compounds were examined by a Perkin Elmer STA 6000 thermogravimetric TG/DSC analyzer (DSC stands for a differential scanning calorimetric signal). Each sample was prepared in an open platinum pan and heated under N_2 or air atmospheres (flow rate of 40 mL/min) with a heating rate of 10 °C/min at a temperature range of 22−600 °C. For each run under N_2, a 10 min isotherm at 22 °C was introduced to assure proper purging of the furnace interior from the ambient air atmosphere before the start of the heating. Temperature calibration of the analyzer was made using melting points of the indium (156.6 °C), zinc (419.5 °C), and aluminum (660.3°) standards. The weight balance was calibrated at room temperature using a standard weight of 50.00 mg. The sample weights used in the measurements were about 1.5−14 mg.

2.2. Other Methods. The ^1H NMR and ^{13}C NMR spectra were recorded in $(CD_3)_2SO$ on a Bruker Avance 300 MHz spectrometer. The chemical shifts were reported in ppm relative to CD_3CD_2HSO (δ 2.50) for ^1H NMR. For the ^{13}C NMR spectra, $(CD_3)_2SO$ (δ 39.52) was used as an internal standard. All of the FTIR spectra were recorded using a Bruker instrument over a range of 4000−400 cm^{-1}. The samples were mildly ground before pressing a small amount on the diamond ATR Prism and were baseline-corrected. Elemental analyses (C, H, and N) were performed in-house using an Elementar EL III elemental analyzer.

2.3. Syntheses. *2.3.1. Synthesis of 4-Amino-3,5-bis(4-pyridyl)-1,2,4-triazole (bpt).* **L** (bpt) was synthesized according to the reported method with slight modification.[46] 4-Cyanopyridine (2.6 g, 25 mmol), hydrazine monohydrate (79%, 3 mL), water (8 mL), and ethanol (1 mL) were sealed in a Teflon-lined autoclave (25 mL) and heated at 120 °C for 48 h (Figure 1). Slow cooling of the autoclave to 22 °C afforded pale brownish orange crystals. The crystals were isolated by filtration followed by washing with water and acetone and dried in vacuo. Yield = 1.1742 g, 39.4%. Anal. Calc. for **L** $C_{12}H_{10}N_6$: C, 60.50; H, 4.23; N, 35.27. Found: C, 61.34; H, 4.659; N, 34.44%.**^{1}H NMR** (300 MHz, DMSO-d_6): δ 8.79 (d, J = 5.5 Hz, 4H), 8.07 (d, J = 5.6 Hz, 4H), 6.51 (s, 2H). **^{13}C NMR** (75 MHz, DMSO-d_6): δ 153.0, 150.1, 133.9, 122.0. ^1H NMR and ^{13}C NMR spectra of a ligand are shown in Figures S1 and S2, respectively.

2.4. Crystallization Methods. *2.4.1. Preparation of H_2LCl_2 (**1**), H_2LBr_2 (**2**), $H_2L(NO_3)_2$ (**3**), $HL(H_2PO_4)$ (**4**), $H_2L(H_2PO_4)_2$ (**5**), $H_2L(SO_4)\cdot H_2O$ (**8**), H_2LSiF_6 (**9**), and $H_2LSiF_6\cdot 2H_2O$ (**10**).* A total of 150 mg of **L** was added to 2 mL of 5 M acid solution (H_2SiF_6 33.5−35%, ∼2.9 M) and shaken thoroughly. After standing undisturbed for 24 h (4 days in the case of salt **9**), single crystals formed in the case of a HNO_3 solution (**3**) were collected and rinsed with water and acetone. To the remaining vials, 2 mL of H_2O was added (except salt **9**), followed by the addition of 8−10 mL of acetone (20 mL of acetone in the case of salt **9**, and dioxane instead of acetone in the case of salt **5**) to precipitate colorless crystals per appropriate LH_x salt (fine powder in case of salt **9**). The solids obtained were filtered, washed with acetone, and air-dried. In the case of **9**, a powder containing a water solution (25 mM) was slowly evaporated to dryness, which afforded crystals suitable for single-crystal X-ray diffraction. The comparison of the FT-ATR-IR (cm^{-1}) of the salts is shown in Figures S3 and S4.

*2.4.1.1. H_2LCl_2 (**1**).* FT-ATR-IR (cm^{-1}): 3159, 3064, 3038, 2967, 2850, 2092, 2051, 2016, 1944, 1895, 1830, 1626, 1588, 1520, 1506, 1483, 1453, 1418, 1364, 1323, 1312, 1287, 1225, 1195, 1182, 1093, 1077, 1051, 1029,1004, 975, 945, 845, 813, 728, 705, 686, 666, 646, 602, 563, 501, 421. Anal. Calc. for $C_{12}H_{12}N_6Cl_2$: C, 46.32; H, 3.887; N, 27.01. Found: C, 46.48; H, 3.769; N, 26.96%.

*2.4.1.2. H_2LBr_2 (**2**).* FT-ATR-IR (cm^{-1}): 3170, 3029, 2936, 2848, 2785, 2166, 2073, 1995, 1926, 1855, 1805, 1627, 1587, 1520, 1506, 1485, 1453, 1418, 1372, 1337, 1323, 1307, 1288, 1272, 1225, 1197, 1186, 1090, 1079, 1051, 1039, 1010, 975, 934, 887, 840, 805, 734, 724, 704, 683, 645, 602, 531, 498, 420. Anal. Calc. for $C_{12}H_{12}N_6Br_2$: C, 36.03; H, 3.023; N, 21.01. Found: C, 35.93; H, 3.107; N, 21.02%.

*2.4.1.3. $H_2L(NO_3)_2$ (**3**).* FT-ATR-IR (cm^{-1}): 3328, 3250, 3111, 3076, 3051, 2630, 2113, 1751, 1627, 1596, 1529, 1518, 1498, 1462, 1392, 1339, 1310, 1294, 1238, 1198, 1127, 1111, 1099, 1086, 1054, 1039, 1006, 994, 979, 949, 886, 836, 821, 736, 719, 688, 665, 649, 602, 531, 508, 473, 418. Anal. Calc. for $C_{12}H_{12}N_8O_6$: C, 39.57; H, 3.320; N, 30.76. Found: C, 39.62; H, 3.324; N, 30.97%.

*2.4.1.4. $H_2L(H_2PO_4)_2$ (**5**).* FT-ATR-IR (cm^{-1}): 3272, 3109, 3061, 2744, 2351, 2164, 1730, 1632, 1516, 1478, 1452, 1362, 1316, 1255, 1094, 1063, 1014, 969, 925, 851, 826, 738, 709, 694, 651, 603, 538, 484, 419. Anal. Calc. for $C_{12}H_{18}N_6O_9P_2$: C, 31.87; H, 4.012; N, 18.58. Found: C, 31.64; H, 3.774; N, 18.80%.

*2.4.1.5. $H_2L(SO_4)\cdot H_2O$ (**8**).* FT-ATR-IR (cm^{-1}): 3478, 3344, 3159, 3036, 2969, 2771, 2163, 2054, 2016, 1939, 1627, 1589, 1520, 1506, 1484, 1454, 1347, 1311, 1242, 1226, 1150, 1092, 1077, 1032, 970, 947, 877, 845, 831, 813, 733, 687, 647, 622, 598, 563, 502, 417. Anal. Calc. for $C_{12}H_{14}N_6O_8S_2$: C, 33.18; H, 3.248; N, 19.35. Found: C, 33.54; H, 3.246; N, 19.32%.

*2.4.1.6. H_2LSiF_6 (**9**).* FT-ATR-IR (cm^{-1}): 3331, 3215, 3086, 2886, 2084, 1632, 1605, 1523, 1505, 1463, 1340, 1309, 1244, 1211, 1098, 984, 956, 829, 735, 724, 690, 659, 636, 601, 529, 507, 473, 418.Anal. Calc. for $C_{12}H_{12}N_6F_6Si$: C, 37.70; H, 3.163; N, 21.98. Found: C, 36.91; H, 3.079; N, 21.98%.

*2.4.2. Preparation of $H_2L(NO_3)_2$ (**7**).* The single crystals formed in the case of the salt (**3**) were dissolved in a 1:1 methanol/water (1 mL) mixture. The faint yellow crystals were afforded within a few days by the slow evaporation of the mixture.

*2.4.3. Preparation of $[H_2L]_2I_4$ (**6**), $H_2L(HF_2)_2$ (**11**), H_3LI_3 (**12**), $H_3L(BF_4)_3$ (**13**), $H_3L(ClO_4)_3$ (**14**), $H_3L(ClO_4)_3\cdot 2H_2O$ (**15**), and $H_3L(H_3O)(SiF_6)_2\cdot 2H_2O$ (**16**).* A total of 150 mg of **L** was added to 2 mL of a 5 M acid solution (H_2SiF_6 33.5−35%, ∼2.9 M) and shaken thoroughly. After standing undisturbed for 24 h, 2 mL of H_2O was added to the iodide salt (**6**) containing solution. All solutions, except salt **15** (closed vial), were left to evaporate in open vials to yield colorless single crystals (red-orange in the case of iodide salts).

*2.4.3.1. $[H_2L]_2I_4$ (**6**).* FT-ATR-IR (cm^{-1}): 3252, 3164, 3090, 3031, 2970, 2910, 2801, 2001, 1916, 1837, 1726, 1625, 1597, 1580, 1510, 1487, 1451, 1363, 1340, 1283, 1239, 1209, 1188, 1100, 1085, 1076, 1051, 1010, 969, 895, 806, 724, 701, 681, 665, 644, 599, 518, 495, 445, 416. Anal. Calc. for $C_{12}H_{12}N_6I_2$: C, 29.17; H, 2.448; N, 17.01. Found: C, 28.94; H, 2.541; N, 17.08%.

*2.4.3.2. $H_2L(HF_2)_2$ (**11**).* FT-ATR-IR (cm^{-1}): 3528, 3333, 3215, 3085, 2885, 1632, 1602, 1525, 1508, 1460, 1363, 1333, 1245, 1214, 1089, 1045, 977, 940, 876, 827, 733, 689, 636, 606, 508, 473, 418. Anal. Calc. for $C_{12}H_{10}N_6$: C, 60.50; H, 4.23; N, 35.27. Found: C, 60.74; H, 4.209; N 34.97%.

*2.4.3.3. $H_3L(BF_4)_3$ (**13**).* FT-ATR-IR (cm^{-1}): 3395, 3271, 3124, 2980, 2905, 1644, 1609, 1556, 1527, 1506, 1481, 1344, 1309, 1292, 1238, 1055, 993, 957, 872, 811, 793, 766, 736, 729, 710, 666, 646, 605, 522, 486, 417. Anal. Calc. for $C_{12}H_{13}N_6F_{12}B_3$: C, 28.73; H, 2.612; N, 16.75. Found: C, 28.98; H, 2.633; N, 17.07%.

*2.4.3.4. $H_3L(ClO_4)_3$ (**14**).* FT-ATR-IR (cm^{-1}): 3376, 3242, 3171, 3112, 2946, 2895, 2791, 2710, 1719, 1643, 1603, 1552, 1523, 1504, 1478, 1412, 1339, 1304, 1235, 1083, 1029, 962, 919, 808, 788, 735, 723, 707, 665, 617, 603, 522, 484, 466. Anal. Calc. for $C_{12}H_{13}N_6O_{12}Cl_3$: C, 26.71; H, 2.428; N, 15.57. Found: C, 26.27; H, 2.534; N, 15.61%.

2.5. Bulk Powder Syntheses. To probe the impact of concentration or pH in the salt formation, the bulk samples were fabricated under three different concentrations (1, 2.5, and 5 M) of acid solutions (HF, HCl, HBr, HI, HNO_3, H_2SO_4, H_3PO_4, HBF_4, $HClO_4$). Note that H_2SiF_6 is an exception, as only 1 and ∼2.9 M were prepared due to the low molarity (33.5−35%, ∼2.9 M) of the commercial acid solution. The complexes were synthesized by adding 150 mg of **L** to 2 mL of different molarity acid solutions and shaking thoroughly. After standing undisturbed for 48 h, 15 mL of acetone was added to precipitate appropriate LH_x salt. The powders obtained (except in the case of $HClO_4$ and HBF_4) were suction filtered, rinsed with acetone, and dried in a desiccator. The remaining vials ($HClO_4$ and HBF_4) were left to evaporate to dryness. The resulting products were collected by filtration and washed with acetonitrile and diethyl ether, respectively, and dried in a desiccator.

3. RESULTS AND DISCUSSIONS

In general, reactions between neutral ligand **L** and selected mineral acids (HCl, HBr, HI, HF, HNO_3, H_3PO_4, H_2SO_4, H_2SiF_6, HBF_4, $HClO_4$) yield either anhydrous or hydrated salts with a di- or triprotonated ligand and the anion(s) corresponding to the acid. The only exception showing a monoprotonated ligand was afforded when the ligand was treated with phosphorus acid in different crystallization conditions.

The reactions generally produced colorless (faint yellow and red-orange in the case of nitrate and iodide salts, respectively) crystals in good to quantitative yields and were readily suitable for single-crystal structure determination without further

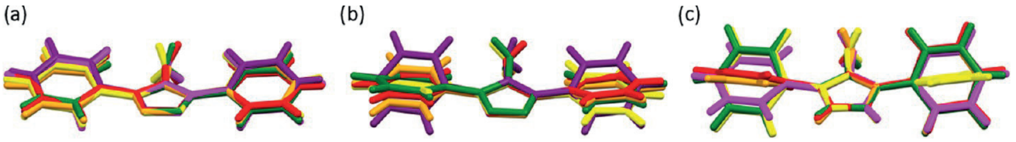

Figure 2. Ligand conformations grouped by their similarity. (a) Group I: (**1**) H_2L chloride (red), (**2**) H_2L bromide (orange), (**3**) H_2L nitrate monoclinic form (yellow), (**4**) HL phosphate (green), (**5**) H_2L phosphate (magenta), and (**6**) $[H_2L]_2$ iodide (purple). (b) Group II: (**7**) H_2L nitrate in triclinic form (red), (**8**) H_2L sulfate (orange), (**9**) H_2L hexafluorosilicate (purple), (**10**) H_2L hexafluorosilicate hydrate (yellow), and (**11**) H_2L bifluoride (green). (c) Group III: (**12**) H_3L iodide (red), (**13**) H_3L tetrafluoroborate (orange), (**14**) H_3L perchlorate (yellow), (**15**) H_3L perchlorate hydrate (green), and (**16**) H_3L hexafluorosilicate (magenta).

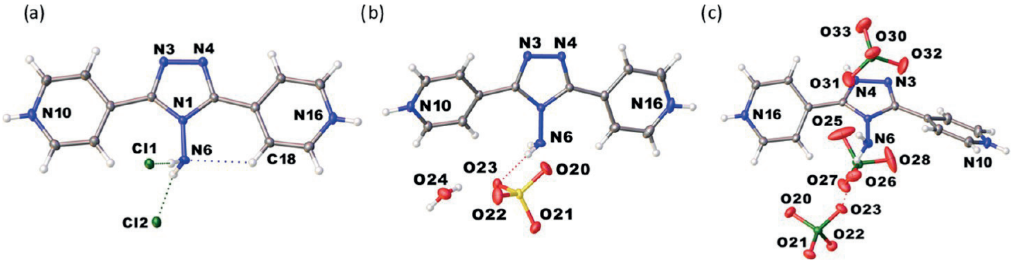

Figure 3. Molecular conformations and the selected atom numbering of (a) group I: H_2LCl_2 (**1**), (b) group II: $H_2L(SO_4)\cdot H_2O$ (**8**), and (c) group III: $H_3L(ClO_4)_3$ (**14**). The atom numbering of the ligand in (a) equals all structures. Weak intramolecular and intermolecular H bonds are exemplified by dashed blue and red (green for chloride salt) colored lines, respectively.

Table 1. Dihedral Angles between Pyridyl Rings and a Central Triazole Ring on Ligand L in Salts (1)−(16)

group I			group II			group III		
comp.	angle 1[a] (deg)	angle 2[b] (deg)	comp.	angle 1[a] (deg)	angle 2[b] (deg)	comp.	angle 1[a] (deg)	angle 2[b] (deg)
1	1.8(2)	−7.3(2)	**7**	16.0(2)	−18.3(2)	**12**	31.4(9)	42.5(9)
2	9.5(3)	−5.2(3)	**8**	−22.22(19)	0.97(18)	**13**	34.08(18)	36.92(18)
3	−11.24(18)	11.44 (18)	**9**	26.9(6)	−13.4(5)	**14**	−35.1(2)	−35.8(2)
4	−0.5(3)	10.8(3)	**10**	27.8(2)	0.4(3)	**15**	37.7(6)	−36.5(6)
5	13.0(2)	−16.1(2)	**11**	22.7(2)	−14.9(2)	**16**	23.9 (2)	−3.4(2)
6	15.5(6)	−15.5(6)						
	13.7(6)[c]	−17.7(6)[d]						

[a]Atoms for the dihedral angles: N3−C2−C7−C12. [b]Atoms for the dihedral angles: N4−C5−C13−C14, for (**6**) [c]Atoms for the dihedral angles: N21−C20−C25−C30 and [d]Atoms for the dihedral angles: N22−C23−C31−C36 for the 2nd ligand in asymmetric unit.

recrystallization, as good quality crystals could be selected directly from the acidic reaction solutions. The structural analysis reveals that the ligand **L** practically adopts (Figure 2) three significantly different molecular conformations, according to which the discussions of the structures are subdivided into future paragraphs. First, the conformational analysis of the ligand is described, followed by the intermolecular interaction and molecular packing analyses of the structures.

3.1. Ligand Conformation Analysis. As shown in Figure 2, group I includes Cl^-, Br^-, I^-, $[NO_3]^-$ (monoclinic structure form), and both $[H_2PO_4]^-$ structures. In all six crystal structures, the ligand shows an almost planar conformation resulting in only very modest dihedral angles between the pyridyl and triazole rings, the highest angles being less than ±17°. In group II (triclinic $[NO_3]^-$, $[SO_4]^{2-}$, both hydrated and anhydrous $[SiF_6]^{2-}$, and F^-), pyridyl groups merely reside on the same plane and are equally tilted from the triazole ring, with angles varying typically between 16 and 27°. Group III contains all triprotonated salts ($[BF_4]^-$, I^-, both $[ClO_4]^-$, $[SiF_6]^{2-}$), wherein one of the pyridyl rings can either be leveled with the central triazole ring and the second pyridyl ring is strongly tilted or both pyridyls are strongly tilted in opposite directions, showing up to 43° dihedral angles in relation to the central triazole ring. For the most tilted ligand conformations, such as in iodide and tetrafluoroborate salts, the pyridyl rings are almost in perpendicular orientation to each other, as shown in Figure 2c.

The six members of group I were obtained by reacting a neutral ligand **L** in acidic water solutions, containing either chloride, bromide, iodide, nitrate, or phosphate anions. All of the formed salts in this group crystallized without solvent molecules in their crystal lattice. Crystallographic data and the selected structure refinement parameters are shown in Table S1, and the asymmetric unit (AU) of the structures of all three groups is available in Figures S5−S7. The selected depictions of AUs per the conformation group are exemplified in Figure 3, and all of the relevant dihedral angles are tabulated in Table 1. In the case of a chloride solution, a diprotonated form of **L**, H_2L^{2+}, was crystallized in triclinic space group *P*-1, giving rise to H_2LCl_2 (**1**) with a single ligand and two chloride anions in the AU. Pyridyl rings of the ligand make dihedral angles of 1.8(2) and −7.3(2)° with the central triazole ring, thus showing close to the planar conformation of the ligand (Figure 3a). In the case of a bromide solution, the diprotonated solvent-free salt H_2LBr_2 (**2**) formed. Similarly to isostructural chloride salt (**1**), the ligand in the bromide salt (**2**) is nearly planar, showing only modest dihedral angles (9.5(3) and −5.2(3)°) between pyridyl rings and the central triazole. In the case of a nitrate solution, two different structure modifications were afforded depending on the reaction conditions, of which the monoclinic $P2_1/c$ form $H_2L(NO_3)_2$ (**3**) and the triclinic *P*-1 form $H_2L(NO_3)_2$ (**7**) belong to the groups I and II, respectively. The monoclinic structure, with a composition of one ligand and two planar nitrate anions, shows dihedral angles of −11.24(18) and 11.44(18)° between the pyridyl and triazole rings, hence having the third least planar ligand geometry within group I. The next two members of group I were cultivated from phosphorus acid solutions and displayed either a mono- or a diprotonated ligand with one or two dihydrogen phosphate anions (**4**, **5**) that crystallized in a monoclinic system with $P2_1/c$ or $I2/a$ symmetries, respectively. For monoprotonated salt (**4**), consisting of a single ligand and a dihydrogen phosphate anion, the dihedral angles between the two pyridine rings and the central triazole ring are 10.8(3) and −0.5(3)°. Whereas for the diprotonated phosphate salt (**5**) with two $[H_2PO_4]^-$ anions, the dihedral angles between the rings are 13.0(2) and −16.1(2)°, thereby showing the second highest tilting of pyridyl rings in this group. In the case of an iodide system, depending on the crystallization conditions, two iodide complexes (**6**, **12**) can be isolated that differ considerably in their molecular conformations despite both the complexes crystallizing in the same triclinic *P*-1 symmetry. The diprotonated complex $[H_2L]_2I_4$ (**6**) has a somewhat planar ligand, but the triprotonated H_3LI_3 salt (**12**) has a strongly tilted ligand and thereby belongs to group III. The asymmetric unit of (**6**) comprises four iodide anions and two ligand molecules that show dihedral angles of 15.5(6) and −15.5(6)° (13.7(6) and −17.7(6)° for the 2nd ligand) between the pyridyl rings and the triazole core, hence being the least planar ligand in group I.

Molecular salts of group II, namely $H_2L(NO_3)_2$ (**7**), $H_2L(SO_4)\cdot H_2O$ (**8**), H_2LSiF_6 (**9**), $H_2LSiF_6\cdot 2H_2O$ (**10**), and $H_2L(HF_2)_2$ (**11**), were afforded from the reactions between a neutral ligand **L** and acid solutions containing either nitrate, sulfate, hexafluorosilicate, or fluoride anions, respectively. The structures of salts (**8**) and (**10**) crystallized with solvent molecules in their crystal lattice. The dihedral angles for this group are provided in Table 1, and the crystal structures are shown in Figure S6. $H_2L(NO_3)_2$ (**7**), crystallizes in triclinic space group *P*-1 with one ligand and two planar nitrate anions in the AU. As shown in Figure S6a, both the pyridyl groups in (**7**) merely reside on the same plane and are almost equally twisted in the same direction, forming dihedral angles of 16.0(2) and −18.3(2)° with respect to the central triazole ring. The sulfate salt $H_2L(SO_4)\cdot H_2O$ (**8**) crystallized in the triclinic space group *P*-1, showing a single ligand, a sulfate anion, and a water molecule in the AU (Figure 3b). In contrast to salt (**7**), one of the pyridyl rings on salt (**8**) is located on the same plane with the central triazole ring, whereas the other pyridyl ring is slightly more tilted from the said plane, as manifested by the dihedral angles of −22.22(19) and 0.97(18)°. Two members of group II resulted from fluorosilicic acid solutions, of which depending on the crystallization conditions, three structurally different salts were obtained. The diprotonated salts H_2LSiF_6 (**9**) and $H_2LSiF_6\cdot 2H_2O$ dihydrated salt (**10**), belonging to group II, crystallized in monoclinic space group $P2_1/c$, whereas one acid solution resulted in a triprotonated hexafluorosilicate salt (**16**) having strongly tilted pyridyl groups (group III). An asymmetric unit of the solvent-free salt (**9**) consists of a single ligand and a $[SiF_6]^{2-}$ anion, and the dihedral angles between the two pyridyl rings and the triazole ring are 26.9(6) and −13.4(5)°. The other hexafluorosilicate salt (**10**) has a $[SiF_6]^{2-}$ anion and two water molecules along with the ligand in an AU and exhibits the highest tilting of the pyridyl rings in group II, dihedral angles being 27.8(2) and 0.4(3)°, respectively. The last salt belonging to group II is $H_2L(HF_2)_2$ (**11**), which crystallizes in a monoclinic $P2_1/c$ space group with an AU comprising one ligand and two $[HF_2]^-$ anions. Analogous to salt (**7**), both the pyridyl groups in (**11**) merely reside on the same plane and are twisted in the same direction, showing dihedral angles of 22.7(2) and −14.9(2)° with relation to the triazole ring.

In group III, triprotonated forms of ligand **L**, H_3L^{3+}, crystallize in the presence of iodide, tetrafluoroborate, perchlorate, and hexafluorosilicate anions, giving rise to H_3LI_3 (**12**), $H_3L(BF_4)_3$ (**13**), $H_3L(ClO_4)_3$ (**14**), $H_3L(ClO_4)_3\cdot 2H_2O$ (**15**), and $H_3L(H_3O)(SiF_6)_2\cdot 2H_2O$ (**16**) salts, respectively (Figure S7). In the case of an iodide solution, salt (**12**) crystallizes in a triclinic space group *P*-1 with one ligand and three iodide anions in an AU. Explicitly, both the pyridyl groups relative to the central triazole ring are strongly tilted in opposite directions, as indicated by the dihedral angles 31.4(9) and 42.5(9)°. The salt (**13**) crystallizes in monoclinic space group $I2/a$ with one ligand and three tetrafluoroborate anions in an AU. Likewise in (**12**), the tetrafluoroborate salt (**13**) represents strong tilting of pyridyl groups in opposite directions with corresponding dihedral angles of 34.08(18) and 36.92(18)°, thus resulting in also the almost perpendicular orientation of pyridyl rings in relation to each other. The next members of this group were afforded from perchloric acid solutions and presented either an anhydrous form $H_3L(ClO_4)_3$ (**14**) when crystallized in an open vial or hydrate form $H_3L(ClO_4)_3\cdot 2H_2O$ (**15**) when a closed vial was used. Both crystallized in the monoclinic crystal system with $I2/a$ or $P2_1/c$ symmetries, respectively. The AU of salt (**14**) consists of one ligand and three perchlorate anions, resembling the crystal structures of (**12**) and (**13**) by showing dihedral angles of −35.1(2) and −35.8(2)°, respectively (Figure 3c). Contrastingly, perchlorate hydrate salt (**15**) with one ligand, three perchlorate anions, and two water molecules in an AU displays strong tilting of pyridyl rings in the same direction as defined by the dihedral angles 37.7(6) and −36.5(6)°. The last one in group III $H_3L(H_3O)(SiF_6)_2\cdot 2H_2O$ (**16**) crystallizes in a monoclinic $P2_1/c$ symmetry with a single ligand, two hexafluorosilicate anions, one hydronium ion, and two water molecules in its AU. Unlike other members of the group with strongly tilted pyridyl groups, one of the pyridyl rings in the hexafluorosilicate salt (**16**) is leveled with the central triazole ring, and only the second pyridyl ring is strongly tilted as reflected by the dihedral angles 23.9(2) and −3.4(2)°, as shown Table 1.

3.2. Hydrogen Bonding and Molecular Packing. In this work, we have focused on recognizing the interaction of a ligand with anionic species and any water molecules with special emphasis on hydrogen bonding, $\pi-\pi$ stacking, and anion−π interactions. We first opted to probe the connections of each of the individual components, namely cationic ligand, anions, and water/hydronium ion, where applicable, in terms of the number of H-bond donor−acceptor units and the nature of interactions. Therefore, the presented H-bonding patterns are categorized based on graph set notations described by Etter et al.[47] From the crystal structures, we were also able to

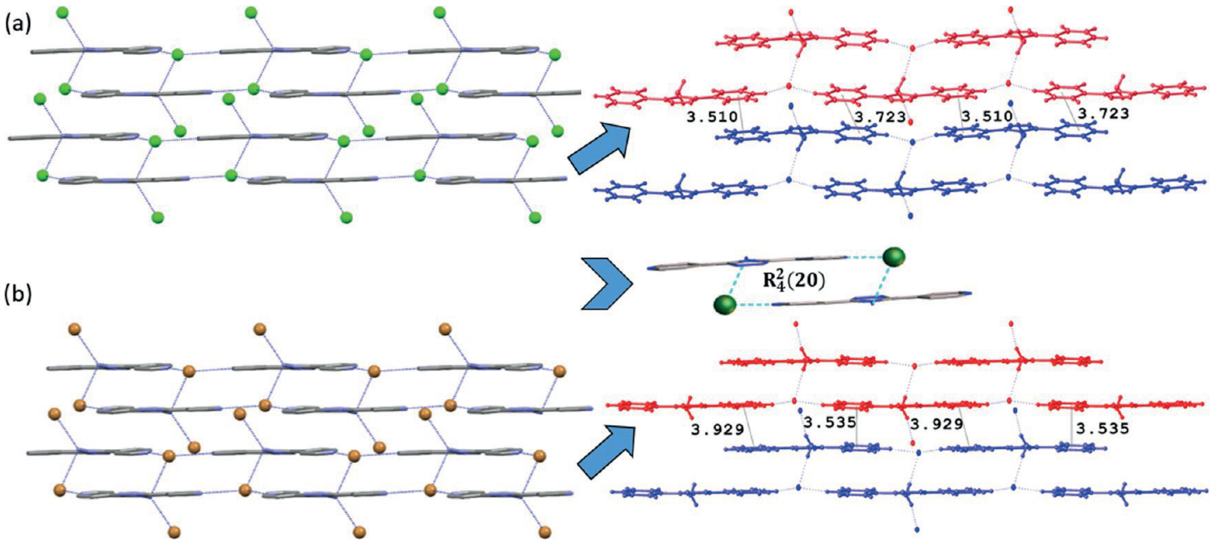

Figure 4. Partial view of molecular packing of the complexes (a) (**1**) and (b) (**2**) along the *b*-axis. The hydrogen-bonded motif present in salt (**1**) is also similar in (**2**). Only relevant atoms are shown. Hydrogen atoms are omitted for clarity. H bonds are exemplified by blue dashed lines (cyan dashed lines in the hydrogen-bonded motif), and the centroid−centroid distances are measured in angstrom (Å).

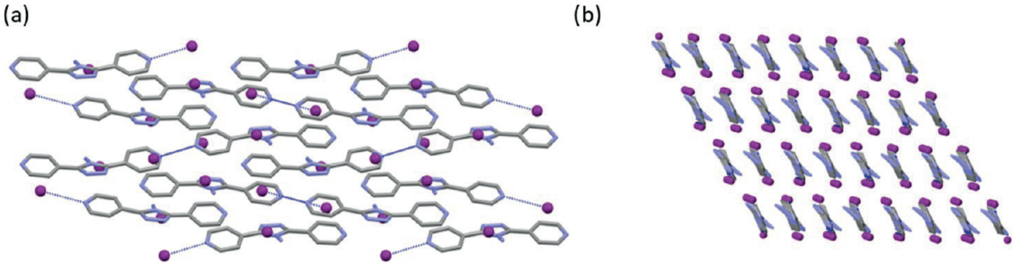

Figure 5. Partial view of molecular packing of salt (**6**) along (a) the *b*-axis and (b) *c*-axis. Hydrogen atoms are omitted for clarity. H bonds are exemplified by blue dashed lines.

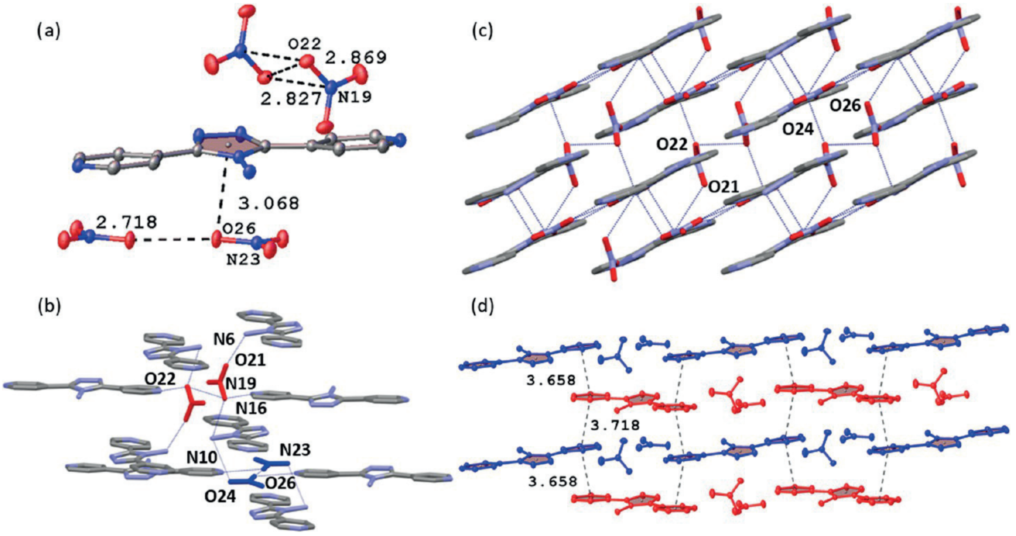

Figure 6. Illustration of salt (**3**) (a) anion−*π* interactions, (b) schematic representation of nitrate anion hydrogen-bonding connectivity, (c) partial view of molecular packing along the *b*-axis, and (d) stacking interactions: *π*-stack layer 1 (blue color) and *π*-stack layer 2 (red color). Only relevant atoms are shown. H bonds are exemplified by blue dashed lines, and the distances are measured in angstrom (Å).

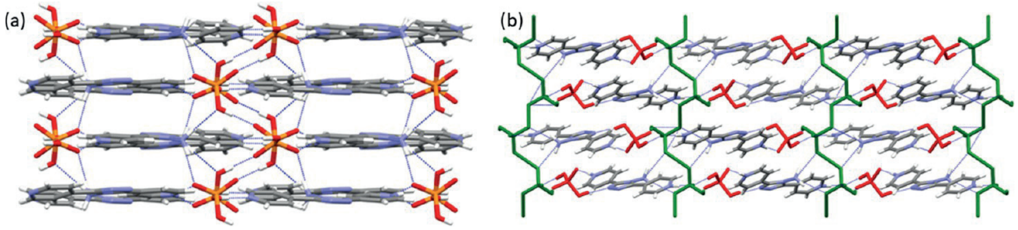

Figure 7. Partial view of molecular packing of the salts (a) (**4**) along the *c*-axis and (b) (**5**) along the *b*-axis. H bonds are exemplified by blue dashed lines.

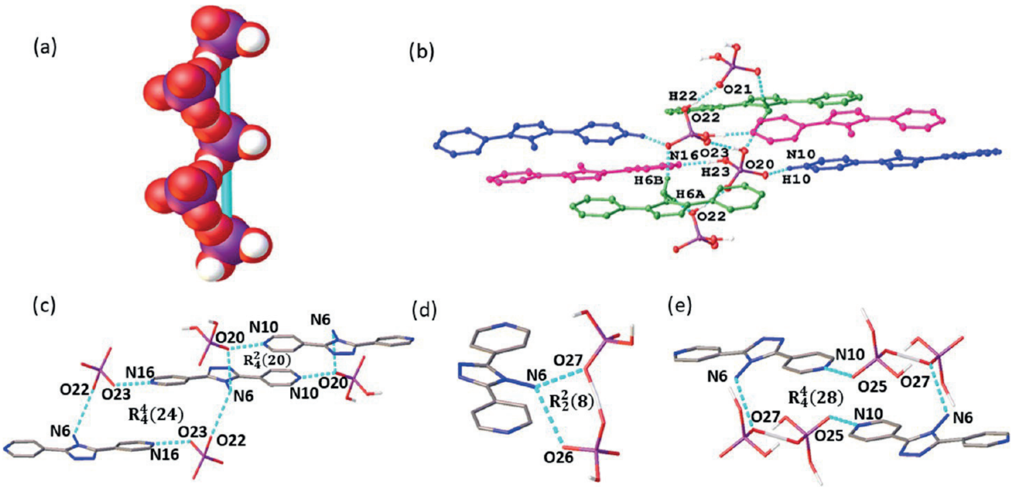

Figure 8. (a) Space-filling representation of hydrogen-bonded dihydrogen phosphate anions forming a helical chain in the salt (**4**) and (b) schematic representation of dihydrogen phosphate anion hydrogen-bonding connectivity. (c) Hydrogen-bonded motifs present in the salt (**4**) and (d, e) in the salt (**5**). H bonds are exemplified by cyan dashed lines. Only relevant atoms are shown.

identify some key structural aspects of anion cluster assembly and anion−water clusters with different counter anions, as presented in following chapters. Hydrogen-bonding geometries for all of the salts are summarized in Table S2. For the sake of simplicity, all of the salts discussed follow the uniform atom labeling of the ligand, as shown in Figure S5a. Additionally, the geometric parameters d_{centroid}, d_{plane}, and d_{offset} were applied to define the location of the anion from the triazole ring,[48,49] and are listed in Table S3.

Not surprisingly, salts (**1**) and (**2**) exhibit practically the same packing modes. Both contain H-bonded linear chains of $C_2^1(14)$ (mediated by pyNH$^+$···X interactions) with $d(\text{N−X}) = \sim3.12$ to 3.36 Å, for X = Cl1/Br1 along the *b*-axis. These H bonds further are joined to larger $R_4^2(20)$ H-bonded rings mediated by four molecules (Figure 4). Additionally, (**1**) and (**2**) feature strong face-to-face π−π interactions in a bricklayer fashion and show centroid−centroid distances of $d(\pi-\pi)$ 3.5105(12)−3.7239(14) and 3.5351(15)−3.9298(15) Å between the pyridyl groups, for (**1**) and (**2**), respectively. Conversely, in the iodide salt (**6**), relatively weak π−π interactions (face-to-face) between the adjacent pyridyl groups were observed, having centroid−centroid and plane-to-plane shift distances of 3.749(2)−3.824(2) and 1.545(7)−1.886(6) Å, respectively (Figure 5), due to the considerable size difference between anions ($\text{Cl}^- < \text{Br}^- < \text{I}^-$). The diprotonated ligands are packed in antiparallel alignment, resembling columns when viewed along the *c*-axis.

In the salt structure (**3**), anion−π interaction is evident with one of the nitrate anions (designated by N23), which is located 3.2221(8) Å from the centroid of the triazole ring (Figure 6a) with an angle of 9.19(5)° to the plane of the triazole ring. The geometric parameters describing the anion−π interactions are as follows: O26···ring−centroid $d(3.0680(11))$ Å and O26···ring−plane $d(3.0569(11))$Å, offset with respect to the normal to the plane is 0.26 Å. The same oxygen atom is involved in strong and almost linear pyNH$^+$···O connections (N−H···O distance, 1.81(2) Å) (Figure 6b). The second oxygen atom (O24) is engaged with amine NH ($d(\text{N−O}) = \sim3.10$ Å), resulting in the formation of infinite zig-zag chains of the ligands with a $C_2^2(12)$ H-bond motif, running parallel to the *c*-axis (Figure 6c). The other nitrate anion (designated by N19) forms an angle of 73.46(5)° to a triazole ring plane, one of its oxygen atoms (O22) bifurcating one short H bond to a pyridinium NH$^+$ and an amine NH, thus forming infinite zig-zag chains of the ligands with $C_2^1(10)$ motifs running parallel to the *b*-axis. The other oxygen atom (O21) shows H bonds with amine NH, of which donor−acceptor distances (N···O) vary from ~2.7 to 3 Å (Figure 6b). This HB arrangement involving amino groups generates H-bonded chains of the $C_2^2(6)$ motif that runs along the crystallographic *a*-axis. In addition to N−H···O H bonds, oxygen atoms participate in a set of weak but potentially structure-stabilizing aromatic C−H···O interactions (Table S2). The partial view of molecular packing along the crystallographic *a*- and *c*-axis is shown in Figure S8. One of the interesting features of this structure is the origin of $[\text{NO}_3]^-$···

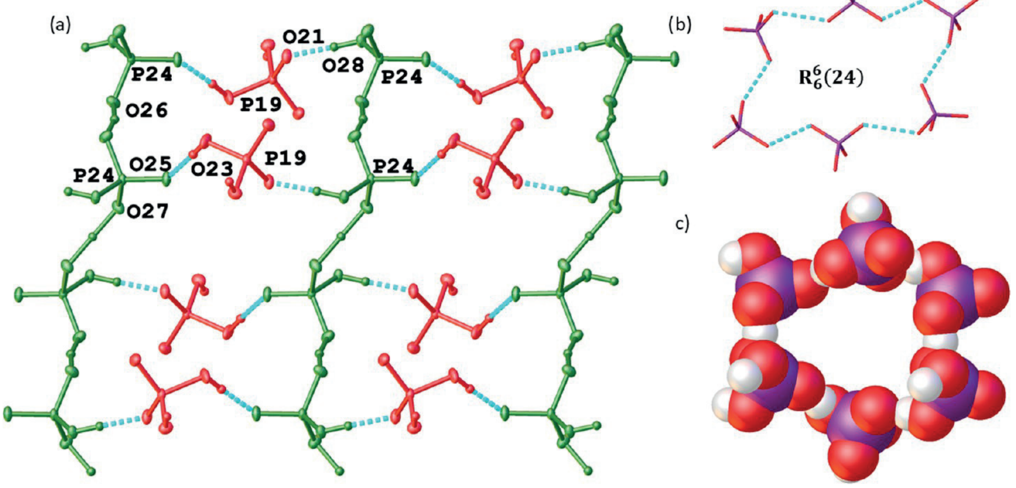

Figure 9. Illustration of the salt (5), (a) dihydrogen phosphate anion assembly, (b) hydrogen-bonding motif found in the $(H_2PO_4^-)_6$ aggregate, and (c) space-filling representation of the anion cluster. Cations are omitted for clarity. Only relevant atoms are shown. H bonds are exemplified by cyan dashed lines.

$[NO_3]^-$ interactions. The nitrate anion (N19) is located adjacent to its symmetry twin with an interplanar distance d(N19−N19′) of 3.2905(10) Å. They seem to participate in weak dimer associations, where the central nitrogen atom associates with the oxygen atom of the symmetry-related anion with a short contact of 2.8272(15) Å and d(O22−O22′) being 2.8689(19) Å (Figure 6). Also, the second nitrate anion (N23) is similarly located close by its symmetry twin having two of the oxygen atoms in a face-to-face orientation with a d(O26−O26′) distance of 2.7177(19) Å. The short contacts between these two like-charged ions have been reported also in the literature, e.g., by Kim et al.,[50−53] who suggested that the short contact between two nitrate ions can possibly be caused by packing constraints or supportive attractive interactions further stabilizing the molecular packing. It is worth mentioning that the intriguing work by Mooibroek and coworkers[54] revealed that $[NO_3]^-$ in the solid state could also tend to behave as Lewis π acids, considering that the negative charge of a $[NO_3]^-$ anion is reasonably dampened by interactions, for instance, H bonding or coordination to a metal.[55−57] The packing arrangement of (**3**) exemplifies an intriguing zig-zag π stack: alternately stacking of π-stack layer 1 and π-stack layer 2. As shown in Figure 6d, complex (**3**) illustrates two kinds of interlayer distances of 3.6584(7) and 3.7185(7) Å.

These results indicate the influence of anion's steric effects on the molecular conformations and the packing. In the salts (**1**) and (**2**), because of the better planarity of ligands and the small size of anions, the interplanar separation between the pyridyl moieties is short, indicating relatively strong $\pi-\pi$ interactions. However, in complex (**3**), nitrate anions exhibit polyhedron conformation, thus forming H bonds with different oxygen atoms and involving other multiple interactions, which stabilize the overall molecular packing. Thus, steric hindrance provided by nitrate anions leads to a modest tilting of pyridyl rings and slightly longer interplanar separation between the pyridyl moieties, indicating relatively weak $\pi-\pi$ stacking.[58]

Salts (**4**) and (**5**) form layered structures composed of chains or H-bond-directed cluster assemblies of dihydrogen phosphate anions (Figure 7). The monoprotonated salt (**4**) also comprises a layered structure of anions and cations like complex (**5**) but with a distinct H-bonding arrangement. The change is reflected in the formation of an infinite helical chain around a 2_1-screw axis sustained by O−H···O H-bonds with d(O22−O21) being 2.5417(18) Å and propagating along the b-axis (Figure 8a). The helical chains are further connected across by the monoprotonated ligand, in a "stair-steps" manner (Figure 8b). Thus, two hydrogen atoms from amino groups, in a *syn* manner, connect the two oxygen atoms (O20 and O22) of $[H_2P(19)O_4]^-$ to form an infinite $C_2^2(6)$ type H-bonded chain that runs parallel to the b-axis and being orthogonal to the H-bonded chain of $C_2^2(16)$ type (mediated via O23−H23···N16 and N10−H10···O20). As a result of the intersection of these chains, the H-bonded ring patterns $R_4^2(20)$ and $R_4^4(24)$ are generated in the structure (Figure 8c). The partial view of the molecular packing along the c-axis is shown in Figure 7a. The complex (**5**) contains two crystallographic distinct dihydrogen phosphate anions $[H_2P(24)O_4]^-$ and $[H_2P(19)O_4]^-$, with $[H_2P(24)O_4]^-$ possessing a disordered hydrogen atom over two positions (H26 and H27) with 0.5 occupancies each. Both dihydrogen phosphate anions exhibit different coordination environments. Anion $[H_2P(24)O_4]^-$ develops an infinite zig-zag chain involving two sets of O−H···O hydrogen bonds (O···O = ∼2.5 Å) that run parallel to the a-axis. Most interestingly, two equivalent zig-zag chains are interlinked by a second phosphate anion via a strong O−H···O H bonds with the $R_6^6(24)$ motif forming a hexameric cluster $(H_2PO_4^-)_6$, which consists of alternating two P(24) and P(19) anions that propagate into a H-bond-directed anion cluster assembly when viewed down the c-axis, as shown in Figure 9. In this $R_6^6(24)$ motif generated, the dihydrogen phosphate anion P(19) is involved in a total of four H bonds with neighboring chains by acting both as an acceptor (O21) and a donor (O23−H23), respectively. Thus, the hexameric cluster identified resembles a cyclohexane-like structure,[17] wherein four dihydrogen phosphate anions (P24) of the cyclic ring reside on the same plane and two other anions (P19) lie above and below the plane. The anion cluster assembly formed is not flat, but it displays kind of a corrugated pattern. The

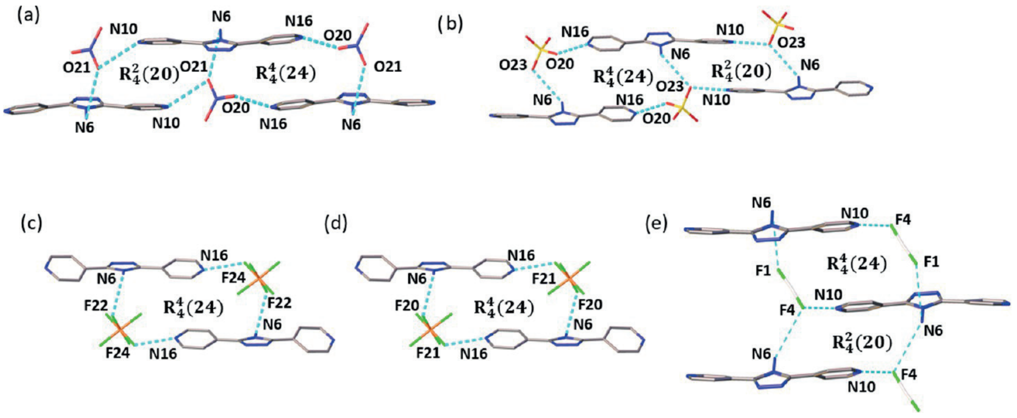

Figure 10. Hydrogen-bonded motifs present in the salts of group II. (a) In salt (**7**), (b) salt (**8**), (c) salt (**9**), (d) salt (**10**), and (e) salt (**11**). Only relevant atoms are shown. Hydrogen atoms are omitted for clarity. H bonds are exemplified by cyan dashed lines.

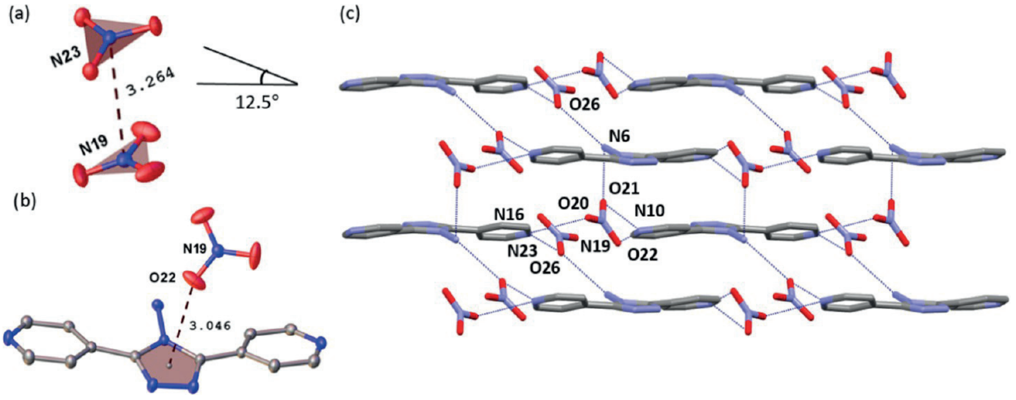

Figure 11. (a) Canted anion pairs in the salt (**7**), (b) anion−π interactions, and (c) partial view of molecular packing along the *b*-axis. Hydrogen atoms are omitted for clarity. H bonds are exemplified by blue dashed lines. Only relevant atoms are shown, and the distances are measured in angstrom (Å).

observed intermolecular O···O contact distances in this anionic hexamer cluster range between 2.51 and 2.63 Å and are similar to one observed by Hoque et al. and Mahé et al.[17,5917,59] Further, the dihydrogen phosphate anion $[H_2P(19)O_4]^-$ interacts with two cationic ligands through a triazole ring nitrogen acceptor (N4) and to a pyridinium NH$^+$ donor (N16−H16) with infinite $C_2^2(11)$ H-bonded motif chains running parallel to the *b*-axis, while the other $[H_2P(24)O_4]^-$ form contacts with a ligand via amino (N6−H6a and N6−H6b) and pyNH$^+$ donors (N10−H10) forming $R_2^2(8)$ and $R_4^4(28)$ geometry types (Figure 8d,e). The partial view of molecular packing along the *b*-axis is shown in Figure 7b.

The molecular packing arrangements of the group II salts (**7**−**11**) exhibit also layered H-bonded networks comprising anions and cationic ligands. Salts (**8**) and (**10**) of the group are slightly different from the others as they also contain water molecules and by that represent a somewhat wider range of H-bonding motifs. Interestingly, two types of H-bonded cyclic ring motifs were observed, namely, $R_4^2(20)$ and/or $R_4^4(24)$ (Figure 10) as structural units governed by the conformation of the bent ligand and the type of the anion.

Differing from the previously considered salt (**3**), in the triclinic nitrate salt (**7**), the nitrate anions do not participate in any dimer associations. The nitrate anion (N19) is located 4.2263(11) Å from the centroid of the triazole core with an angle of 125.31(7)° to a triazole ring plane, while another nitrate anion (N23) is 5.5793(12) Å apart with an angle of 42.41(6)° to the said plane. The nitrate anions occur in pairs with an interplanar distance of 3.2642(10) Å and are canted by 12.5° relative to each other (Figure 11a). The hydrogen bonding of salt (**7**) is also significantly different compared to salt (**3**). Both pyNH$^+$ donors are engaged in bifurcated H-bonding, wherein one protonated pyridyl (N10) bifurcates two oxygen atoms (O21 and O22) of one anion to form the $R_1^2(4)$ structural motif, whereas the other protonated pyridyl (N16) bifurcates two oxygen atoms (O20 and O26) of two anions, overall facilitating the formation of infinite linear H-bonded chains of $C_2^2(16)$ type, running parallel to the *c*-axis (Figure 11c). The hydrogen atoms of the 6-NH$_2$ groups act as H-bond donors to the oxygen atom (O21) of one nitrate anion (N19) and the oxygen atom (O26) of a second nitrate anion (N23) and unite these chains into layers via N−H···O H bonds (d(N···O) = ~2.8 to 3.0 Å), forming a combination of two H-bonded ring patterns of $R_4^2(20)$ and $R_4^4(24)$ types (Figure 10a). The intermolecular H bonds are further stabilized by weak C−H···O interactions, π−π stacking interactions between the adjacent pyridyl groups (N10) with a centroid−centroid distance $d(\pi-\pi)$ of 3.7574(7) Å, and anion−π interactions

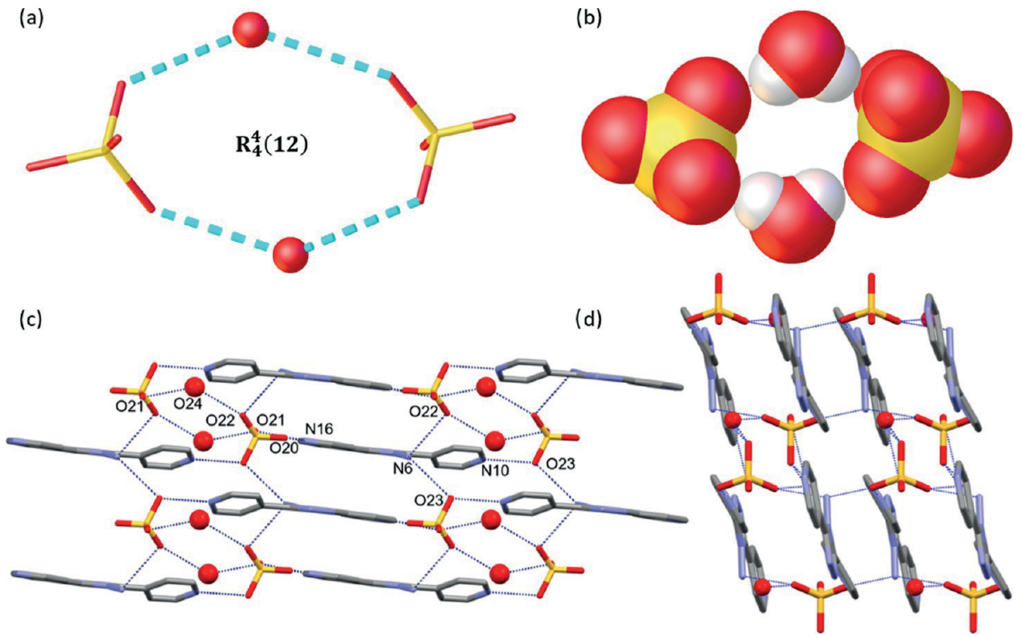

Figure 12. (a) Hydrogen-bonding motif found in the sulfate−water cluster in the salt (**8**), (b) space-filling representation of the sulfate−water tetramer, and partial view of molecular packing along the (c) *b*-axis and (d) *c*-axis. Hydrogen atoms are omitted for clarity. H bonds are exemplified by blue dashed lines (cyan dashed lines in the sulfate−water cluster). Only relevant atoms are shown.

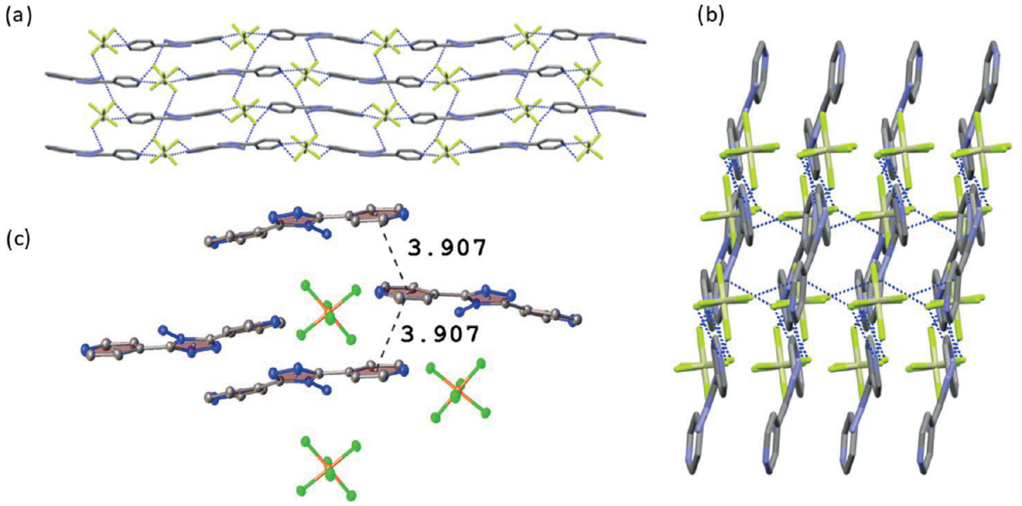

Figure 13. Partial view of molecular packing of the salt (**9**) (a) along the *a*-axis, (b) along the *b*-axis, and (c) stacking interactions. Only relevant atoms are shown. H bonds are exemplified by blue dashed lines, and the centroid−centroid distances are measured in angstrom (Å).

d(O22−centroid\offset distances of 3.0455(16)/1.26 Å), as shown in Figure 11b. The molecules are assembled in layers parallel to the *ac*-plane, as shown in Figure 11c.

The most appealing feature of (**8**) is the presence of an anion−water cluster.[17] The single water molecule (O24) is H-bonded with two neighboring sulfate anions [O24···O22 = 2.7955(17) Å and O24···O21 = 2.7921(17) Å] to give a cyclic tetramer $[(SO_4)_2-(H_2O)_2]^{4-}$ cluster of $R_4^4(12)$ geometry type, located around the inversion center (Figure 12). Noticeably, the small sulfate−water cluster does not engage in any interactions between themselves but instead forms contacts with pyridinium NH$^+$ and 6-NH$_2$ groups. As shown in Figure 12c, one hydrogen atom of the protonated pyridyl (N16) bifurcates two oxygen atoms of a sulfate anion (O21 and O20) to construct the $R_1^2(4)$ structural motif and the other, pyridinium (N10) forms a single bond with sulfate oxygen (O23). The N−H$^+$···O bonds link the cationic ligands and anions into infinite chains of $C_2^2(16)$ type parallel to the *c*-axis with N···O distances of about 2.65−2.98 Å. The 6-NH$_2$ groups are engaged in a $C_2^2(6)$ chain which propagates along the *a*-axis orthogonal to the $C_2^2(16)$ H-bonded chain. As a result, the combination of HB geometries generates $R_4^2(20)$ and $R_4^4(24)$ types of H-bonded rings mediated by four molecules, as shown in Figure 10b. The molecular packing along the *b*-axis displays

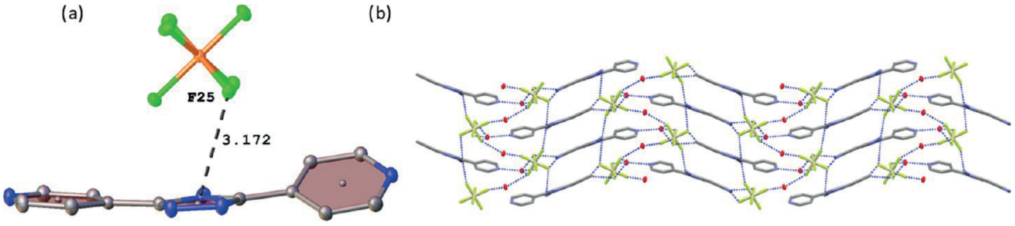

Figure 14. (a) Anion−π interactions and (b) partial view of molecular packing along the *a*-axis in salt (**10**). Only relevant atoms are shown. H bonds are exemplified by cyan dashed lines, and the distance is measured in angstrom (Å).

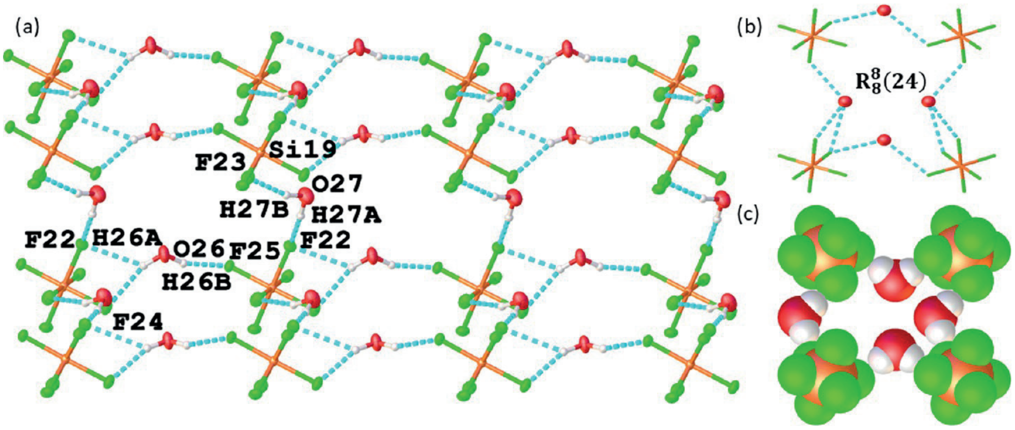

Figure 15. Illustrations of the salt (**10**). (a) Anion−water assembly, (b) hydrogen-bonding motif found in the cyclic octameric cluster, and (c) space-filling representation of the anion−water cluster. Cations are omitted for clarity. Only relevant atoms are shown. H bonds are exemplified by cyan dashed lines.

a layered array of cationic ligands with the inclusion of a sulfate−water cluster inserted in the space between H_2L^{2+}, as shown in Figure 12.

The hexafluorosilicate salts displayed a diverse range of structural features. Two of the hexafluorosilicate structures (**10**) and (**16**) comprise water in their lattice, while (**9**) is anhydrous. As shown in Figure 13, salt (**9**) exhibits wave-like layers of ions when viewed along the *a*-axis. The 6-NH_2 groups are engaged in N−H···F interactions, forming H-bonded chains of $C_2^2(6)$ type parallel to the *c*-axis, whereas wave-like H-bonded chains of $C_2^2(16)$ type (mediated by protonated pyridyl rings and fluorine atoms) go along the *b*-axis. There is also $R_4^4(24)$ H-bonded geometry type analogous to those observed for other members of this group (Figure 10c). Moreover, the packing is facilitated by C−H···F contacts and weak face-to-face $\pi\cdots\pi$ stacking with the pyridyl groups' centroid−centroid distance being $d(\pi-\pi)$ 3.9079(11) Å (Figure 13).

Contrary to (**9**), in the salt (**10**), the layered array of cationic ligands and fluorosilicate anion exists, as alternating anion−water sheets, to generate a wave-like layered structure when viewed along the *a*-axis (Figure 14). The H-bond environment around the hexafluorosilicate unit is intriguing, where each $[SiF_6]^{2-}$ anion accepts eight hydrogen bonds, out of which, 6-NH_2 groups and pyridinium NH^+ of cationic ligands contribute to three N−H···F interactions and water molecules via five O−H···F H-bond interactions. The water molecule (O26) also acts as a H-bond acceptor toward the pyridinium (N10) group via a single N−H···O H-bond, while as H donors they connect two $[SiF_6]^{2-}$ anions, with one bifurcating hydrogen (H26) and one with a single contact (H26B) to form infinite chains of $C_2^2(6)$, running parallel to the *a*-axis. Two identical chains are further strongly stitched via a second water molecule (O27) via two O27−H27A···F22 and O27−H27b···F23 H-bonds, forming cyclic octameric clusters $[(SiF_6)_4-(H_2O)_4]_\infty^{8-}$ with a structural motif $R_8^8(24)$ that results in undulated sheet propagating along the *a*-axis (Figure 15a).[60,61] Further, each cationic ligand bridges the anion−water cluster assembly via N−H···O and N−H···F H bonds, resulting in structural motifs $R_4^4(24)$ with D···A distances of about 2.6−3.0 Å (Figure 10d). Apart from N−H···O, O−H···F, and N−H···F H-bond interactions, the hydrogen bonding-driven assembly is further stabilized by anion−π interactions *d*(F25−centroid\offset distances of 3.1717(12)/1.35 Å), as shown in Figure 14a.

Ions in the salt (**11**) pack as layered sheets held by a network of N−H···F and C−H···F interactions, as shown in Figure S9. The F2 atom of $[H(2)F_2]^-$ ions is linked with pyridine NH^+ units that assemble into linear H-bonded chains of $C_2^1(14)$ running parallel to the *a*-axis. These chains are further linked in the second direction via C9−H9···F3 interactions (Table S2). Further, H bonds involving 6-NH_2 groups are centered on F1 and F4 atoms of the second $[H(2)F_2]^-$ ion facilitating H-bonded chains of $C_2^2(6)$ type running parallel to the *b*-axis. The F4 atom also forms contacts via N10−H10···F4 and C15−H15···F4 interactions in alternating layers. As a result, analogous to previous structures, the crystal structure of (**11**) is also built by the combination of $R_4^2(20)$ and $R_4^4(24)$ H-bonded ring patterns (Figure 10e).

The iodide salt (**12**) in group III differs completely from the iodide structure (**6**) belonging to group I, as it exhibits

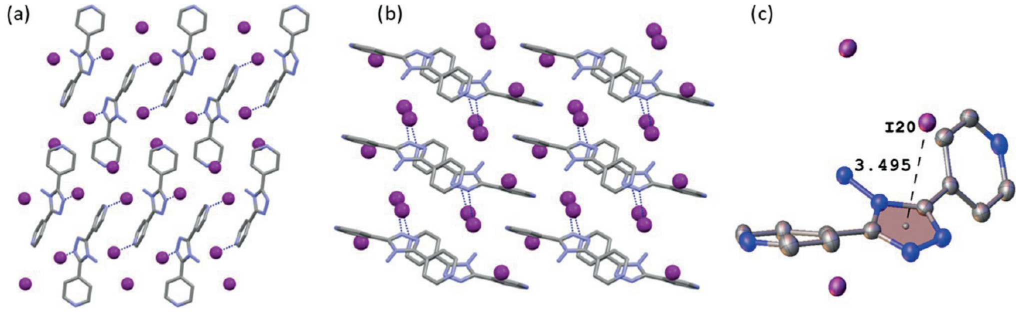

Figure 16. Partial view of molecular packing of (**12**) (a) along the *a*-axis, (b) along the *b*-axis, and (c) anion−π interactions. Hydrogen atoms are omitted for clarity. Only relevant atoms are shown. H bonds are exemplified by blue dashed lines, and the distance is measured in angstrom (Å).

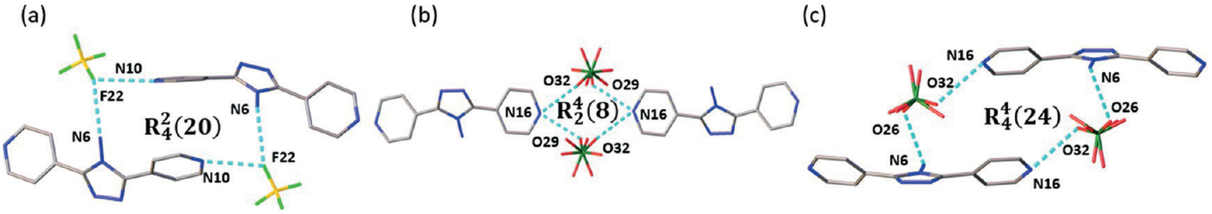

Figure 17. Hydrogen-bonding motifs present in the salts of group III. (a) In salt (**13**) and (b) and (c) in salt (**15**). Only relevant atoms are shown. Hydrogen atoms are omitted for clarity. H bonds are exemplified by cyan dashed lines.

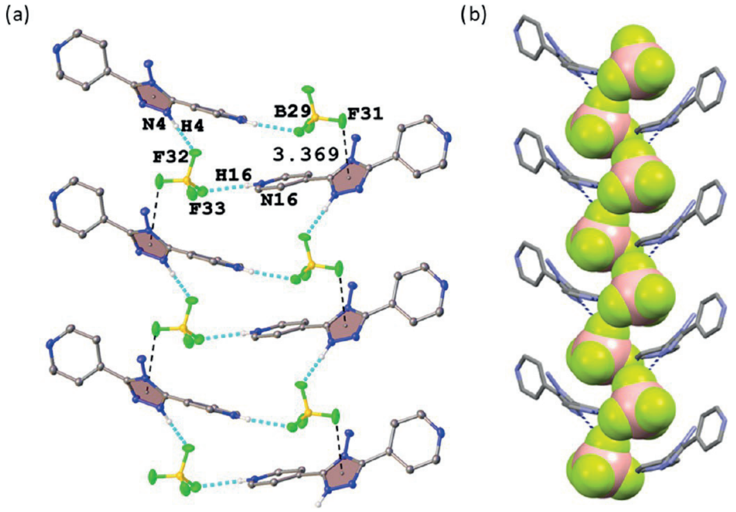

Figure 18. Illustrations of salt (**13**) (a) anion−π interactions and (b) hydrogen-bonded 1D chain along the *c*-axis. Only relevant atoms are shown. H bonds are exemplified by cyan dashed lines.

anion−π interaction with the following features: I20···ring−centroid distance *d*(3.495(2)) Å and I20···ring−plane distance *d*(3.456(3)) Å with the offset of 0.52 Å to the normal of the plane. The same anion (I20) is also involved in a weak N10−H10···I20 H-bond interaction with a distance *d*(N−I) of 3.506(7) Å. The partial view of molecular packing displaying anion−π interactions along the *a*- and *b*-axes is shown in Figure 16.

The structure of salt (**13**) reveals a layered arrangement stabilized by mainly N−H···F H-bonds (Figure 17) and anion−π interactions, as shown in Figure S10. In total, three tetrafluoroborate anions accept seven H bond interactions with N···F distances varying from ∼2.7 to 3 Å. One tetrafluoroborate anion $[B(29)F_4]^-$ involves two different fluoride atoms to link two cationic ligands via N4−H4···F32 and N16−H16···F33 H bonds in a continuous fashion, forming 1D chains ($C_2^2(11)$) related by the 2_1-screw axis (Figure 18) that develops along the *b*-axis. In this H-bonded 1D chain, one of the fluorine atoms (F31) being only 3.3691(14) Å apart from the triazole ring centroid appears to engage in anion−π interactions (Figure 18). These 1D H-bonded chains are then assembled into a 2D layered arrangement along the *b*-axis by another $[B(19)F_4]^-$ anion that serves as a bridge to link these adjacent chains via N10−H10···F22 and N6−H6A···F22 (Figure 19), resulting in the $R_4^2(20)$ H-bonded structural motif (Figure 17a). The third tetrafluoroborate $[B(24)F_4]^-$

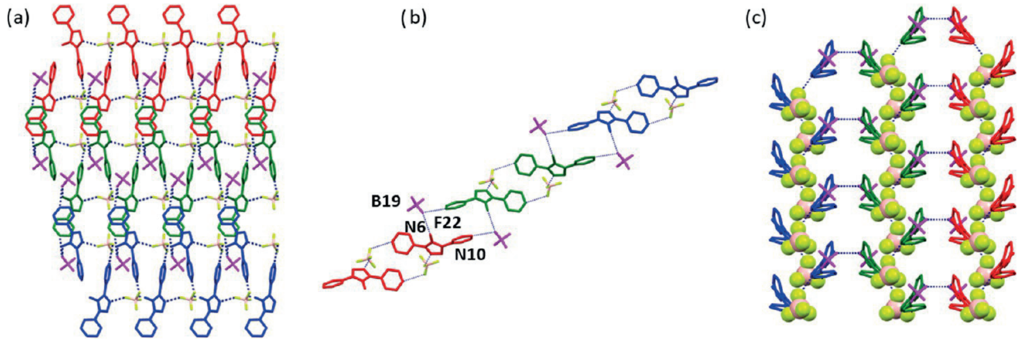

Figure 19. Partial view of the 2D layer of (**13**) (a) along the *a*-axis, (b) along the *b*-axis, and (c) along the *c*-axis. Hydrogen atoms are omitted for clarity. Only relevant atoms are shown. H bonds are exemplified by blue dashed lines.

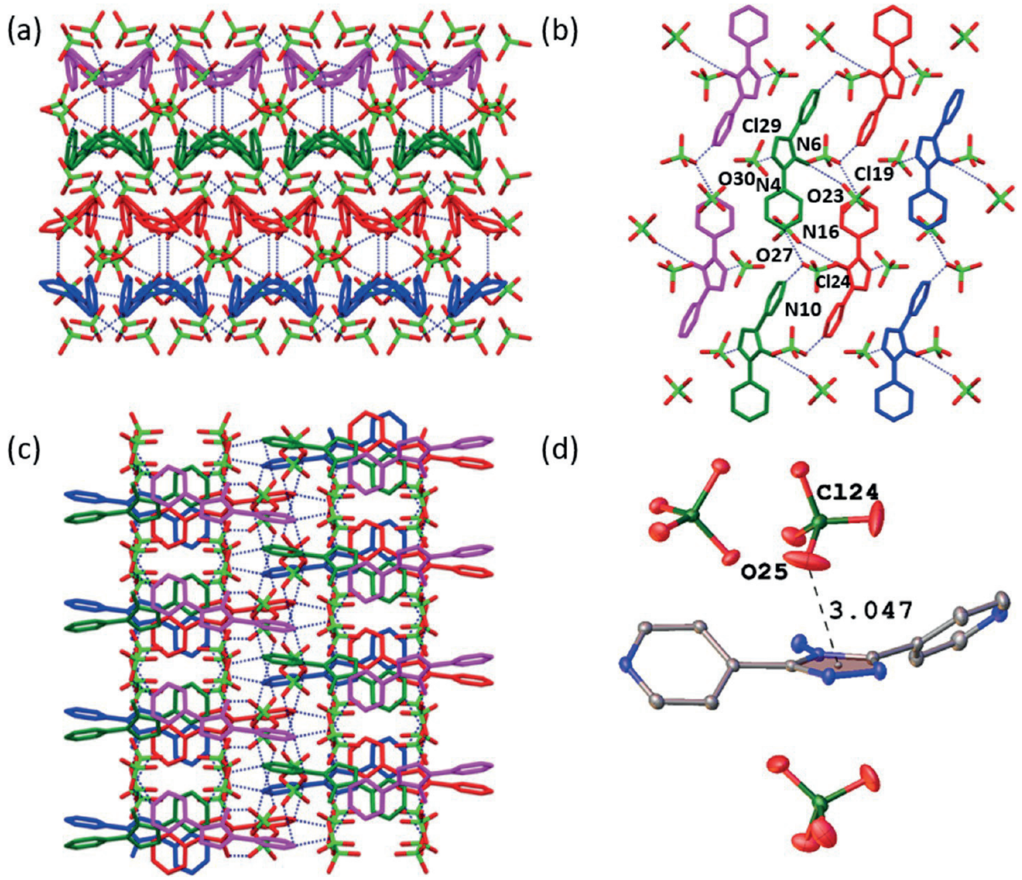

Figure 20. Partial views of molecular packing of (**14**) (a) along the *a*-axis, (b) along the *b*-axis, (c) along the *c*-axis, and (d) anion−π interactions. Hydrogen atoms are omitted for clarity. H bonds are exemplified by blue dashed lines, and the distance is measured in angstrom (Å).

anion engages in three N−H···F H-bond interactions, where the fluoride atom (F26) behaves as a bifurcated H-bond acceptor involving protonated pyridyl (N10−H10···F26 and N16−H16···F26) to form a helical chain of the $C_2^1(14)$ structural motif, which propagates parallel to the *c*-axis (Figure S10). The further link of the fluoride atom (F25) of the $[B(24)F_4]^-$ anion with an amino group (N6−H6A···F25) facilitates the formation of a double chain arrangement ($C_2^2(12)$) along the *b*-axis, as shown in Figure S10.

In the perchlorate salt (**14**), the ligand is triprotonated with three perchlorate anions of which molecular packings are shown in Figure 20 along *a*-, *b*-, and *c*-axes. The $[Cl(24)O_4]^-$ oxygen atom (O27) is engaged in two H bonds with two protonated ligands forming an infinite zig-zag H-bonded chain of the $C_2^1(14)$ motif, propagating along the *a*-axis. Both the triazole (N4) and amino (N6) are connected to the other two perchlorate anions $Cl(29)O_4^-$ and $Cl(19)O_4^-$ via N−H···O H bonds, respectively. Interestingly, there are also anion−anion interactions between the perchlorate anions with distances of

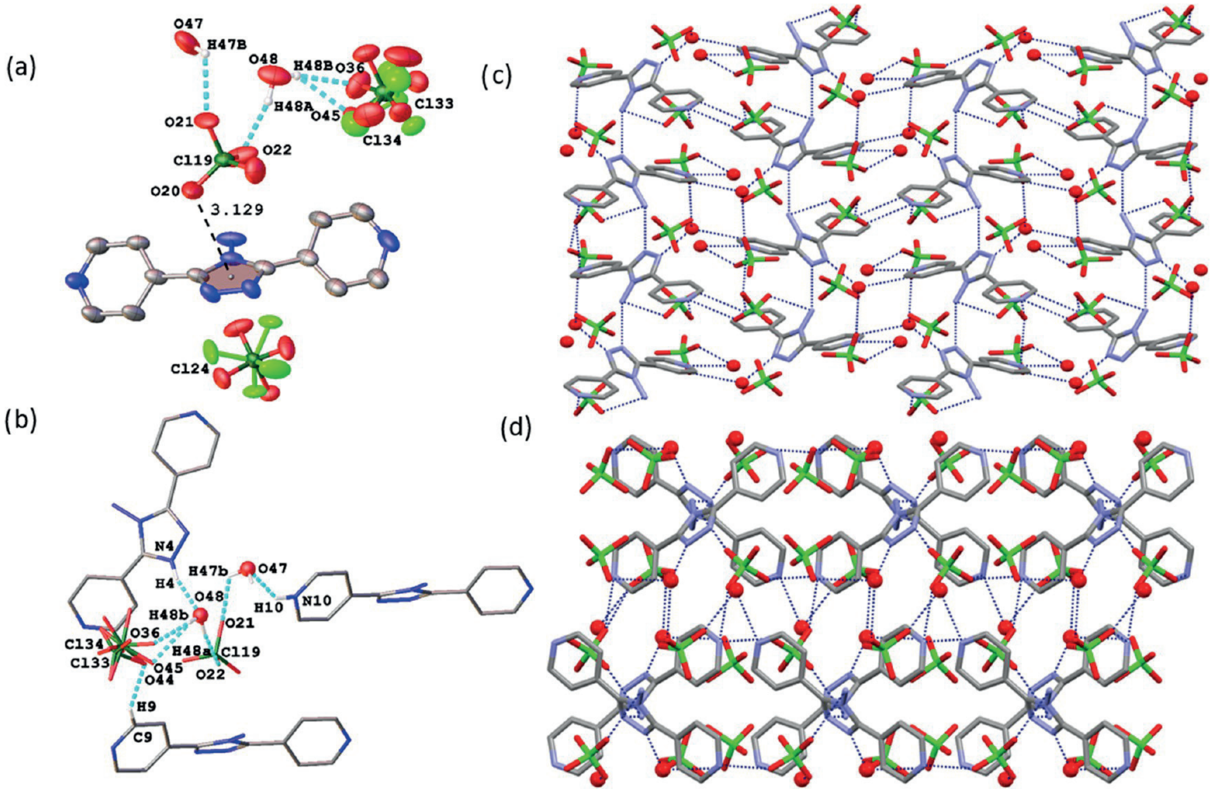

Figure 21. Illustration of (**15**) (a) acyclic $(ClO_4^-)_2(H_2O)_2$ tetramer and anion−π interactions, (b) coordination environment around the acyclic $(ClO_4^-)_2(H_2O)_2$ tetramer, and (c) molecular packing along the *a*-axis and (d) along the *c*-axis. Only relevant atoms are shown. Hydrogen atoms are omitted for clarity. H bonds are exemplified by cyan dashed lines (blue dashed lines in molecular packing), and the distance is measured in angstrom (Å).

3.006(2), 2.9631(19), and 3.040(2) Å for *d*(O33−O22), *d*(O23−O27), and *d*(O27−O33), respectively.[61] Notably, the oxygen atom (O25) of $[Cl(24)O_4]^-$ is also in close proximity to the triazole ring centroid with an O25⋯ring−centroid distance of *d*(3.0468(17)) Å and an O25⋯ring−plane distance of *d*(2.845(2)) Å with an offset distance of 1.09 Å, indicating anion−π interaction (Figure 20d).

Considerably different structural features are observed for the salt (**15**) containing water molecules, which seems to participate in the formation of an acyclic $(ClO_4^-)_2(H_2O)_2$ tetramer moiety (Figure 21a). One of the $[ClO_4]^-$ anions is disordered with approximate occupancies of 0.8 and 0.2, respectively, for Cl34 and Cl33, and the four oxygen atoms for the same anion are disordered over three positions with approximate occupancies of 0.4:0.4:0.2. Similarly, in case of the second $[Cl(24)O_4]^-$ anion, its oxygen atoms are disordered over two positions with approximate occupancies of 0.6 and 0.4. In contrast to another perchlorate salt (**14**), the number of H bonds varies significantly due to the presence of water molecules. In total, three cationic ligands surround the acyclic cluster via N−H⋯O and C−H⋯O H-bond interactions (Figure 21b). In this perchlorate−water−perchlorate−water cluster, there are two crystallographically distinct perchlorate ions and two crystallographically distinct water molecules (O48 and O47). The $[Cl(19)O_4]^-$ anion is not H-bonded to the protonated ligand but instead has two water O−H⋯O intracluster H bonds (O47−H47B⋯O21 and O48−H48A⋯O22). Both water molecules are then H-bonded to the cationic ligand (Figure 21b). The oxygen (O47) of a water molecule is engaged with pyridinium N10−H10B⋯O47, whereas the second water molecule (O48) is coordinated through a strong N4−H4⋯O48 H bond, forming zig-zag chains parallel to the *b*-axis (Figure 21c). The coordination environment of the third perchlorate ion $[Cl(24)O_4]^-$ is entirely different, as it only bounds to the protonated ligand and has no contact with nearby water molecules (Figure 21c). Each $[Cl(24)O_4]^-$ participates in three N−H⋯O bonds by three cationic ligands. The perchlorate oxygen atoms O29 and O32 (0.6 occupancy each) are in contact with pyridine hydrogen donor N16−H16, forming a centrosymmetric $R_2^4(8)$ H-bonded ring motif (Figure 17b). The amino group hydrogen (N6−H6B) is shared by the third oxygen atom O26 of $[Cl(24)O_4]^-$, facilitating the formation of H-bonded chains $C_2^2(12)$, propagating along the *a*-axis and being part of the $R_4^4(24)$ H-bonding motif (Figure 17c). Interestingly, the direct interactions between two cationic ligands are also observed. This mediates via an amino donor (N6−H6B) and a triazole nitrogen acceptor (N3) with a contact distance *d*(N6−N3) of 2.981(5) Å, and also facilitates the formation of $C_1^1(5)$ H-bonded chains propagating along the *c*-axis (Figure 21c). The molecular packing when viewed along the *c*-axis shows the criss-cross orientation of cationic ligands (Figure 21d). Besides the multisite (N−H⋯O, C−H⋯O and O−H⋯O) H-bond interactions around the anions, the molecular packing is further stabilized by anion−π contacts.

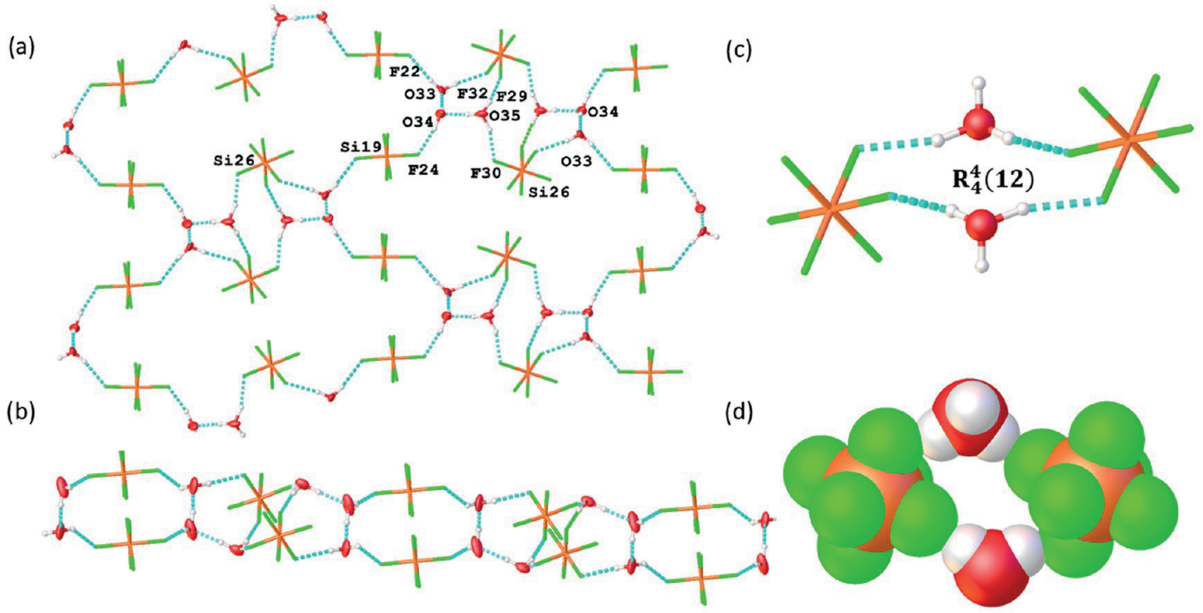

Figure 22. Illustrations of (**16**) (a) hydrogen-bonded sheet of water molecules, hexafluorosilicate anions and hydronium ions, (b) side view of the same sheet, (c) hydrogen-bonding motif found in the cyclic tetrameric cluster, and (d) space-filling representation of the cyclic tetrameric cluster. Cations are omitted for clarity. Only relevant atoms are shown. H bonds are exemplified by cyan dashed lines.

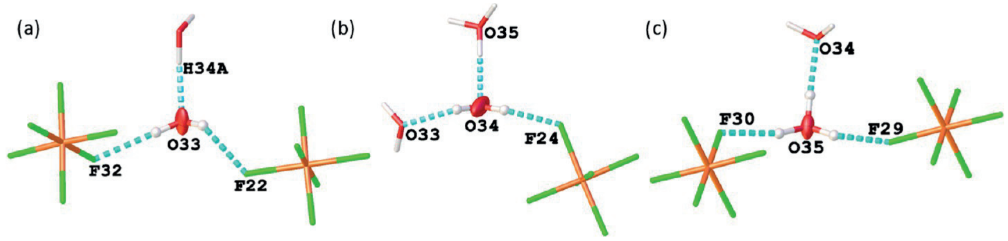

Figure 23. Hydrogen-bonding environment of different water molecules and the hydronium ion in the structure (**16**). Only relevant atoms are shown. H bonds are exemplified by cyan dashed lines.

The perchlorate anion $[Cl(19)O_4]^-$ contributes to anion−π interactions, as one of its oxygen atoms (O20, with no disorder) is at close proximity from the triazole ring with a distance d(O20−centroid) of 3.129(4) Å and an offset of 1.19 Å to the centroid (Figure 21a).

Different from the other hexafluorosilicate structures, the ligand in the salt (**16**) is triprotonated, and the salt contains water along with the anions of which also a hydronium ion was found to balance the overall charge due to two hexafluorosilicate anions. In this structure, infinite H-bonded sheets comprised of water molecules, hexafluorosilicate anions, and hydronium ions can be observed. The sheet-like arrangement features several cyclic motifs, namely, tetrameric and 16-membered cyclic motifs, all interconnected, as shown in Figure 22. In the cyclic tetramer ring, a hydronium ion (O35) serves as a H-bond donor toward F29 and F30 of $[Si(26)F_6]^{2-}$, giving a centrosymmetric $R_4^4(12)$ H-bonded structural motif that eventually brings together two hydronium units and two $[Si(26)F_6]^{2-}$ anions. Thus, the hydronium ion (O35) is situated between two $Si(26)F_6{}^{2-}$ anions and one water molecule (O34), instead of between two water molecules. Therefore, aggregation can be described in terms of $[Si(26)F_6]^{2-}$ and $[Si(19)F_6]^{2-}$ anions interconnecting $[H_7O_3]^+$ ions. The second four-membered ring is completed by two crystallographically distinct water molecules, a hydronium ion and one $[Si(26)F_6]^{2-}$ anion. In this ring, the hydronium ion (O35) serves as a H-bond donor toward F29, the water molecule (O34), and a water molecule (O34) acts as an H-bond donor toward the second water molecule (O33), and the water molecule (O33) acts as a H-bond donor toward F32 of the $[Si(26)F_6]^{2-}$ anion. The H-bonding environment of different water molecules and a hydronium ion is highlighted in Figure 23, and detailed H-bonding parameters are provided in Table S2. Next, the 16-membered cyclic motifs comprise crystallographically distinct water molecules, hexafluorosilicate anions, and hydronium ion units, creating a supramolecular assembly that propagates along the b-axis.

Apart from O−H···F interactions, anions are engaged with cationic ligands via N−H···F contacts. The $[Si(26)F_6]^{2-}$ anion reveals the bicoordinated nature of H-bonding acceptance of one fluoride atom (F27) and in total binds two cationic ligands via protonated pyridyls (N10−H10···F27 and N16−H16···F27 contacts) with the formation of $C_2^1(14)$ H-bonded zig-zag chains parallel to the a-axis. In contrast, the second

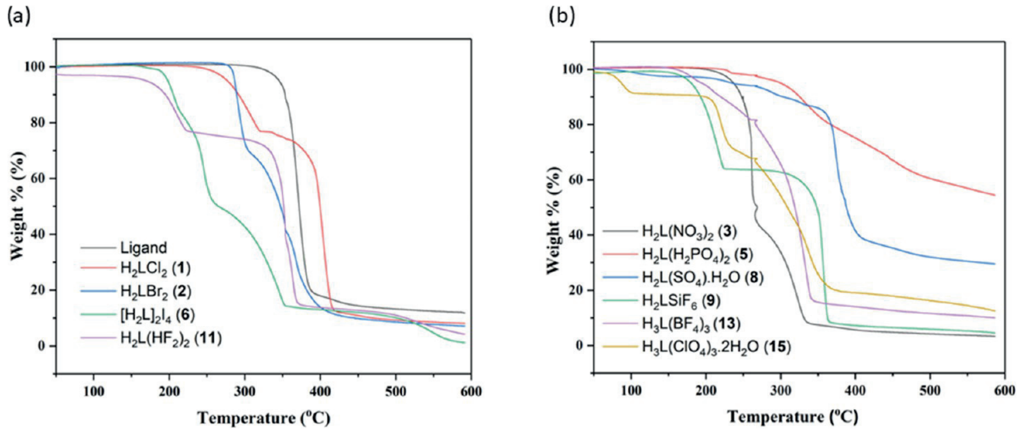

Figure 24. TG curves of the (a) ligand **L**, H_2LCl_2 (**1**), H_2LBr_2 (**2**), $[H_2L]_2I_4$ (**6**), and $H_2L(HF_2)_2$ (**11**) and (b) $H_2L(NO_3)_2$ (**3**), $H_2L(H_2PO_4)_2$ (**5**), $H_2L(SO_4)\cdot H_2O$ (**8**), H_2LSiF_6 (**9**), $H_3L(BF_4)_3$ (**13**), and $H_3L(ClO_4)_3\cdot 2H_2O$ (**15**).

hexafluorosilicate $[Si(19)F_6]^{2-}$ anion accepts three H bonds from three cationic ligands out of which two are contributed by an amino group, such that the $C_2^2(6)$ H-bonded chain is formed, which is mediated via two trans-fluoride ligands (N6−H6A···F25 and N6−H6B···F20) parallel to the *b*-axis. The third H bond is assisted by triazole nitrogen (N3) and facilitates the generation of $C_2^2(9)$ H-bonded linear chains mediated by *cis*-fluoride ligands (N6−H6A···F25Si(19)F23···H3−N3), running along the $C_2^2(6)$ H-bonded chains. As a result, bilayer arrangement is sustained by intermolecular H-bond interactions when viewed down the *b*-axis. The molecular packings along the *a*-, *b*-, and *c*-axes are shown in Figure S11. Additionally, anion−π interactions further contribute to the strengthening of the hydrogen bonding-driven assembly. The triazole ring establishes anion−π interactions involving both crystallographically distinct hexafluorosilicate anions with the fluorine atoms F21 and F32 of the $[Si(19)F_6]^{2-}$ and $[Si(26)F_6]^{2-}$ anions being only 2.7913(13) and 2.7690(13) Å apart from the ring centroid, respectively (Figure S11).

3.3. Thermogravimetry. Thermogravimetric analyses were made to examine and compare the thermal stability of the ligand and the prepared salts at 10 °C/min under a N_2 flow. As shown in Table S4 and Figure 24, the neutral ligand **L** has an onset decomposition temperature of 328 °C, and all of the examined salts illustrate decomposition temperatures between 154 and 240 °C, with salt (**11**) having the lowest and salt (**2**) the highest decomposition temperature. The observed decomposition temperatures and the corresponding weight losses indicate that the (first dehydrated in the case of hydrates) salts demonstrate the decomposition of anions as a free acid, followed by the formation of volatile products in the first stage. For instance, chloride and bromide salts underwent three prominent rapid weight losses, where the first step ended at around 283 and 270 °C with a weight loss of about 23.58 wt % (calcd. 23%) and 33.08 wt % (calcd. 40%) owing to the expected formation of volatile products such as HCl and HBr, respectively. The following weight loss corresponds to the decomposition of the ligand **L** itself, which is analogous to the behavior seen for the other halide salts (Figure 24). Regarding thermal stability, halide salts exhibited pronounced differences showing a gradual decline with the sequence of bromide, chloride, iodide, and fluoride.

The TG curve of $H_2L(NO_3)_2$ (**3**) demonstrates a sharp mass loss (58 wt %) at 159−273 °C corresponding to exothermic decomposition. This can be the result of the decomposition of nitrate anion $[NO_2 + 1/2H_2O + 1/4O_2\ (20\%)]$. Nevertheless, at this temperature range, there are combinations of changes occurring as a byproduct of some chemical process accompanied by effusion of the gaseous species. Complex $H_2L(H_2PO_4)_2$ (**5**) experienced gentle descending weight loss (2.15 wt %) corresponding to an endothermic reaction, which ended at around 237 °C, suggesting that this originates from surface-bound water, which is also consistent with aggregable EA results indicating the presence of a single water molecule. As shown in Figure 24, there is no clear-cut plateau on the TG curve of salt (**5**), hence deducing plausible polymerization of dihydrogen phosphate ions. The TG curve of salt $H_2L(SO_4)\cdot H_2O$ (**8**) displays a weight loss of 2.45 and 2.92 wt % (calcd. 5.07%) in two steps, originating from a loss of the water molecule in the temperature range of 62−140 and 140−242 °C, respectively. It can be speculated that the relatively high release temperature observed for the water molecule can be attributed to the strong H-bonding interactions by two sulfate anions involved in a cyclic sulfate−water cluster, which was shown in the single-crystal structure. The salt H_2LSiF_6 (**9**) shows the first weight loss of about 35.41 wt % (calcd. 37.67%) up to 231 °C corresponding to an endothermic reaction, which can be ascribed to the decomposition of a $[SiF_6]^{2-}$ anion. This is then followed by the thermal decomposition of the neutral ligand. The observed results are consistent with both crystallographic and elemental analysis results. The hydrated salt $H_3L(ClO_4)_3\cdot 2H_2O$ (**15**) decomposes in four stages of which the first step occurs in the temperature range of 44−104 °C, with a weight loss of about 7.92 wt % (calcd. 6.25%) corresponding to the release of crystal water and surface moisture. This is then followed by the initiation (onset 206 °C) of exothermic decomposition that ends at around 244 °C. The final two weight losses occurring in the temperature range of 244−375 °C (50.17 wt %) and 375−588 °C (7.51 wt %), respectively, correspond to the decomposition of the remaining ligand. Note that, as indicated by TG/DSC graphs, no melting points were observed before decomposition for all of the salts. Among the examined salts, H_2LBr_2 (**2**) salt shows the highest decomposition temperature, which is close to 240 °C. $H_2L(HF_2)_2$ (**11**), $H_3L(BF_4)_3$ (**13**), and H_2LSiF_6 (**9**) display the lowest thermal stability, which is <163 °C. Chloride-, iodide-, nitrate-, sulfate-, phosphate-, and perchlorate-based salts demonstrated onset decomposition temperatures in the intermediate range, which is >163 and <240 °C and can be assembled in the following series: $H_2L(HF_2)_2$ < (**11**) $H_3L(BF_4)_3$ (**13**) < H_2LSiF_6 (**9**) < $[H_2L]_2I_4$ < (**6**) $H_2L(SO_4)\cdot H_2O$ (**8**) < $H_3L(ClO_4)_3\cdot 2H_2O$ (**15**) < $H_2L(NO_3)_2$ (**3**) ≈ H_2LCl_2 (**1**) < $H_2L(H_2PO_4)_2$ (**5**) < H_2LBr_2 (**2**). All of the thermal analysis results are presented in Table S4 for comparison.

3.4. Powder X-ray Diffraction Methods (PXRD). For the most part, the Pawley refinement of the lattice parameters for each of the bulk powders was determined to be structurally analogous to the respective single-crystal structures. The fitted diffraction graphs, refined unit cells, and resulting R-factors/goodness-of-fits are shown in Figures S12−S21 and Table S5, respectively. According to obtained results, phase purity of the powder samples at all three different concentrations was confirmed for H_2LCl_2 (**1**), H_2LBr_2 (**2**), and $[H_2L]_2I_4$ (**6**). In the case of nitrate, where both monoclinic and triclinic structure modifications were obtained, the PXRD analysis clearly indicates that the bulk material corresponds to the monoclinic $H_2L(NO_3)_2$ (**3**) salt in 2.5 and 5 M concentrations used in the reactions. However, with a low concentration (1 M), along with the major monoclinic product, some unreacted ligands remained as well, indicating that milder 1 M HNO_3 is not sufficient to fully protonate the ligand within the tested reaction conditions (Figure S14). For both phosphate structures, displaying either mono- or diprotonated ligand with one or two dihydrogen phosphate anions (**4**, **5**), the PXRD analysis confirmed that the bulk powder corresponds to the $H_2L(H_2PO_4)_2$ (**5**) salt in all three different concentrations.

The biggest differences between single crystals and their corresponding bulk powders were witnessed for the $H_2L(SO_4)\cdot H_2O$ (**8**) and $H_2L(HF_2)_2$ (**11**). For the salt (**8**), powders resulting from the tested acid concentrations differed significantly. The PXRD pattern of the powder product yielded from a 1 M solution corresponds somewhat well to the simulated pattern of the single-crystal data. The powder product obtained from a 2.5 M acid concentration contained a trace amount of a polymorph. However, the pattern measured from the 5 M concentration was completely different from the expected simulated patterns and can be assumed to be either some polymorph of the sulfate salt or hydrogen sulfate salt, agreeably confirmed with elemental analysis results. For crystal structure $H_2L(HF_2)_2$ (**11**), based on the Pawley fit, all three acid concentrations resulted in bulk powders consisting merely of the neutral ligand, which was also confirmed by the elemental analysis. This could be possibly attributed to the weak acidic nature of the acid, ligand neutralization, or salt instability. For the salt $H_3L(BF_4)_3$ (**13**), the powder product obtained from a 1 M acid concentration contained a trace amount of some unknown impurity, which does not match the simulated pattern or the PXRD pattern of the neutral ligand. However, the bulk products obtained at other concentrations (2.5 and 5 M) were structurally similar to the single-crystal X-ray structure of salt (**13**), as shown in Figure S20. The best Pawley fits were made with H_2LSiF_6 (**9**) and $H_3L(ClO_4)_3$ (**14**), as the PXRD patterns from all three acid concentrations match the corresponding single-crystal structures.

4. CONCLUSIONS

In this study, we have focused on designing new anion-templated supramolecular assemblies of the bent 4-amino-3,5-bis(4-pyridyl)-1,2,4-triazole ligand constituting distinct H-bonded geometry ring [$R_2^2(8)$, $R_2^4(8)$, $R_4^2(20)$, $R_4^4(24)$, and $R_4^4(28)$] and chain [$C_1^1(5)$, $C_2^1(10)$, $C_2^1(14)$, $C_2^2(6)$, $C_2^2(9)$, $C_2^2(11)$, $C_2^2(12)$, $C_2^2(16)$] patterns. We explored how subtle modulation in a crystallization environment and conditions offers the possibility to yield entirely different forms of molecular salts with mono-, di-, or triprotonated ligands. Three significantly different conformations of these 16 molecular salts were differentiated, and the influence of anion's steric effects on the molecular conformations suggested that steric hindrance provided by the polyhedron conformation of anions accounts for the twisted conformation of the ligand. On the other hand, ligands showcased better planarity with smaller spherical anions (Cl^- and Br^-), with strong $\pi-\pi$ interactions (bricklayer fashion) further reinforcing the molecular packing. With in-depth studies on the crystal structures, we were able to unveil some key structural aspects of hexameric anion cluster assembly $[(H_2PO_4^-)_6]$ of the $R_6^6(24)$ motif and anion−water clusters ranging from a cyclic tetramer $[(SO_4)_2-(H_2O)_2]^{4-}$ of the $R_4^4(12)$ motif and an octameric cluster $[(SiF_6)_4-(H_2O)_4]_\infty^{8-}$ of the $R_8^8(24)$ structural motif to an acyclic tetramer $[(ClO_4^-)_2(H_2O)_2]$.

Focusing on intrinsic anion chemistry, we demonstrate key structural insights into vast and varied ranging supramolecular networks of the bent ligand manifested by a synergistic interplay of multiple noncovalent interactions with a panel of different anion geometries ranging from linear ($[HF_2]^-$), spherical (Cl^-, Br^-, I^-), trigonal planar ($[NO_3]^-$), and tetrahedral ($[ClO_4]^-$, $[SO_4]^{2-}$, $[H_2PO_4]^-$, $[BF_4]^-$) to octahedral ($[SiF_6]^{2-}$). The hydrogen bonding-driven assemblies alongside anion−π interactions and $\pi-\pi$ stacking emerged as key players in establishing entirely diverse supramolecular entities, distinctive H-bonded motifs, and intriguing anion−water clusters. Thus, this work with detailed examples of specific inorganic anions warrants the relevant information associated with the rational design of anion-mediated supramolecular entities and aids in understanding how the coexistence of different noncovalent interactions mutually influences the supramolecular systems. Indeed, insights obtained can be grasped to acquire a wider understanding of new families of synthetic molecular systems and leverage the application of noncovalent interactions as a supramolecular tool to manipulate preferred binding systems for the complexation of a particular anion.

ASSOCIATED CONTENT

Supporting Information

The Supporting Information is available free of charge at https://pubs.acs.org/doi/10.1021/acs.cgd.3c00393.

> ^1H NMR and ^{13}C NMR spectra; FTIR spectroscopy; molecular conformations; crystallographic data; hydrogen-bonding distances (Å) and bond angles (deg); geometric parameters $d_{centroid}$, d_{plane}, and d_{offset}; partial view of molecular packing; thermogravimetric results; Pawley analysis of bulk powders; percent yields of bulk powders; and Pawley refinement plots (PDF)

Accession Codes

CCDC 2252716−2252731 contain the supplementary crystallographic data for this paper. These data can be obtained free of charge via www.ccdc.cam.ac.uk/data_request/cif, or by emailing data_request@ccdc.cam.ac.uk, or by contacting The Cambridge Crystallographic Data Centre, 12 Union Road, Cambridge CB2 1EZ, UK; fax: +44 1223 336033.

AUTHOR INFORMATION

Corresponding Author

Manu Lahtinen − *Department of Chemistry, University of Jyväskylä, FI-40014 Jyväskylä, Finland;* orcid.org/0000-0001-5561-3259; Email: manu.k.lahtinen@jyu.fi

Authors

Shreya Mahajan − *Department of Chemistry, University of Jyväskylä, FI-40014 Jyväskylä, Finland*
Antti Marttinen − *Department of Chemistry, University of Jyväskylä, FI-40014 Jyväskylä, Finland*
Samu Forsblom − *Department of Chemistry, University of Jyväskylä, FI-40014 Jyväskylä, Finland*

Complete contact information is available at: https://pubs.acs.org/10.1021/acs.cgd.3c00393

Notes

The authors declare no competing financial interest.

ACKNOWLEDGMENTS

This study was financially supported by the Academy of Finland (Decision Number 329314) and the University of Jyväskylä.

REFERENCES

(1) Lehn, J.-M. From Supramolecular Chemistry towards Constitutional Dynamic Chemistry and Adaptive Chemistry. *Chem. Soc. Rev.* **2007**, *36*, 151−160.

(2) Plais, R.; Boufroura, H.; Gouarin, G.; Gaucher, A.; Haldys, V.; Brosseau, A.; Clavier, G.; Salpin, J. Y.; Prim, D. Design and Property Investigation on a Five-Interaction-Based Fluorescent Anion Receptor Clip. *RSC Adv.* **2021**, *11*, 9476−9487.

(3) Plais, R.; Gouarin, G.; Bournier, A.; Zayene, O.; Mussard, V.; Bourdreux, F.; Marrot, J.; Brosseau, A.; Gaucher, A.; Clavier, G.; Salpin, J.; Prim, D. Chloride Binding Modulated by Anion Receptors Bearing Tetrazine and Urea. *ChemPhysChem* **2023**, *24*, No. 2200524.

(4) Molina, P.; Zapata, F.; Caballero, A. Anion Recognition Strategies Based on Combined Noncovalent Interactions. *Chem. Rev.* **2017**, *117*, 9907−9972.

(5) Li, H.; Valkenier, H.; Thorne, A. G.; Dias, C. M.; Cooper, J. A.; Kieffer, M.; Busschaert, N.; Gale, P. A.; Sheppard, D. N.; Davis, A. P. Anion Carriers as Potential Treatments for Cystic Fibrosis: Transport in Cystic Fibrosis Cells, and Additivity to Channel-Targeting Drugs. *Chem. Sci.* **2019**, *10*, 9663−9672.

(6) Yamada, S. Cation−π Interactions in Organic Synthesis. *Chem. Rev.* **2018**, *118*, 11353−11432.

(7) Chifotides, H. T.; Dunbar, K. R. Anion−π Interactions in Supramolecular Architectures. *Acc. Chem. Res.* **2013**, *46*, 894−906.

(8) Janiak, C. A Critical Account on π−π Stacking in Metal Complexes with Aromatic Nitrogen-Containing Ligands. *J. Chem. Soc., Dalton Trans.* **2000**, *21*, 3885−3896.

(9) Peuronen, A.; Valkonen, A.; Kortelainen, M.; Rissanen, K.; Lahtinen, M. Halogen Bonding-Based "Catch and Release": Reversible Solid-State Entrapment of Elemental Iodine with Monoalkylated DABCO Salts. *Cryst. Growth Des.* **2012**, *12*, 4157−4169.

(10) Xia, X.; Zhang, S.; Li, S.; Zhang, L.; Wang, G.; Zhang, L.; Wang, J.; Li, Z. The Cycle of Nitrogen in River Systems: Sources, Transformation, and Flux. *Environ. Sci.: Processes Impacts* **2018**, *20*, 863−891.

(11) Eytel, L. M.; Fargher, H. A.; Haley, M. M.; Johnson, D. W. The Road to Aryl CH···anion Binding Was Paved with Good Intentions: Fundamental Studies, Host Design, and Historical Perspectives in CH Hydrogen Bonding. *Chem. Commun.* **2019**, *55*, 5195−5206.

(12) Mahadevi, A. S.; Sastry, G. N. Cooperativity in Noncovalent Interactions. *Chem. Rev.* **2016**, *116*, 2775−2825.

(13) Custelcean, R. Anions in Crystal Engineering. *Chem. Soc. Rev.* **2010**, *39*, 3675−3685.

(14) Hoque, M. N.; Das, G. Overview of the Strategic Approaches for the Solid-State Recognition of Hydrated Anions. *CrystEngComm* **2017**, *19*, 1343−1360.

(15) Hossain, M. A.; Işiklan, M.; Pramanik, A.; Saeed, M. A.; Fronczek, F. R. Anion Cluster: Assembly of Dihydrogen Phosphates for the Formation of a Cyclic Anion Octamer. *Cryst. Growth Des.* **2012**, *12*, 567−571.

(16) Chutia, R.; Dey, S. K.; Das, G. Self-Assembly of a Tris(Urea) Receptor as Tetrahedral Cage for the Encapsulation of a Discrete Tetrameric Mixed Phosphate Cluster $(H_2PO_4^-{\cdot}HPO_4^{2-})_2$. *Cryst. Growth Des.* **2015**, *15*, 4993−5001.

(17) Hoque, M. N.; Das, G. Cationic Tripodal Receptor Assisted Formation of Anion and Anion-Water Clusters: Structural Interpretation of Dihydrogen Phosphate Cluster and Sulfate-Water Tetramer $[(SO_4)_2{-}(H_2O)_2]^{4-}$. *Cryst. Growth Des.* **2014**, *14*, 2962−2971.

(18) Pramanik, S.; Thordarson, P.; Day, V. W.; Bowman-James, K. Oligomeric Phosphate Clusters in Macrocyclic Channels. *CrystEngComm* **2022**, *24*, 8047−8051.

(19) He, Q.; Tu, P.; Sessler, J. L. Supramolecular Chemistry of Anionic Dimers, Trimers, Tetramers, and Clusters. *Chem* **2018**, *4*, 46−93.

(20) White, N. G. Antielectrostatically Hydrogen Bonded Anion Dimers: Counter-Intuitive, Common and Consistent. *CrystEngComm* **2019**, *21*, 4855−4858.

(21) Zhao, W.; Flood, A. H.; White, N. G. Recognition and Applications of Anion−Anion Dimers Based on Anti-Electrostatic Hydrogen Bonds (AEHBs). *Chem. Soc. Rev.* **2020**, *49*, 7893−7906.

(22) Gale, P. A.; Howe, E. N. W.; Wu, X.; Spooner, M. J. Anion Receptor Chemistry: Highlights from 2016. *Coord. Chem. Rev.* **2018**, *375*, 333−372.

(23) Jagleniec, D.; Dobrzycki, Ł.; Karbarz, M.; Romański, J. Ion-Pair Induced Supramolecular Assembly Formation for Selective Extraction and Sensing of Potassium Sulfate. *Chem. Sci.* **2019**, *10*, 9542−9547.

(24) Beckendorf, S.; Asmus, S.; Mancheño, O. G. H-Donor Anion Acceptor Organocatalysis-The Ionic Electrophile Activation Approach. *ChemCatChem* **2012**, *4*, 926−936.

(25) Coles, M. P. Bicyclic-Guanidines, -Guanidinates and -Guanidinium Salts: Wide Ranging Applications from a Simple Family of Molecules. *Chem. Commun.* **2009**, *25*, 3659.

(26) Busschaert, N.; Caltagirone, C.; Van Rossom, W.; Gale, P. A. Applications of Supramolecular Anion Recognition. *Chem. Rev.* **2015**, *115*, 8038−8155.

(27) Liu, T. P.; Huo, L. H.; Deng, Z. P.; Zhao, H.; Gao, S. Supramolecular Architectures and Luminescent Properties of the Salts Containing Flexible Bis(Pyridyl) Cations with Aliphatic Diamine Spacer: Effects of Inorganic Anions, Alkalinity and Conformation of the Bis(Pyridyl) Cations. *RSC Adv.* **2014**, *4*, 40693−40710.

(28) Zhang, Z.-Y.; Deng, Z.-P.; Huo, L.-H.; Zhao, H.; Gao, S. Inorganic Anion Induced Supramolecular Architectures of Flexible Unsymmetrical Bis(Pyridyl) Ionic Salts Mediated by Various Non-Covalent Interactions. *CrystEngComm* **2013**, *15*, 5261.

(29) Ding, X.-H.; Wang, S.; Li, Y.-H.; Huang, W. Inorganic Anion-Assisted Supramolecular Assemblies of Bent Dipyridines: Effects of Anionic Geometries on Hydrogen-Bonding Networks. *Inorg. Chem. Front.* **2015**, *2*, 263−272.

(30) Roubeau, O. Triazole-Based One-Dimensional Spin-Crossover Coordination Polymers. *Chem. − Eur. J.* **2012**, *18*, 15230−15244.

(31) Dupouy, G.; Marchivie, M.; Triki, S.; Sala-Pala, J.; Gómez-García, C. J.; Pillet, S.; Lecomte, C.; Létard, J.-F. Photoinduced HS

State in the First Spin-Crossover Chain Containing a Cyanocarbanion as Bridging Ligand. *Chem. Commun.* **2009**, *23*, 3404.

(32) White, N. G.; Brooker, S. Metal Acetates Form Diverse Polynuclear Complexes with 4-Amino-3,5-Di(2-Pyridyl)-1,2,4-Triazole (Adpt). *Supramol. Chem.* **2013**, *25*, 806−811.

(33) White, N. G.; Kitchen, J. A.; Brooker, S. A Structural Investigation of Anion−Triazole Interactions: Observation of "Π-Pockets" and "Π-Sandwiches.". *Eur. J. Inorg. Chem.* **2009**, *2009*, 1172−1180.

(34) Qin, B.; Zhang, X.; Zhang, J. A New Multifunctional Zinc−Organic Framework with Rare Interpenetrated Tripillared Bilayers as a Luminescent Probe for Detecting Ni^{2+} and PO_4^{3-} in Water. *Cryst. Growth Des.* **2020**, *20*, 5120−5128.

(35) Lee, L.-W.; Kao, Y.-C.; Chung, M.-Y.; Chang, B.-C.; Lee, G.-H.; Peng, S.-M.; Wang, C.-M.; Liu, Y.-H.; Lee, S.-L.; Lu, K.-L. Rare Metal-Ion Metathesis of a Tetrahedral Zn(II) Core of a Noncentrosymmetric (3,4)-Connected 3D MOF. *Dalton Trans.* **2019**, *48*, 1950−1954.

(36) Chatterjee, N.; Oliver, C. L. A Dynamic, Breathing, Water-Stable, Partially Fluorinated, Two-Periodic, Mixed-Ligand Zn(II) Metal−Organic Framework Modulated by Solvent Exchange Showing a Large Change in Cavity Size: Gas and Vapor Sorption Studies. *Cryst. Growth Des.* **2018**, *18*, 7570−7578.

(37) Mahajan, S.; Lahtinen, M. Recent Progress in Metal-Organic Frameworks (MOFs) for CO_2 Capture at Different Pressures. *J. Environ. Chem. Eng.* **2022**, *10*, No. 108930.

(38) Du, M.; Jiang, X.-J.; Tan, X.; Zhang, Z.-H.; Cai, H. Co-Crystallization of a Versatile Building Block 4-Amino- 3,5-Bis(4-Pyridyl)-1,2,4-Triazole with R-Isophthalic Acids (R = −H, $-NH_2$, $-SO_3H$, and −COOH): Polymorphism and Substituent Effect on Structural Diversity. *CrystEngComm* **2009**, *11*, 454−462.

(39) *CrysAlisPRO*; Oxford Diffraction/Agilent Technologies UK Ltd.: Yarnton, England.

(40) Sheldrick, G. M. SHELXT - Integrated Space-Group and Crystal-Structure Determination. *Acta Crystallogr., Sect. A* **2015**, *71*, 3−8.

(41) Sheldrick, G. M. Crystal Structure Refinement with SHELXL. *Acta Crystallogr., Sect. C* **2015**, *71*, 3−8.

(42) Dolomanov, O. V.; Bourhis, L. J.; Gildea, R. J.; Howard, J. A. K.; Puschmann, H. OLEX2: A Complete Structure Solution, Refinement and Analysis Program. *J. Appl. Crystallogr.* **2009**, *42*, 339−341.

(43) Gruene, T.; Hahn, H. W.; Luebben, A.; Meilleur, F.; Sheldrick, G. M. Refinement of Macromolecular Structures against Neutron Data with SHELXL2013. *J. Appl. Crystallogr.* **2014**, *47*, 462−466.

(44) Degen, T.; Sadki, M.; Bron, E.; König, U.; Nénert, G. The HighScore Suite. *Powder Diffr.* **2014**, *29*, S13−S18.

(45) Pawley, G. S. Unit-Cell Refinement from Powder Diffraction Scans. *J. Appl. Crystallogr.* **1981**, *14*, 357−361.

(46) Bentiss, F.; Lagrenée, M.; Traisnel, M.; Mernari, B.; Elattari, H. A Simple One Step Synthesis of New 3,5-Disubstituted-4-Amino-1,2,4-Triazoles. *J. Heterocycl. Chem.* **1999**, *36*, 149−152.

(47) Etter, M. C.; MacDonald, J. C.; Bernstein, J. Graph-set Analysis of Hydrogen-bond Patterns in Organic Crystals. *Acta Crystallogr., Sect. B* **1990**, *46*, 256−262.

(48) Savastano, M.; Bazzicalupi, C.; Giorgi, C.; García-Gallarín, C.; López De La Torre, M. D.; Pichierri, F.; Bianchi, A.; Melguizo, M. Anion Complexes with Tetrazine-Based Ligands: Formation of Strong Anion-π Interactions in Solution and in the Solid State. *Inorg. Chem.* **2016**, *55*, 8013−8024.

(49) Berryman, O. B.; Bryantsev, V. S.; Stay, D. P.; Johnson, D. W.; Hay, B. P. Structural Criteria for the Design of Anion Receptors: The Interaction of Halides with Electron-Deficient Arenes. *J. Am. Chem. Soc.* **2007**, *129*, 48−58.

(50) Kim, H.-J. Assembly of Sn(IV)-Porphyrin Cation Exhibiting Supramolecular Interactions of Anion···Anion and Anion···π Systems. *Molbank* **2022**, *2022*, M1454.

(51) Hursthouse, M. B.; Montis, R.; Niitsoo, L.; Sarson, J.; Threlfall, T. L.; Asiri, A. M.; Khan, S. A.; Obaid, A. Y.; Al-Harbi, L. M. Anhydrates and/or Hydrates in Nitrate, Sulphate and Phosphate Salts of 4-Aminopyridine, (4-AP) and 3,4-Diaminopyridine (3,4-DAP): The Role of the Water Molecules in the Hydrates. *CrystEngComm* **2014**, *16*, 2205−2219.

(52) Arunachalam, M.; Ghosh, P. A Versatile Tripodal Amide Receptor for the Encapsulation of Anions or Hydrated Anions via Formation of Dimeric Capsules. *Inorg. Chem.* **2010**, *49*, 943−951.

(53) Nath, J. K.; Baruah, J. B. Water Assisted Anion Chains and Anion Dependent Fluorescence Emission in Salts of N,N′-Bis(3-Imidazol-1-Ylpropyl)Naphthalenediimide. *New J. Chem.* **2013**, *37*, 1509−1519.

(54) Bauzá, A.; Frontera, A.; Mooibroek, T. J. NO3− Anions Can Act as Lewis Acid in the Solid State. *Nat. Commun.* **2017**, *8*, No. 14522.

(55) Franconetti, A.; Frontera, A.; Mooibroek, T. J. Intramolecular π−Hole Interactions with Nitro Aromatics. *CrystEngComm* **2019**, *21*, 5410−5417.

(56) Mooibroek, T. J. Coordinated Nitrate Anions Can Be Directional π-Hole Donors in the Solid State: A CSD Study. *CrystEngComm* **2017**, *19*, 4485−4488.

(57) Bauzá, A.; Frontera, A.; Mooibroek, T. J. Π-Hole Interactions Involving Nitro Aromatic Ligands in Protein Structures. *Chem. − Eur. J.* **2019**, *25*, 13436−13443.

(58) Zhang, G.; Zhang, X.; Kong, L.; Wang, S.; Tian, Y.; Tao, X.; Yang, J. Anion-Controlled Dimer Distance Induced Unique Solid-State Fluorescence of Cyano Substituted Styrene Pyridinium. *Sci. Rep.* **2016**, *6*, No. 37609.

(59) Mahé, N.; Nicolaï, B.; Allouchi, H.; Barrio, M.; Do, B.; Céolin, R.; Tamarit, J. L.; Rietveld, I. B. Crystal Structure and Solid-State Properties of 3,4-Diaminopyridine Dihydrogen Phosphate and Their Comparison with Other Diaminopyridine Salts. *Cryst. Growth Des.* **2013**, *13*, 708−715.

(60) Gelmboldt, V. O.; Ganin, E.; Fonari, M. S.; Simonov, Y. A.; Koroeva, Lv.; Ennan, A. A.; Basok, S. S.; Shova, S.; Kählig, H.; Arion, V. B.; Keppler, B. K. Two New "Onium" Fluorosilicates, the Products of Interaction of Fluorosilicic Acid with 12-Membered Macrocycles: Structures and Spectroscopic Properties. *Dalton Trans.* **2007**, *27*, 2915−2924.

(61) Hoque, M. N.; Manna, U.; Das, G. Discrepancy in Anion Coordination Directed by Isomeric Pyridine−Urea Receptors: Solid State Recognition of Hydrated Anions. *Polyhedron* **2016**, *119*, 307−316.

II

3D ZINC–ORGANIC FRAMEWORKS BASED ON MIXED THIOPHENE DICARBOXYLATE AND 4-AMINO-3,5-BIS(4-PYRIDYL)-1,2,4-TRIAZOLE LINKERS: SYNTHESES, STRUCTURAL DIVERSITY, AND SINGLE-CRYSTAL-TO-SINGLE-CRYSTAL TRANSFORMATIONS

by

Mahajan, S.; Lahtinen, M. 2024

Crystal Growth & Design, 24(2), 747-762

https://doi.org/10.1021/acs.cgd.3c01172

CRYSTAL GROWTH & DESIGN

3D Zinc–Organic Frameworks Based on Mixed Thiophene Dicarboxylate and 4-Amino-3,5-bis(4-pyridyl)-1,2,4-triazole Linkers: Syntheses, Structural Diversity, and Single-Crystal-to-Single-Crystal Transformations

Shreya Mahajan and Manu Lahtinen*

Cite This: *Cryst. Growth Des.* 2024, 24, 747–762

Read Online

ACCESS | Metrics & More | Article Recommendations | Supporting Information

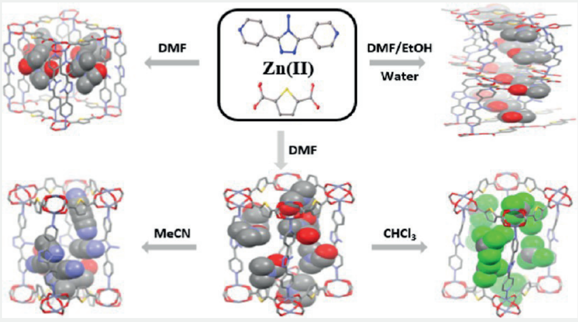

ABSTRACT: In this study, for the first time two new interpenetrated 3D pillared-layer metal–organic frameworks (MOFs), namely, $\{[Zn(bpt)(tdc)]\cdot dmf\}_n$ (MOF-**1**-Zn) and $\{[Zn_2(bpt)(tdc)_2]\cdot 2(dmf)\}_n$ (MOF-**2**-Zn), as well as a homochiral 3D framework $\{[Zn(bpt)(tdc)(H_2O)]\cdot dmf\}_n$ (MOF-**3**-Zn), were prepared under different synthesis conditions (bpt = 4-amino-3,5-bis(4-pyridyl)-1,2,4-triazole, H_2tdc = 2,5-thiophenedicarboxylic acid, and dmf = *N*,*N*′-dimethylformamide). Synthesis products were thoroughly characterized by single-crystal and powder X-ray diffraction and thermoanalytical methods. Remarkably, in the case of MOF-**2**-Zn, dmf molecules in the voids can be exchanged for different solvents, e.g., chloroform, methanol, ethanol, isopropyl alcohol, acetonitrile, acetone, tetrahydrofuran, 1,4-dioxane, and cyclohexane in a single-crystal-to-single-crystal (SCSC) manner. With different solvent types, the bpt ligands adapted slightly different conformations by adjusting the orientation of the NH_2-triazole core unit and the tilting of the pyridyl groups. In comparison, most changes for planar tdc ligands were observed on the dihedral angles of the adjacent thiophene rings (e.g., 69.5 vs 78.5° for MOF-**2**-Zn and **2**-$CHCl_3$, respectively). Desolvation of the MOF illustrated systematic structural adaptability of $\{Zn_2\}$-"paddlewheel" in SCSC fashion, and the MOF's crystallinity and 3D networked structure were preserved even after vacuum and heat-assisted desolvation. Finally, preliminary CO_2 adsorption tests for MOFs were conducted utilizing a custom-built fixed-bed adsorption/desorption device, resulting in about 0.1 $mmol_{CO_2}/g_{sorbent}$ at 400–4000 ppmv CO_2 and about 1 $mmol_{CO_2}/g_{sorbent}$ at 15 vol % CO_2.

1. INTRODUCTION

Metal–organic frameworks (MOFs) are highly ordered crystalline structures possessing potential voids.[1] MOFs are derived from metal nodes linked by polytopic organic linkers and nowadays are at the forefront in the material science field and chemistry research.[2] Over the past few decades, MOFs have successfully established themselves as a highly competitive candidate for their practical utility in the plethora of chemistry-related fields varying from gas/liquid separations, storage applications, drug delivery, and chemical sensors to catalysis and beyond.[3−8] Among the wealth of MOFs, most structures have "rigid" networks and only limited examples have been reported to have structural flexibility as a characteristic feature of a MOF. In such cases, network structure can undergo a structural transition in response to a wide range of external chemical or physical stimuli (e.g., guest change and removal, heat, light, or mechanical pressure). Such structures form an appealing subclass of MOFs frequently recognized as flexible or breathing MOFs or simply soft porous crystals.[1,9−11]

In general, structural flexibility can be realized in different ways, including displacement of interpenetrated frameworks,[12] ligand motions,[13] and deformations at M−L bonds,[9] to name a few.[14] Thanks to single-crystal X-ray diffraction (SCXRD), these structural details can be directly determined and visualized. However, the shear force and stress generated by the solvent exchange can often significantly increase a crystal's mosaicity and fragmentation, resulting in unmeasurable single crystals. Therefore, single-crystal-to-single-crystal (SCSC) transformation is often challenging to observe structurally

Received: October 4, 2023
Revised: December 11, 2023
Accepted: December 12, 2023
Published: December 26, 2023

and is a topical subject in the MOF community, as indicated by continually growing publishing output. Consequently, this phenomenon is a powerful tool for producing the most accurate property−structure correlations in atomic resolution. However, discovering new coordination frameworks that sustain sufficient crystallinity through the SCSC transformation is a continuous challenge.[11,15−18]

In this study, we present three new mixed-ligand MOFs prepared from identical starting components by mixing 4-amino-3,5-bis(4-pyridyl)-1,2,4-triazole (bpt) ligand, 2,5-thiophenedicarboxylic acid (H_2tdc), and $Zn(NO_3)_2$. Compositionally different MOFs were obtained concomitantly under identical solvothermal conditions, with a formula of $\{[Zn(bpt)(tdc)]\cdot dmf\}_n$ and $\{[Zn_2(bpt)(tdc)_2]\cdot 2(dmf)\}_n$, henceforth named MOF-**1**-Zn and MOF-**2**-Zn, respectively. The former MOF could also be isolated alone by a judicious selection of synthetic conditions. Along with attempts to optimize single-crystal growth and phase purity, a third structural modification with a formula of $\{[Zn(bpt)(tdc)(H_2O)]\cdot dmf\}_n$, named MOF-**3**-Zn, was also obtained.

The bpt ligand used in the syntheses was selected based on our previous studies,[19] wherein the ligand conformational changes were examined by crystallizing it from different mineral acids. Investigation resulted in 16 distinct crystal structures, demonstrating the ligand's ability to exhibit a versatile spectrum of molecular conformations ranging from planar to nearly perpendicularly tilted pyridyl end groups. To date, the bpt ligand has already been utilized in the MOF syntheses;[20−22] however, pairing it with the tdc ligand has not yet been reported. Second, considering aspects of a secondary building unit (SBU) with metal centers supported by carboxylates, tdc ligand may provide alternative binding modes, potentially endowing frameworks with unique coordination environments. Additionally, structural changes involving the "kneecap" rotational axis of the carboxylates may further contribute to a greater flexibility of the framework.[23]

With bpt, we envisaged that its versatile molecular conformations might enable structurally altered frameworks via a guest exchange, which could be monitored through SCSC transformations. Several solvents were employed to test whether they may replace dmf molecules and induce observable SCSC transformation. As a result, along with the crystal structures of three new pristine MOFs, their ten solvent exchange products and one desolvated crystal structure were obtained. Thermal stabilities of the crystalline products were also characterized by thermogravimetric analysis. Powder X-ray diffraction (PXRD) studies provided insights into the phase purity of bulk powders and in-depth structural insights into the framework's flexibility. In addition, the CO_2 adsorption capabilities of pillared-layer MOFs were also examined, utilizing a custom-built fixed-bed adsorption/desorption device under dry 400, 4000 ppm, and 15% CO_2 balanced with N_2.

2. METHODS

2.1. Material Syntheses and Characterization. The synthetic procedures for the 4-amino-3,5-bis(4-pyridyl)-1,2,4-triazole (bpt) ligand can be found in the Supporting Information. In general, the synthesis of bpt ligand followed the procedure reported in the literature.[19]

*2.1.1. Preparation of MOF-**1**-Zn.* A mixture of $Zn(NO_3)_2\cdot 6H_2O$ [120.19 mg, 0.404 mmol], 4-amino-3,5-bis(4-pyridyl)-1,2,4-triazole (bpt) [65.04 mg, 0.273 mmol], and thiophene-2,5-dicarboxylic acid (H_2tdc) [47.00 mg, 0.273 mmol] was added to dimethylformamide (dmf) [12 mL] in a Teflon-lined steel-made reaction vessel [22 mL] and heated at 120 °C for 72 h, followed by cooling to room temperature over a period of 24 h in an oven. The colorless plate-shaped crystals obtained were isolated by filtration, washed with dmf, and briefly air-dried (yield 117.70 mg, ∼78.84%, based on bpt). Anal. Calcd for $C_{21}H_{19}N_7O_5SZn$: C, 46.12; H, 3.50; N, 17.93. Found: C, 45.33; H, 3.33; N, 17.80%.

*2.1.2. Preparation of MOF-**2**-Zn.* A procedure similar to that of MOF-**1**-Zn was followed but with the exception of component ratio, as a 1:1:1 metal-to-ligands ratio was used instead of 1.48:1:1. The reaction produced simultaneously single crystals of MOF-**2**-Zn and MOF-**1**-Zn. The quantities used in the synthesis for $Zn(NO_3)_2\cdot 6H_2O$, bpt, H_2tdc, and dmf were [89.24 mg, 0.3 mmol], [71.48 mg, 0.3 mmol], [51.65 mg, 0.3 mmol], and [24 mL], respectively. Synthesis resulted in plate- and block-like single crystals, indicating the presence of both MOF-**1**-Zn and MOF-**2**-Zn, respectively. The colorless crystals obtained were filtered, washed with dmf, and briefly dried in air (yield 120.30 mg, % yield, and EA not calculated because of a mixture).

*2.1.3. Preparation of MOF-**3**-Zn.* $Zn(NO_3)_2\cdot 6H_2O$ [44.92 mg, 0.151 mmol], bpt [23.83 mg, 0.1 mmol], and H_2tdc [17.22 mg, 0.1 mmol] were dissolved separately in deionized water [5 mL], hot ethanol EtOH [30 mL], and dmf [5 mL], respectively. A clear solution of the zinc salt and bpt was mixed, and subsequently, the H_2tdc solution was added dropwise to this solution with vigorous stirring at 80 °C. After 1 h, the cooled solution was filtered to remove the remaining residue. Finally, colorless rod-shaped crystals were afforded by slow solvent evaporation at room temperature from the resulting solution within a week. The crystals obtained were decanted from the mother liquor and stirred in fresh dmf for a few hours to ensure the removal of unreacted materials and unwanted species and then dried in air (yield 17.30 mg, ∼30.63% based on bpt). Anal. Calcd for $C_{21}H_{21}N_7O_6SZn$: C, 44.65; H, 3.75; N, 17.36. Found: C, 44.37; H, 3.53; N, 17.07%.

2.2. Single-Crystal X-ray Diffraction. Single crystals suitable for the SCXRD analyses were typically picked directly from the crystallization solvent. For testing solvent exchange, fresh crystals of pristine MOF type were submerged into the desired solvent for 2−7 days, and the solvent was changed at 12- or 24 h intervals three times (more details in the Supporting Information).

Crystal data for MOF-**1**-Zn, MOF-**2**-Zn, MOF-**3**-Zn, and for other samples were collected sample dependently by Rigaku XtaLAB Synergy-R high flux rotating anode X-ray diffractometer equipped with HyPix-Arc 100° curved photon counting detector, and PhotonJet-R source with MicroMax-007 rotating anode (Cu K_α, λ = 1.54184 Å); Rigaku SuperNova single-source diffractometer (Eos CCD detector) using mirror-monochromatized Mo K_α radiation (λ = 0.71073 Å); or Rigaku SuperNova dual-source (Cu and Mo microsources) X-ray diffractometer equipped with Atlas CCD detector (for few samples, HyPix-Arc 100°) and multilayer optics producing monochromatized Cu K_α radiation (λ = 1.54184 Å). Data collection, reduction, and analytical face-index-based absorption correction methods were performed using the CrysAlisPRO[24] program. All structures were solved by the ShelXT[25] (intrinsic phasing) program implemented in the Olex^2(v.1.5)[26] and refined on F^2 by full-matrix least-squares techniques with the ShelXL[27] program. All non-hydrogen atoms were refined anisotropically. Hydrogen atoms were calculated to their ideal positions using isotropic temperature factors 1.2 or 1.5 times their parent atom and were refined as riding atoms. Occupancies of disordered moieties were first determined using free variables in the refinement but, at the final stages, were typically fixed to help converge the refinement, particularly in the case of solvent molecules with low occupancies. Electron densities of severely disordered solvents were removed on the final refinement of the structure through the OLEX^2 solvent mask (SM) tool after their chemical composition was confirmed first (when applicable). The removed electron density was not considered when determining the chemical formula. The contact surface calculations to determine void spaces (radius: 1.2 Å) and figures were generated by the Mercury program.[28] Further details about all of the SCXRD structures can be found in the provided crystallographic information

Scheme 1. Representation of tdc^{2-} Carboxylate Group Binding Modes, Dihedral Angles between the Two-Pyridine Rings and the Central Triazole Ring of bpt, Coordination Geometry around Zn^{II} Ion in MOF-1-Zn, MOF-2-Zn, and MOF-3-Zn, Respectively; Only Relevant Atoms Are Shown

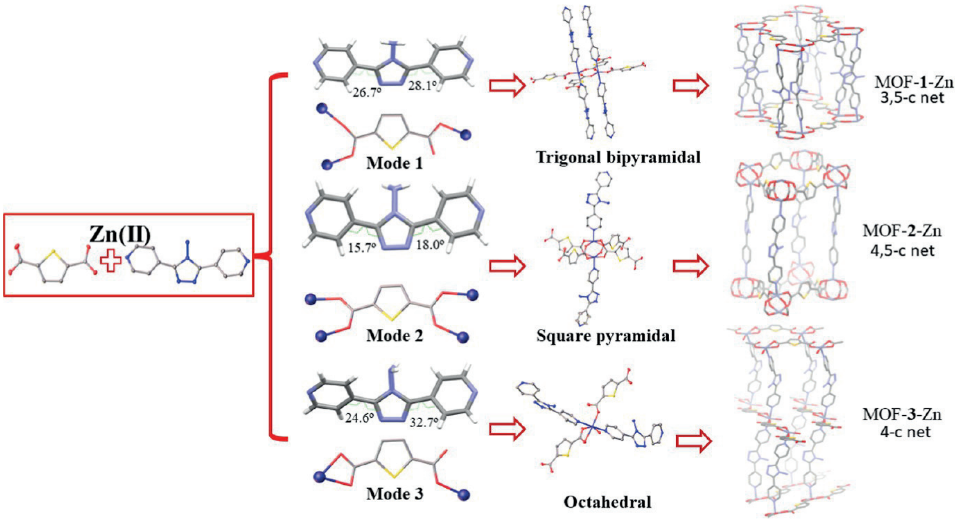

files deposited at the Cambridge Crystallographic Data Centre (CCDC) under deposition numbers CCDC 2279907 [MOF-**1**-Zn], 2279908 [MOF-**2**-Zn], 2279909 [MOF-**3**-Zn], 2279898 [**2**-CH_3Cl], 2279904 [**2**-MeOH], 2279901 [**2**-EtOH], 2279902 [**2**-*i*-PrOH], 2279903 [**2**-MeCN], 2279897 [**2**-acetone], 2279905 [**2**-THF], 2279900 [**2**-dioxane], 2279899 [**2**-cyclohexane], 2279906 [guest-freed, **2**-gf], and 2279896 [**1**-MeOH].

2.3. Powder X-ray Diffraction. PXRD data were measured using a Panalytical X'Pert PRO MPD diffractometer with Cu K_α radiation (λ = 1.54184 Å; Ni β-filter; 45 kV, 40 mA). Each powder sample was placed on a silicon-made "zero-background signal generating" plate using petrolatum jelly as an adhesive. Diffraction intensities were recorded by an X'Celerator detector at room temperature with 2θ-range of 3−60°, a step size of 0.017°, and a counting time of 70 s per step. Data processing, search-match phase analyses, and Pawley whole-pattern fits were carried out by the program X̌pert HighScore Plus (v. 4.9). Search-match phase identification analyses were made against the ICDD-PDF4+ database (version 2022) implemented in the HighScore.[29,30] In the Pawley fits, the unit cell parameters of the PXRD patterns were refined using the corresponding single crystal structure parameters as the basis of least-squares refinement. Variables for the fits were as follows: zero-offset, polynomial background, sample height displacement, unit cell parameters, and peak profile parameters, including peak width, shape, and asymmetry.

2.4. Thermal Analysis. The thermal properties of the compounds were examined using a PerkinElmer STA 6000 simultaneous thermogravimetric-calorimetric TG/DSC analyzer. Each sample was measured in an open platinum pan and heated under an N_2 atmosphere (flow rate of 40 mL/min) with a heating rate of 10 °C/min on a temperature range of 22−600 °C. For each run under N_2, 10 min isotherm at 22 °C was introduced to ensure proper purging of the furnace interior from the ambient air atmosphere before the start of the heating step. Temperature calibration of the analyzer was made using melting points of the indium (156.6 °C), zinc (419.5 °C), and aluminum (660.3 °C) standards. The weight balance was calibrated at room temperature using a standard weight of 50.00 mg. The sample weights used in the measurements were about 1−8 mg.

2.5. CO_2 Adsorption Tests. CO_2 adsorption tests were conducted at VTT Technical Research Centre of Finland using a custom-built fixed-bed adsorption/desorption device used earlier for lab-scale direct air capture experiments with an amine-functionalized resin.[31,32] Approximately, 100 mg of the MOF sample was packed into the adsorption column with quartz wool below and above the adsorbent bed. The sample was first regenerated using nitrogen purge at 100 °C, then cooled down to the adsorption temperature of 12 °C. Adsorption was then initiated using dry 400, 4000 ppm, or 15% CO_2 balanced with N_2. Desorption was carried out at 100 °C using N_2. The total flow rate was 200 mL/min, corresponding to a superficial velocity of 0.052 m/s inside the column. The CO_2 capacities were calculated by numerical integration of the flow rate and CO_2 concentration profiles and using the ideal gas law.

The effect of the dead volume of the adsorption rig and the CO_2 analyzer lag was considered by measuring CO_2 capacities in the same conditions without a sample and subtracting these capacities from the ones measured with the sample. The adsorption results in the 15% CO_2 tests were measured using a %-scale CO_2 analyzer, while the desorption results were measured using the ppm-scale sensor. Although the ppm-scale sensor only measured up to 5000 ppm, its higher accuracy in the ppm region allowed for better comparison between the two samples. However, for this reason, it should be noted that the reported desorption results may be lower than the actual total desorption capacity, and care should be taken in comparison to literature values. More details of the experimental device and the calculation methods can be found in ref 33 while an in-depth discussion of the experimental uncertainty of the device is available elsewhere.[32] The methanol-exchanged MOF-**1**-Zn sample was activated at 120 °C overnight under vacuo, and the mixture was heated at 180 °C overnight under vacuo before the CO_2 adsorption tests.

3. RESULTS AND DISCUSSION

3.1. Syntheses and Structure. All three compounds, MOF-**1**-Zn, MOF-**2**-Zn, and MOF-**3**-Zn, were synthesized under somewhat different synthetic conditions, resulting in structures with distinct void volumes, featuring different coordination geometries, binding modes, and alignments of organic ligands, as well as dissimilar topologies (Scheme 1). MOF-**1**-Zn and MOF-**2**-Zn, as well as their mixtures, resulted from solvothermal reactions (at 120 °C) using different metal-to-ligand ratios and solvent volumes (more details in the Supporting Information). MOF-**3**-Zn was obtained by slow evaporation from an EtOH/water/dmf solvent mixture. All three crystal structures were solved by SCXRD. The reaction

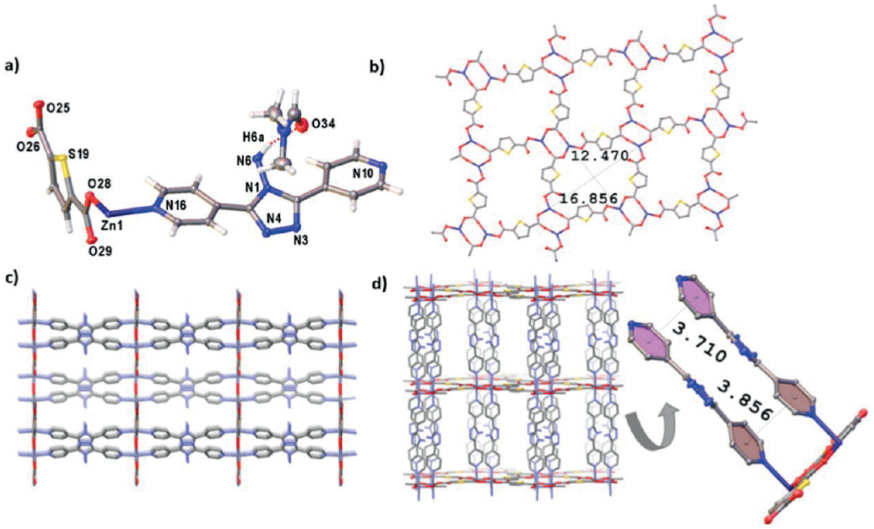

Figure 1. Depiction of the crystal structure of MOF-**1**-Zn. (a) Coordination environment around Zn^{II}, (b) partial view of 2D networked layer, and (c,d) views of the single-net 3D pillared-layer framework along the *a*- and *c*-axes, respectively, with a view of $\pi-\pi$ interactions between bpt ligands. All hydrogen atoms are omitted for clarity; only relevant atoms are shown; interatomic distances are given in Å (applies to all figures).

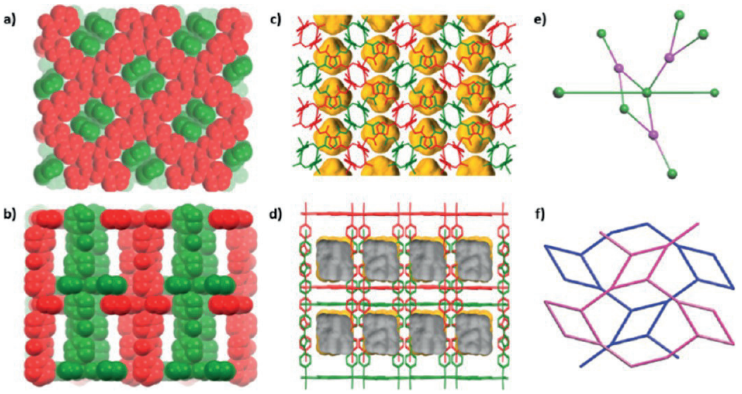

Figure 2. Depiction of the crystal structure of MOF-**1**-Zn. (a,b) Space-filling representation of 2-fold interpenetration (red and green) along the *b*- and *c*-axes, respectively, (c,d) potential void space visualized by yellow/gray (outer/inner) colors, and (e,f) simplified view of a (3,5)-connected network.

of bpt, H_2tdc, and $Zn(NO_3)_2 \cdot 6H_2O$ in a molar ratio 1:1:1.48 at 120 °C for 72 h resulted in MOF-**1**-Zn obtained as plate-shaped crystals. It is built on trigonal bipyramidal coordination geometry where tdc^{2-} adopts coordination mode 1 (Scheme 1). Under the same conditions but with a changed concentration and a molar ratio of 1:1:1, it resulted in a mixture of MOF-**1**-Zn and MOF-**2**-Zn, entailing the same metal and organic building blocks. MOF-**2**-Zn was obtained as block-shaped crystals built on paddlewheel units, where each tdc^{2-} adopts alternative bridging mode 2 (Scheme 1). The underlying reason for the dissimilar geometries of SBU could be that both trigonal bipyramidal and square pyramidal coordination geometries have nearly the same energies. Thus, the switching from trigonal bipyramidal to square pyramidal or vice versa is reasonably straightforward.[34] From the available literature, we know that paddlewheel core is common in flexible MOFs with zinc- and copper-based systems, and the Zn-based paddlewheel MOFs have overall lower stability and higher flexibility in comparison to copper-based systems attributed to respective electronic structures [d^{10} Zn(II) and d^9 Cu(II)].[35] Contrarily, Zn^{II} in MOF-**3**-Zn adopted octahedral geometry instead of trigonal bipyramidal or square pyramidal, as in this case, water molecules (solvent) interfere by directly coordinating to the Zn center, in contrast to solvothermal conditions wherein dmf molecules do not show any interaction with a metal center. Significant differences observed between the frameworks are further examined in detail in Sections 3.1.1−3.1.3. Crystallographic data and the selected structure refinement parameters are summarized in (Table S1).

3.1.1. *Crystal Structure of MOF-1-Zn.*

Based on the X-ray crystallographic structure determination, MOF-**1**-Zn crystallizes in the orthorhombic space group *Pcca* (Figure 1a), having a single Zn^{II}, bpt ligand, fully deprotonated tdc^{2-} ligand, and a single dmf molecule in an asymmetric unit (AU). As visualized in Scheme 1, the Zn^{II} center site, exhibiting a distorted trigonal bipyramidal coordination geometry, is defined by three carboxylate oxygen atoms from three tdc^{2-} ligands located in

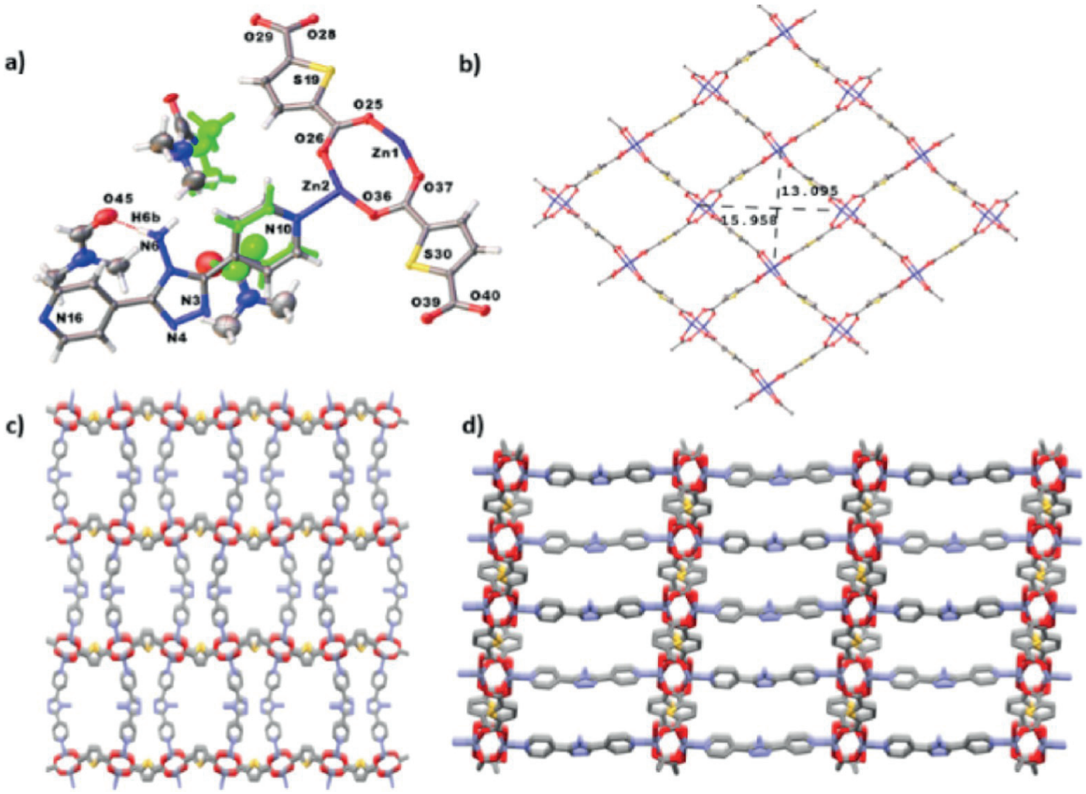

Figure 3. Depiction of the crystal structure of MOF-**2**-Zn. (a) Coordination environment around the Zn^{II}, (b) view of the 2D networked layer, and (c,d) views of the single-net 3D pillared-layer framework along the *a*- and *b*-axes, respectively.

the equatorial plane. Two pyridyl nitrogen atoms (N10 and N16) from two bpt ligands occupy the axial positions, respectively. Both pyridyl rings of the bpt ligand feature almost equal and significant twisting in parallel directions with respect to the central triazole ring, as manifested by dihedral angles 26.79(11) and 28.17(11)°, respectively.

Herein, each tdc^{2-} adopts binding mode 1 (Scheme 1), bound to three different Zn^{II}, where one carboxylate group adopts monodentate and the other carboxylate functions as bridging mode, respectively. Thus, the dimeric unit built by carboxylate groups separates Zn···Zn by 4.1655(6) Å and propagates along the *ac*-plane to form a planar 2D layer with square grid dimensions of about 12.4699(7) × 16.8556 (5) Å^2 (based on Zn···Zn separation) along the *b*-axis (Figure 1b). Furthermore, the neutral ditopic bpt ligands act as pillars where each bpt coordinates with two Zn^{II} by its two pyridyl end groups to interconnect the resulting 2D layers, affording a 3D pillared-layer MOF (Figure 1c,d). Interestingly, two similar 3D nets interpenetrate each other in such a way that a 2-fold interpenetrating network holds 23.4% solvent-accessible void corresponding to ~1026 Å^3 volume, as determined by contact surface calculations (Figure 2).

The structure of MOF-**1**-Zn is also stabilized both by $\pi-\pi$ interactions between the adjacent pyridyl groups of bpt with a centroid−centroid $d(\pi-\pi)$ distance being 3.710(2)−3.856(2) Å, and via framework−solvent interactions involving between pendant $-NH_2$ group of bpt pillar and the oxygen atom of the solvent molecule (dmf). Topological examination of the MOF-**1**-Zn structure made with the TopoPro program reveals the structure to be an unusual (3,5)-connected net (Figure 2e,f).[36]

3.1.2. Crystal Structure of MOF-2-Zn.

MOF-**2**-Zn crystallizes in a monoclinic *I*2/*a* space group and has two Zn^{II} atoms, one bpt ligand, two fully deprotonated tdc^{2-} ligands, and two disordered dmf guest molecules in an AU. One pyridyl group is disordered over two positions with approximate occupancies of 0.6:0.4 on its carbon atoms (Figure 3a). Each Zn^{II} furnishes a distorted square-pyramidal [ZnO_4N] geometry coordinated equatorially to four oxygen atoms from four different tdc^{2-} ligands and apically to one nitrogen atom of the bpt ligand. Unlike in MOF-**1**-Zn, each tdc^{2-} in MOF-**2**-Zn adopts binding mode 2 (Scheme 1), wherein Zn^{II} is in a bridging mode and as a result [$Zn_2(tdc)_2$] lattice forms rhombic grids with diagonal distances about ca. 13.0950(3) × 15.9577(4) Å^2 along the crystallographic *c*-axis (Figure 3b). In terms of nodal geometry (SBU), Zn-node is a typical {Zn_2}-"paddlewheel", which is bridged by bpt pillars along the axial position of the paddlewheel, and in overall furnishing 3D pillared-layer MOF-**2**-Zn (Figure 3c,d). Compared to MOF-**1**-Zn, some characteristic differences in the molecular conformation of the pillar can be noted as the MOF-**2**-Zn does not contain any $\pi-\pi$ stacking interactions of bpt pillars. In addition, there are noticeable differences in dihedral angles between the pyridyl groups and the central triazole ring, indicating modest tilting of the pyridyl groups with the central triazole ring [18.0(3) and 15.73(18)°]. The 2D layers in MOF-**2**-Zn are kind of corrugated, whereas in MOF-**1**-Zn, they are planar. However, MOF-**2**-Zn is also an interpenetrated 3D framework (Figure

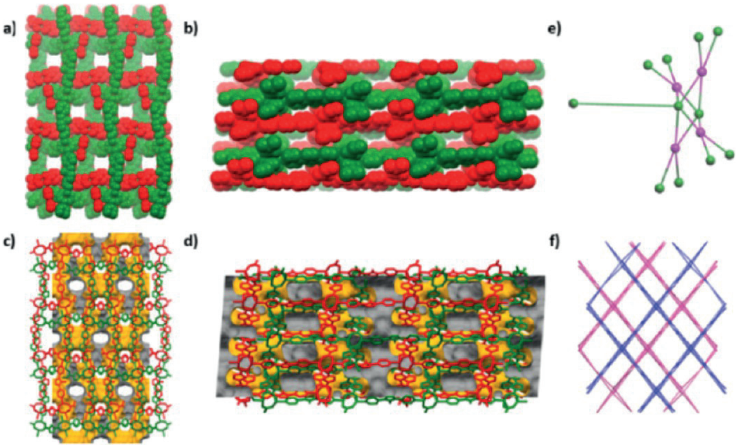

Figure 4. Partial views of MOF-**2**-Zn crystal structure. (a,b) Space-filling representation of 2-fold interpenetration along the *a*- and *b*-axes, respectively, (c,d) potential void space visualized by yellow/gray (outer/inner) colors, and (e,f) simplified view of a (4,5)-connected network.

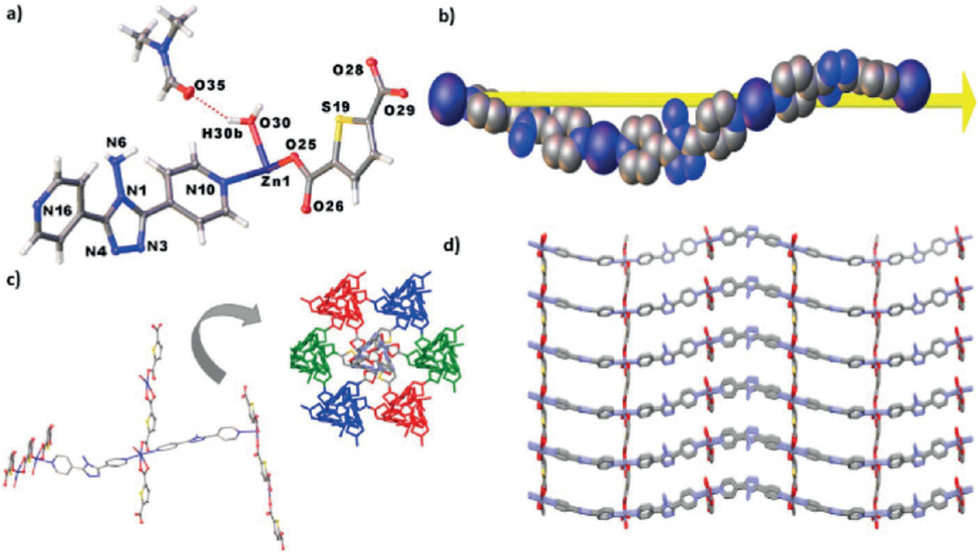

Figure 5. Depiction of the crystal structure of MOF-**3**-Zn. (a) Coordination environment around Zn^{II}, (b) space-filling view of the 3_1-helix along the *b*-axis, (c) view of three different orientations of tdc^{2-} linkers (A: blue, B: red, and C: green), and (d) single-net of the 3D framework along the *b*-axis.

4a,b) having an adequate free volume of 35.3% (corresponding to 2544 Å^3 when solvents are removed), as shown in Figure 4c,d. Topologically, MOF-**2**-Zn can be represented as (4,5)-connected net (Figure 4e,f).

*3.1.3. Crystal Structure of MOF-**3**-Zn.* MOF-**3**-Zn features a homochiral 3D framework with high hexagonal symmetry (space group $P6_1$) formed despite achiral bpt and tdc^{2-} ligands. As illustrated in Figure 5a, AU consists of a single Zn^{II}, bpt, fully deprotonated tdc^{2-} ligand, single water coordinated to the Zn, and one dmf molecule hydrogen-bonded to the coordinated water molecule. In MOF-**3**-Zn, Zn^{II} adopts a distorted octahedral geometry containing three carboxylate oxygen atoms from two tdc^{2-} ligands, one in monodentate and the other in chelating binding mode (mode 3, Scheme 1), as well as one oxygen atom of a water molecule, and two pyridyl nitrogen atoms from two adjacent bpt ligands.

Notably, both the pyridyl rings of the bpt ligand are significantly tilted in the opposite direction relative to each other [56.61(10)°]. Dihedral angles of the pyridyls to the central triazole ring are 24.69(11) and 32.73(11)°, respectively. Overall, infinite single-stranded one-handed wavy 3_1-helices are formed via Zn-bpt bridging that progress along the *c*-axis. All helical chains are arranged in parallel and are further interconnected, forming the 3D honeycomb framework along the *c*-axis, as shown in Figure 5. Described interconnections are formed via tdc^{2-} ligands, which bind to Zn^{II} by a single carboxylate in bidentate and the other one in monodentate fashion to form 1-D linear chains that are rotated by 120° along the crystallographic *c*-axis. These chains, while passing from one to the next successive layer, possess three different orientations (Figure 5c).

Noteworthily, MOF-**3**-Zn features a 2-fold interpenetrating network (Figure 6a,b) wherein the subnets interact via

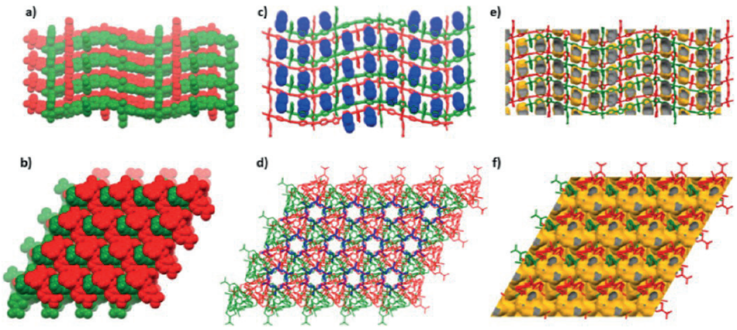

Figure 6. Depiction of the crystal structure of MOF-**3**-Zn. (a,b) Space-filling representation of 2-fold interpenetration along the *b*- and *c*-axes, respectively, (c,d) dmf (in blue) filled channels viewed along the *b*- and *c*-axes, respectively, and (e,f) potential void space along the *b*- and *c*-axes respectively, visualized by yellow/gray (outer/inner) colors.

multiple hydrogen-bond interactions involving coordinated water molecule and the nitrogen atom of the triazole ring [$d(\mathrm{O}\cdots\mathrm{N}) = 2.69$ Å]. Moreover, the $-\mathrm{NH_2}$ group of bpt ligand is H-bonded to both the coordinated as well as uncoordinated carboxyl groups on the tdc^{2-} linkers with $d(\mathrm{N}-\mathrm{O})$ distances of ∼2.82−2.89 Å (Figure S1a). When viewed along the *b*-axis, the channels are filled with dmf molecules in a row formation, arranged as hexagonal helical chains along the *c*-axis (Figure 6c,d). The guest-freed MOF-**3**-Zn incorporates a potential free volume of about 22.9%, equivalent to ∼812 $\mathrm{Å}^3$ (Figure 6e,f). Topologically, MOF-**3**-Zn exhibits a uninodal 4-connected net (Figure S1b), which differs from the nets in MOF-**1**-Zn and MOF-**2**-Zn, respectively.

3.2. Single-Crystal-to-Single-Crystal Guest Exchange.

The presence of elastic paddlewheel units in the pillared-layer MOFs typically endows the framework with inherent flexibility.[1,37,38] With this in mind, the guest-exchange properties of MOF-**2**-Zn (henceforth **2**) were further examined to observe whether solvents can be removed and introduced to the voids in the single-crystal-to-single-crystal (SCSC) manner. The first solvent selected for the tests was chloroform, widely used in MOF-activation procedures (Figure 7). In the experiment, single crystals of **2** were submersed in chloroform for 48 h under ambient conditions (Figure 8). Crystals obtained from the solvent exchange showed some cracking and some degree of fragmentation for larger crystals. However, there was no evident change in color (still transparent), and the fact that even the crystal fragments retained their crystalline features; some crystals were subjected to SCXRD analysis. As a result, the solvent exchanged **2**-$\mathrm{CHCl_3}$ crystallizes in the $P2_1/c$ space group ($I2/a$ for **2** with dmf in the pores), and the asymmetric unit comprises four $\mathrm{Zn^{II}}$, two bpt ligands of which one triazole and pyridyl ring of a single bpt are disordered over two locations with occupancies of 0.85:0.15. The AU also contains four fully deprotonated tdc^{2-} linkers and 3.85 $\mathrm{CHCl_3}$ molecules, of which all except one $\mathrm{CHCl_3}$ are disordered. A single $\mathrm{CHCl_3}$ is disordered over two locations (0.9:0.1), whereas one $\mathrm{CHCl_3}$ shows partial Cl disorder over two locations (0.6:0.4), and a single $\mathrm{CHCl_3}$ with 0.85 occupancies and is located as disorder pair for the disordered pyridyl group of bpt. Compared to structure **2**, the volumetric (V) change of the new unit cell is −0.49%, the β-angle increases by +1.08% while more markedly *a*-, *b*-, and *c*-axes change by +6.08, −5.20 and −0.89%, respectively as shown by the unit cell parameters of **2** and **2**-$\mathrm{CHCl_3}$, respectively: $a = 13.095/13.890$ Å, $b = 15.957/15.127$ Å, $c = 34.566/34.259$ Å, $\beta = 94.306/95.321$, and $V = 7202/7167$ $\mathrm{Å}^3$.

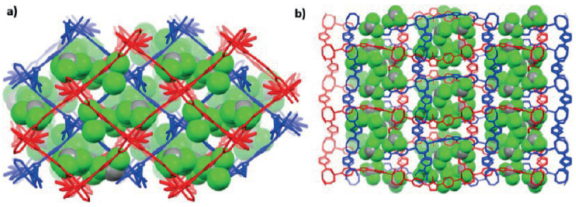

Figure 7. Crystal structure illustration of **2**-$\mathrm{CHCl_3}$. The 2-fold interpenetration (red and blue nets) of a 3D pillared framework displaying accommodated chloroform molecules (space-fill representation) along the (a) *a*-axis and (b) *c*-axis.

The exchange of $\mathrm{CHCl_3}$ molecules to the structure of **2** induces the most pronounced changes in the pillar region (Figure 9). Interestingly, the changes in the shape of the channels (Figure S2) are provoked by the changes in molecular conformations of the pillars (bpt), which are accompanied by subtle alterations in the metal-carboxylate bonding scheme. Evidently, two $\mathrm{Zn^{II}}$ nodes and pillared ligands deviate slightly from linearity, as indicated by the $\mathrm{N}-\mathrm{Zn}\cdots\mathrm{Zn}-\mathrm{N}$ torsion angles, which were changed from 163.5(15) to 157.2(16)/179.2(19)° for **2** and **2**-$\mathrm{CHCl_3}$, respectively. Concurrently, across the bpt direction (Zn···Zn-(bpt)-Zn···Zn), the $\mathrm{Zn_2}\cdots\mathrm{Zn_2}$ angles have clearly changed from 32.45(8) to 22.49(10)/36.60(9)°, respectively. The modest variation in the angle between the Zn−N coordination bond and the pyridine plane (angle of ligation) and the angle between the $\mathrm{C_{triazole}}-\mathrm{C_{pyridine}}$ covalent bond and pyridine plane are further responsible for the observed distortion on the $\mathrm{Zn_2}\cdots\mathrm{Zn_2}$ angles. The conformational flexibility of the pillar can also be verified by broadly varied tilting between the pyridyl and triazole rings, as shown by the range of dihedral angles 18.0(3)−15.73(18) and 22.1(3)−28.3(3)/30.3(3)−31.2(2)° for **2** and **2**-$\mathrm{CHCl_3}$, respectively. In the case of structure **2**, both pyridyl rings are almost perfectly aligned on the same plane in relation to each other [5.8(2)°], whereas, in the **2**-$\mathrm{CHCl_3}$, pyridyls are strongly tilted in opposite directions to each other [dihedral angle ∼60.6(3)°]. Besides tilting the pyridyl units, the bpt pillar can readjust the $\mathrm{NH_2}$-triazole ring in response to the guest solvent (Figure 8). The angle "Ø", defined as the angle between two adjacent planes of triazole rings, describes the orientation of the triazole core. Particularly, the change in the orientation of the triazole core from 45.9(3) to 37.7(5)/40.0(4)° in part

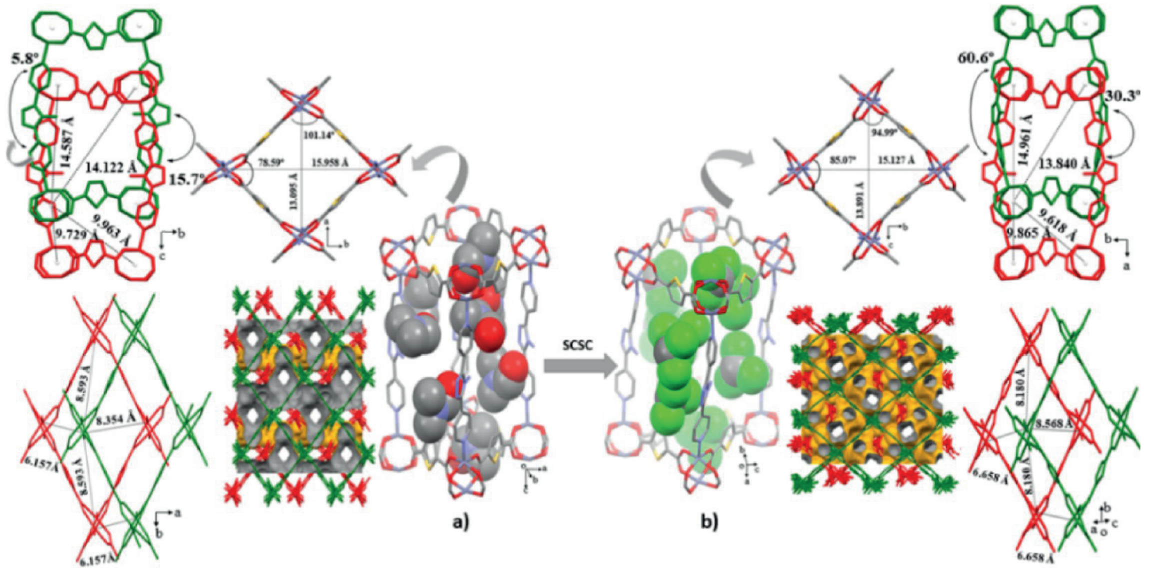

Figure 8. Guest-responsive SCSC structural transformation determined by SCXRD. Views in (a) **2** (with dmf) and (b) **2**-$CHCl_3$ "image sides" demonstrate structural transformation along the pillar (bpt)-axis; packing diagram along the pillar (bpt)-axis with potential void space shown by yellow/gray (outer/inner) colors; views of the two interpenetrated frameworks (red and green) viewed along linker (tdc^{2-})-axis and pillar (bpt)-axis, respectively.

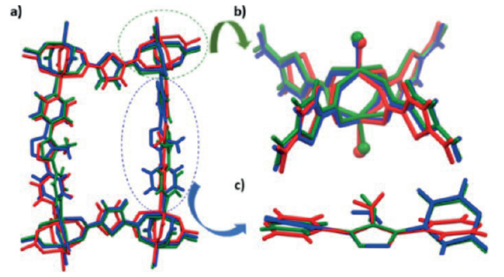

Figure 9. (a) Overlay of single frameworks emphasizing the relative distortion at metal-carboxylate junction and bpt ligand conformations on **2** (dmf) and **2**-$CHCl_3$ (**2** in red and **2**-$CHCl_3$ in green and blue). The overlays are set considering the Zn^{II} atoms on the coordination sphere (a,b), and triazole ring atoms on the bpt ligands (c) as matching atoms.

facilitates the host framework to accept chloroform solvent. Concurrently with the observed rhombohedral distortion along the pillar (bpt) axis, distinct rectangular-shaped channels (rect) emerge. As a result of the structural changes described above, the free void volume (on guest-freed structure) in the lattice decreased from 2544 Å^3 (35.3%) of **2** to 2264 Å^3 (31.6%) on **2**-$CHCl_3$ (Figure 8).

More intriguingly, in framework **2**, the dihedral angles of metal-carboxylate junctions vary from 5.2(4)−13.3(5) to 6.4(5)−12.1(5)° for O−Zn−Zn−O and to carboxylate plane (O_2−C−), respectively. However, in **2**-$CHCl_3$, the corresponding junctions are somewhat less bend with dihedral angles of 3.7(5)−12.4(7), 3.3(7)−5.6(7), 4.7(3)−12.6(6), and 8.2(4)−12.3(6)°. Concurrently, the dihedral angles between two adjacent thiophene rings (herein, designated as δ) increase from 69.5(17) to 78.5(2)° on **2** and **2**-$CHCl_3$, with increasing elongation in the rhombic grids. Another intriguing feature discerned in **2**-$CHCl_3$ is the slight subnetwork displacements. This further reflects the framework's flexibility, which is typically suggested to be driven by the combined effects of the sliding of interpenetrated nets, ligands motion, and metal-node coordination sphere changes.[1,13,39−41]

Encouraged by the successful structural evaluation of the chloroform exchange test, MOF-**2**-Zn was subjected to three new classes of organic solvents, each with different sizes and polarities as determined by the normalized (E_N^T)[42,43] value (Table S2). The resulting solvated structures were analyzed, and some generalized correlations were identified, as shown in Figure 10 and Tables S3−S6. The selected solvents comprised polar protic solvents (methanol, ethanol, isopropyl alcohol), polar aprotic solvents (acetonitrile, acetone, tetrahydrofuran, 1,4-dioxane), and one nonpolar solvent (cyclohexane).

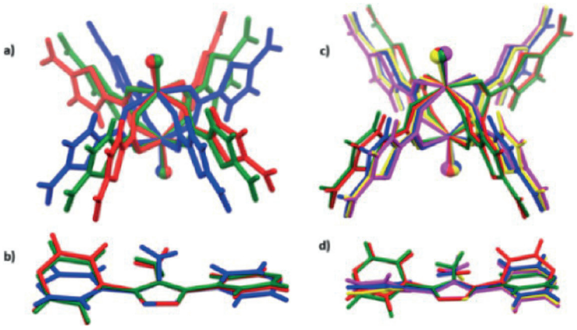

Figure 10. Overlay with emphasis on the relative distortion at metal-carboxylate junction and pillar conformations. Polar protic solvents: (a,b) **2**-MeOH (blue), **2**-EtOH (red), **2**-*i*-PrOH (green); polar aprotic and nonpolar solvents: (c,d) **2**-MeCN (red), **2**-acetone (blue), **2**-THF (green), **2**-dioxane (magenta), and **2**-cyclohexane (yellow). The overlays are set considering the Zn^{II} atoms on the coordination sphere (a,c) and triazole ring atoms on the bpt ligands (b,d) as matching atoms.

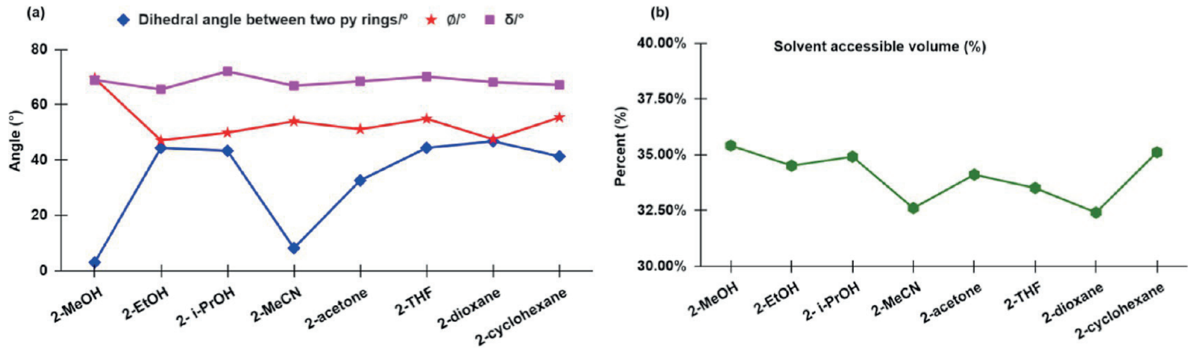

Figure 11. Comparative analysis of the structural differences between the SCSC guest exchange complexes. (a) Dihedral angles between the pyridyl rings (blue), Ø-(red), and δ-angles (pink), and (b) solvent-accessible volume (green).

Interestingly, the crystal structures revealed complete replacement of dmf molecules when using polar and polar aprotic solvents, while only partial exchange occurred with nonpolar cyclohexane. This shows the clearest evidence that the host−guest interactions depend on the proper interplay between the H-bonding donors and acceptors. Hence, with rather noninteractive cyclohexane, no proper H-bond acceptor is available for the strongly H-bonding amino group during the exchange. Therefore, a single dmf molecule per AU remains H-bonded to the $-NH_2$ group on the bpt ligand, while the remaining void is changed to cyclohexane.

In general, it can also be noted that the $-NH_2$ group and two nitrogen atoms of the triazole rings of the pillar (bpt) are disordered over two positions with approximate occupancies of 0.67:0.33 and 0.6:0.4 for **2**-MeOH and **2**-dioxane structures, respectively. Moreover, in the case of **2**-*i*-PrOH, **2**-acetone, **2**-THF, and **2**-dioxane structures, one of the pyridyl rings is disordered over two positions with its four carbon atoms having occupancy shares of 0.75:0.25, 0.6:0.4, 0.5:0.5, and 0.5:0.5, respectively. In **2**-MeCN, the tdc^{2-} linker is disordered over two positions, with its two carbon atoms sharing 0.5:0.5 occupancies.

To avoid complexity in the discussion, the following conformation analysis of the pillars considers only the structural interpretation via the dominant parts of the pillaring ligands. For further interest, all the structural values corresponding to the ligand orientations with lesser occupancies are gathered in Tables S3−S5. Unlike **2**-$CHCl_3$, all the other solvent-exchanged structures exhibit the same monoclinic space group $I2/a$ (equal to **2**) with just marginal variations in their unit cell settings. Typically, per structure-related differences are seen as mild contractions along β-angle, *c*-, and *a*- or *b*-axes with simultaneous increase along *a*- or *b*-axes. Among the organic solvents employed in this study, MeCN exchanged structure **2**-MeCN is the only one manifesting contraction of all three-unit cell axes with β-angle reduction of −3.66%, as a result of which volumetric reduction of about −2.14% is observed for the structure. The observed shrinkage of the framework may be related to the less steric shape of the MeCN, which enables better molecular packing arrangement of the solvent molecules and adaption of the framework dimensions.

Examination of the conformation modes of the bpt ligands per different solvent exchange structures reveals that the dihedral angles between the pyridyl rings depend on the kinetic diameter of solvent molecules. For instance, smaller MeCN and MeOH molecules in **2**-MeCN and **2**-MeOH cause the pyridyl rings of the bpt ligand to adopt a near-planar orientation (dihedral angles varying ∼2−8°) in relation to each other (Figure 11). However, under the influence of steric hindrance of larger solvents, a considerable degree of variation in the tilting of the pyridyl rings is observed, as recognized in the dihedral angles ranging from ∼32 to 46°. As anticipated, these results suggest that the orientation of the pyridyl rings in the pillars is highly influenced by the molecular size of the guest solvents.[19]

Further inspection of the pillars suggests that the conformation of the amino-triazole ring is driven by its feasibility of forming host−guest interactions via H-bonding. For instance, as seen in Figure 11, while the highly polar (E_N^T = 0.762) protic and small MeOH molecules accommodate the voids, the afforded structure demonstrates a striking difference in amino-triazole ring orientation (69.6°) as compared to other solvated structures that typically covers an angular Ø range of ∼47−55°. MeOH fits perfectly in the channels with prominent host−guest interactions, enabling the $-NH_2$ group and one of the triazole nitrogen atoms to H-bond with MeOH, which also participates in intermolecular H-bonding between MeOH molecules and with the carboxyl group of the tdc^{2-} linker located in the adjacent framework (Figure S3).

As described above, the frameworks accommodating guest molecules to their confided space undergo structural alterations, which can be seen as changes in the δ-angles and geometric changes on the metal-carboxylate junctions (Figure 10). However, the δ-angles do not seem to illustrate a clear correlation with the kinetic diameter or polarity of the confined guest (Figure 11). The 2D line chart showing the comparison of the dihedral angles between the metal-carboxylate and thiophene planes in the solvated structures is presented in (Figure S4).

Figure 11b illustrates the range of solvent-accessible volumes accomplished upon different guest solvent exchanges in the host frameworks. MeOH and cyclohexane lead to larger solvent-accessible volumes, whereas MeCN exhibits the smallest void volume. The discrepancies witnessed in the voids involving two solvents (MeOH and MeCN) with near identical sizes but different E_N^T can be partially explained by the effective interactions that the highly polar MeOH molecules have with the host framework (as described above). Consequently, more H-bonds are formed with the framework, resulting in a higher number of guest molecules being accommodated inside the channels of **2**-MeOH. In the case

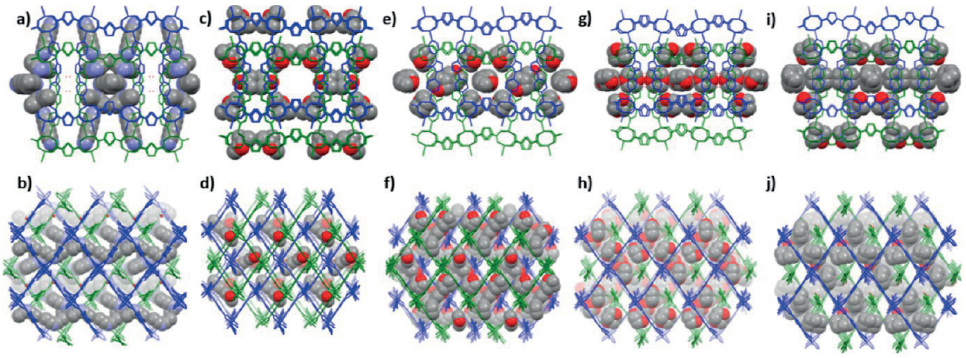

Figure 12. Illustration of solvent molecules (a,b) MeCN, (c,d) acetone, (e,f) THF, (g,h) 1,4 dioxane, and (i,j) cyclohexane/dmf mixture (in space-fill representations) filling the voids along the *a*- and *c*-axes, respectively.

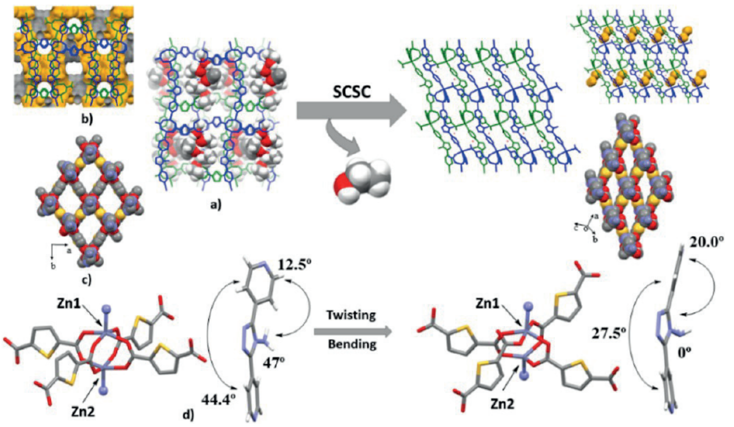

Figure 13. In response to guest removal, SCSC structural transformations between **2**-EtOH and guest-freed **2**-gf (a) along the *a*-axis, (b) potential void space visualized by yellow/gray (outer/inner) colors with two interpenetrated frameworks in blue and green, (c) a view demonstrating structural transformation when viewed along the pillar (bpt)-axis, and (d) illustration of changes in the coordination geometry of Zn^{II} nodes and bpt different angles.

of **2**-cyclohexane, wherein only partial exchange of dmf molecules resulted in a solvent mixture of dmf and cyclohexane in a 1:2 ratio, somewhat more steric crowding, and imperfect molecular packing occurs between solvent molecules that are mismatching in their size, shape, and interaction properties. Collectively, favorable framework−solvent interactions (N−H···O) and the steric hindrance imparted by solvent molecules are likely the underlying reason for the relatively larger void observed in **2**-cyclohexane. Overall, it is apparent that the pore structure is adaptive in the sense that it can accommodate various solvent guests without losing the structural integrity and crystallinity of the resulting frameworks (Figures 12 and S5).

3.3. Single-Crystal-to-Single-Crystal Guest Removal.

The observed structural changes with retained crystallinity on the solvent exchange process prompted us to explore whether crystal structure could be obtained for a solvent-free framework. Structure determination was attempted with a desolvated framework of **2**-EtOH, in which single crystals were kept at 110 °C in vacuo for 5 h. Upon visual inspection, the quality of the individual crystals was lowered significantly due to the desolvation process. Nevertheless, with few attempts, a crystal with bearable quality resulted in a data set sufficient for structure determination (see the Supporting Information).

The guest-freed crystal structure **2**-gf was solved in triclinic space group $P\bar{1}$ symmetry with two Zn^{II}, one bpt ligand, two tdc^{2-} ligands, and one water molecule in an AU. With a different symmetry, some ∼80% reduction in the unit-cell volume was observed compared to **2** (or **2**-EtOH). While the crystal structure of **2**-gf preserves the overall framework connectivity like in **2**, the network undergoes severe changes during the desolvation, contracting solvent-accessible voids to only 56 Å^3 (4.0%) with the transformation of the channels into discrete voids as shown in Figure 13. Accordingly, the diagonal dimensions of the channel changed from 12.71 × 16.17 Å (**2**-EtOH) to 10.50 × 16.67 Å, and the angles changed from 76.44 × 103.69° (**2**-EtOH) to 64.37 × 115.63°, joined with a considerable reduction of δ-angle from 65.6° (**2**-EtOH) to 36.7°, resulting in narrowing of the lozenge-shaped channels.

As evident in Figure 13, the coordination geometry of the zinc center changes dramatically. In contrast to the paddlewheel structure in **2**, the **2**-gf experiences a structural transition to the distorted paddle wheel. One Zn^{II} geometry remains in square pyramidal as in parent framework **2**, whereas the other zinc ion transforms toward distorted tetrahedral geometry with one of the bridging carboxylate groups being splintered to monodentate binding mode. Following this deformation, the ligated oxygen atoms try to enlarge their

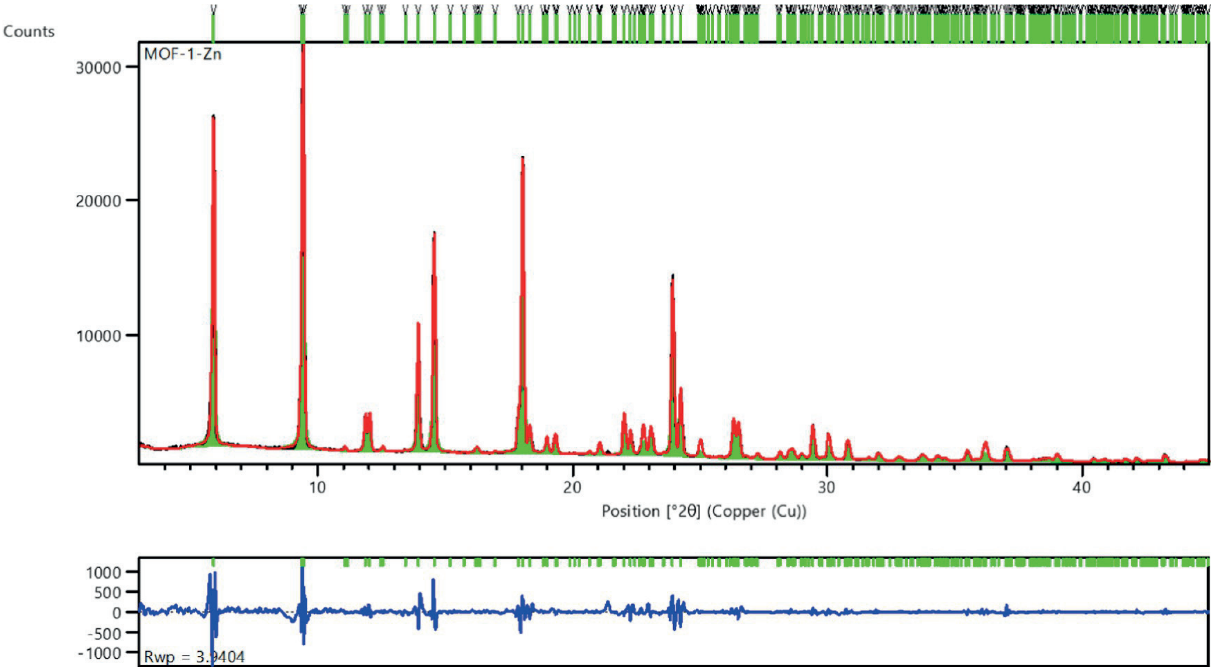

Figure 14. Pawley refinement plot of MOF-**1**-Zn. The experimental pattern is shown in black and the refined profile in red, whereas green colored markers on top correspond to characteristic Bragg peak positions of the refined unit cell of MOF-**1**-Zn. The difference plot of the experimental vs refined profile is shown below in blue.

mutual distances, having a significant distortion of adjacent ∠(O−Zn−O) bond angles. The distances for the cleaved bonds are 3.446(12) Å for *d*(Zn1−O25) and 6.014(12) for *d*(Zn2−O25), respectively. Concurrently, the two zinc atoms spacing inside the cluster changes with *d*(Zn−Zn) being 3.374(3) Å, which is markedly different from the "classical" paddlewheel unit (average 2.7 Å).[44] Somewhat similar behavior has been reported for the "classical" Zn-paddlewheel unit in case of the $Zn_2(bdc)_2L$ MOF (where L = 2,3-difluoro-1,4-bis(4-pyridyl)-benzene). The transition of the geometry from a square pyramidal to a tetrahedral geometry is accompanied by the change in *d*(Zn−Zn) from 3.00 Å (parent framework) to 3.43 Å (evacuated framework) during the "gate opening."[44,45]

In terms of structural properties, the plausible explanation for this alteration could be to compensate for the free space induced by the solvent removal, which then propagates to the bending of the strong metal−ligand bonds instead of bond cleavage.[46] By this, the **2**-gf undergoes extreme deformation, sequentially weakening and breaking one of the bonds in a bidentate carboxylic group. This deformation also leads to pillar tilting while preserving the periodic connectivity and movement of the two interpenetrated nets (Figure S6). Hence, these observations are indicative that the pillared-layer framework does not "collapse" during desolvation. Indeed, it adapts its structural conformations to minimize empty void space while maintaining its integrity as a 3D framework.

3.4. Powder X-ray Diffraction Methods.

The Pawley refinements were facilitated using the X́pert HighScore Plus program to examine the purity of the studied MOFs and to confirm the correspondence of the bulk powder structures by fitting the expected unit-cell dimensions obtained by the single-crystal structures to the measured PXRD patterns. The resulting crystallographic data are tabulated in Tables S7 and S8. As verified by SCXRD data, the PXRD patterns obtained for the prepared MOFs also confirm that all three MOFs possess different structures, which can be established by the obvious differences in the respective PXRD plots (Figure S7). The high phase purity of MOF-**1**-Zn was confirmed by the excellent fit with corresponding single crystal unit cell parameters (Figure 14). For MOF-**2**-Zn, the best Pawley fit was achieved using unit cell parameters of both MOF-**1**-Zn and MOF-**2**-Zn (approximately in equal weight fraction), as shown in Figure S8. Several attempts were made to isolate MOF-**2**-Zn as a pure phase. However, none of the synthesis strategies was fully successful, as MOF-**1**-Zn and MOF-**2**-Zn either coexisted (from dominant to minor) or MOF-**1**-Zn was the sole phase evident in the PXRD patterns (Figures S26 and S27). The PXRD pattern obtained for the MOF-**3**-Zn agreed well with the corresponding SCXRD data, indicating the high phase purity of the synthesis product (Figure S9).

For most solvent-exchanged samples analyzed, the Pawley fits suggested that bulk powder is structurally consistent with corresponding SCXRD data (Figures S10−S21). For example, after immersing the mixture in chloroform, only MOF-**2**-Zn was exchanged with chloroform, supported by the PXRD pattern corresponding to **2**-$CHCl_3$ and dmf containing MOF-**1**-Zn phases. Indeed, this was also reflected by our several failed attempts to exchange a range of solvents in an SCSC manner to MOF-**1**-Zn. For MOF-**1**-Zn, the polarity, particularly the solvent size, plays an essential role in dictating the success or failure of the solvent exchange in the case of pure MOF-**1**-Zn phase. As shown by the crystal structure, dmf molecules are somewhat locked in the pore structure and are hydrogen bonded to the NH_2 group, which may limit their removal, as discussed above. After several attempts, we could

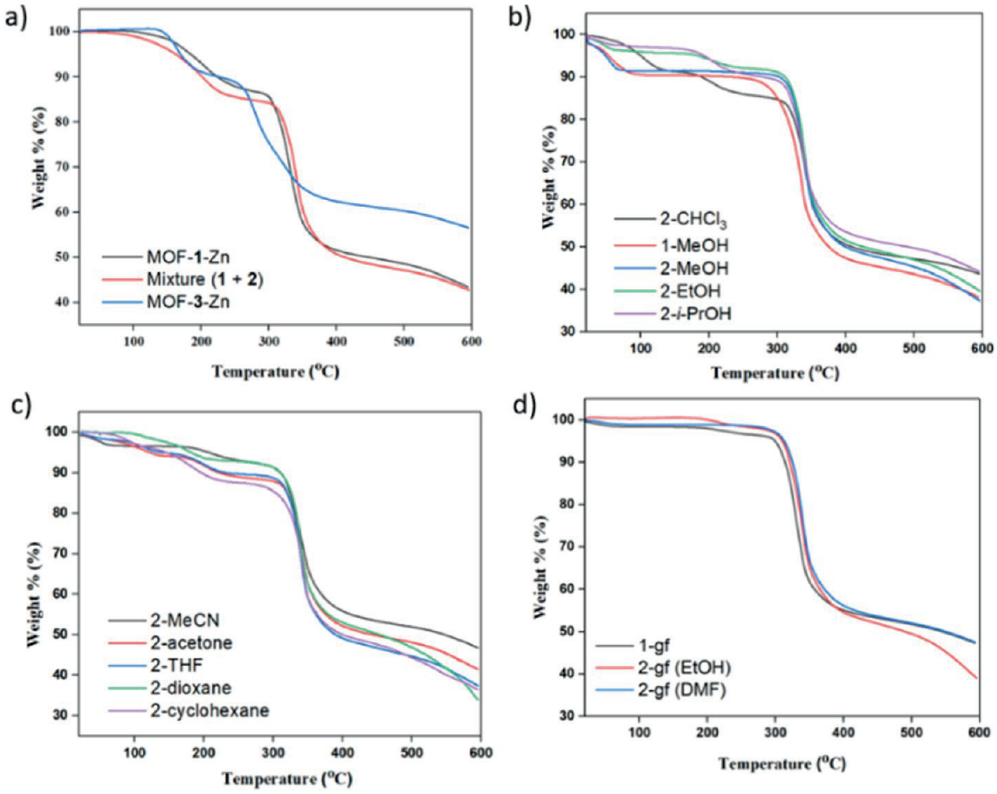

Figure 15. (a) TG curves of the MOF-**1**-Zn (black), phase mixture (MOF-**1**-Zn + MOF-**2**-Zn, red), and MOF-**3**-Zn (blue), (b) TG curves of the MOF-**1**-Zn exposed to MeOH, and phase mixture exposed to chloroform and alcohols, **2**-$CHCl_3$ (black), **1**-MeOH (red); and in case of polar protic solvents: **2**-MeOH (blue), **2**-EtOH (green), **2**-*i*-PrOH (purple), (c) TG curves of the phase mixture exposed to polar aprotic and nonpolar solvents: **2**-MeCN (black), **2**-acetone (red), **2**-THF (blue), **2**-dioxane (green), and **2**-cyclohexane (purple), and (d) TG curves of the partially desolvated MOF-**1**-Zn and phase mixture, guest-freed **1**-gf (black), guest-freed **2**-gf (EtOH, red), and guest-freed **2**-gf (dmf, blue).

successfully determine the single crystal structure for partially exchanged dmf with MeOH molecules. The obtained **1**-MeOH structure shows a rather disordered mixture of dmf and MeOH, which was also confirmed by the thermogravimetric analysis. The Pawley refinement plot for **1**-MeOH is shown in Figure S21. It can also be noted that the Pawley refinement of the PXRD pattern corresponding to **2**-MeOH bulk powder is in excellent agreement with SCXRD data of both **2**-MeOH and **1**-MeOH structures. This further proves that MOF-**1**-Zn undergoes at least partial solvent exchange when exposed to MeOH, as shown in Figure S11.

Pawley analyses of both **2**-EtOH and **2**-*i*-PrOH were consistent with unit-cell dimensions determined for corresponding SCXRD structures. Likewise, similar results were observed for all the polar aprotic and nonpolar solvents (Figures S14−S18), except for **2**-MeCN, which showed a couple of unindexed diffraction peaks in the fit, suggesting the presence of some minor unknown phase (Figure S14).

In the case of various guest-freed samples analyzed by PXRD, it is clearly seen that the **2**-EtOH sample heated at 110 °C for 5 h under vacuo (or phase mixture heated at 180 °C overnight under vacuo) shows no signs of degradation, implying that MOFs remains intact even after being subjected to high-temperature heating for extended hours. However, after the desolvation process, both examples still contained some dmf, indicating that it is challenging to remove from the pore structure of MOF-**1**-Zn. For the solvated and solvent-evacuated PXRD patterns, the refined unit-cell parameters of PXRD and SCXRD data are tabulated in Tables S7 and S8, suggesting that subtle changes in unit-cell dimensions originate from the framework flexibility.

3.5. Thermogravimetry. The thermal stability of studied materials was evaluated using thermogravimetric analyses at 10 °C min^{-1} under a N_2 flow. All pillared-layer MOFs and the products from solvent exchange tests were analyzed using this method. Representative TG runs for MOF-**1**-Zn, phase mixture, and MOF-**3**-Zn are demonstrated in Figure 15. The determined onset decomposition temperatures for the studied MOFs appear <310 °C and can be arranged in the following series: MOF-**3**-Zn (257.25 °C) < MOF-**1**-Zn (298.38 °C) < phase mixture (309.84 °C). MOF-**1**-Zn starts to lose weight between ~84 and 282 °C, demonstrating a weight loss of 13.54 wt % (calcd. 13.36%) assigned to releasing dmf trapped in the pores. However, the phase mixture sample and MOF-**3**-Zn loss dmf between ~70−269 and 120−247 °C corresponding to weight losses of 14.70 wt % (calcd. 15.63%) for the phase mixture (assuming a 1:1 ratio), and 11.61 wt % (calcd. 12.93%) for MOF-**3**-Zn, respectively. Above the given temperatures, gradual weight loss can be seen, seemingly involving the breakdown of organic moieties. The loss of solvent up to the temperature of 282 °C (bp of dmf 153° vs 282 °C for its desolvation) in the case of the MOF-**1**-Zn confirms the strong interaction of dmf with the framework as mentioned above.

Table 1. CO_2 Adsorption Experimental Conditions and the Measured Capacities

experiment	c_{CO_2} (vol %)	T_{ads} (°C)	T_{des} (°C)	$q_{CO_2,ads}$ ($mmol_{CO_2}$/g)	$q_{CO_2,des}$ ($mmol_{CO_2}$/g)
MOF-**1**-Zn	0.04	12	100	0.01 ± 0.00	0.00 ± 0.00
MOF-**1**-Zn	0.4	12	100	0.04 ± 0.00	0.05 ± 0.00
MOF-**1**-Zn	15	12	100	0.18 ± 0.11	0.16 ± 0.01[a]
phase mixture, cycle 1	15	12	100	0.24 ± 0.14	0.13 ± 0.00[a]
phase mixture, cycle 2	15	12	100	0.33 ± 0.19	0.17 ± 0.01[a]
phase mixture, cycle 3	15	12	100	0.88 ± 0.52	0.17 ± 0.01[a]

[a] Measured with ppm-scale sensor, thus omitting possible CO_2 desorption at concentrations above 5000 ppm.

As mentioned earlier, the solvent exchange tests were made using phase mixture samples, and considering the complexity of solvates included (guest solvent, dmf, and water impurities in some cases), it is not straightforward to calculate the correct ratios of solvents trapped inside the frameworks. However, for the comparison, the detailed wt. losses (%) observed in the respective temperature range are shown in Table S10 for all the samples. Typically, solvent-exchanged phase mixture samples demonstrate weight loss covering the region ∼22−150 °C, varying by the type of the solvent and by the host−guest-related physicochemical properties prevailing in the solvated structures (more details in the Supporting Information). For instance, in **2**-$CHCl_3$, the loss of solvents proceeds in two steps, the first being from room temperature to ∼142 °C (bp of $CHCl_3$ = 61.2 °C), representing the release of $CHCl_3$ from MOF-**2**-Zn phase. The second step extends to ∼274 °C, indicating the gradual release of dmf from the MOF-**1**-Zn phase. Thermal decomposition of the phase mixture starts above ∼307 °C (Figure 15).

Thermogravimetric analyses were also made for the solvent-freed samples (Figure 15). For the vacuo evacuated **1**-MeOH (**1**-gf), the curve is practically unchanged until ∼187−268 °C, wherein modest weight loss indicates the removal of residual amounts of dmf molecules followed by initiation of thermal decomposition above 296 °C. The **2**-gf sample afforded from the evacuation of **2**-EtOH (5 h at 110 °C) shows 2.37% mass loss at 187−275 °C corresponding to the removal of dmf from the channels, indicating incomplete exchange of dmf to EtOH, as verified by the PXRD results. However, the second **2**-gf (overnight under vacuo at 180 °C) sample remained stable until 230 °C, beyond which decomposition gradually started. Based on the PXRD analyses, the sample still contains residual amounts of pristine MOF-**1**-Zn with dmf, which gradually releases the remaining dmf prior to the decomposition at ∼301 °C (Table S10).

3.6. CO_2 Adsorption Studies. Based on the literature, incorporating thiophene moieties in the MOFs has enhanced CO_2 and improved CO_2/N_2 adsorption selectivity owing to the induced dipole interactions.[23,47] Hence, we hypothesize that the available pendant NH_2 group of the bpt ligand might be capable of interacting with quadrupolar CO_2. In addition, channels decorated with polarizable sulfur atoms realized in these MOFs may bind CO_2 via an induced dipole interaction. Therefore, considering these framework−CO_2 interactions that may prove beneficial in CO_2 sorption experiments, we carried out the CO_2 adsorption tests using a custom-built fixed-bed adsorption/desorption device under dry 400, 4000 ppm, and 15% CO_2 balanced with N_2 (more details in the Methods).

However, the experimental CO_2 adsorption capacities measured for both samples were relatively low, as shown in Table 1. In the ultradilute region, CO_2 adsorption on MOF-**1**-Zn is nearly negligible, resulting in only around 0.04−0.05 $mmol_{CO_2}/g_{MOF}$ at 4000 ppm, while at 400 ppm, the measured capacities were close to zero. At 15% CO_2, around 0.2 $mmol_{CO_2}/g_{MOF}$ is measured in adsorption and desorption phases for the pure MOF-**1**-Zn. Based on the above observations, only 15% CO_2 condition was tested for the phase mixture samples. With three repeats made for the phase mixture samples, CO_2 adsorptions ranged from around 0.2 up to 0.9 $mmol_{CO_2}/g_{MOF}$, imparting that the %-scale measurement had a high uncertainty. However, the desorption results for the MOF-**1**-Zn and the phase mixture are comparable, although the possibility of unaccounted CO_2 desorption should be considered, as mentioned in the Methods section. Indeed, the main reason for the high uncertainty in the %-scale measurements was the small amount of sample combined with the low adsorption capacity of the samples, which is why the response curves with and without sample differed only slightly, as shown in Figure 16.

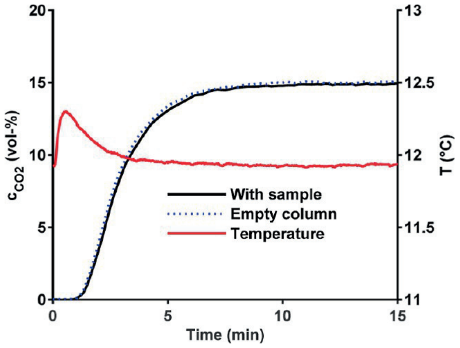

Figure 16. Adsorption breakthrough data using 15% CO_2 on MOF-**1**-Zn.

These results suggest that the samples do not host a significant CO_2 adsorption performance in postcombustion capture (PCC) conditions, let alone in direct air capture conditions. Presumably, this might be associated with a shrunk framework after solvent evacuation, resulting in severe channel contraction that could hamper CO_2 diffusion. It is worth noting that these tests were conducted below room temperature (12 °C), though this temperature is not relevant for the PCC scenario. Likely, the CO_2 uptakes are expected to be even lower at higher temperatures since the adsorption-based process is exothermic, and CO_2 uptake reduces at elevated temperatures. However, to properly characterize the CO_2 adsorption performance of the samples, a larger amount of measurement points at higher partial pressures should be conducted at different temperatures. This is especially true for the pressure-swing adsorption application of flexible MOFs, which may have steep isotherm shapes at certain partial pressure ranges.[23,41]

4. CONCLUSIONS

In conclusion, three new mixed-ligand MOFs from identical components have been synthesized and structurally characterized. The resulting interpenetrated 3D MOFs exhibit different coordination environments around the Zn node, ranging from trigonal bipyramidal and square pyramidal to octahedral. Additionally, various binding modes were observed for the thiophene carboxylate ligand, including monodentate, bidentate, and bridge binding modes. Interestingly, structural variations associated with network topologies, and in turn intermolecular and intramolecular interactions, manifested significant differences between the MOFs, for instance, in forms of void spaces (varying from ∼23 to 35%) and solvent-exchange properties being robust for MOF-**2**-Zn structure type but severely restricted in MOF-**1**-Zn.

We further elaborated that pillared-layer MOF-**2**-Zn, entailing elastic paddlewheel building units, which readily undergoes single-crystal-to-single-crystal transformation upon guest exchange of dmf solvent with chloroform and eight other solvents of distinct kinetic diameters and different polarities, including polar protic and aprotic, as well as nonpolar solvents. Intriguing structural peculiarities in the frameworks were realized through molecular conformations of the pillar and distortion at the metal-carboxylate junction.

Interestingly, the SCXRD studies revealed that the integration of MeOH into the channels subtly directs the orientation of the NH_2-triazole core, favoring guest−guest, host−host (adjacent H-bond acceptors on the thiophene carboxylates), and host−guest interactions with the solvent guest. Additionally, the mutual effect of steric hindrance and weak interactions imposed by relatively larger solvents leads to the tilting of pyridyl rings and a less favored orientation of the triazole core. MOF-**2**-Zn showed a specific differentiation between polar and nonpolar solvents, indicating the clearest evidence of host−guest interactions. Altogether, upon different guest solvent exchanges, we observed that the void space adapts depending on the solvent type via the framework's flexibility.

Furthermore, we illustrated how, in the guest release process, a SCSC transformation takes place. In the case of solvent-emptied MOF (e.g., **2**-EtOH to **2**-gf), the structure had undergone severe contraction during the evacuation, showing significantly diminished solvent-accessible voids and transforming the channels into discrete voids. The structural changes are attributed to the variation of alterations such as deformation in paddlewheel moiety, the transformation of channel shape and sizes, and the closer proximity of two interpenetrated nets. This is a notable example showing the fragility of $\{Zn_2\}$-“paddlewheel” triggered by MOF solvent evacuation. More importantly, we demonstrate that the pillared-layer framework sustains its crystallinity and 3D networked structure under vacuum and heating-assisted desolvation.

Overall, a detailed picture of the different framework−guest interactions was accomplished via SCXRD, PXRD, and TG analyses, providing meaningful insights into a system that behaves adaptively while illustrating subtle structural transformations induced by the solvent molecules. The key properties demonstrated in this study are desirable in applications that depend on understanding how MOFs respond to external stimuli, like molecular sensing, catalysis, and separation. It is anticipated that the presented results will not only broaden the knowledge of structural isomers in MOF synthesis but also foster the understanding of delicate host−guest chemistry that plays a critical role in MOF changing its geometrical features.

■ ASSOCIATED CONTENT

Supporting Information

The Supporting Information is available free of charge at https://pubs.acs.org/doi/10.1021/acs.cgd.3c01172.

> Material syntheses; crystallographic data; H-bonding scheme and topological representation of MOF-3-Zn; description of the crystal structure of 2-$CHCl_3$; physical properties of guest-exchanged solvents; H-bonding scheme in 2-MeOH; the comparison of the dihedral angle between the Zn-carboxylate and the thiophene plane between the SCSC guest exchange complexes; illustration of solvent molecules in **2**-MeOH, **2**-EtOH, and **2**-*i*-PrOH; interpenetrated frameworks of **2**-EtOH and guest-freed **2**-gf; comparative analysis of the structural differences between crystal structures; comparison of crystal data parameters between crystal structures; PXRD patterns and Pawley refinement plots; synthesis optimization and scale-up; summary of products obtained by altering metal-to-ligand ratios and concentrations; thermogravimetric results; FT-IR spectroscopy; and ToposPro output files for MOF-1-Zn, MOF-2-Zn, and MOF-3-Zn (PDF)

Accession Codes

CCDC 2279896−2279909 contain the supplementary crystallographic data for this paper. These data can be obtained free of charge via www.ccdc.cam.ac.uk/data_request/cif, or by emailing data_request@ccdc.cam.ac.uk, or by contacting The Cambridge Crystallographic Data Centre, 12 Union Road, Cambridge CB2 1EZ, UK; fax: +44 1223 336033.

CCDC 2279896−2279909 contains the supplementary crystallographic data for this paper. These data can be obtained free of charge via http://www.ccdc.cam.ac.uk/data_request/cif, or by emailing data_request@ccdc.cam.ac.uk, or by contacting The Cambridge Crystallographic Data Centre, 12 Union Road, Cambridge CB21EZ, UK; fax: + 44 1223 336033.

■ AUTHOR INFORMATION

Corresponding Author

Manu Lahtinen − *Department of Chemistry, University of Jyväskylä, FI-40014 Jyväskylän, Finland;* orcid.org/0000-0001-5561-3259; Email: manu.k.lahtinen@jyu.fi

Author

Shreya Mahajan − *Department of Chemistry, University of Jyväskylä, FI-40014 Jyväskylän, Finland*

Complete contact information is available at:
https://pubs.acs.org/10.1021/acs.cgd.3c01172

Notes

The authors declare no competing financial interest.

■ ACKNOWLEDGMENTS

The authors gratefully acknowledge Jere Elfving (Research Scientist at VTT Technical Research Centre of Finland) for conducting and analyzing the CO_2 adsorption tests and the meaningful suggestions contributing to the manuscript quality. This study was financially supported by the Academy of Finland (decision number 329314) and the University of Jyväskylä.

■ REFERENCES

(1) Senkovska, I.; Bon, V.; Abylgazina, L.; Mendt, M.; Berger, J.; Kieslich, G.; Petkov, P.; Luiz Fiorio, J.; Joswig, J.; Heine, T.; Schaper, L.; Bachetzky, C.; Schmid, R.; Fischer, R. A.; Pöppl, A.; Brunner, E.; Kaskel, S. Understanding MOF Flexibility: An Analysis Focused on Pillared Layer MOFs as a Model System. *Angew. Chem., Int. Ed.* **2023**, *62* (33), No. e202218076.

(2) Dong, J.; Wee, V.; Zhao, D. Stimuli-Responsive Metal-Organic Frameworks Enabled by Intrinsic Molecular Motion. *Nat. Mater.* **2022**, *21* (12), 1334−1340.

(3) Mahajan, S.; Lahtinen, M. Recent Progress in Metal-Organic Frameworks (MOFs) for CO_2 Capture at Different Pressures. *J. Environ. Chem. Eng.* **2022**, *10* (6), 108930.

(4) Bavykina, A.; Kolobov, N.; Khan, I. S.; Bau, J. A.; Ramirez, A.; Gascon, J. Metal-Organic Frameworks in Heterogeneous Catalysis: Recent Progress, New Trends, and Future Perspectives. *Chem. Rev.* **2020**, *120* (16), 8468−8535.

(5) Lawson, H. D.; Walton, S. P.; Chan, C. Metal-Organic Frameworks for Drug Delivery: A Design Perspective. *ACS Appl. Mater. Interfaces* **2021**, *13* (6), 7004−7020.

(6) Nalaparaju, A.; Jiang, J. Metal-Organic Frameworks for Liquid Phase Applications. *Adv. Sci.* **2021**, *8* (5), 2003143.

(7) Kreno, L. E.; Leong, K.; Farha, O. K.; Allendorf, M.; Van Duyne, R. P.; Hupp, J. T. Metal-Organic Framework Materials as Chemical Sensors. *Chem. Rev.* **2012**, *112* (2), 1105−1125.

(8) Li, X.; Liu, Y.; Wang, J.; Gascon, J.; Li, J.; Van der Bruggen, B. Metal-Organic Frameworks Based Membranes for Liquid Separation. *Chem. Soc. Rev.* **2017**, *46* (23), 7124−7144.

(9) Morris, R. E.; Brammer, L. Coordination Change, Lability and Hemilability in Metal-Organic Frameworks. *Chem. Soc. Rev.* **2017**, *46* (17), 5444−5462.

(10) Chen, Y.; Idrees, K. B.; Son, F. A.; Wang, X.; Chen, Z.; Xia, Q.; Li, Z.; Zhang, X.; Farha, O. K. Tuning the Structural Flexibility for Multi-Responsive Gas Sorption in Isonicotinate-Based Metal-Organic Frameworks. *ACS Appl. Mater. Interfaces* **2021**, *13* (14), 16820−16827.

(11) Zhang, J.-P.; Liao, P.-Q.; Zhou, H.-L.; Lin, R.-B.; Chen, X.-M. Single-Crystal X-Ray Diffraction Studies on Structural Transformations of Porous Coordination Polymers. *Chem. Soc. Rev.* **2014**, *43* (16), 5789−5814.

(12) Grape, E. S.; Xu, H.; Cheung, O.; Calmels, M.; Zhao, J.; Dejoie, C.; Proserpio, D. M.; Zou, X.; Inge, A. K. Breathing Metal-Organic Framework Based on Flexible Inorganic Building Units. *Cryst. Growth Des.* **2020**, *20* (1), 320−329.

(13) Wang, S.-Q.; Mukherjee, S.; Zaworotko, M. J. Spiers Memorial Lecture: Coordination Networks That Switch between Nonporous and Porous Structures: An Emerging Class of Soft Porous Crystals. *Faraday Discuss.* **2021**, *231*, 9−50.

(14) Schneemann, A.; Bon, V.; Schwedler, I.; Senkovska, I.; Kaskel, S.; Fischer, R. A. Flexible Metal-Organic Frameworks. *Chem. Soc. Rev.* **2014**, *43* (16), 6062−6096.

(15) Wang, H.; Warren, M.; Jagiello, J.; Jensen, S.; Ghose, S. K.; Tan, K.; Yu, L.; Emge, T. J.; Thonhauser, T.; Li, J. Crystallizing Atomic Xenon in a Flexible MOF to Probe and Understand Its Temperature-Dependent Breathing Behavior and Unusual Gas Adsorption Phenomenon. *J. Am. Chem. Soc.* **2020**, *142* (47), 20088−20097.

(16) Ding, B.; Wang, Y. Y.; Liu, S. X.; Wu, X. X.; Zhu, Z. Z.; Huo, J. Z.; Liu, Y. Y. A Series of Multi-Dimensional Metal-Organic Frameworks with trans-4,4′-Azo-1,2,4-Triazole: Polymorphism, Guest Induced Single-Crystal-to-Single-Crystal Transformation and Solvatochromism. *CrystEngComm* **2015**, *17* (29), 5396−5409.

(17) Ju, H.; Habata, Y.; Lee, S. S. Temperature-Dependent Supramolecular Isomeric Zn(II)-Metal-Organic Frameworks and Their Guest Exchange. *Cryst. Growth Des.* **2020**, *20* (7), 4640−4648.

(18) Manos, M. J.; Kyprianidou, E. J.; Papaefstathiou, G. S.; Tasiopoulos, A. J. Insertion of Functional Groups into a Nd^{3+} Metal-Organic Framework via Single-Crystal-to-Single-Crystal Coordinating Solvent Exchange. *Inorg. Chem.* **2012**, *51* (11), 6308−6314.

(19) Mahajan, S.; Marttinen, A.; Forsblom, S.; Lahtinen, M. Inorganic Anion-Mediated Supramolecular Entities of 4-Amino-3,5-Bis(4-Pyridyl)-1,2,4-Triazole Salts Assisted by the Interplay of Noncovalent Interactions. *Cryst. Growth Des.* **2023**, *23* (7), 5144−5162.

(20) Goswami, R.; Mandal, S. C.; Seal, N.; Pathak, B.; Neogi, S. Antibiotic-Triggered Reversible Luminescence Switching in Amine-Grafted Mixed-Linker MOF: Exceptional Turn-on and Ultrafast Nanomolar Detection of Sulfadiazine and Adenosine Monophosphate with Molecular Keypad Lock Functionality. *J. Mater. Chem. A* **2019**, *7* (33), 19471−19484.

(21) Lee, L.-W.; Kao, Y.-C.; Chung, M.-Y.; Chang, B.-C.; Lee, G.-H.; Peng, S.-M.; Wang, C.-M.; Liu, Y.-H.; Lee, S.-L.; Lu, K.-L. Rare Metal-Ion Metathesis of a Tetrahedral Zn(II) Core of a Noncentrosymmetric (3,4)-Connected 3D MOF. *Dalton Trans.* **2019**, *48* (6), 1950−1954.

(22) Qin, B.; Zhang, X.; Zhang, J. A New Multifunctional Zinc-Organic Framework with Rare Interpenetrated Tripillared Bilayers as a Luminescent Probe for Detecting Ni^{2+} and PO_4^{3-} in Water. *Cryst. Growth Des.* **2020**, *20* (8), 5120−5128.

(23) Shi, Y.-X.; Li, W.-X.; Zhang, W.-H.; Lang, J.-P. Guest-Induced Switchable Breathing Behavior in a Flexible Metal-Organic Framework with Pronounced Negative Gas Pressure. *Inorg. Chem.* **2018**, *57* (14), 8627−8633.

(24) *CrysAlisPRO*; Oxford Diffraction/Agilent Technologies UK Ltd: Yarnton, England.

(25) Sheldrick, G. M. SHELXT - Integrated Space-Group and Crystal-Structure Determination. *Acta Crystallogr., Sect. A* **2015**, *71* (1), 3−8.

(26) Dolomanov, O. V.; Bourhis, L. J.; Gildea, R. J.; Howard, J. A. K.; Puschmann, H. OLEX2: A Complete Structure Solution, Refinement and Analysis Program. *J. Appl. Crystallogr.* **2009**, *42* (2), 339−341.

(27) Sheldrick, G. M. Crystal Structure Refinement with SHELXL. *Acta Crystallogr., Sect. C: Struct. Chem.* **2015**, *71*, 3−8.

(28) Macrae, C. F.; Sovago, I.; Cottrell, S. J.; Galek, P. T. A.; McCabe, P.; Pidcock, E.; Platings, M.; Shields, G. P.; Stevens, J. S.; Towler, M.; Wood, P. A. Mercury 4.0: From Visualization to Analysis, Design and Prediction. *J. Appl. Crystallogr.* **2020**, *53* (1), 226−235.

(29) Degen, T.; Sadki, M.; Bron, E.; König, U.; Nénert, G. The HighScore Suite. *Powder Diffr.* **2014**, *29*, S13−S18.

(30) Pawley, G. S. Unit-Cell Refinement from Powder Diffraction Scans. *J. Appl. Crystallogr.* **1981**, *14* (6), 357−361.

(31) Elfving, J.; Sainio, T. Kinetic Approach to Modelling CO_2 Adsorption from Humid Air Using Amine-Functionalized Resin: Equilibrium Isotherms and Column Dynamics. *Chem. Eng. Sci.* **2021**, *246*, 116885.

(32) Elfving, J.; Kauppinen, J.; Jegoroff, M.; Ruuskanen, V.; Järvinen, L.; Sainio, T. Experimental Comparison of Regeneration Methods for CO_2 Concentration from Air Using Amine-Based Adsorbent. *Chem. Eng. J.* **2021**, *404*, 126337.

(33) Elfving, J. Direct Capture of CO_2 from Air Using Amine-Functionalized Resin-Effect of Humidity in Modelling and Evaluation of Process Concepts. Ph.D. Dissertation, Lappeenranta-Lahti University of Technology LUT, 2021. https://lutpub.lut.fi/handle/10024/163524 (accessed Aug 10, 2023).

(34) Alzahrani, K. A. H.; Deeth, R. J. Density Functional Calculations Reveal a Flexible Version of the Copper Paddlewheel Unit: Implications for Metal Organic Frameworks. *Dalton Trans.* **2016**, *45* (30), 11944−11948.

(35) Bureekaew, S.; Amirjalayer, S.; Schmid, R. Orbital Directing Effects in Copper and Zinc Based Paddle-Wheel Metal Organic

Frameworks: The Origin of Flexibility. *J. Mater. Chem.* **2012**, *22* (20), 10249−10254.

(36) Blatov, V. A.; Shevchenko, A. P.; Proserpio, D. M. Applied Topological Analysis of Crystal Structures with the Program Package ToposPro. *Cryst. Growth Des.* **2014**, *14* (7), 3576−3586.

(37) Dybtsev, D. N.; Chun, H.; Kim, K. Rigid and Flexible: A Highly Porous Metal-Organic Framework with Unusual Guest-Dependent Dynamic Behavior. *Angew. Chem., Int. Ed.* **2004**, *43* (38), 5033−5036.

(38) Henke, S.; Schneemann, A.; Wütscher, A.; Fischer, R. A. Directing the Breathing Behavior of Pillared-Layered Metal-Organic Frameworks via a Systematic Library of Functionalized Linkers Bearing Flexible Substituents. *J. Am. Chem. Soc.* **2012**, *134* (22), 9464−9474.

(39) Zhu, A.-X.; Yang, Q.-Y.; Kumar, A.; Crowley, C.; Mukherjee, S.; Chen, K.-J.; Wang, S.-Q.; O'Nolan, D.; Shivanna, M.; Zaworotko, M. J. Coordination Network That Reversibly Switches between Two Nonporous Polymorphs and a High Surface Area Porous Phase. *J. Am. Chem. Soc.* **2018**, *140* (46), 15572−15576.

(40) Song, B.-Q.; Yang, Q.-Y.; Wang, S.-Q.; Vandichel, M.; Kumar, A.; Crowley, C.; Kumar, N.; Deng, C.-H.; GasconPerez, V.; Lusi, M.; Wu, H.; Zhou, W.; Zaworotko, M. J. Reversible Switching between Nonporous and Porous Phases of a New SIFSIX Coordination Network Induced by a Flexible Linker Ligand. *J. Am. Chem. Soc.* **2020**, *142* (15), 6896−6901.

(41) Yang, Q.; Lama, P.; Sen, S.; Lusi, M.; Chen, K.; Gao, W.; Shivanna, M.; Pham, T.; Hosono, N.; Kusaka, S.; Perry, J. J.; Ma, S.; Space, B.; Barbour, L. J.; Kitagawa, S.; Zaworotko, M. J. Reversible Switching between Highly Porous and Nonporous Phases of an Interpenetrated Diamondoid Coordination Network That Exhibits Gate Opening at Methane Storage Pressures. *Angew. Chem., Int. Ed.* **2018**, *57* (20), 5684−5689.

(42) Reichardt, C. Solvatochromic Dyes as Solvent Polarity Indicators. *Chem. Rev.* **1994**, *94* (8), 2319−2358.

(43) de J Velásquez-Hernández, M.; López-Cervantes, V. B.; Martínez-Ahumada, E.; Tu, M.; Hernández-Balderas, U.; Martínez-Otero, D.; Williams, D. R.; Martis, V.; Sánchez-González, E.; Chang, J.-S.; Lee, J. S.; Balmaseda, J.; Ameloot, R.; Ibarra, I. A.; Jancik, V. CCIQS-1: A Dynamic Metal-Organic Framework with Selective Guest-Triggered Porosity Switching. *Chem. Mater.* **2022**, *34* (2), 669−677.

(44) Bon, V.; Senkovska, I.; Wallacher, D.; Többens, D. M.; Zizak, I.; Feyerherm, R.; Mueller, U.; Kaskel, S. In Situ Observation of Gating Phenomena in the Flexible Porous Coordination Polymer $Zn_2(BPnDC)_2(Bpy)$ (SNU-9) in a Combined Diffraction and Gas Adsorption Experiment. *Inorg. Chem.* **2014**, *53* (3), 1513−1520.

(45) Seo, J.; Bonneau, C.; Matsuda, R.; Takata, M.; Kitagawa, S. Soft Secondary Building Unit: Dynamic Bond Rearrangement on Multinuclear Core of Porous Coordination Polymers in Gas Media. *J. Am. Chem. Soc.* **2011**, *133* (23), 9005−9013.

(46) Aggarwal, H.; Bhatt, P. M.; Bezuidenhout, C. X.; Barbour, L. J. Direct Evidence for Single-Crystal to Single-Crystal Switching of Degree of Interpenetration in a Metal-Organic Framework. *J. Am. Chem. Soc.* **2014**, *136* (10), 3776−3779.

(47) Bolotov, V. A.; Kovalenko, K. A.; Samsonenko, D. G.; Han, X.; Zhang, X.; Smith, G. L.; MCormick, L. J.; Teat, S. J.; Yang, S.; Lennox, M. J.; Henley, A.; Besley, E.; Fedin, V. P.; Dybtsev, D. N.; Schröder, M. Enhancement of CO_2 Uptake and Selectivity in a Metal-Organic Framework by the Incorporation of Thiophene Functionality. *Inorg. Chem.* **2018**, *57* (9), 5074−5082.

III

EVALUATING THE VIABILITY OF ETHYLENEDIAMINE-FUNCTIONALIZED MG-MOF-74 IN DIRECT AIR CAPTURE: THE CHALLENGES OF STABILITY AND SLOW ADSORPTION RATE

by

Mahajan, S.; Elfving, J.; Lahtinen, M. 2024

Journal of Environmental Chemical Engineering, 12(2), 112193

https://doi.org/10.1016/j.jece.2024.112193

Journal of Environmental Chemical Engineering 12 (2024) 112193

Contents lists available at ScienceDirect

Journal of Environmental Chemical Engineering

journal homepage: www.elsevier.com/locate/jece

Evaluating the viability of ethylenediamine-functionalized Mg-MOF-74 in direct air capture: The challenges of stability and slow adsorption rate

Shreya Mahajan[a], Jere Elfving[b], Manu Lahtinen[a,*]

[a] Department of Chemistry, University of Jyväskylä, P.O. Box 35, FI-40014 Jyväskylä, Finland
[b] VTT Technical Research Centre of Finland Ltd., Koivurannantie 1, FI-40101 Jyväskylä, Finland

ARTICLE INFO

Keywords:
Direct air capture
CO_2 adsorption
Metal-organic framework

ABSTRACT

Carbon removal technologies, such as direct air capture (DAC), hold great potential in mitigating anthropogenic CO_2 emissions. Amine-tethered metal-organic frameworks (MOFs) that capture CO_2 selectively *via* chemisorption have been highlighted as frontrunners for CO_2 removal technologies. To this end, ethylenediamine (ED) was employed to decorate the metal sites of Mg-MOF-74, and both bare and amine-modified frameworks were thoroughly characterized and studied for DAC using an automated fixed-bed sorption device. The material exhibited a promising CO_2 capacity of up to 1.8 mmol/g from 400 ppmv CO_2 in humid conditions, although the amount of adsorbed H_2O was several times higher. The highest adsorption capacities were measured at 25–35 °C, while decreased capacity was observed at 12 °C due to slower adsorption rate. In dry cyclic adsorption-desorption tests, the cyclic CO_2 capacity reduced slightly in 18 cycles. However, at 2 vol% humidity, the capacity dropped rapidly over successive cycles, revealing poor hydrolytic stability. Preliminary coating experiments were conducted on stainless steel plates and cordierite monoliths, suggesting that reasonably even coating layers could be achieved on these substrates with relatively simple coating techniques. High water adsorption, slow adsorption rate at low temperatures, and the rapid cyclic capacity decrease in humid conditions may limit the application of the studied adsorbent for DAC. The vital aspects of the real application of MOFs in DAC, such as adsorption kinetics and stability in humid conditions, are rarely explored in detail in the literature, and these results indicate that these aspects warrant extensive study for the development of practically applicable DAC adsorbents.

1. Introduction

The average global temperature has already risen by 1 °C (relative to pre-industrial levels), and it is projected to reach 1.5 °C within the next decade, amplifying the risk of surpassing 2 °C. The approach to limiting the temperature rise is to reduce emissions while, in parallel, implementing the negative emissions on a multi-Gt/y scale of CO_2. These negative emission technologies (NETs) [1] accelerate the removal of already released CO_2 and come in various types, for example, biochar (BC), afforestation and reforestation (AR), bioenergy with carbon capture and storage (BECCS), and direct air capture (DAC) in conjunction with carbon storage, to name a few [2]. Three of these NETs employ photosynthesis to capture CO_2 from the air, while DAC extracts atmospheric CO_2 using physicochemical processes (including solvents or solid adsorbents) [3,4]. Of all the NETs, DAC is particularly advantageous due to its smaller land requirement and significantly lower water usage, [5] albeit it still needs further technological development to be fully realized [6].

In direct air capture, atmospheric air is typically blown through a contactor containing the CO_2-capturing material until the desired saturation is achieved. After the capture step, the CO_2-capturing material is regenerated, typically with heat, to produce high-concentration CO_2, which can be compressed, reliably stored, or utilized [7–9]. Among an array of CO_2-capturing materials, a high volume of research has been conducted on amine-modified porous solids, which are made by combining amines with support materials such as silica, carbon, alumina, and porous polymers [10–14]. In principle, these adsorbents are highly recognized for their relatively enhanced adsorption and favorable single-gas selectivity among other CO_2-capturing materials, even at low concentrations and in the presence of moisture. Compared to solvent-based DAC [7], using amine-adsorbents enables a relatively simple temperature-vacuum swing adsorption (TVSA) DAC process

---

* Corresponding author.
E-mail address: manu.k.lahtinen@jyu.fi (M. Lahtinen).

https://doi.org/10.1016/j.jece.2024.112193
Received 12 October 2023; Received in revised form 20 December 2023; Accepted 9 February 2024

where the adsorbent can be regenerated only at around 80–100 °C [8,9].

Unfortunately, amine-functionalized sorbents often incur severe challenges that hamper their applicability for DAC. These can be related to CO_2 capacity, adsorption/desorption kinetics, regenerability, and cyclic stability under varying atmospheric conditions. A combination of sub-optimal parameters or one undesirable characteristic, such as fast degradation over repeated adsorption/desorption cycles [15], can render a CO_2 sorbent practically useless for CO_2 capture from air. Despite the drawbacks mentioned above, amine-based solid materials have been identified as a vital component in DAC technology. The supported molecular amines possess the ability to chemisorb low-concentration CO_2 from the atmospheric air, resulting in enhanced adsorption. Therefore, the prominent role of amines makes them a significant area of focus for atmospheric CO_2 capture.

Advanced porous hybrid materials called Metal-organic frameworks (MOFs) [10,16–19] are an emerging material group that holds tremendous promise in surmounting these challenges and have been highlighted as frontrunners for CO_2 capture technologies. Among the library of MOFs explored, the MOFs repleted with unsaturated or open metal sites (OMSs) on the surfaces of the pores have been revealed to be outstanding for gas adsorption and separation [18,19]. For instance, the pore size (~11 Å) and high density of OMSs within evacuated Mg-MOF-74 (Mg_2(dobdc), H_4dobdc = 2,5-dioxidobenzene-1,4-dicarboxylic acid; CPO-27-Mg) [20–24] lined along its 1D channels have enabled them to be exceedingly examined for CO_2 adsorption. Therefore, Mg-MOF-74 is one of the best-studied adsorbents for higher concentrations of CO_2 (10–15%) relevant to post-combustion capture [21]. Previous studies on M-dobdc series (M stands for a metal center, *i.e.*, M = Mg^{2+}, Ni^{2+}, Co^{2+}, Zn^{2+}) have demonstrated that these exposed metal cations engage strongly with incoming CO_2 because of its greater polarizability (29.1×10^{-25} cm^{-3}) and quadrupole moment (13.4×10^{-40} $C{\cdot}m^2$) [17,25]. However, the Mg-MOF-74 is considerably sensitive toward moisture owing to the tendency of H_2O to out-compete CO_2 [26]. As a result, the structure experiences a reduction in reactive sites [27,28], which has been measured to result in only 16% of the initial capacity after regeneration for post-combustion capture under 70% relative humidity [29]. Seemingly, chemical instability under humid conditions and low CO_2 selectivity obviates its applicability in realistic DAC operations [19].

An important point to note is that the adsorbents desirable for flue gas CO_2 capture are not primed to excel in DAC because of the lower concentration of CO_2 in the air (~0.04%) as opposed to flue gas (~5–15%). For that reason, an adsorbent with reasonably strong binding to CO_2 is required to attain an appreciable amount of gas uptake but not so strong as to impede the regeneration process [30]. Taking advantage of MOFs with exposed metal cations, they can be modified through post-synthetic functionalization by introducing diamine groups into their pores. For example, in Mg-MOF-74, attaching one amine of the diamine directly to the Mg^{2+} and utilizing terminal amine (free Lewis's base) as a CO_2 adsorptive site to selectively capture CO_2 *via* chemisorption.

In a study by Choi et *al.* [31], Mg-MOF-74 was functionalized with ethylenediamine (ED) to capture CO_2 from dry simulated air (400 ppm CO_2/Ar) on a TGA. The aminated-MOF adsorbed 1.51 $mmol_{CO2}/g_{sorbent}$, around a 12% enhancement to its pristine MOF. To investigate the regenerability of the adsorbents, a 4-cycle adsorption-desorption experiment was conducted following temperature-swing adsorption (TSA), where the parent MOF experienced a 20% drop in its initial CO_2 uptake (1.35 to 1.06 $mmol_{CO2}/g_{sorbent}$). At the same time, aminated-MOF maintained its capacity without any decline. In a follow-up study, both ED-grafted Mg_2(dobdc) and bare Mg_2(dobdc) were subjected to steam treatment (110 °C in steam/N_2, 48 h) utilizing an autoclave reactor [32]. The TGA adsorption experiment (pure CO_2 at 25 °C) showed a negligible loss in CO_2 capacity for the aminated-MOF (4.66 to 4.47 $mmol_{CO2}/g_{sorbent}$), while bare Mg_2(dobdc) experienced a 60% loss, dropping from 4.27 to 1.71 $mmol_{CO2}/g_{sorbent}$. To date, no studies have been conducted on the co-adsorption of CO_2 and H_2O in ED-grafted Mg_2(dobdc), nor has there been any research on its ability to undergo extended adsorption-desorption cycles under a humid DAC environment. In fact, the kinetics of CO_2 adsorption under DAC conditions remain understudied. Indeed, it is reasonable to say that the lack of this valuable data limits the feasibility of this material for dilute streams.

Thus, to facilitate the deployment of DAC at the global level, it is pivotal to investigate and understand how CO_2 sorbent materials perform under realistic working conditions. For example, the temperature at which adsorption occurs is crucial in DAC research [19]. Since the realistic DAC systems operate in different climatic environments with a relatively broad temperature range (−30 to 50 °C), testing the adsorbent's performance under a range of operating conditions, not just at room temperature (25 °C), is necessary [30,33]. In addition to temperature, moisture in the air is another benchmark parameter that can drastically impact CO_2 capacity and influence the overall operation of the DAC process. For example, an investigation was conducted to determine the impact of humidity on the performance of the M-dobdc series using a gas-flow apparatus under conditions that are pertinent to post-combustion capture [29]. After regeneration from hydration at 70% RH, it was discovered that Co_2(dobdc), Ni_2(dobdc), and Mg_2(dobdc) experienced a reduction in CO_2 capacity of 15%, 40%, and 84%, respectively [29,30]. In a separate study, Adil et *al.* [34] demonstrated that the mmen-Mg_2(dobpdc) had a high breakthrough time after exposure to dry mixed-gas adsorption (CO_2/N_2:10/90 mixture) conditions. However, its performance was compromised immensely over the course of 5 humid cycles, noticeable by a 30% drop in CO_2 retention time. Although the data reported corresponds to mostly studying flue gas, the results imply the need for focused studies on CO_2/H_2O competitive adsorption at realistic dilute CO_2 concentrations [30].

Additionally, when assessing MOFs for the DAC potential, it is essential to consider that sorbent stability is just as crucial as the adsorption temperature and humidity. It is a particularly key parameter because any economically viable DAC adsorbent should withstand thousands of adsorption-desorption cycles without exhibiting performance decay [15]. Eventually, the degradation of amine-based adsorbents may be a crucial bottleneck for the application of DAC in the required Gt-scale, as well as from an environmental point-of-view, if left unsolved [1]. Besides, prior to industrial utilization, it is necessary to formulate amine-based powdered adsorbents into larger pellets or apply the adsorbent as a coating on different substrates to prevent intrinsic hurdles with processing, *e.g.,* handling, pressure drops, and fluidization of the MOF particles [35–37].

On these described key aspects, the work aims to assess the performance of ED-functionalized Mg_2(dobdc) (hereafter ED@MOF-74) in both dry and humid DAC-relevant conditions using a fixed-bed adsorption setup, which has never been systematically studied to the best of our knowledge. In this study, both nonfunctionalized Mg-MOF-74 and amine-modified framework were thoroughly characterized using Powder X-ray diffraction (PXRD), thermogravimetric analysis (TGA), Fourier transform infrared spectroscopy (FT-IR), scanning electron microscopy (SEM), and Elemental analyses (EA). Herein, we report the first detailed study of ED@MOF-74 in temperature-concentration swing adsorption (TCSA) mode and provide insight into how varying operating conditions, such as temperature, adsorption time and humidity, impact CO_2 adsorption. Finally, we performed cyclic experiments under both dry and humid conditions. The samples were fully evaluated post-cycling experiment using PXRD, FT-IR, and EA. We deliberately selected ED@MOF-74 because its long-term use for carbon capture is unknown. Notably, we also explored the coating of the ED@MOF-74 on stainless steel plates and cordierite monoliths, the preliminary results of which are included in this article.

2. Syntheses and methods

All the reagents and solvents were purchased from standard commercial sources and utilized as received unless otherwise stated.

2.1. Syntheses

2.1.1. Synthesis of Mg-MOF-74

The synthesis of Mg-MOF-74 was performed successfully on a gram scale at room temperature following the reported method with slight modification [38]. $Mg(NO_3)_2 \cdot 6H_2O$ [5.18 g, 20.19 mmol] and linker 2,5-dihydroxyterephthalic acid (H_4dobdc) [2.00 g, 10.09 mmol] were dissolved separately in methanol (MeOH) [49.7 mL], and an aqueous solution of sodium hydroxide [1 M, 40 mL, 40 mmol] respectively. Subsequently, the clear linker solution was slowly added to the magnesium salt solution with continuous stirring at room temperature. After 24 h, the precipitate was isolated *via* filtration, then thoroughly washed with MeOH [3 × 50 mL] and deionized water [5 × 100 mL]. Finally, it was dried overnight at 150 ºC in *vacuo*, resulting in a yellow solid (Yield: 64.1%). Anal. Calc. for $C_8H_9Mg_2O_{9.5}$: C, 31.43; H, 2.97. Found: C, 31.75; H, 3.18%. FT-IR (cm^{-1}): 3341, 2188, 1585, 1423, 1371, 1235, 1215, 1120, 1022, 888, 819, 583, 488.

2.1.2. Synthesis of ED@MOF-74

Prior to amine functionalization, 1 g of Mg-MOF-74 was loaded in a two-neck round-bottom flask and activated under high *vacuo* at 200 ºC for 2 h and then reacted with ethylenediamine (ED) [~4 g] in anhydrous toluene [100 mL] *via* extensive refluxing under inert atmosphere for 24 h. The dark yellowish powder was collected by filtration, rinsed with copious amounts of toluene and hexane, and dried at 120 ºC in *vacuo* for 4 h (Yield: 89.5%). Anal. Calc. for $C_{11.6}H_{21.8}N_{3.6}Mg_2O_{8.7}$: C, 34.87; H, 5.50; N, 12.62. Found: C, 35.15; H, 5.06; N, 13.11%. FT-IR (cm^{-1}): 3352, 3290, 2943, 2868, 1574, 1453, 1415, 1370, 1212, 1114, 967, 911, 884, 817, 639, 579, 480, 406. The comparison of the FT-IR spectra (cm^{-1}) is illustrated in Fig. 3.

2.2. Characterization of the MOFs

2.2.1. Powder X-ray diffraction (PXRD)

PXRD data were measured using a Panalytical X′Pert PRO diffractometer with Cu K_α radiation ($\lambda = 1.54187$ Å; Ni β-filter; 45 kV, 40 mA). Each powder sample was attached to a silicon-made "zero-background signal generating" plate using petrolatum jelly as an adhesive. Diffraction intensities were recorded by an X′Celerator detector at room temperature with 2θ-range of 3–60°, a step size of 0.017°, and a counting time of 70 s per step. Data processing, search-match phase analyses and the Pawley fits were carried out by the program X´pert HighScore Plus (v. 4.9). Search-match phase identification analyses were made against the ICDD-PDF4 + database (version 2022) implemented in the HighScore [39,40]. In the Pawley fit, the refined parameters were zero-offset, polynomial background, sample height displacement, unit cell parameters, and peak profile parameters (peak width, shape, and asymmetry).

2.2.2. Thermal analysis

The thermal properties of the materials have been analyzed using a Perkin Elmer STA 6000 simultaneous thermogravimetric/calorimetric (TG/DSC) analyzer. Each sample was prepared in an open platinum pan and heated under N_2 (flow rate of 40 mL/min) with a heating rate of 10 °C/min in a temperature range of 22–600 °C. Temperature calibration of the analyzer was made using melting points of the indium (156.6 °C), zinc (419.5 °C), and aluminum (660.3 °C) standards. The weight balance was calibrated at room temperature using a standard weight of 50.00 mg. The sample weights used in the measurements were about 5–10 mg.

2.2.3. Other methods

The morphology analysis of the samples was performed using Zeiss EVO-50XVP scanning electron microscopy (SEM). The Fourier transform infrared (FT-IR) spectra were recorded using Bruker Alpha II ATR instrument over a 4000–400 cm^{-1} range with 2 cm^{-1} spectral resolution. Prior to pressing a small amount of a sample onto the diamond ATR Prism, the sample was mildly ground, and the spectrum obtained was baseline corrected. Elemental analyses (C, H, and N) were conducted in-house using an Elementar EL III analyzer.

2.3. Fixed-bed DAC experiments

An automated fixed-bed adsorption/desorption device was used to investigate the applicability of the ED@MOF-74 for CO_2 adsorption from air. Examples of this device include the adsorption of CO_2 from ultra-dilute concentrations in dry and humid conditions [41], cyclic adsorption/desorption experiments, and a comparison of different desorption methods [42]. The device's instrumentation, operation, scheme of the setup and other details can be found in [42,43]. Approximately 0.1 g of the studied MOF was loaded into the adsorption column. With the measured bulk density of 0.4 g/mL, the length of the adsorbent bed is thus around 0.4 cm. Therefore, the temperature sensor inside the column was around 0.6 cm above the sample, measuring the temperature of the adsorption column rather than the sample bed. Approximately 0.15 g of quartz wool was inserted above the sample to prevent the downstream loss of the small MOF particles.

The CO_2 adsorption runs were based on the temperature-concentration swing adsorption (TCSA) scheme. The sample was typically regenerated at 120 °C under nitrogen flow for several hours until no CO_2 was detected in the outlet, then cooled down to the adsorption temperature. Adsorption was conducted using dry or humidified feed with around 400 ppmv CO_2 using 1% CO_2/N_2, with purities of 3.5 CO_2 and 5.0 N_2, balanced with 5.0 N_2. After the adsorption step, the purge step was initiated by switching the CO_2-containing feed to pure nitrogen, and the total desorption was achieved by heating the sample again to the regeneration temperature under nitrogen flow. The total flow rate was kept at 200 mL/min during adsorption and desorption. All breakthrough experiments were run at approximately 1 bar total pressure.

One experiment was conducted on Mg-MOF-74 using the temperature-vacuum-concentration swing adsorption (TVCSA) scheme. This experiment differed from the TCSA scheme by incorporating vacuuming in addition to purge and temperature swing steps. During the vacuuming step, the feed N_2 flow rate remained constant at 100 mL/min, and the column pressure was decreased in a stepwise manner by opening the pressure control valve in small increments.

Adsorption-desorption experiments with the ED@MOF-74 were conducted using variable temperature, adsorption time, and humidity conditions. These conditions and the measured capacity results are found in Section 3.2 below. In cyclic stability tests (Section 3.3), the adsorption time was 5 h, and the adsorption temperature was 25 °C. Otherwise, all these experiments followed the TCSA scheme as described above. Two different experiments were conducted to study the effect of adsorption temperature on CO_2 capacity. In the first one, a constant feed of around 400 ppmv CO_2 was used, and the temperature was increased in a stepwise fashion. The Supporting Information describes these results and the method in more detail. The second experiment was conducted using a similar scheme for the cyclic stability tests, except that the 12-hour adsorption step varied in adsorption temperature. To differentiate it from the shorter cyclic stability tests, this experiment is referred to as the "long cyclic" experiment in the text, and the results are presented in Section 3.2.1.

The adsorption and desorption capacities were calculated by numerical integration ("cumtrapz"-function in Matlab) of the adsorption/desorption profile and using ideal gas law, as described in more detail in [43]. The feed was typically measured from the outlet when bypassing the column before the adsorption step was begun, like in earlier work [41–43]. However, due to the low flow rate, in some cases, the feed CO_2 concentration was not stabilized during the time that the feed was directed through the bypass. In these cases, the feed was either measured at the end of the adsorption step or separately after the desorption. On the other hand, in the case of H_2O, the feed was measured from the end of adsorption or from the highest concentration value during adsorption in most cases. This way, the mass balance between adsorption and desorption of H_2O was better maintained compared to measuring the feed from the bypass. The effect of the feed concentration and challenges related to measuring the feed and experimental uncertainty are discussed in more detail in the Supporting Information.

3. Results & discussion

3.1. Structural characterization

The crystallinity and phase purity of the materials were corroborated *via* Powder X-ray diffraction (PXRD). The Pawley refinement was facilitated using the X'pert HighScore Plus program to verify the phase purity of the synthesized pristine MOF (Fig. 1). The Pawley refinement of the unit cell parameters for the powdered material prepared at room temperature (24 h) was structurally equivalent to the single crystal structure of CPO-27-Mg reported by Dietzel et *al.* [23] (Table S1). The two prominent Bragg diffraction peaks, [31] at 2θ = 6.8 and 11.8, confirmed the successful bulk synthesis of Mg-MOF-74 without any phase impurity peaks detected.

The PXRD results also revealed that the framework integrity remained intact following the ED grafting procedure, with only slight shifts in peak positions and a few relatively lowered peak intensities (Fig. 2).

The Fourier transform infrared spectroscopy (FT-IR) measurement was further conducted to establish the successful synthesis of Mg-MOF-74 and confirm the presence of amine sites in ED@MOF-74. The spectral changes occurring in both materials are visualized in Fig. 3. First, by comparing the IR spectrum of the 2,5-dihydroxyterephthalic acid ligand (H_4dobdc) with pristine MOF, it was observed that the characteristic peak at ~1640 cm^{-1} attributed to the free carboxylic acid group was present in the linker but vanished in Mg-MOF-74. Instead, new bands associated with $\nu_{as}(COO^-)$ and $\nu_s(COO^-)$ modes developed and are recorded at ~1585 and 1371 cm^{-1}, respectively, demonstrating the successful carboxylate coordination to the Mg^{2+} sites. In addition, the characteristic band corresponding to the phenolic group stretch ν(C–O) is centered at ~1235 cm^{-1}[44] (Fig. 3a). Thus, on this basis, both carboxylic and hydroxyls were practically identified to be deprotonated during the room temperature synthesis. Further, with the introduction of ED, new spectral features emerged related to amine modes, and the spectral bands associated with the linker experienced a tiny shift. Noticeably, in ED@MOF-74, bands associated with $\nu_{as}(COO^-)$ and $\nu_s(COO^-)$ modes are slightly shifted to ~1574 and 1370 cm^{-1}, respectively. The new principal bands detected in ~3352–3290 and ~2943–2868 cm^{-1} are ascribed to N–H and aliphatic C–H bond stretching modes, respectively (Zoomed-in data, Fig. 3b). In addition, the deformation mode of CH_2 and aliphatic C–C stretching are observed around 1453 and 967 cm^{-1}, respectively, highlighting the successful incorporation of ED [44,45].

The ED content was further quantified through thermogravimetric analyses conducted at 10 °C/min under a nitrogen flow. Fig. 4a compares the thermograms of Mg-MOF-74 and ED@MOF-74, with results tabulated in Table S2. As can be seen in Fig. 4, the Mg-MOF-74 displays a gentle descending two-step decomposition route, wherein a first region, the weight loss of 20.02 wt.-% (calcd. 20.60%) up to 310 °C, is attributable to the release of occluded and coordinated water molecules, which is consistent with the previous literature [46]. The ED@MOF-74, on the other hand, demonstrated a weight loss of approximately 8.87 wt.-% (calcd. 9.01%) and 6.53 wt.-% (calcd. 7.52%) in two steps, which correlates to the loss of non-coordinated water and ED molecules in the temperature range of 23–124 °C and 124–218 °C, respectively. Further, the third mass decay of 21.67 wt.-% (calcd. 22.70%) between 218–440 °C resulted from the removal of metal-bound water and ED molecules, and finally, above 440 °C the weight loss was associated with the primary decomposition process. Thus, in accordance with the EA results of the studied ED@MOF-74 sample, the proposed formula $[Mg_2(dobdc)(H_2O)_{0.7}(ed)_{1.3}]\cdot 2\ H_2O\cdot 0.5(ed)$ is in close agreement as

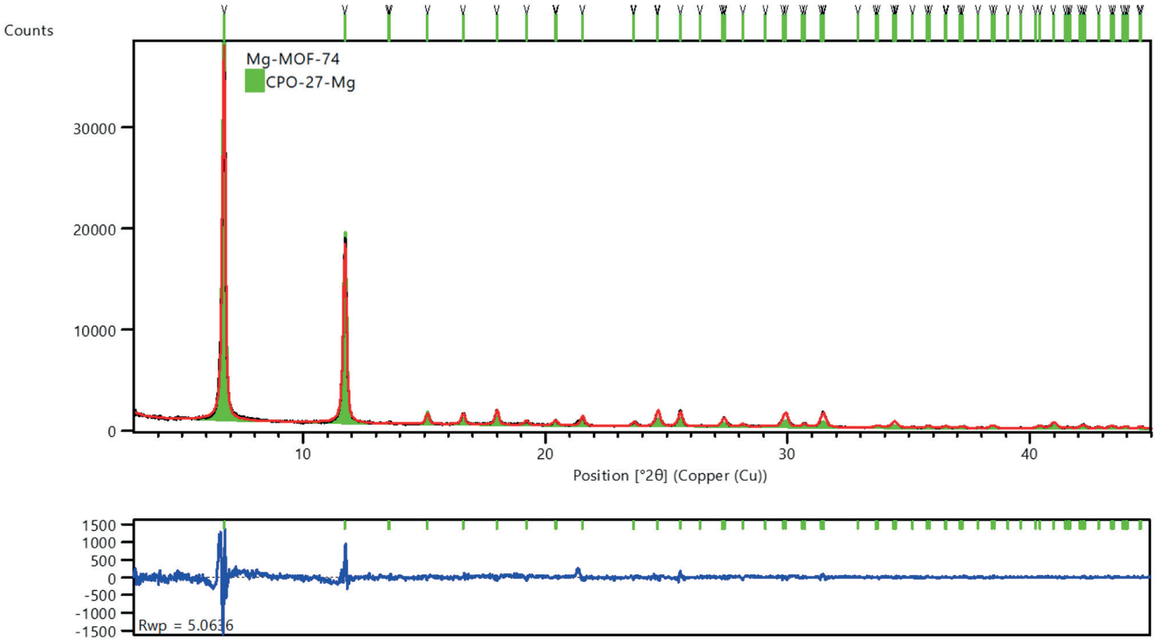

Fig. 1. Pawley refinement plot of Mg-MOF-74. The experimental pattern is black, and the refined profile is red. In contrast, green colored markers on top correspond to characteristic Bragg peak positions of the refined unit cell of the structure reported by Dietzel et *al.* [23] (CSD entry: MOHGOI). The difference plot of experimental *vs.* refined profiles is shown below in blue.

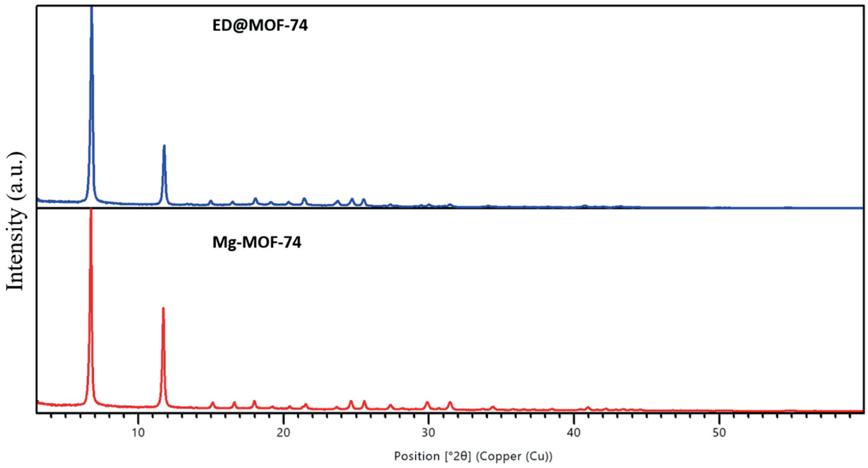

Fig. 2. Powder X-ray Diffraction Patterns of Mg-MOF-74 (red) and ED@MOF-74 (blue).

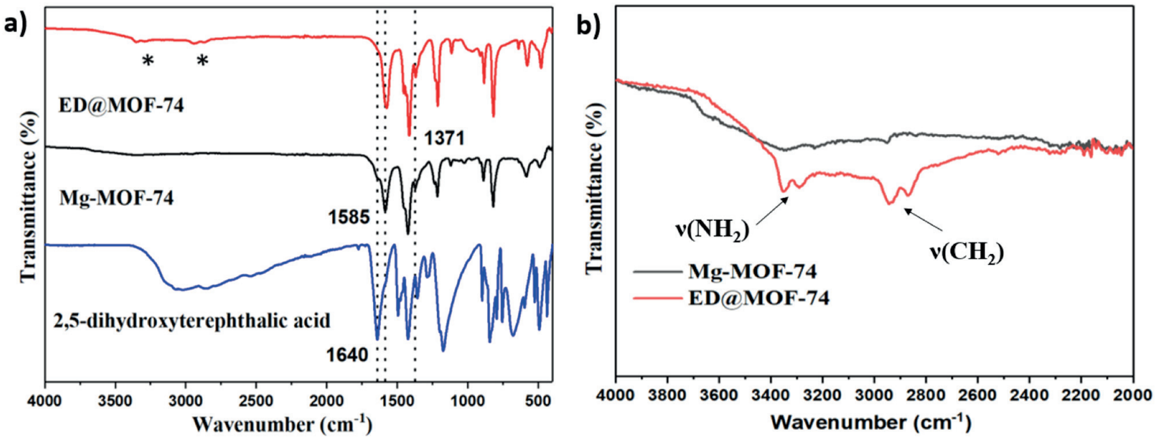

Fig. 3. a) FT-IR (cm^{-1}) spectra of 2,5-dihydroxyterephthalic acid ligand (H_4dobdc, blue), Mg-MOF-74 (black), and ED@MOF-74 (red). b) Magnification of the bands marked with *(region of ED).

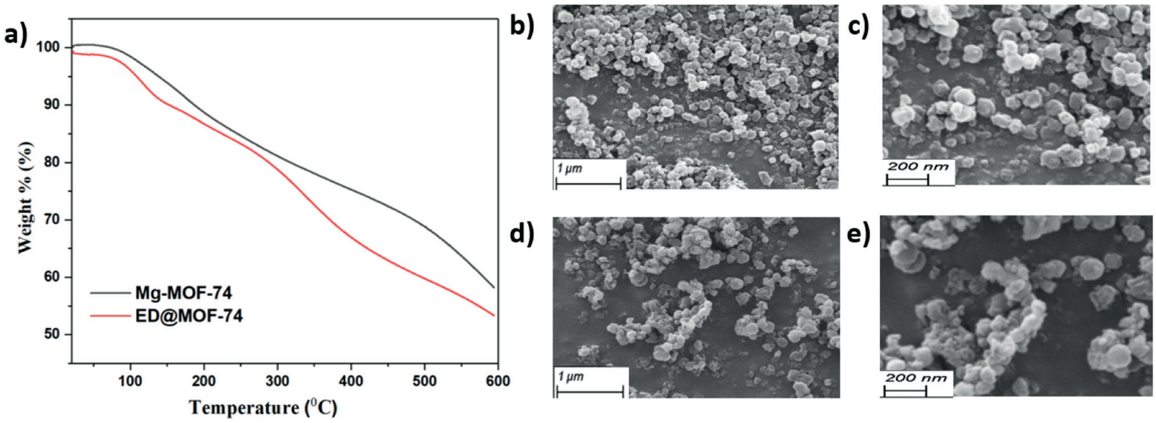

Fig. 4. a) TG curves of Mg-MOF-74 (black) and ED@MOF-74 (red), SEM images for b, c) Mg-MOF-74, and d, e) ED@MOF-74 at different magnifications.

supported by the thermogravimetric analysis.

Scanning Electron Microscopy (SEM) was performed to corroborate the morphology following the ED modification. SEM images for Mg-MOF-74 and ED@MOF-74 demonstrate that their morphology remained intact after functionalization (Fig. 4b-e). The particles have a softer, powdery texture resembling small conglomerates with a cotton-ball-like morphology, with an average size of about 300–400 nm [38].

3.2. CO_2 adsorption from air

A set of adsorption experiments was conducted in variable conditions to screen the performance of the MOFs in DAC conditions. The pristine Mg-MOF-74 was tested first using the TVCSA scheme, as described in Section 2.3. The adsorption capacity of the pristine MOF in the presence of 400 ppmv CO_2 at 25 °C was around 0.03 mmol$_{CO2}$/g$_{sorbent}$. Since the estimated minimum fluidization velocity was much exceeded in the studied conditions, vacuuming was not employed in the following runs to avoid the loss of adsorbent from the bed. In the first experiment with ED@MOF-74, the sample was regenerated at 100 °C, and adsorption was conducted in dry conditions for 12 h. The sample reached pseudo-equilibrium based on the outlet CO_2 concentration reaching the feed. The achieved CO_2 adsorption capacity was around 0.4 mmol$_{CO2}$/g$_{sorbent}$, imparting a significant enhancement in adsorption performance in DAC conditions compared to the unmodified MOF. A summary of the measured capacities in different experiments conducted in this study is shown in Table 1, while a more detailed table is available in the Supporting Information.

It is shown in Table 1 that the adsorption results are higher in most cases than the respective desorption capacities. Similar behavior has been observed earlier in the case of H_2O, while for CO_2, this difference has been relatively small, if any [41]. The main reason for this difference between adsorption and desorption capacities originates from the adsorption measurement method, as discussed in previous work [41, 47]. The measured feed's uncertainty significantly affects the calculated adsorption capacity, as shown in the Supporting Information. However, the differences between adsorption and desorption capacities fall within the experimental uncertainty, and the mass balance between the steps is well maintained.

In the following experiment, a higher regeneration temperature of 120 °C was used (100 °C in the first test) to achieve more complete regeneration, as it was suspected to be incomplete at 100 °C. The higher temperature was selected as the capacity resulting in the first experiment was deemed low in comparison to 1.5 mmol$_{CO2}$/g$_{sorbent}$ in dry DAC conditions reported by Choi et *al.* [31]. Consequently, the higher regeneration temperature increased the CO_2 capacity from approximately 0.4 mmol$_{CO2}$/g$_{sorbent}$ to 0.7 mmol$_{CO2}$/g$_{sorbent}$ and 0.8 mmol$_{CO2}$/g$_{sorbent}$ in adsorption and desorption, respectively. However, after three cycles in different conditions of humidity and adsorption temperature, the adsorption was measured again in dry conditions at 25 °C, resulting in an even higher adsorption capacity of 0.98 mmol$_{CO2}$/g$_{sorbent}$. A repeated cycle in similar adsorption conditions resulted in a slightly lower capacity of 0.90 mmol$_{CO2}$/g$_{sorbent}$, although the difference falls within experimental uncertainty. The increase in adsorption capacity from the second experiment done in similar conditions compared to the sixth and seventh experiments could be due to changes in the sample due to multiple repeats of adsorption and desorption. Another reason could be the introduction of humidity in the third and fourth experiments. Although the removal of H_2O was deemed complete after the humid cycles, as no humidity was detected in the outlet at the end of desorption, it is possible that humidity within the MOF structure enabled a complete regeneration when purging the sample with nitrogen at 120 °C. The effect of adsorption temperature and humidity on the adsorption of CO_2 is discussed in more detail below.

3.2.1. Effect of adsorption temperature

The adsorption of CO_2 on amine-functionalized materials is governed by adsorption equilibrium and mass transfer, which is why it is essential to study the rate of adsorption and the measured final adsorption uptakes at different temperatures. Fig. 5 shows the CO_2 adsorption breakthrough data on the ED@MOF-74 at different temperatures in the long cyclic experiment. The feed was reached earlier at higher temperatures, which could be attributed to both lower adsorption capacity and increased kinetics at higher temperatures. For example, at 77 °C and 102 °C, the CO_2 concentration sharply increases towards the feed already at the start of the experiment. On the other hand, the CO_2 concentration increases slower towards the feed at 25 °C and 35 °C, in which cases the adsorption started to slow down significantly only during the few final hours of the experiment (see Supporting Information Fig. S2).

At 12 °C, the adsorption rate was clearly lower than at higher temperatures. As shown in Fig. 5a, at 12 °C, the CO_2 concentration increases quickly in the first minutes of the run, but then the increase slows down. It could be observed in this experiment that the CO_2 concentration and, thus, the CO_2 uptake increased for the whole duration of the 12-hour adsorption phase (Fig. S2). Additionally, the adsorption rate at 12 °C stays at a higher level during 5–10 h from the start of adsorption, decreasing from around 0.032 to 0.017 mmol$_{CO2}$/(g$_{sorbent}$·h) (see Supporting Information S.10). In comparison, at 25 °C, the adsorption rate drops from 0.035 to around 0.008 mmol$_{CO2}$/(g$_{sorbent}$·h) over the same period. Thus, it seems that the sample did not reach saturation at the end of the 12 °C adsorption experiment compared to the 25 °C and higher adsorption temperatures. Still, as shown in Fig. 6, the final CO_2 uptake is lower at 12 °C compared to 25, 35, and even 52 °C due to a much lower adsorption rate in the initial hours of adsorption (see Fig. 5a). Notably, adsorption/desorption capacities measured at 25 °C and 35 °C were approximately the same, around 0.9 mmol$_{CO2}$/g$_{sorbent}$ in the long cyclic run. The results were similar in the adsorption experiments 5–7 (see Table 1), where the adsorption/desorption capacities were approximately 0.9–1.0 mmol$_{CO2}$/g$_{sorbent}$ and 1.0–1.1 mmol$_{CO2}$/g$_{sorbent}$ at 25 and 35 °C, respectively.

Table 1

Adsorption-desorption capacities of the ED@MOF-74 in different experiments and conditions. Experiments 2–7 were done in successive cycles using the same sample.

Experiment	c_{H2O} (vol%)	t_{ads} (h)	T_{ads} (°C)	T_{des} (°C)	$q_{CO2,ads}$ (mmol$_{CO2}$/g)	$q_{CO2,des}$ (mmol$_{CO2}$/g)	$q_{H2O,ads}$ (mmol$_{H2O}$/g)	$q_{H2O,des}$ (mmol$_{H2O}$/g)
1	0	12	25	100	0.42 ± 0.05	0.36 ± 0.03		
2	0	16	26	120	0.67 ± 0.08	0.77 ± 0.06		
3	1.6	16	25	120	1.79 ± 0.22	1.68 ± 0.14	11.60 ± 0.81	11.76 ± 0.42
4	1.6	16	35	120	0.66 ± 0.08	0.77 ± 0.06	8.42 ± 0.59	9.44 ± 0.33
5	0	16	35	120	1.14 ± 0.14	0.98 ± 0.08		
6	0	16	25	120	0.98 ± 0.12	0.87 ± 0.07		
7	0	16	25	120	0.90 ± 0.11	0.84 ± 0.07		
Dry cyclic[a]	0	5	25	120	0.82 ± 0.10	0.75 ± 0.06		
Humid cyclic[b]	1.9	5	25	120	1.07 ± 0.13	0.90 ± 0.07	10.08 ± 0.7	10.95 ± 0.39
Long cyclic	0	12	25	120	0.91 ± 0.11	0.94 ± 0.08		
Long cyclic	0	12	35	120	0.95 ± 0.12	0.89 ± 0.07		

[a] The highest result of the dry cyclic experiment.

[b] Result from cycle 1 of humid cycling. The same sample was used as in the dry cyclic run.

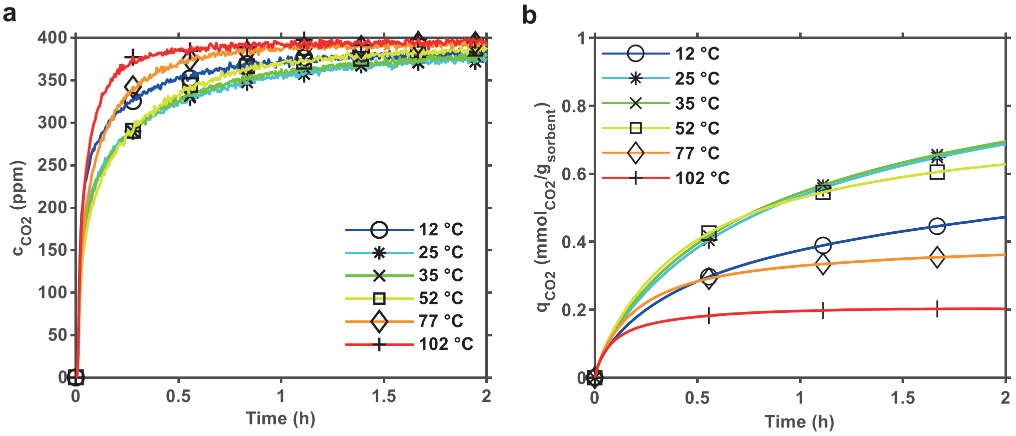

Fig. 5. Experimental a) CO_2 concentration and b) uptake profiles at different adsorption temperatures from the first two hours of adsorption. Feed was approximately 400 ppmv CO_2 in N_2. The uptake data in b) is not corrected with empty column breakthrough data.

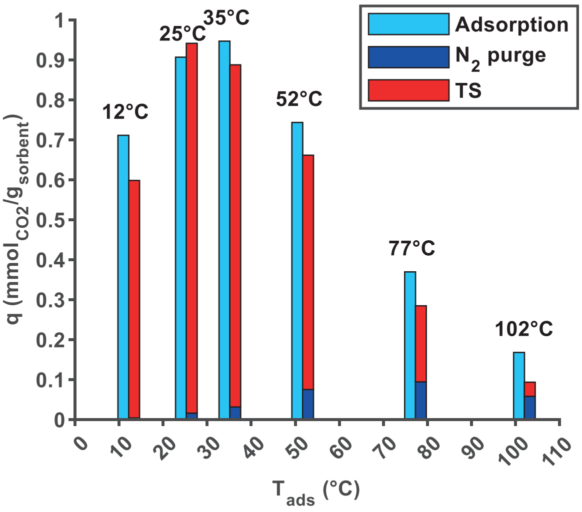

Fig. 6. Experimental CO_2 adsorption and desorption capacities at different adsorption temperatures from approximately 400 ppm dry CO_2. Adsorption time was 12 h. Temperature swing (TS) was done at 120 °C.

These results suggest that the ED@MOF-74 suffers from a limited adsorption rate in the adsorption of CO_2 from the air, especially at temperatures lower than 25 °C. These results could have implications for the practical applicability of the sorbent for DAC in cold climates. Although the measured adsorption capacities at the lowest adsorption temperatures could be higher with longer adsorption times, a prolonged adsorption phase can drastically reduce the CO_2 productivity of the DAC process [48] and thus increase the cost of captured CO_2.

The measured adsorption capacities at different temperatures shown in Fig. 6 can be utilized to estimate the achievable working capacity in a temperature-swing adsorption (TSA) process. As an example, from the measured adsorption capacities, with adsorption at 25 °C and desorption at 77 °C or 102 °C resulted in working capacities of around 0.54 $mmol_{CO2}/g_{sorbent}$ or 0.74 $mmol_{CO2}/g_{sorbent}$, respectively. These correspond to approximately 59% or 81% of the adsorption capacity at 25 °C, respectively. In this regard, the ED@MOF-74 differs significantly from the pore-expanded version of Mg-MOF-74 modified with ED [en-Mg_2(dobpdc)], for which CO_2 adsorption tests at 0.39 mbar resulted in 2.83 $mmol_{CO2}/g_{sorbent}$, 0.11 $mmol_{CO2}/g_{sorbent}$, and negligible adsorption at 25 °C, 50 °C and 75 °C, respectively [49]. In an actual DAC process, the desorption is typically achieved through either temperature-vacuum swing (TVS) [50,51], steam-stripping [52], or a combination of these [53–55]. The comparison of the working capacities based on adsorption capacities measured in dry TSA/TCSA conditions has limited practical utility but can provide a preliminary estimate of the working temperature range. For example, it is clear that if less than 60% of the adsorption capacity is achievable with a regeneration temperature of 77 °C in TSA, it is likely that a higher temperature is required in a TVSA process to achieve a similar working capacity, where the achievable working capacity can be much lower than in TSA operation [42]. On the other hand, steam acts as both the stripping gas and the conveyor of heat, which can result in a higher working capacity if steam-stripping regeneration is used. Therefore, using a regeneration temperature of 100 °C in a steam-stripping operation may result in a higher working/adsorption capacity ratio than 81%.

The impact of adsorption temperature was also investigated in an adsorption isobar experiment, where the feed was in constant condition while only the temperature was varied. The results of this run were similar to those presented above, although the measured CO_2 uptakes were slightly lower in the adsorption isobar experiment. However, at 25 °C, the CO_2 uptake was lower than at around 50 °C, which contradicts the results shown in Fig. 6. The results are different due to the much shorter adsorption times, which likely explains why adsorption was not close to equilibrium. In the adsorption isobar experiment, adsorption was also measured at 120 °C, where the CO_2 uptake was already lower than 0.1 $mmol_{CO2}/g_{sorbent}$. It was also found that after N_2 purge at 120 °C, increasing the desorption temperature beyond 133 °C did not result in any significant further desorption. Based on these results, in terms of working capacity, it does not seem reasonable to use a temperature higher than 120 °C to regenerate the ED@MOF-74. However, as previously discussed, the productivity of DAC is greatly affected by the length of adsorption-desorption cycles, so higher regeneration temperature may be beneficial from a kinetic and productivity point-of-view. Moreover, other processes, such as TVSA, may benefit more from a higher desorption temperature. The adsorption isobar results are shown and discussed in more detail in the Supporting Information.

3.2.2. *Effect of humidity*

In DAC processes, CO_2/water co-adsorption is an unavoidable challenge because ambient air always contains a certain humidity, up to 84 g/m^3 worldwide [30]. Humidity can change the type of reaction in amine-based sorbents, shifting the reaction product of CO_2 and amines from ammonium carbamate to species such as bicarbonate or hydronium carbamate, thus increasing the CO_2 adsorption capacity [41,56,57].

On the other hand, co-adsorbed water causes parasitic heat loss during desorption, significantly increasing the energy demand of the DAC process [48]. Additionally, most MOFs tend to experience a reduction in crystallinity and BET surface area when exposed to humid conditions [58]. However, it is known that the stabilization of MOFs with exposed metal cations under humid conditions is often improved by functionalization with amines. Generally, for amine-containing adsorbents, the formation of urea leads to the deactivation of amines under dry conditions, thus reducing CO_2 capacity. However, under humid conditions, urea formation is obstructed [59], which may, in turn, improve the water stability of the amine-functionalized adsorbents [60].

It is well established that studying humid CO_2 adsorption is vital when assessing materials for the DAC potential. However, literature is still scarce in this aspect, particularly in the case of amine-modified MOFs, and the nearest examples can usually be found in articles related to post-combustion capture. For example, a study by Mason et *al.* [61] investigated a series of MOF systems for CO_2 adsorption using a multicomponent adsorption analyzer considering a gas mixture composed of water, CO_2, and N_2. Amine appended CuBTTri demonstrated a slightly decreased equilibrium CO_2 capacity after exposure to water. On the other hand, CO_2 adsorption on mmen-Mg_2(dobpdc) was promoted in the presence of 14% CO_2/N_2 up to 32% RH conditions and found to be 14% higher (nearly 4.2 $mmol_{CO2}/g_{sorbent}$) compared to dry conditions. Remarkably, the isostructural nickel analogue, mmen-Ni_2(-dobpdc), which has been reported not to undergo carbamate insertion in CO_2 presence, was found to display a noticeable enhancement in the CO_2 capture, close to 3-fold, in comparison to the dry case [61]. In another example, after exposure to humid conditions (100% RH), MOFs possessing diamines with side alkyl substituents, such as men-Mg_2(dobpdc) and den-Mg_2(dobpdc), yielded only a marginal difference in CO_2 capacity. In comparison, CO_2 capacity of en-Mg_2(dobpdc) decreased roughly by 67% (4.30 *versus* 2.88 $mmol_{CO2}/g_{sorbent,}$ under 15% CO_2/N_2 at 40 °C). The hydrolytic stability was ascribed to the fact that branched diamines contain methyl groups, which can help safeguard the Mg–N bonds from hydrolyzing [56,62].

For ED@MOF-74, as indicated in Table 1 above, the highest adsorption capacity of approximately 1.8 $mmol_{CO2}/g_{sorbent}$ was obtained in humid conditions at 25 °C, using a feed with 400 ppm CO_2 with around 2 vol% humidity, demonstrating the positive impact of humidity. However, at 35 °C, the adsorption capacity decreased to around 0.7 $mmol_{CO2}/g_{sorbent,}$ marking a considerable capacity decrease of about 60% in only a 10 °C temperature swing. Nonetheless, as discussed in the previous section, no reduction in CO_2 capacity was found in dry adsorption conditions at 25 °C compared to 35 °C. Kwon et *al.* [63] also made a similar observation for aminopolymer-impregnated meso/macroporous silica sorbent under DAC conditions, suggesting

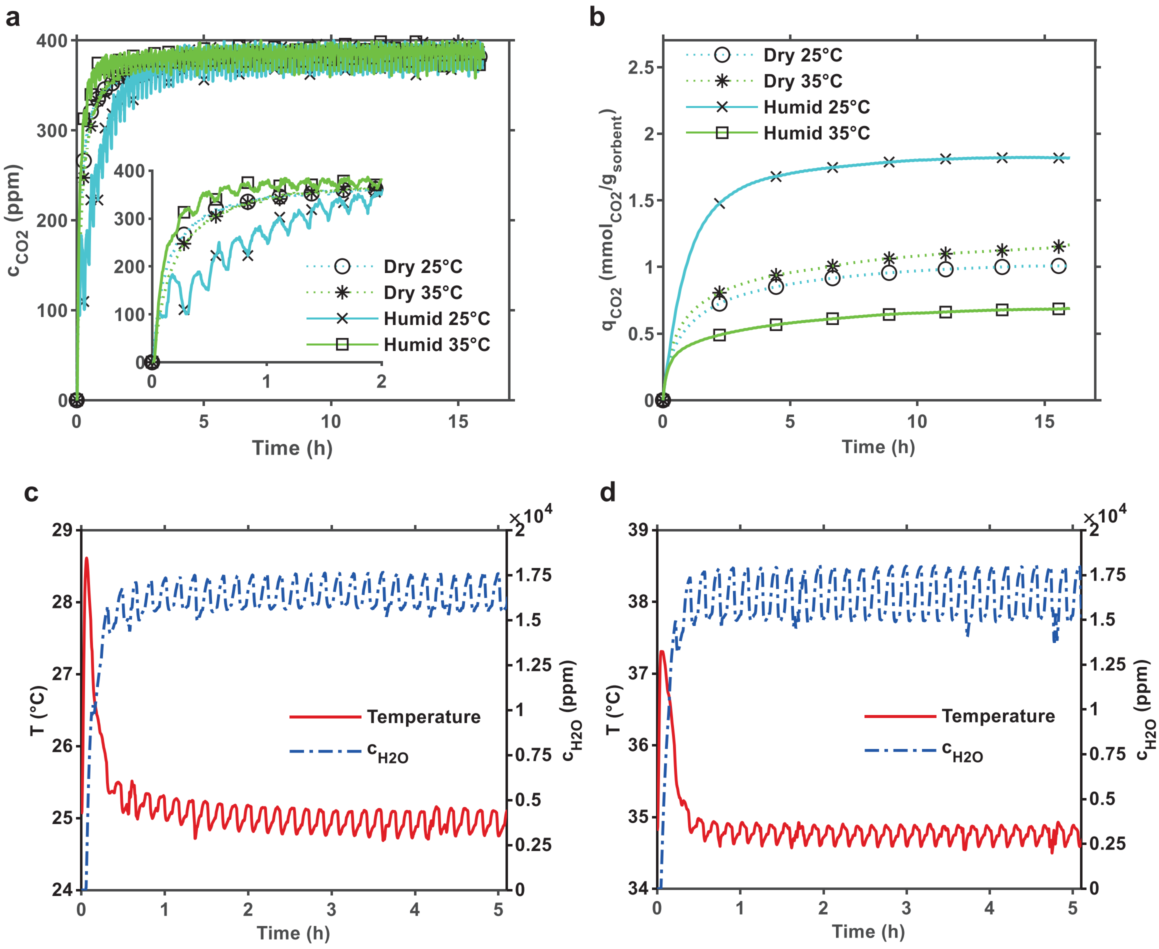

Fig. 7. Experimental a) CO_2 concentration; b) CO_2 uptake profiles in dry and humid conditions at 25 °C and 35 °C. Temperature and H_2O concentration from the first 5 h of adsorption in the humid experiments c) at 25 °C; d) 35 °C. Feed was approximately 400 ppmv CO_2 in N_2. The uptake data in b) is not corrected with empty column breakthrough data. The markers are a guide to the eye.

water vapor presence mitigates kinetic limitations.

Fig. 7 compares adsorption breakthrough data in dry and humid conditions. As shown in Fig. 7a, the CO_2 concentration increases significantly slower towards the feed in the humid 25 °C experiment compared to dry conditions or the humid 35 °C. Consequently, the uptake curve in Fig. 7b shows a much higher adsorption rate during the first two hours in the humid 25 °C experiment. This is also shown in the moving average adsorption rate plots in Supplementary Information (S.10). At 25 °C in humid conditions, the adsorption rate starts from 1.34 $mmol_{CO2}/(g_{sorbent}\cdot h)$ and drops to around 1.06 $mmol_{CO2}/(g_{sorbent}\cdot h)$ after 30 min of adsorption (around 21% drop). On the other hand, in dry conditions at 25 °C, the respective values are 0.82 and 0.55 $mmol_{CO2}/(g_{sorbent}\cdot h)$ (33% drop). The adsorption rate in humid conditions clearly exceeds the adsorption rate measured for an amine-functionalized resin in similar CO_2 and H_2O concentration conditions and adsorption temperature, which was 0.88 $mmol_{CO2}/(g_{sorbent}\cdot h)$ [41] (calculated from the first 30 min). However, it should be noted that the gas/solid ratio in this work was around twice compared to [41,42] and the amino resin had a much larger particle size median of 600 μm [64] compared to an average of 0.4 μm for the ED@MOF-74 (measured from SEM). In pelletized form, it is expected that the ED@MOF-74 has a slower adsorption rate than that measured here.

Fig. 7c and d show the temperature peaks observed in the humid experiments. No clearly observable temperature peak was seen in the dry experiments. Additionally, as shown in Table 1, the measured H_2O adsorption and desorption capacities were several times higher than the CO_2 capacities. Therefore, it can be construed that the measured temperature increase during adsorption was due to the adsorption of H_2O rather than increased CO_2 uptake. Similar findings were found for the amino resin examined in earlier work [41]. However, as mentioned in Section 2.3, the temperature probe was above the sample; thus, the temperature profiles shown in Fig. 7 do not represent the actual sample temperature. Therefore, the temperature increase caused by CO_2 may not be evident due to the dispersion of the temperature profile. The H_2O concentration profiles are also displayed in Fig. 7c and d. Notably, the "noisy" behavior of the CO_2 profile in Fig. 7a is due to the highly variable H_2O concentration. This is due to air in the capillaries of the humidity calibrator used to humidify the feed, which has also been discussed in earlier work [41].

Fig. 8 shows the adsorption breakthrough data in dry and humid conditions in a multi-cycle experiment. Since the cycling was done with the same sample by continuing with humid cycling after dry cycling, the data of the last dry cycle and the first humid cycle are compared here. Notably, while the CO_2 adsorption uptakes calculated from the first 5 h of adsorption between different experiments in dry conditions matched, in humid conditions, there is a significant difference in CO_2 adsorption uptakes between the two experiments shown in Figs. 7 and 8, approximately 1.8 *vs.* 1.1 $mmol_{CO2}/g_{sorbent}$, respectively. The main reason for

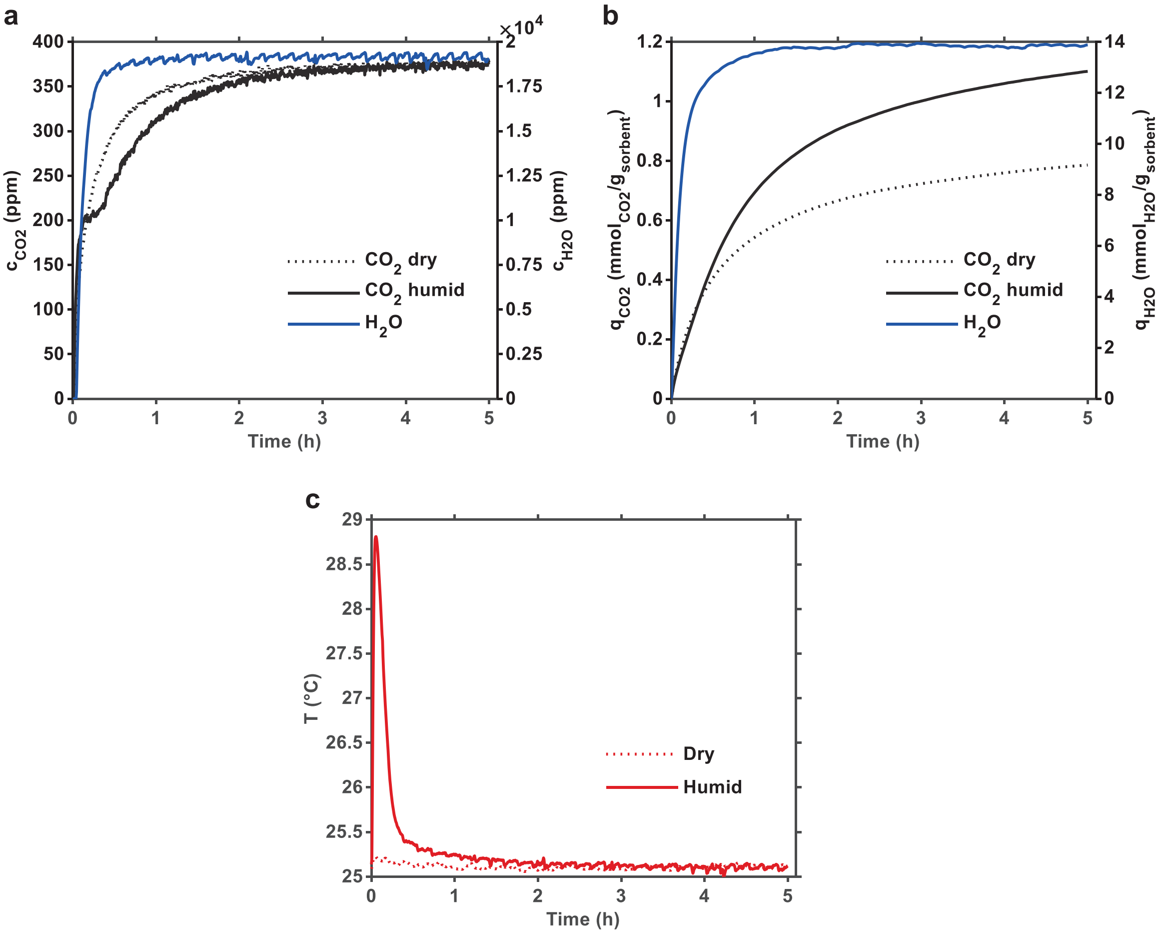

Fig. 8. Experimental a) CO_2 and H_2O concentration; b) CO_2 and H_2O uptake; c) temperature profiles from the adsorption phase of two consecutive adsorption-desorption cycles in dry and humid conditions using the same sample. The dry data is from the last cycle of the dry cyclic stability experiment, while the humid data is from the first cycle of the humid cyclic stability experiment. The uptake data in b) is not corrected with empty column breakthrough data.

the much lower adsorption uptake measured in the multi-cycle experiment is that the sample had undergone 18 dry adsorption-desorption cycles before initiating the humid cycling. The drop in capacity and stability of the ED@MOF-74 is discussed in more detail in the next section below (3.3.2).

The results shown in Fig. 8 allow a better comparison of the breakthrough curve shape between dry and humid conditions than in Fig. 7 due to a much steadier H_2O concentration profile during the humid run. It is shown in Fig. 8a that unlike in the dry run, in humid conditions, the CO_2 concentration first increases quickly to around 200 ppm but then continues on a much slower path toward the feed. This can be explained by the temperature increase shown in Fig. 8c, which slows down the adsorption of CO_2 during the first 20–30 min of adsorption. The temperature increase in this experiment is reasonably similar to that shown in Fig. 7, which is almost 4 °C. Additionally, the measured H_2O adsorption/desorption capacities were around 12 $mmol_{H2O}/g_{sorbent}$ in experiment 3 (see Table 1) and 10–11 $mmol_{H2O}/g_{sorbent}$ in the multi-cycle experiment. This is around double to that measured for the proprietary amino resin studied earlier [41] or the commercial Lewatit VP OC 1065 [65]. As for MOFs, Mason et *al.* [61] compared the performance of different MOFs under conditions that are pertinent to power plant flue gas and reported H_2O uptake up to 9.5, 5.4, 14.2, 18.2 $mmol_{H2O}/g_{sorbent}$ for mmen-Mg_2(dobpdc), mmen-CuBTTri, Mg_2(dobdc) and HKUST-1, respectively. Thus, consistent with ED@MOF-74, H_2O adsorption capacities in these hybrid materials remained more dominant than the corresponding CO_2 capacities.

The adsorption of H_2O can thus have three significant practical implications for using this adsorbent for DAC. Firstly, a high amount of adsorbed H_2O significantly enhances the regeneration energy requirement of the DAC process. For example, suppose the q_{H2O}/q_{CO2} ratio is 6.4, as in experiment 3 (see Table 1). In that case, the isosteric heat of H_2O adsorption using the heat of H_2O vaporization of 44 kJ/mol at 25 °C constitutes around 6.4 MJ/kg_{CO2}. The latent heat due to H_2O desorption is thus a significant part of the total energy requirement of DAC, with upper limits estimated from around 12 MJ/kg_{CO2} [53] to 19 MJ/kg_{CO2} [66]. The second practical implication also arises from the isosteric heat of H_2O adsorption since, as shown in the data above, the H_2O adsorption causes a temperature increase, which reduces the adsorption of CO_2. In the results shown here, the heat transfer in the adsorption column can be regarded as reasonably optimal due to the small diameter column, which may not be true for process-scale DAC adsorption columns. Therefore, this phenomenon is likely more prominent in the process-scale DAC and may lead to a reduced adsorption rate in the beginning, causing a delay in the adsorption phase or reduced working capacity and thus reduced productivity of CO_2. Analogously, while the adsorption heat may delay the adsorption phase, the cooling effect during the desorption of the gases may delay the regeneration phase. It should also be considered that the laboratory-scale adsorption column was actively cooled during adsorption through the column wall using a heat-transfer fluid. Therefore, with adsorbents that capture significant amounts of H_2O, the heat transfer and the active cooling of the adsorption column during adsorption become more important. The third and possibly the most critical implication of humidity for the long-term use of DAC is the possible degradation of the MOF, which is investigated in the next section.

3.3. *Cyclic stability*

The assessment of CO_2 adsorption during repetitive adsorption-desorption cycles is the true measure in evaluating the material's tolerance to operating conditions, its long-term viability for a practical capture process, and minimizing the cost related to DAC operation. To assess the stability of the ED@MOF-74, dry and humid cyclic adsorption-desorption experiments were conducted, after which the samples were analyzed with PXRD, FT-IR, and EA. In total, there were two characterized samples. The first sample underwent 18 dry and 18 humid adsorption/desorption cycles, and the second sample underwent the dry adsorption isobar and long cyclic tests. In Section 3.3.2, these two samples are referred to as "ED@MOF-74-CO_2-humid" and "ED@MOF-74-CO_2-dry" respectively.

3.3.1. *Cyclic DAC experiments*

Intriguingly, as shown in Fig. 9, it was found that the cyclic adsorption and desorption capacities were lower in the first adsorption-desorption cycles compared to the following ones. This finding was consistent with the preliminary experiments, where the adsorption and desorption capacities of experiment 2 were lower than in experiments 6 and 7, which were conducted in similar conditions and used the same sample. After the fourth cycle, the cyclic capacities seem to stabilize. In cycles 5 to 18, a slightly decreasing trend can be observed in the cyclic capacities. The adsorption and desorption capacities drop from around 0.85 and 0.75 $mmol_{CO2}/g_{sorbent}$ in the 5th cycle to around 0.79 and 0.73 $mmol_{CO2}/g_{sorbent}$ in the 18th cycle, respectively. Calculated from the desorption capacity values, the drop in capacity corresponds to around 2.7%, or 0.2%/cycle. This capacity drop rate is comparable to the 0.18%/cycle measured for a proprietary amino resin over 19 dry TCSA cycles with the same device [42].

Even though the regeneration was deemed complete between cycles, it is possible that the lower cyclic capacities observed in the first four cycles are due to incomplete regeneration and thus reaching a cyclic steady state by cycle nr. 5. Another reason may be that the sample required a more extended activation due to blockage of some of the pores with physically bound ethylenediamine, which was then removed after a few cycles with regeneration temperature near the evaporation temperature of free ED (see TGA results in Section 3.1). This could also explain why higher results were gained in the preliminary experiments after a few adsorption-desorption cycles, as discussed in Section 3.2. To avoid this from affecting the results of the humid cycling, the humid cycling was continued with the same sample after the last dry cycle.

Although the capacity drop observed in the dry cycling was rather moderate, the humid adsorption and desorption capacities at the start of the humid cycling were much lower compared to the preliminary experiment done in similar conditions, as discussed in Section 3.2.2. Thus, it appears that degradation of the adsorption sites was more prominent during the dry cycling than what could be observed based on the evolution of the measured CO_2 capacities. One reason for this could

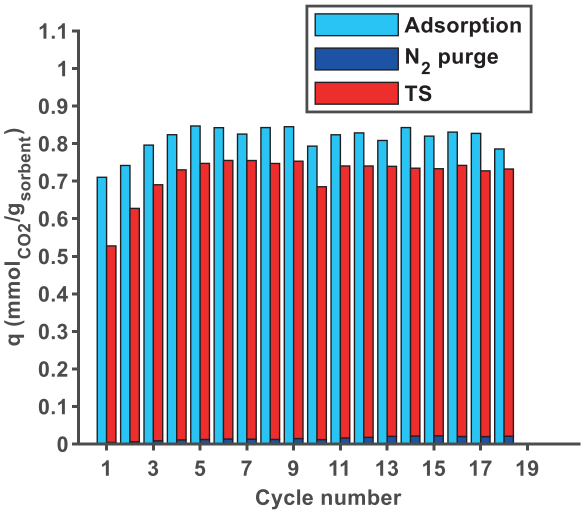

Fig. 9. Experimental CO_2 adsorption and desorption capacities in the repeated cycles of dry temperature-concentration swing adsorption. Adsorption was conducted at 25 °C with around 400 ppmv CO_2. Desorption was conducted at 120 °C using pure N_2 feed.

be that humidity enables the adsorption of CO_2 on amine sites that are both more susceptible to degradation and cannot adsorb CO_2 in dry conditions. When such amines are degraded due to, *e.g.,* the high regeneration temperature, the drop in adsorption capacity is not observed in dry cycles. Humidity may disrupt the H-bonded networks between adjacent primary amine groups, thereby incrementing CO_2 binding sites (more accessible free amines) [61,67–69]. Therefore, a fair amount of the diamine molecules exist in the MOF pores as free amines, thus being unbound to the metal sites, and thereby cannot adsorb CO_2 in dry conditions. Such amines are then easily leached out due to evaporation by heating, which may justify why the CO_2 capacity at the start of the humid cycling was much lower than in experiment 3. The existence of free ED is evidenced by the TGA results in Section 3.1.

A drastic decline in CO_2 and H_2O capacities could be observed in humid conditions, as shown in Fig. 10. The cyclic CO_2 capacity, as shown in Fig. 10a, drops rapidly at the beginning but slows down after the 7th cycle. The CO_2 desorption capacity drops from around 0.90 to 0.44 $mmol_{CO2}/g_{sorbent}$ in the first 7 cycles, corresponding to over 50% drop, around 7%/cycle. However, from the 7th to the 18th cycle, the CO_2 desorption capacity drops to around 0.23 $mmol_{CO2}/g_{sorbent}$, corresponding to a drop rate of 4%/cycle. In total, the desorption capacity decreased by around 74% as compared to the first cycle. On the other hand, the decreasing trend in the cyclic H_2O capacities in Fig. 10b seems somewhat constant throughout the experiment, although it slows down in the last few cycles. The desorption H_2O capacity drops from around 11 to 8.5 $mmol_{H2O}/g_{sorbent}$, corresponding to around a 23% drop, or 1.3%/cycle. The major loss of CO_2 capacity may refer to significant changes in the underlying framework or the loss of active amine sites. The cause of the capacity loss was studied by characterizing the samples after the cycling tests, as shown in the next Section (3.3.2).

3.3.2. *Characterization of ED@MOF-74 post-cycling*

The progressive decrease in capacity after repeated tests under both dry and humid conditions can be most likely explained by the partial structural collapse, or the material propensity towards amine loss upon regeneration, or the adverse impact of moisture. PXRD, FT-IR, and EA were conducted after subsequent cyclic tests to corroborate the structural changes and verify the nitrogen content in the post-cycling samples to support this interpretation. Upon adsorption\desorption cycling under dry and humid conditions, both ED@MOF-74 samples experienced a dramatic reduction in crystallinity, as evidenced by the broadened and markedly lowered intensities of characteristic diffraction peaks, as can be seen in the PXRD pattern shown in Fig. 11. The decrease in crystallinity may be plausibly caused by the continuous adsorption and desorption cycling, resulting in the fractionation of bigger crystals into smaller ones and causing crystal defects. Nevertheless, in our study, the PXRD pattern still displays the retention of original MOF diffraction peaks (Fig. S5). Such retention of the PXRD pattern is possible even with a major change in the MOF structure. For example, Kumar et *al.* [58] found that the presence of moisture caused an appreciable decline in the adsorption performance of Mg-MOF-74. While its PXRD pattern exhibited no change, the BET surface area decreased to 74% after one day of humidity exposure and became negligible (6 m^2/g) after prolonged exposure (7 or 14 days), implying partial pore blockage, possibly by rearrangement of amine groups or pore collapse. Literature suggests that the considerable loss of surface area provides strong evidence for amorphization and partial structural degradation [70].

Accordingly, as seen in Fig. 12, FT-IR spectra of all the samples, regardless of whether from dry or humid conditions, exhibit a significant loss of the spectral bands' intensity associated with the amine modes, particularly the doublet attributed to ν_s and ν_{as} (N-H) stretching modes of amines (as discussed earlier). This indeed suggests that there was some amine loss during CO_2 capture/releasing cycles, which was confirmed by elemental analysis (see Table S7). In Fig. 12, it can be observed that the bands in ED@MOF-74 samples associated with the amine modes are shifted to 3281 cm^{-1} for ED@MOF-74-CO_2-humid, and 3309 cm^{-1} for ED@MOF-74-CO_2-dry, respectively. Additionally, a new weak shoulder has been registered roughly around 1680 cm^{-1} on both the post adsorption\desorption cycling samples. This band has been previously attributed to the $O= C= O$ bending mode during chemisorption [71,72]. Therefore, it is feasible that a reduction in CO_2 capacity could result from a small portion of the adsorbed CO_2 remaining in a stable and strongly chemisorbed form in the ED@MOF-74, making the adsorption–desorption process partially non-reversible. However, there is insufficient conclusive evidence for this interpretation as the shoulder observed is very weak, possibly due to H-bonding, and other bands are not well distinguishable. Moreover, it is very challenging to detect infrared bands of the adsorbed species that produce signals typically between 1800 – 1200 cm^{-1}[66] due to the overlapping of bands by the organic bridging linker in this region.

It needs to be mentioned that the downward trend in capacity because of the diamine leaching has also been observed in other diamine-appended MOF systems [34,73–76]. For example, Adil et *al.* [34] exploited the performance stability of amine-functionalized material under humid conditions by using the flow-mode breakthrough system, simulating practical post-combustion carbon capture scenarios. The authors demonstrated that mmen-Mg_2(dobpdc) is not stable in cyclic mode, reflected by a notable decrease (~30%) in CO_2 retention time observed after five cycles, suggesting the amine's detachment from OMSs as water molecules compete for them. They explained that the

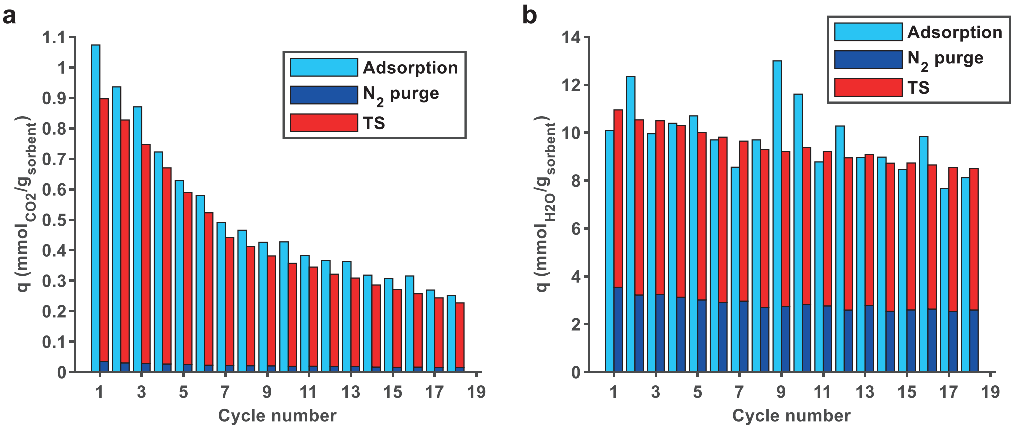

Fig. 10. Adsorption and desorption capacities in the repeated cycles of humid temperature-concentration swing adsorption of a) CO_2 and b) H_2O. Adsorption was conducted at 25 °C with around 400 ppmv CO_2 and 2 vol% H_2O in N_2. Desorption was conducted at 120 °C using pure N_2 feed.

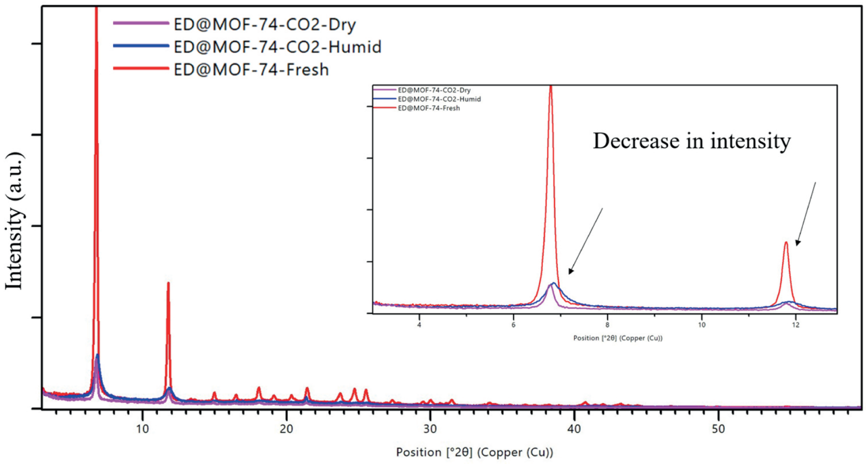

Fig. 11. PXRD pattern of ED@MOF-74 before and after adsorption/desorption cycling under dry and humid conditions.

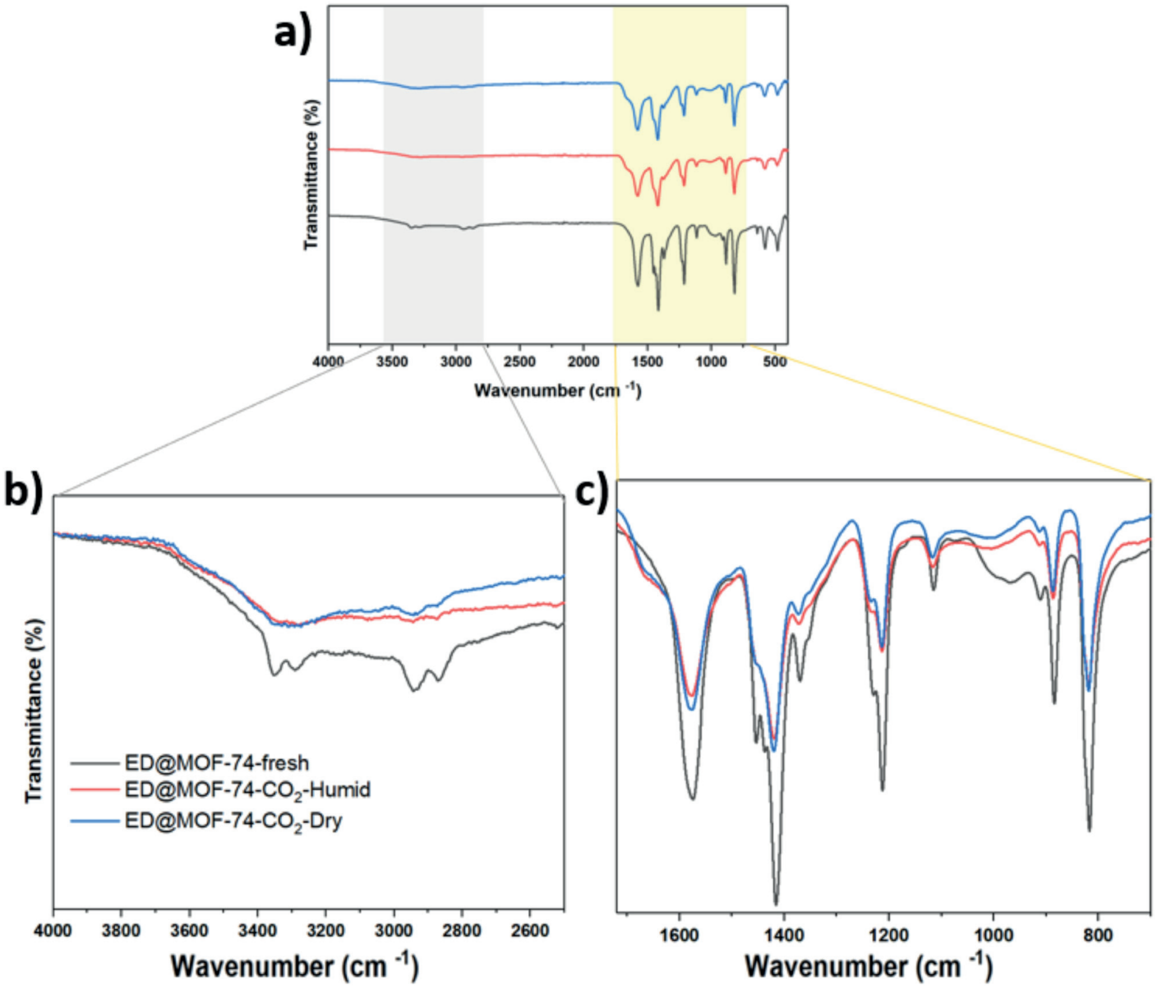

Fig. 12. FT-IR of ED@MOF-74 before and after adsorption/desorption cycling under dry and humid conditions a) complete spectra, magnification of the b) 3500 to 2600 cm^{-1} and c) 1700 to 800 cm^{-1} regions.

relatively strong binding energy between H_2O and Mg^{2+} compared to Mg–amine disrupts coordinated diamines, thus leading to the amine loss and gradual reduction in CO_2 uptake [34]. In the literature, the degradation of amine-supported adsorbents was investigated under dry conditions and CO_2 capacity loss was correlated with the deactivation of primary amines by urea species formation [59,77].

Since amine-functionalization holds tremendous promise for atmospheric CO_2 capture, future studies should pay close attention to humid instability issues to further enhance the performance of these desirable adsorbent systems under humid DAC conditions. Coating diamine-functionalized MOFs with polymers that induce hydrophobic properties is recommended to reduce the dramatic impact of water vapor [78, 79]. The adsorbent Choe et al. [74] studied relied on the fabrication of diamine-appended Mg_2(dobpdc)-alumina\silane\epoxide composites. They concluded that the epoxide's ring-opening reaction with diamines appended to exposed metal cations afforded improved hydrophobicity, hindered water vapor penetration into the pores, and reduced the diamine volatilization.

4. Conclusions

In the present work, we investigated the effectiveness of ED@MOF-74 for direct air capture using an automated fixed-bed adsorption setup combined with physicochemical characterization. We evaluated the carbon capture performance of the adsorbent in both dry and humid DAC-relevant conditions and tested its stability through adsorption/desorption TCSA cycling. Our evaluation included a more comprehensive range of operating conditions compared to existing literature, such as temperature and humidity, which were found to impact the ED@MOF-74 performance dramatically.

In dry conditions using 12-hour adsorption, the measured CO_2 uptake dropped progressively at adsorption temperatures higher than 35 °C. The adsorption/desorption capacities registered at 25 °C and 35 °C were similar, around 0.9 $mmol_{CO2}/g_{sorbent}$. However, at 12 °C, the CO_2 uptake was lowered to roughly 0.7 $mmol_{CO2}/g_{sorbent}$. It was noted that the sample was not reaching saturation at the end of the 12 °C adsorption experiment compared to 25 °C or at higher temperatures used, suggesting that ED@MOF-74 could suffer from mass-transfer limitations in the CO_2 capture from the air at temperatures much below 25 °C. In humid conditions at 25 °C, the difference in CO_2 uptake under dry *vs.* humid conditions was the highest, measuring 1.8 $mmol_{CO2}/g_{sorbent}$ using a feed with 400 ppm CO_2 and around 2 vol% humidity. However, in contrast to the trend observed in the dry CO_2 stream at a temperature of 35 °C, the adsorption capacity decreased drastically to around 0.7 $mmol_{CO2}/g_{sorbent}$, marking a decline of nearly 60% in only a 10 °C temperature swing. Additionally, the amount of adsorbed H_2O was multiple times that of $CO_{2,}$ being around 10–11 $mmol_{H2O}/g_{sorbent}$. In consecutive TCSA cycles using the ED@MOF-74, only a small cyclic capacity drop of around 3% occurred in 18 cycles during dry conditions. However, over continued cycling at 2 vol% humidity, the capacity drop was significantly pronounced, leading to around 74% loss of CO_2 uptake compared to the first humid cycle result.

Characterization of ED@MOF-74 following dry experiments and dry \humid TCSA cycling using PXRD and EA analyses revealed that the samples lost both crystallinity and nitrogen content. Furthermore, the FT-IR studies illustrated that both samples experienced a loss of intensity in the spectral bands associated with amines compared to the fresh ED@MOF-74. As demonstrated by the TGA results, a significant portion of the ethylenediamine in the ED@MOF-74 existed in the form of free amines, volatilizing slightly above 120 °C. Altogether, characterization results suggest that the material propensity towards amine loss could be responsible for the performance decrease after successive TCSA cycles, and here, we propose two potential mechanisms for the amine loss. Firstly, in dry conditions, the free amines present in the sample are progressively removed after repeated temperature elevation from the adsorption temperature up to 120 °C. Secondly, in humid conditions, the water molecules may strip the ED groups from the grafted sites after repeated humid cycles. It is also plausible that because there was a high amount of adsorbed H_2O, ED might have dissolved in the water and then left as droplets during desorption.

This study shows that the ED@MOF-74 has multiple challenges when it comes to its real-life application as a viable DAC adsorbent, especially due to the high required desorption temperature, low adsorption rate at low temperature, high H_2O uptake, and structural degradation. Decreasing the regeneration temperature may prevent degradation in dry conditions but will significantly compromise the achievable cyclic working capacity, especially if temperature-vacuum swing adsorption is used. Based on humid experiments at 25 °C and 35 °C, humidity facilitates the regeneration process, which could mean a lower regeneration temperature could be used in humid conditions. However, humidity also clearly renders the adsorbent useless over multiple cycles through active amine site loss, which may promote using this adsorbent in significantly dried air. Another reason against applying the adsorbent in a high-humidity climate is the tendency to capture high amounts of H_2O, increasing the energy requirement of the process. On the other hand, application in dry air usually means cold, sub-zero conditions, which seem to entail kinetic limitations. Moreover, the process-scale application of the MOF would require either pelletizing or coating the adsorbent on a structured monolith. On a positive note, this study showed that even straightforward techniques can be used to achieve porous layers of CO_2-adsorbing MOFs on different substrates.

Only a few studies cover the critical aspects necessary for effectively employing MOFs in DAC-relevant conditions, specifically kinetics and stability in humid environments. Overall, the results presented in this work emphasize the necessity of directing more attention toward these aspects to incorporate amine-decorated porous supports in a realistic DAC process successfully. In future studies, more comprehensive CO_2 adsorption testing at varying relative humidities and temperatures, along with TVSA cycling, would complement the current knowledge of amine-modified MOFs. Another critical element to be systematically explored is the long-term stability of the amines. An in-depth exploration of underlying chemical and structural parameters that affect degradation would provide valuable guidance in constructing effective amine-rich sorbents. This would ensure that adsorbents maintain their high adsorption capacities over a few months, thereby maximizing the applicability of such CO_2 adsorbents for direct air capture.

CRediT authorship contribution statement

Jere Elfving: Formal analysis, Visualization, Writing – original draft, Writing – review & editing, Methodology. **Shreya Mahajan:** Investigation, Methodology, Visualization, Writing – original draft, Writing – review & editing, Formal analysis. **Manu Lahtinen:** Conceptualization, Funding acquisition, Project administration, Supervision, Writing – review & editing.

Declaration of Competing Interest

The authors declare that they have no known competing financial interests or personal relationships that could have appeared to influence the work reported in this paper.

Data availability

Data will be made available on request.

Acknowledgments

This study was conducted as a part of the DAC2.0 project funded by the Academy of Finland under grant numbers 329312 and 329314 and the University of Jyväskylä. The authors would also like to thank Jessica

Ekholm for conducting the coating experiments and Dr. Pekka Simell for his valuable feedback and supervision during the coating experiments.

Supporting information

The Supporting Information includes details about: Structural characterization; Experimental uncertainty; The effect of feed concentration on adsorption capacity; Adsorption-desorption results; CO_2 concentration and uptake profiles at different temperatures; Adsorption isobar experiment; Characterization of ED@MOF-74 post-cycling; Coating experiments; CO_2 concentration profiles on logarithmic time scale; CO_2 adsorption rate profiles.

Notes

The authors declare no competing financial interest.

Appendix A. Supporting information

Supplementary data associated with this article can be found in the online version at doi:10.1016/j.jece.2024.112193.

References

[1] S. Fuss, W.F. Lamb, M.W. Callaghan, J. Hilaire, F. Creutzig, T. Amann, T. Beringer, W. de Oliveira Garcia, J. Hartmann, T. Khanna, G. Luderer, G.F. Nemet, J. Rogelj, P. Smith, J.L.V. Vicente, J. Wilcox, M. del Mar Zamora Dominguez, J.C. Minx, Negative emissions—Part 2: costs, potentials and side effects, Environ. Res. Lett. 13 (2018) 063002, https://doi.org/10.1088/1748-9326/aabf9f.

[2] P. Smith, S.J. Davis, F. Creutzig, S. Fuss, J. Minx, B. Gabrielle, E. Kato, R. B. Jackson, A. Cowie, E. Kriegler, D.P. van Vuuren, J. Rogelj, P. Ciais, J. Milne, J. G. Canadell, D. McCollum, G. Peters, R. Andrew, V. Krey, G. Shrestha, P. Friedlingstein, T. Gasser, A. Grübler, W.K. Heidug, M. Jonas, C.D. Jones, F. Kraxner, E. Littleton, J. Lowe, J.R. Moreira, N. Nakicenovic, M. Obersteiner, A. Patwardhan, M. Rogner, E. Rubin, A. Sharifi, A. Torvanger, Y. Yamagata, J. Edmonds, C. Yongsung, Biophysical and economic limits to negative CO_2 emissions, Nat. Clim. Chang. 6 (2016) 42–50, https://doi.org/10.1038/nclimate2870.

[3] M. Erans, E.S. Sanz-Pérez, D.P. Hanak, Z. Clulow, D.M. Reiner, G.A. Mutch, Direct air capture: process technology, techno-economic and socio-political challenges, Energy Environ. Sci. 15 (2022) 1360–1405, https://doi.org/10.1039/D1EE03523A.

[4] Y. Abdullatif, A. Sodiq, N. Mir, Y. Bicer, T. Al-Ansari, M.H. El-Naas, A.I. Amhamed, Emerging trends in direct air capture of CO_2: a review of technology options targeting net-zero emissions, RSC Adv. 13 (2023) 5687–5722, https://doi.org/10.1039/D2RA07940B.

[5] J. Fuhrman, H. McJeon, P. Patel, S.C. Doney, W.M. Shobe, A.F. Clarens, Food–energy–water implications of negative emissions technologies in a $+1.5\,^{\circ}C$ future, Nat. Clim. Chang. 10 (2020) 920–927, https://doi.org/10.1038/s41558-020-0876-z.

[6] R. Gonzalez Sanchez, A. Chatzipanagi, G. Kakoulaki, M. Buffi, S. Szabo, The role of direct air capture in eu's decarbonisation and associated carbon intensity for synthetic fuels production, Energies 16 (2023) 3881, https://doi.org/10.3390/en16093881.

[7] D.W. Keith, G. Holmes, D. St. Angelo, K. Heidel, A Process for Capturing CO_2 from the atmosphere, Joule 2 (2018) 1573–1594, https://doi.org/10.1016/j.joule.2018.05.006.

[8] C.J. E. Bajamundi, J. Koponen, V. Ruuskanen, J. Elfving, A. Kosonen, J. Kauppinen, J. Ahola, Capturing CO_2 from air: technical performance and process control improvement, J. CO_2 Util. 30 (2019) 232–239, https://doi.org/10.1016/j.jcou.2019.02.002.

[9] Climeworks, subsite: "direct air capture," (2023), (n.d.). https://www.climeworks.com (accessed August 28, 2023).

[10] D. Panda, V. Kulkarni, S.K. Singh, Evaluation of amine-based solid adsorbents for direct air capture: a critical review, React. Chem. Eng. 8 (2023) 10–40, https://doi.org/10.1039/D2RE00211F.

[11] W. Lu, J.P. Sculley, D. Yuan, R. Krishna, H.-C. Zhou, Carbon dioxide capture from air using amine-grafted porous polymer networks, J. Phys. Chem. C 117 (2013) 4057–4061, https://doi.org/10.1021/jp311512q.

[12] J. Wang, H. Huang, M. Wang, L. Yao, W. Qiao, D. Long, L. Ling, Direct capture of low-concentration CO_2 on mesoporous carbon-supported solid amine adsorbents at ambient temperature, Ind. Eng. Chem. Res. 54 (2015) 5319–5327, https://doi.org/10.1021/acs.iecr.5b01060.

[13] W. Chaikittisilp, H.-J. Kim, C.W. Jones, Mesoporous alumina-supported amines as potential steam-stable adsorbents for capturing CO_2 from simulated flue gas and ambient air, Energy Fuels 25 (2011) 5528–5537, https://doi.org/10.1021/ef201224v.

[14] A. Sayari, Q. Liu, P. Mishra, Enhanced adsorption efficiency through materials design for direct air capture over supported polyethylenimine, ChemSusChem 9 (2016) 2796–2803, https://doi.org/10.1002/cssc.201600834.

[15] H. Azarabadi, K.S. Lackner, A sorbent-focused techno-economic analysis of direct air capture, Appl. Energy 250 (2019) 959–975, https://doi.org/10.1016/j.apenergy.2019.04.012.

[16] S. Mahajan, M. Lahtinen, Recent progress in metal-organic frameworks (MOFs) for CO_2 capture at different pressures, J. Environ. Chem. Eng. 10 (2022) 108930, https://doi.org/10.1016/j.jece.2022.108930.

[17] K. Sumida, D.L. Rogow, J.A. Mason, T.M. McDonald, E.D. Bloch, Z.R. Herm, T.-H. Bae, J.R. Long, Carbon dioxide capture in metal–organic frameworks, Chem. Rev. 112 (2012) 724–781, https://doi.org/10.1021/cr2003272.

[18] Ü. Kökçam-Demir, A. Goldman, L. Esrafili, M. Gharib, A. Morsali, O. Weingart, C. Janiak, Coordinatively unsaturated metal sites (open metal sites) in metal–organic frameworks: design and applications, Chem. Soc. Rev. 49 (2020) 2751–2798, https://doi.org/10.1039/C9CS00609E.

[19] E.S. Sanz-Pérez, C.R. Murdock, S.A. Didas, C.W. Jones, Direct capture of CO_2 from ambient air, Chem. Rev. 116 (2016) 11840–11876, https://doi.org/10.1021/acs.chemrev.6b00173.

[20] L. Valenzano, B. Civalleri, S. Chavan, G.T. Palomino, C.O. Areán, S. Bordiga, Computational and experimental studies on the adsorption of CO, N_2, and CO_2 on Mg-MOF-74, J. Phys. Chem. C 114 (2010) 11185–11191, https://doi.org/10.1021/jp102574f.

[21] S.R. Caskey, A.G. Wong-Foy, A.J. Matzger, Dramatic tuning of carbon dioxide uptake via metal substitution in a coordination polymer with cylindrical pores, J. Am. Chem. Soc. 130 (2008) 10870–10871, https://doi.org/10.1021/ja8036096.

[22] D. Britt, H. Furukawa, B. Wang, T.G. Glover, O.M. Yaghi, Highly efficient separation of carbon dioxide by a metal-organic framework replete with open metal sites, Proc. Natl. Acad. Sci. 106 (2009) 20637–20640, https://doi.org/10.1073/pnas.0909718106.

[23] P.D.C. Dietzel, R. Blom, H. Fjellvåg, Base-induced formation of two magnesium metal-organic framework compounds with a bifunctional tetratopic ligand, Eur. J. Inorg. Chem. (2008) 3624–3632, https://doi.org/10.1002/ejic.200701284.

[24] A.R. Millward, O.M. Yaghi, Metal−organic frameworks with exceptionally high capacity for storage of carbon dioxide at room temperature, J. Am. Chem. Soc. 127 (2005) 17998–17999, https://doi.org/10.1021/ja0570032.

[25] G.Y. Yoo, W.R. Lee, H. Jo, J. Park, J.H. Song, K.S. Lim, D. Moon, H. Jung, J. Lim, S. S. Han, Y. Jung, C.S. Hong, Adsorption of carbon dioxide on unsaturated metal sites in M_2(dobpdc) frameworks with exceptional structural stability and relation between lewis acidity and adsorption enthalpy, Chem. Eur. J. 22 (2016) 7444–7451, https://doi.org/10.1002/chem.201600189.

[26] K. Tan, S. Zuluaga, Q. Gong, Y. Gao, N. Nijem, J. Li, T. Thonhauser, Y.J. Chabal, Competitive coadsorption of CO_2 with H_2O, NH_3, SO_2, NO, NO_2, N_2, O_2, and CH_4 in M-MOF-74 (M = Mg, Co, Ni): the role of hydrogen bonding, Chem. Mater. 27 (2015) 2203–2217, https://doi.org/10.1021/acs.chemmater.5b00315.

[27] A.H. Farmahini, S. Krishnamurthy, D. Friedrich, S. Brandani, L. Sarkisov, Performance-based screening of porous materials for carbon capture, Chem. Rev. 121 (2021) 10666–10741, https://doi.org/10.1021/acs.chemrev.0c01266.

[28] J.B. DeCoste, G.W. Peterson, B.J. Schindler, K.L. Killops, M.A. Browe, J.J. Mahle, The effect of water adsorption on the structure of the carboxylate containing metal–organic frameworks Cu-BTC, Mg-MOF-74, and UiO-66, J. Mater. Chem. A 1 (2013) 11922, https://doi.org/10.1039/c3ta12497e.

[29] A.C. Kizzie, A.G. Wong-Foy, A.J. Matzger, Effect of humidity on the performance of microporous coordination polymers as adsorbents for CO_2 capture, Langmuir 27 (2011) 6368–6373, https://doi.org/10.1021/la200547k.

[30] F. Kong, G. Rim, M. Song, C. Rosu, P. Priyadarshini, R.P. Lively, M.J. Realff, C. W. Jones, Research needs targeting direct air capture of carbon dioxide: material & process performance characteristics under realistic environmental conditions, Korean J. Chem. Eng. 39 (2022) 1–19, https://doi.org/10.1007/s11814-021-0976-0.

[31] S. Choi, T. Watanabe, T.-H. Bae, D.S. Sholl, C.W. Jones, Modification of the Mg/DOBDC MOF with amines to enhance CO_2 adsorption from ultradilute gases, J. Phys. Chem. Lett. 3 (2012) 1136–1141, https://doi.org/10.1021/jz300328j.

[32] D. Andirova, Y. Lei, X. Zhao, S. Choi, Functionalization of metal-organic frameworks for enhanced stability under humid carbon dioxide capture conditions, ChemSusChem 8 (2015) 3405–3409, https://doi.org/10.1002/cssc.201500580.

[33] Y. Miao, Z. He, X. Zhu, D. Izikowitz, J. Li, Operating temperatures affect direct air capture of CO_2 in polyamine-loaded mesoporous silica, Chem. Eng. J. 426 (2021) 131875, https://doi.org/10.1016/j.cej.2021.131875.

[34] K. Adil, P.M. Bhatt, Y. Belmabkhout, S.M.T. Abtab, H. Jiang, A.H. Assen, A. Mallick, A. Cadiau, J. Aqil, M. Eddaoudi, Valuing metal-organic frameworks for postcombustion carbon capture: a benchmark study for evaluating physical adsorbents, Adv. Mater. 29 (2017) 1702953, https://doi.org/10.1002/adma.201702953.

[35] B. Yeskendir, J.-P. Dacquin, Y. Lorgouilloux, C. Courtois, S. Royer, J. Dhainaut, From metal–organic framework powders to shaped solids: recent developments and challenges, Mater. Adv. 2 (2021) 7139–7186, https://doi.org/10.1039/D1MA00630D.

[36] F. Rezaei, M.A. Sakwa-Novak, S. Bali, D.M. Duncanson, C.W. Jones, Shaping amine-based solid CO_2 adsorbents: effects of pelletization pressure on the physical and chemical properties, Microporous Mesoporous Mater. 204 (2015) 34–42, https://doi.org/10.1016/j.micromeso.2014.10.047.

[37] M.A. Sakwa-Novak, C.-J. Yoo, S. Tan, F. Rashidi, C.W. Jones, Poly(ethylenimine)-functionalized monolithic alumina honeycomb adsorbents for CO_2 capture from air, ChemSusChem 9 (2016) 1859–1868, https://doi.org/10.1002/cssc.201600404.

[38] S.M. Vornholt, S.E. Henkelis, R.E. Morris, Low temperature synthesis study of metal–organic framework CPO-27: investigating metal, solvent and base effects down to −78 °C, Dalton Trans. 46 (2017) 8298–8303, https://doi.org/10.1039/C7DT01223C.

[39] T. Degen, M. Sadki, E. Bron, U. König, G. Nénert, The highscore suite, Powder Diffr. 29 (2014) S13–S18, https://doi.org/10.1017/S0885715614000840.

[40] G.S. Pawley, Unit-cell refinement from powder diffraction scans, J. Appl. Crystallogr. 14 (1981) 357–361, https://doi.org/10.1107/S0021889881009618.

[41] J. Elfving, T. Sainio, Kinetic approach to modelling CO_2 adsorption from humid air using amine-functionalized resin: equilibrium isotherms and column dynamics, Chem. Eng. Sci. 246 (2021) 116885, https://doi.org/10.1016/j.ces.2021.116885.

[42] J. Elfving, J. Kauppinen, M. Jegoroff, V. Ruuskanen, L. Järvinen, T. Sainio, Experimental comparison of regeneration methods for CO_2 concentration from air using amine-based adsorbent, Chem. Eng. J. 404 (2021) 126337, https://doi.org/10.1016/j.cej.2020.126337.

[43] J. Elfving, 2021, Direct Capture of CO2 from Air Using Amine-functionalized Resin - Effect of Humidity in Modelling and Evaluation of Process Concepts, Lappeenranta-Lahti University of Technology LUT. https://urn.fi/URN:ISBN:978–952-335–765-5 (accessed August 10, 2023).

[44] K.I. Hadjiivanov, D.A. Panayotov, M.Y. Mihaylov, E.Z. Ivanova, K.K. Chakarova, S. M. Andonova, N.L. Drenchev, Power of infrared and Raman spectroscopies to characterize metal-organic frameworks and investigate their interaction with guest molecules, Chem. Rev. 121 (2021) 1286–1424, https://doi.org/10.1021/acs.chemrev.0c00487.

[45] T.P. Chopra, R.C. Longo, K. Cho, M.D. Halls, P. Thissen, Y.J. Chabal, Ethylenediamine grafting on oxide-free H-, 1/3 mL F-, and Cl-terminated Si(111) surfaces, Chem. Mater. 27 (2015) 6268–6281, https://doi.org/10.1021/acs.chemmater.5b03156.

[46] D. Villarroel-Rocha, A.A. Godoy, C. Toncón-Leal, J. Villarroel-Rocha, M.S. Moreno, M.C. Bernini, G.E. Narda, K. Sapag, Synthesis of micro–mesoporous CPO-27-Mg@KIT-6 composites and their test in CO_2 adsorption, N. J. Chem. 44 (2020) 10056–10065, https://doi.org/10.1039/C9NJ06358G.

[47] J. Elfving, C. Bajamundi, J. Kauppinen, T. Sainio, Modelling of equilibrium working capacity of PSA, TSA and TVSA processes for CO_2 adsorption under direct air capture conditions, J. CO_2 Util. 22 (2017) 270–277, https://doi.org/10.1016/j.jcou.2017.10.010.

[48] A. Luukkonen, J. Elfving, E. Inkeri, Improving adsorption-based direct air capture performance through operating parameter optimization, Chem. Eng. J. 471 (2023) 144525, https://doi.org/10.1016/j.cej.2023.144525.

[49] W.R. Lee, S.Y. Hwang, D.W. Ryu, K.S. Lim, S.S. Han, D. Moon, J. Choi, C.S. Hong, Diamine-functionalized metal–organic framework: exceptionally high CO_2 capacities from ambient air and flue gas, ultrafast CO_2 uptake rate, and adsorption mechanism, Energy Environ. Sci. 7 (2014) 744–751, https://doi.org/10.1039/C3EE42328J.

[50] C.J. E. Bajamundi, J. Koponen, V. Ruuskanen, J. Elfving, A. Kosonen, J. Kauppinen, J. Ahola, Capturing CO_2 from air: technical performance and process control improvement, J. CO_2 Util. 30 (2019) 232–239, https://doi.org/10.1016/j.jcou.2019.02.002.

[51] J.A. Wurzbacher, C. Gebald, N. Piatkowski, A. Steinfeld, Concurrent separation of CO_2 and H_2O from air by a temperature-vacuum swing adsorption/desorption cycle, Environ. Sci. Technol. 46 (2012) 9191–9198, https://doi.org/10.1021/es301953k.

[52] W. Li, S. Choi, J.H. Drese, M. Hornbostel, G. Krishnan, P.M. Eisenberger, C. W. Jones, Steam-stripping for regeneration of supported amine-based CO_2 adsorbents, ChemSusChem 3 (2010) 899–903, https://doi.org/10.1002/cssc.201000131.

[53] X. Zhu, T. Ge, F. Yang, R. Wang, Design of steam-assisted temperature vacuum-swing adsorption processes for efficient CO_2 capture from ambient air, Renew. Sust. Energ. Rev. 137 (2021) 110651, https://doi.org/10.1016/j.rser.2020.110651.

[54] V. Stampi-Bombelli, M. van der Spek, M. Mazzotti, Analysis of direct capture of CO_2 from ambient air via steam-assisted temperature–vacuum swing adsorption, Adsorption 26 (2020) 1183–1197, https://doi.org/10.1007/s10450-020-00249-w.

[55] R.P. Wijesiri, G.P. Knowles, H. Yeasmin, A.F.A. Hoadley, A.L. Chaffee, Desorption process for capturing CO_2 from Air with supported amine sorbent, Ind. Eng. Chem. Res. 58 (2019) 15606–15618, https://doi.org/10.1021/acs.iecr.9b03140.

[56] J.M. Kolle, M. Fayaz, A. Sayari, Understanding the effect of water on CO_2 adsorption, Chem. Rev. 121 (2021) 7280–7345, https://doi.org/10.1021/acs.chemrev.0c00762.

[57] C. Gebald, J.A. Wurzbacher, A. Borgschulte, T. Zimmermann, A. Steinfeld, Single-component and binary CO_2 and H_2O adsorption of amine-functionalized cellulose, Environ. Sci. Technol. 48 (2014) 2497–2504, https://doi.org/10.1021/es404430g.

[58] A. Kumar, D.G. Madden, M. Lusi, K. Chen, E.A. Daniels, T. Curtin, J.J. Perry, M. J. Zaworotko, Direct air capture of CO_2 by Physisorbent Materials, Angew. Chem. Int. Ed. 54 (2015) 14372–14377, https://doi.org/10.1002/anie.201506952.

[59] A. Sayari, Y. Belmabkhout, Stabilization of amine-containing CO_2 adsorbents: dramatic effect of water vapor, J. Am. Chem. Soc. 132 (2010) 6312–6314, https://doi.org/10.1021/ja1013773.

[60] M. Yang, C. Ma, M. Xu, S. Wang, L. Xu, Recent advances in CO_2 adsorption from air: a review, Curr. Pollut. Rep. 5 (2019) 272–293, https://doi.org/10.1007/s40726-019-00128-1.

[61] J.A. Mason, T.M. McDonald, T.-H. Bae, J.E. Bachman, K. Sumida, J.J. Dutton, S. S. Kaye, J.R. Long, Application of a high-throughput analyzer in evaluating solid adsorbents for post-combustion carbon capture via multicomponent adsorption of CO_2, N_2, and H_2O, J. Am. Chem. Soc. 137 (2015) 4787–4803, https://doi.org/10.1021/jacs.5b00838.

[62] H. Jo, W.R. Lee, N.W. Kim, H. Jung, K.S. Lim, J.E. Kim, D.W. Kang, H. Lee, V. Hiremath, J.G. Seo, H. Jin, D. Moon, S.S. Han, C.S. Hong, Fine-tuning of the carbon dioxide capture capability of diamine-grafted metal-organic framework adsorbents through amine functionalization, ChemSusChem 10 (2017) 541–550, https://doi.org/10.1002/cssc.201601203.

[63] H.T. Kwon, M.A. Sakwa-Novak, S.H. Pang, A.R. Sujan, E.W. Ping, C.W. Jones, Aminopolymer-impregnated Hierarchical silica structures: unexpected equivalent CO_2 uptake under simulated air capture and flue gas capture conditions, Chem. Mater. 31 (2019) 5229–5237, https://doi.org/10.1021/acs.chemmater.9b01474.

[64] J. Elfving, C. Bajamundi, J. Kauppinen, Characterization and performance of direct air capture sorbent, Energy Procedia 114 (2017) 6087–6101, https://doi.org/10.1016/j.egypro.2017.03.1746.

[65] R. Veneman, N. Frigka, W. Zhao, Z. Li, S. Kersten, W. Brilman, Adsorption of H_2O and CO_2 on supported amine sorbents, Int. J. Greenh. Gas Control 41 (2015) 268–275, https://doi.org/10.1016/j.ijggc.2015.07.014.

[66] A. Sinha, M.J. Realff, A parametric study of the techno-economics of direct CO_2 air capture systems using solid adsorbents, AIChE J. 65 (2019), https://doi.org/10.1002/aic.16607.

[67] S.A. Didas, M.A. Sakwa-Novak, G.S. Foo, C. Sievers, C.W. Jones, Effect of amine surface coverage on the Co-Adsorption of CO_2 and Water: spectral deconvolution of adsorbed species, J. Phys. Chem. Lett. 5 (2014) 4194–4200, https://doi.org/10.1021/jz502032c.

[68] J.S.A. Carneiro, G. Innocenti, H.J. Moon, Y. Guta, L. Proaño, C. Sievers, M. A. Sakwa-Novak, E.W. Ping, C.W. Jones, Insights into the Oxidative degradation mechanism of solid amine sorbents for CO_2 capture from air: roles of atmospheric water, Angew. Chem. Int. Ed. 62 (2023), https://doi.org/10.1002/anie.202302887.

[69] Z. Bacsik, N. Ahlsten, A. Ziadi, G. Zhao, A.E. Garcia-Bennett, B. Martín-Matute, N. Hedin, Mechanisms and kinetics for sorption of CO_2 on bicontinuous mesoporous silica modified with *n* -propylamine, Langmuir 27 (2011) 11118–11128, https://doi.org/10.1021/la202033p.

[70] A.A. Voskanyan, V.G. Goncharov, N. Novendra, X. Guo, A. Navrotsky, Thermodynamics drives the stability of the MOF-74 family in water, ACS Omega 5 (2020) 13158–13163, https://doi.org/10.1021/acsomega.0c01189.

[71] J.M. Veleta, R.A. Arrieta, Y. Wu, M.A. Baeza, K. Castañeda, D. Villagrán, Enhanced gas adsorption on $Cu_3(BTC)_2$ metal–organic framework by post-synthetic cation exchange and computational analysis, Langmuir 39 (2023) 8091–8099, https://doi.org/10.1021/acs.langmuir.3c00455.

[72] A. Justin, J. Espín, I. Kochetygov, M. Asgari, O. Trukhina, W.L. Queen, A Two step postsynthetic modification strategy: appending short chain polyamines to Zn-NH_2-BDC MOF for enhanced CO_2 adsorption, Inorg. Chem. 60 (2021) 11720–11729, https://doi.org/10.1021/acs.inorgchem.1c01216.

[73] J.S. Yeon, W.R. Lee, N.W. Kim, H. Jo, H. Lee, J.H. Song, K.S. Lim, D.W. Kang, J. G. Seo, D. Moon, B. Wiers, C.S. Hong, Homodiamine-functionalized metal–organic frameworks with a MOF-74-type extended structure for superior selectivity of CO_2 over N_2, J. Mater. Chem. A 3 (2015) 19177–19185, https://doi.org/10.1039/C5TA02357B.

[74] J.H. Choe, H. Kim, M. Kang, H. Yun, S.Y. Kim, S.M. Lee, C.S. Hong, Functionalization of diamine-appended MOF-based adsorbents by ring opening of epoxide: long-term stability and CO_2 recyclability under humid conditions, J. Am. Chem. Soc. 144 (2022) 10309–10319, https://doi.org/10.1021/jacs.2c01488.

[75] P.J. Milner, J.D. Martell, R.L. Siegelman, D. Gygi, S.C. Weston, J.R. Long, Overcoming double-step CO_2 adsorption and minimizing water co-adsorption in bulky diamine-appended variants of Mg_2(dobpdc), Chem. Sci. 9 (2017) 160–174, https://doi.org/10.1039/c7sc04266c.

[76] M. Jahandar Lashaki, S. Khiavi, A. Sayari, Stability of amine-functionalized CO_2 adsorbents: A multifaceted puzzle, Chem. Soc. Rev. 48 (2019) 3320–3405, https://doi.org/10.1039/c8cs00877a.

[77] A. Sayari, A. Heydari-Gorji, Y. Yang, CO_2-induced degradation of amine-containing adsorbents: reaction products and pathways, J. Am. Chem. Soc. 134 (2012) 13834–13842, https://doi.org/10.1021/ja304888a.

[78] M. Kang, J.E. Kim, D.W. Kang, H.Y. Lee, D. Moon, C.S. Hong, A diamine-grafted metal–organic framework with outstanding CO_2 capture properties and a facile coating approach for imparting exceptional moisture stability, J. Mater. Chem. A 7 (2019) 8177–8183, https://doi.org/10.1039/C8TA07965J.

[79] Y. Seok Chae, S. Park, D. Won Kang, D. Won Kim, M. Kang, D. San Choi, J. Hyeak Choe, C. Seop Hong, Moisture-tolerant diamine-appended metal–organic framework composites for effective indoor CO_2 capture through facile spray coating, Chem. Eng. J. 433 (2022) 133856, https://doi.org/10.1016/j.cej.2021.133856.

DEPARTMENT OF CHEMISTRY, UNIVERSITY OF JYVÄSKYLÄ
RESEARCH REPORT SERIES

1. Vuolle, Mikko: Electron paramagnetic resonance and molecular orbital study of radical ions generated from (2.2)metacyclophane, pyrene and its hydrogenated compounds by alkali metal reduction and by thallium(III)trifluoroacetate oxidation. (99 pp.) 1976
2. Pasanen, Kaija: Electron paramagnetic resonance study of cation radical generated from various chlorinated biphenyls. (66 pp.) 1977
3. Carbon-13 Workshop, September 6-8, 1977. (91 pp.) 1977
4. Laihia, Katri: On the structure determination of norbornane polyols by NMR spectroscopy. (111 pp.) 1979
5. Nyrönen, Timo: On the EPR, ENDOR and visible absorption spectra of some nitrogen containing heterocyclic compounds in liquid ammonia. (76 pp.) 1978
6. Talvitie, Antti: Structure determination of some sesquiterpenoids by shift reagent NMR. (54 pp.) 1979
7. Häkli, Harri: Structure analysis and molecular dynamics of cyclic compounds by shift reagent NMR. (48 pp.) 1979
8. Pitkänen, Ilkka: Thermodynamics of complexation of 1,2,4-triazole with divalent manganese, cobalt, nickel, copper, zinc, cadmium and lead ions in aqueous sodium perchlorate solutions. (89 pp.) 1980
9. Asunta, Tuula: Preparation and characterization of new organometallic compounds synthesized by using metal vapours. (91 pp.) 1980
10. Sattar, Mohammad Abdus: Analyses of MCPA and its metabolites in soil. (57 pp.) 1980
11. Bibliography 1980. (31 pp.) 1981
12. Knuuttila, Pekka: X-Ray structural studies on some divalent 3d metal compounds of picolinic and isonicotinic acid N-oxides. (77 pp.) 1981
13. Bibliography 1981. (33 pp.) 1982
14. 6th National NMR Symposium, September 9-10, 1982, Abstracts. (49 pp.) 1982
15. Bibliography 1982. (38 pp.) 1983
16. Knuuttila, Hilkka: X-Ray structural studies on some Cu(II), Co(II) and Ni(II) complexes with nicotinic and isonicotinic acid N-oxides. (54 pp.) 1983
17. Symposium on inorganic and analytical chemistry May 18, 1984, Program and Abstracts. (100 pp.) 1984
18. Knuutinen, Juha: On the synthesis, structure verification and gas chromatographic determination of chlorinated catechols and guaiacols occuring in spent bleach liquors of kraft pulp mill. (30 pp.) 1984
19. Bibliography 1983. (47 pp.) 1984
20. Pitkänen, Maija: Addition of BrCl, B_2 and Cl_2 to methyl esters of propenoic and 2-butenoic acid derivatives and ^{13}C NMR studies on methyl esters of saturated aliphatic mono- and dichlorocarboxylic acids. (56 pp.) 1985
21. Bibliography 1984. (39 pp.) 1985
22. Salo, Esa: EPR, ENDOR and TRIPLE spectroscopy of some nitrogen heteroaromatics in liquid ammonia. (111 pp.) 1985

DEPARTMENT OF CHEMISTRY, UNIVERSITY OF JYVÄSKYLÄ
RESEARCH REPORT SERIES

23. Humppi, Tarmo: Synthesis, identification and analysis of dimeric impurities of chlorophenols. (39 pp.) 1985
24. Aho, Martti: The ion exchange and adsorption properties of sphagnum peat under acid conditions. (90 pp.) 1985
25. Bibliography 1985 (61 pp.) 1986
26. Bibliography 1986. (23 pp.) 1987
27. Bibliography 1987. (26 pp.) 1988
28. Paasivirta, Jaakko (Ed.): Structures of organic environmental chemicals. (67 pp.) 1988
29. Paasivirta, Jaakko (Ed.): Chemistry and ecology of organo-element compounds. (93 pp.) 1989
30. Sinkkonen, Seija: Determination of crude oil alkylated dibenzothiophenes in environment. (35 pp.) 1989
31. Kolehmainen, Erkki (Ed.): XII National NMR Symposium Program and Abstracts. (75 pp.) 1989
32. Kuokkanen, Tauno: Chlorocymenes and Chlorocymenenes: Persistent chlorocompounds in spent bleach liquors of kraft pulp mills. (40 pp.) 1989
33. Mäkelä, Reijo: ESR, ENDOR and TRIPLE resonance study on substituted 9,10-anthraquinone radicals in solution. (35 pp.) 1990
34. Veijanen, Anja: An integrated sensory and analytical method for identification of off-flavour compounds. (70 pp.) 1990
35. Kasa, Seppo: EPR, ENDOR and TRIPLE resonance and molecular orbital studies on a substitution reaction of anthracene induced by thallium(III) in two fluorinated carboxylic acids. (114 pp.) 1990
36. Herve, Sirpa: Mussel incubation method for monitoring organochlorine compounds in freshwater recipients of pulp and paper industry. (145 pp.) 1991
37. Pohjola, Pekka: The electron paramagnetic resonance method for characterization of Finnish peat types and iron (III) complexes in the process of peat decomposition. (77 pp.) 1991
38. Paasivirta, Jaakko (Ed.): Organochlorines from pulp mills and other sources. Research methodology studies 1988-91. (120 pp.) 1992
39. Veijanen, Anja (Ed.): VI National Symposium on Mass Spectrometry, May 13-15, 1992, Abstracts. (55 pp.) 1992
40. Rissanen, Kari (Ed.): The 7. National Symposium on Inorganic and Analytical Chemistry, May 22, 1992, Abstracts and Program. (153 pp.) 1992
41. Paasivirta, Jaakko (Ed.): CEOEC'92, Second Finnish-Russian Seminar: Chemistry and Ecology of Organo-Element Compounds. (93 pp.) 1992
42. Koistinen, Jaana: Persistent polychloroaromatic compounds in the environment: structure-specific analyses. (50 pp.) 1993
43. Virkki, Liisa: Structural characterization of chlorolignins by spectroscopic and liquid chromatographic methods and a comparison with humic substances. (62 pp.) 1993
44. Helenius, Vesa: Electronic and vibrational excitations in some

biologically relevant molecules. (30 pp.) 1993

45. Leppä-aho, Jaakko: Thermal behaviour, infrared spectra and x-ray structures of some new rare earth chromates(VI). (64 pp.) 1994
46. Kotila, Sirpa: Synthesis, structure and thermal behavior of solid copper(II) complexes of 2-amino-2- hydroxymethyl-1,3-propanediol. (111 pp.) 1994
47. Mikkonen, Anneli: Retention of molybdenum(VI), vanadium(V) and tungsten(VI) by kaolin and three Finnish mineral soils. (90 pp.) 1995
48. Suontamo, Reijo: Molecular orbital studies of small molecules containing sulfur and selenium. (42 pp.) 1995
49. Hämäläinen, Jouni: Effect of fuel composition on the conversion of fuel-N to nitrogen oxides in the combustion of small single particles. (50 pp.) 1995
50. Nevalainen, Tapio: Polychlorinated diphenyl ethers: synthesis, NMR spectroscopy, structural properties, and estimated toxicity. (76 pp.) 1995
51. Aittola, Jussi-Pekka: Organochloro compounds in the stack emission. (35 pp.) 1995
52. Harju, Timo: Ultrafast polar molecular photophysics of (dibenzylmethine)borondifluoride and 4-aminophthalimide in solution. (61 pp.) 1995
53. Maatela, Paula: Determination of organically bound chlorine in industrial and environmental samples. (83 pp.) 1995
54. Paasivirta, Jaakko (Ed.): CEOEC'95, Third Finnish-Russian Seminar: Chemistry and Ecology of Organo-Element Compounds. (109 pp.) 1995
55. Huuskonen, Juhani: Synthesis and structural studies of some supramolecular compounds. (54 pp.) 1995
56. Palm, Helena: Fate of chlorophenols and their derivatives in sawmill soil and pulp mill recipient environments. (52 pp.) 1995
57. Rantio, Tiina: Chlorohydrocarbons in pulp mill effluents and their fate in the environment. (89 pp.) 1997
58. Ratilainen, Jari: Covalent and non-covalent interactions in molecular recognition. (37 pp.) 1997
59. Kolehmainen, Erkki (Ed.): XIX National NMR Symposium, June 4-6, 1997, Abstracts. (89 pp.) 1997
60. Matilainen, Rose: Development of methods for fertilizer analysis by inductively coupled plasma atomic emission spectrometry. (41 pp.) 1997
61. Koistinen, Jari (Ed.): Spring Meeting on the Division of Synthetic Chemistry, May 15-16, 1997, Program and Abstracts. (36 pp.) 1997
62. Lappalainen, Kari: Monomeric and cyclic bile acid derivatives: syntheses, NMR spectroscopy and molecular recognition properties. (50 pp.) 1997
63. Laitinen, Eira: Molecular dynamics of cyanine dyes and phthalimides in solution: picosecond laser studies. (62 pp.) 1997
64. Eloranta, Jussi: Experimental and theoretical studies on some

quinone and quinol radicals. (40 pp.) 1997

65. Oksanen, Jari: Spectroscopic characterization of some monomeric and aggregated chlorophylls. (43 pp.) 1998
66. Häkkänen, Heikki: Development of a method based on laser-induced plasma spectrometry for rapid spatial analysis of material distributions in paper coatings. (60 pp.) 1998
67. Virtapohja, Janne: Fate of chelating agents used in the pulp and paper industries. (58 pp.) 1998
68. Airola, Karri: X-ray structural studies of supramolecular and organic compounds. (39 pp.) 1998
69. Hyötyläinen, Juha: Transport of lignin–type compounds in the receiving waters of pulp mills. (40 pp.) 1999
70. Ristolainen, Matti: Analysis of the organic material dissolved during totally chlorine-free bleaching. (40 pp.) 1999
71. Eklin, Tero: Development of analytical procedures with industrial samples for atomic emission and atomic absorption spectrometry. (43 pp.) 1999
72. Välisaari, Jouni: Hygiene properties of resol-type phenolic resin laminates. (129 pp.) 1999
73. Hu, Jiwei: Persistent polyhalogenated diphenyl ethers: model compounds syntheses, characterization and molecular orbital studies. (59 pp.) 1999
74. Malkavaara, Petteri: Chemometric adaptations in wood processing chemistry. (56 pp.) 2000
75. Kujala Elena, Laihia Katri, Nieminen Kari (Eds.): NBC 2000, Symposium on Nuclear, Biological and Chemical Threats in the 21st Century. (299 pp.) 2000
76. Rantalainen, Anna-Lea: Semipermeable membrane devices in monitoring persistent organic pollutants in the environment. (58 pp.) 2000
77. Lahtinen, Manu: *In situ* X-ray powder diffraction studies of Pt/C, CuCl/C and Cu_2O/C catalysts at elevated temperatures in various reaction conditions. (92 pp.) 2000
78. Tamminen, Jari: Syntheses, empirical and theoretical characterization, and metal cation complexation of bile acid-based monomers and open/closed dimers. (54 pp.) 2000
79. Vatanen, Virpi: Experimental studies by EPR and theoretical studies by DFT calculations of α-amino-9,10-anthraquinone radical anions and cations in solution. (37 pp.) 2000
80. Kotilainen, Risto: Chemical changes in wood during heating at 150-260 °C. (57 pp.) 2000
81. Nissinen, Maija: X-ray structural studies on weak, non-covalent interactions in supramolecular compounds. (69 pp.) 2001
82. Wegelius, Elina: X-ray structural studies on self-assembled hydrogen-bonded networks and metallosupramolecular complexes. (84 pp.) 2001
83. Paasivirta, Jaakko (Ed.): CEOEC'2001, Fifth Finnish-Russian Seminar: Chemistry and Ecology of Organo-Element Compounds. (163 pp.) 2001
84. Kiljunen, Toni: Theoretical studies on spectroscopy and

atomic dynamics in rare gas solids. (56 pp.) 2001

85. Du, Jin: Derivatives of dextran: synthesis and applications in oncology. (48 pp.) 2001
86. Koivisto, Jari: Structural analysis of selected polychlorinated persistent organic pollutants (POPs) and related compounds. (88 pp.) 2001
87. Feng, Zhinan: Alkaline pulping of non-wood feedstocks and characterization of black liquors. (54 pp.) 2001
88. Halonen, Markku: Lahon havupuun käyttö sulfaattiprosessin raaka-aineena sekä havupuun lahontorjunta. (90 pp.) 2002
89. Falábu, Dezsö: Synthesis, conformational analysis and complexation studies of resorcarene derivatives. (212 pp.) 2001
90. Lehtovuori, Pekka: EMR spectroscopic studies on radicals of ubiquinones Q-*n*, vitamin K_3 and vitamine E in liquid solution. (40 pp.) 2002
91. Perkkalainen, Paula: Polymorphism of sugar alcohols and effect of grinding on thermal behavior on binary sugar alcohol mixtures. (53 pp.) 2002
92. Ihalainen, Janne: Spectroscopic studies on light-harvesting complexes of green plants and purple bacteria. (42 pp.) 2002
93. Kunttu, Henrik, Kiljunen, Toni (Eds.): 4th International Conference on Low Temperature Chemistry. (159 pp.) 2002
94. Väisänen, Ari: Development of methods for toxic element analysis in samples with environmental concern by ICP-AES and ETAAS. (54 pp.) 2002
95. Luostarinen, Minna: Synthesis and characterisation of novel resorcarene derivatives. (200 pp.) 2002
96. Louhelainen, Jarmo: Changes in the chemical composition and physical properties of wood and nonwood black liquors during heating. (68 pp.) 2003
97. Lahtinen, Tanja: Concave hydrocarbon cyclophane π-prismands. (65 pp.) 2003
98. Laihia, Katri (Ed.): NBC 2003, Symposium on Nuclear, Biological and Chemical Threats – A Crisis Management Challenge. (245 pp.) 2003
99. Oasmaa, Anja: Fuel oil quality properties of wood-based pyrolysis liquids. (32 pp.) 2003
100. Virtanen, Elina: Syntheses, structural characterisation, and cation/anion recognition properties of nano-sized bile acid-based host molecules and their precursors. (123 pp.) 2003
101. Nättinen, Kalle: Synthesis and X-ray structural studies of organic and metallo-organic supramolecular systems. (79 pp.) 2003
102. Lampiselkä, Jarkko: Demonstraatio lukion kemian opetuksessa. (285 pp.) 2003
103. Kallioinen, Jani: Photoinduced dynamics of $Ru(dcbpy)_2(NCS)_2$ – in solution and on nanocrystalline titanium dioxide thin films. (47 pp.) 2004
104. Valkonen, Arto (Ed.): VII Synthetic Chemistry Meeting and XXVI Finnish NMR Symposium. (103 pp.) 2004

DEPARTMENT OF CHEMISTRY, UNIVERSITY OF JYVÄSKYLÄ
RESEARCH REPORT SERIES

105. Vaskonen, Kari: Spectroscopic studies on atoms and small molecules isolated in low temperature rare gas matrices. (65 pp.) 2004
106. Lehtovuori, Viivi: Ultrafast light induced dissociation of Ru(dcbpy)$(CO)_2I_2$ in solution. (49 pp.) 2004
107. Saarenketo, Pauli: Structural studies of metal complexing Schiff bases, Schiff base derived *N*-glycosides and cyclophane π-prismands. (95 pp.) 2004
108. Paasivirta, Jaakko (Ed.): CEOEC'2004, Sixth Finnish-Russian Seminar: Chemistry and Ecology of Organo-Element Compounds. (147 pp.) 2004
109. Suontamo, Tuula: Development of a test method for evaluating the cleaning efficiency of hard-surface cleaning agents. (96 pp.) 2004
110. Güneş, Minna: Studies of thiocyanates of silver for nonlinear optics. (48 pp.) 2004
111. Ropponen, Jarmo: Aliphatic polyester dendrimers and dendrons. (81 pp.) 2004
112. Vu, Mân Thi Hong: Alkaline pulping and the subsequent elemental chlorine-free bleaching of bamboo (*Bambusa procera*). (69 pp.) 2004
113. Mansikkamäki, Heidi: Self-assembly of resorcinarenes. (77 pp.) 2006
114. Tuononen, Heikki M.: EPR spectroscopic and quantum chemical studies of some inorganic main group radicals. (79 pp.) 2005
115. Kaski, Saara: Development of methods and applications of laser-induced plasma spectroscopy in vacuum ultraviolet. (44 pp.) 2005
116. Mäkinen, Riika-Mari: Synthesis, crystal structure and thermal decomposition of certain metal thiocyanates and organic thiocyanates. (119 pp.) 2006
117. Ahokas, Jussi: Spectroscopic studies of atoms and small molecules isolated in rare gas solids: photodissociation and thermal reactions. (53 pp.) 2006
118. Busi, Sara: Synthesis, characterization and thermal properties of new quaternary ammonium compounds: new materials for electrolytes, ionic liquids and complexation studies. (102 pp.) 2006
119. Mäntykoski, Keijo: PCBs in processes, products and environment of paper mills using wastepaper as their raw material. (73 pp.) 2006
120. Laamanen, Pirkko-Leena: Simultaneous determination of industrially and environmentally relevant aminopolycarboxylic and hydroxycarboxylic acids by capillary zone electrophoresis. (54 pp.) 2007
121. Salmela, Maria: Description of oxygen-alkali delignification of kraft pulp using analysis of dissolved material. (71 pp.) 2007
122. Lehtovaara, Lauri: Theoretical studies of atomic scale impurities in superfluid ^{4}He. (87 pp.) 2007
123. Rautiainen, J. Mikko: Quantum chemical calculations of structures, bonding, and spectroscopic properties of some sulphur and selenium iodine cations. (71 pp.) 2007
124. Nummelin, Sami: Synthesis, characterization, structural and

retrostructural analysis of self-assembling pore forming dendrimers. (286 pp.) 2008

125. Sopo, Harri: Uranyl(VI) ion complexes of some organic aminobisphenolate ligands: syntheses, structures and extraction studies. (57 pp.) 2008
126. Valkonen, Arto: Structural characteristics and properties of substituted cholanoates and *N*-substituted cholanamides. (80 pp.) 2008
127. Lähde, Anna: Production and surface modification of pharmaceutical nano- and microparticles with the aerosol flow reactor. (43 pp.) 2008
128. Beyeh, Ngong Kodiah: Resorcinarenes and their derivatives: synthesis, characterization and complexation in gas phase and in solution. (75 pp.) 2008
129. Välisaari, Jouni, Lundell, Jan (Eds.): Kemian opetuksen päivät 2008: uusia oppimisympäristöjä ja ongelmalähtöistä opetusta. (118 pp.) 2008
130. Myllyperkiö, Pasi: Ultrafast electron transfer from potential organic and metal containing solar cell sensitizers. (69 pp.) 2009
131. Käkölä, Jaana: Fast chromatographic methods for determining aliphatic carboxylic acids in black liquors. (82 pp.) 2009
132. Koivukorpi, Juha: Bile acid-arene conjugates: from photoswitchability to cancer cell detection. (67 pp.) 2009
133. Tuuttila, Tero: Functional dendritic polyester compounds: synthesis and characterization of small bifunctional dendrimers and dyes. (74 pp.) 2009
134. Salorinne, Kirsi: Tetramethoxy resorcinarene based cation and anion receptors: synthesis, characterization and binding properties. (79 pp.) 2009
135. Rautiainen, Riikka: The use of first-thinning Scots pine (*Pinus sylvestris*) as fiber raw material for the kraft pulp and paper industry. (73 pp.) 2010
136. Ilander, Laura: Uranyl salophens: synthesis and use as ditopic receptors. (199 pp.) 2010
137. Kiviniemi, Tiina: Vibrational dynamics of iodine molecule and its complexes in solid krypton - Towards coherent control of bimolecular reactions? (73 pp.) 2010
138. Ikonen, Satu: Synthesis, characterization and structural properties of various covalent and non-covalent bile acid derivatives of N/O-heterocycles and their precursors. (105 pp.) 2010
139. Siitonen, Anni: Spectroscopic studies of semiconducting single-walled carbon nanotubes. (56 pp.) 2010
140. Raatikainen, Kari: Synthesis and structural studies of piperazine cyclophanes – Supramolecular systems through Halogen and Hydrogen bonding and metal ion coordination. (69 pp.) 2010
141. Leivo, Kimmo: Gelation and gel properties of two- and three-component Pyrene based low molecular weight organogelators. (116 pp.) 2011
142. Martiskainen, Jari: Electronic energy transfer in light-harvesting complexes isolated from *Spinacia oleracea* and from three

photosynthetic green bacteria *Chloroflexus aurantiacus*, *Chlorobium tepidum*, and *Prosthecochloris aestuarii*. (55 pp.) 2011

143. Wichmann, Oula: Syntheses, characterization and structural properties of [O,N,O,X´] aminobisphenolate metal complexes. (101 pp.) 2011
144. Ilander, Aki: Development of ultrasound-assisted digestion methods for the determination of toxic element concentrations in ash samples by ICP-OES. (58 pp.) 2011
145. The Combined XII Spring Meeting of the Division of Synthetic Chemistry and XXXIII Finnish NMR Symposium. Book of Abstracts. (90 pp.) 2011
146. Valto, Piia: Development of fast analysis methods for extractives in papermaking process waters. (73 pp.) 2011
147. Andersin, Jenni: Catalytic activity of palladium-based nanostructures in the conversion of simple olefinic hydro- and chlorohydrocarbons from first principles. (78 pp.) 2011
148. Aumanen, Jukka: Photophysical properties of dansylated poly(propylene amine) dendrimers. (55 pp.) 2011
149. Kärnä, Minna: Ether-functionalized quaternary ammonium ionic liquids – synthesis, characterization and physicochemical properties. (76 pp.) 2011
150. Jurček, Ondřej: Steroid conjugates for applications in pharmacology and biology. (57 pp.) 2011
151. Nauha, Elisa: Crystalline forms of selected Agrochemical actives: design and synthesis of cocrystals. (77 pp.) 2012
152. Ahkola, Heidi: Passive sampling in monitoring of nonylphenol ethoxylates and nonylphenol in aquatic environments. (92 pp.) 2012
153. Helttunen, Kaisa: Exploring the self-assembly of resorcinarenes: from molecular level interactions to mesoscopic structures. (78 pp.) 2012
154. Linnanto, Juha: Light excitation transfer in photosynthesis revealed by quantum chemical calculations and exiton theory. (179 pp.) 2012
155. Roiko-Jokela, Veikko: Digital imaging and infrared measurements of soil adhesion and cleanability of semihard and hard surfaces. (122 pp.) 2012
156. Noponen, Virpi: Amides of bile acids and biologically important small molecules: properties and applications. (85 pp.) 2012
157. Hulkko, Eero: Spectroscopic signatures as a probe of structure and dynamics in condensed-phase systems – studies of iodine and gold ranging from isolated molecules to nanoclusters. (69 pp.) 2012
158. Lappi, Hanna: Production of Hydrocarbon-rich biofuels from extractives-derived materials. (95 pp.) 2012
159. Nykänen, Lauri: Computational studies of Carbon chemistry on transition metal surfaces. (76 pp.) 2012
160. Ahonen, Kari: Solid state studies of pharmaceutically important molecules and their derivatives. (65 pp.) 2012

DEPARTMENT OF CHEMISTRY, UNIVERSITY OF JYVÄSKYLÄ
RESEARCH REPORT SERIES

161. Pakkanen, Hannu: Characterization of organic material dissolved during alkaline pulping of wood and non-wood feedstocks. (76 pp.) 2012
162. Moilanen, Jani: Theoretical and experimental studies of some main group compounds: from closed shell interactions to singlet diradicals and stable radicals. (80 pp.) 2012
163. Himanen, Jatta: Stereoselective synthesis of Oligosaccharides by *De Novo* Saccharide welding. (133 pp.) 2012
164. Bunzen, Hana: Steroidal derivatives of nitrogen containing compounds as potential gelators. (76 pp.) 2013
165. Seppälä, Petri: Structural diversity of copper(II) amino alcohol complexes. Syntheses, structural and magnetic properties of bidentate amino alcohol copper(II) complexes. (67 pp.) 2013
166. Lindgren, Johan: Computational investigations on rotational and vibrational spectroscopies of some diatomics in solid environment. (77 pp.) 2013
167. Giri, Chandan: Sub-component self-assembly of linear and non-linear diamines and diacylhydrazines, formulpyridine and transition metal cations. (145 pp.) 2013
168. Riisiö, Antti: Synthesis, Characterization and Properties of Cu(II)-, Mo(VI)- and U(VI) Complexes With Diaminotetraphenolate Ligands. (51 pp.) 2013
169. Kiljunen, Toni (Ed.): Chemistry and Physics at Low Temperatures. Book of Abstracts. (103 pp.) 2013
170. Hänninen, Mikko: Experimental and Computational Studies of Transition Metal Complexes with Polydentate Amino- and Aminophenolate Ligands: Synthesis, Structure, Reactivity and Magnetic Properties. (66 pp.) 2013
171. Antila, Liisa: Spectroscopic studies of electron transfer reactions at the photoactive electrode of dye-sensitized solar cells. (53 pp.) 2013
172. Kemppainen, Eeva: Mukaiyama-Michael reactions with α-substituted acroleins – a useful tool for the synthesis of the pectenotoxins and other natural product targets. (190 pp.) 2013
173. Virtanen, Suvi: Structural Studies of Dielectric Polymer Nanocomposites. (49 pp.) 2013
174. Yliniemelä-Sipari, Sanna: Understanding The Structural Requirements for Optimal Hydrogen Bond Catalyzed Enolization – A Biomimetic Approach.(160 pp.) 2013
175. Leskinen, Mikko V: Remote β-functionalization of β'-keto esters. (105 pp.) 2014
176. 12th European Conference on Research in Chemistry Education (ECRICE2014). Book of Abstracts. (166 pp.) 2014
177. Peuronen, Anssi: N-Monoalkylated DABCO-Based N-Donors as Versatile Building Blocks in Crystal Engineering and Supramolecular Chemistry. (54 pp.) 2014
178. Perämäki, Siiri: Method development for determination and recovery of rare earth elements from industrial fly ash. (88 pp.) 2014

DEPARTMENT OF CHEMISTRY, UNIVERSITY OF JYVÄSKYLÄ
RESEARCH REPORT SERIES

179. Chernyshev, Alexander, N.: Nitrogen-containing ligands and their platinum(IV) and gold(III) complexes: investigation and basicity and nucleophilicity, luminescence, and aurophilic interactions. (64 pp.) 2014
180. Lehto, Joni: Advanced Biorefinery Concepts Integrated to Chemical Pulping. (142 pp.) 2015
181. Tero, Tiia-Riikka: Tetramethoxy resorcinarenes as platforms for fluorescent and halogen bonding systems. (61 pp.) 2015
182. Löfman, Miika: Bile acid amides as components of microcrystalline organogels. (62 pp.) 2015
183. Selin, Jukka: Adsorption of softwood-derived organic material onto various fillers during papermaking. (169 pp.) 2015
184. Piisola, Antti: Challenges in the stereoselective synthesis of allylic alcohols. (210 pp.) 2015
185. Bonakdarzadeh, Pia: Supramolecular coordination polyhedra based on achiral and chiral pyridyl ligands: design, preparation, and characterization. (65 pp.) 2015
186. Vasko, Petra: Synthesis, characterization, and reactivity of heavier group 13 and 14 metallylenes and metalloid clusters: small molecule activation and more. (66 pp.) 2015
187. Topić, Filip: Structural Studies of Nano-sized Supramolecular Assemblies. (79 pp.) 2015
188. Mustalahti, Satu: Photodynamics Studies of Ligand-Protected Gold Nanoclusters by using Ultrafast Transient Infrared Spectroscopy. (58 pp.) 2015
189. Koivisto, Jaakko: Electronic and vibrational spectroscopic studies of gold-nanoclusters. (63 pp.) 2015
190. Suhonen, Aku: Solid state conformational behavior and interactions of series of aromatis oligoamide foldamers. (68 pp.) 2016
191. Soikkeli, Ville: Hydrometallurgical recovery and leaching studies for selected valuable metals from fly ash samples by ultrasound-assisted extraction followed by ICP-OES determination. (107 pp.) 2016
192. XXXVIII Finnish NMR Symposium. Book of Abstracts. (51 pp.) 2016
193. Mäkelä, Toni: Ion Pair Recognition by Ditopic Crown Ether Based bis-Urea and Uranyl Salophen Receptors. (75 pp.) 2016
194. Lindholm-Lehto, Petra: Occurrence of pharmaceuticals in municipal wastewater treatment plants and receiving surface waters in Central and Southern Finland. (98 pp.) 2016
195. Härkönen, Ville: Computational and Theoretical studies on Lattice Thermal conductivity and Thermal properties of Silicon Clathrates. (89 pp.) 2016
196. Tuokko, Sakari: Understanding selective reduction reactions with heterogeneous Pd and Pt: climbing out of the black box. (85 pp.) 2016
197. Nuora, Piia: Monitapaustutkimus LUMA-Toimintaan liittyvissä oppimisympäristöissä tapahtuvista kemian oppimiskokemuksista. (171 pp.) 2016

DEPARTMENT OF CHEMISTRY, UNIVERSITY OF JYVÄSKYLÄ
RESEARCH REPORT SERIES

198. Kumar, Hemanathan: Novel Concepts on The Recovery of By-Products from Alkaline Pulping. (61 pp.) 2016
199. Arnedo-Sánchez, Leticia: Lanthanide and Transition Metal Complexes as Building Blocks for Supramolecular Functional Materials. (227 pp.) 2016
200. Gell, Lars: Theoretical Investigations of Ligand Protected Silver Nanoclusters. (134 pp.) 2016
201. Vaskuri, Juhani: Oppiennätyksistä opetussuunnitelman perusteisiin - lukion kemian kansallisen opetussuunnitelman kehittyminen Suomessa vuosina 1918-2016. (314 pp.) 2017
202. Lundell Jan, Kiljunen Toni (Eds.): 22nd Horizons in Hydrogen Bond Research. Book of Abstracts. 2017
203. Turunen, Lotta: Design and construction of halogen-bonded capsules and cages. (61 pp.) 2017
204. Hurmalainen, Juha: Experimental and computational studies of unconventional main group compounds: stable radicals and reactive intermediates. (88 pp.) 2017
205. Koivistoinen Juha: Non-linear interactions of femtosecond laser pulses with graphene: photo-oxidation, imaging and photodynamics. (68 pp.) 2017
206. Chen, Chengcong: Combustion behavior of black liquors: droplet swelling and influence of liquor composition. (39 pp.) 2017
207. Mansikkamäki, Akseli: Theoretical and Computational Studies of Magnetic Anisotropy and Exchange Coupling in Molecular Systems. (190 p. + included articles) 2018.
208. Tatikonda, Rajendhraprasad: Multivalent N-donor ligands for the construction of coordination polymers and coordination polymer gels. (62 pp.) 2018
209. Budhathoki, Roshan: Beneficiation, desilication and selective precipitation techniques for phosphorus refining from biomass derived fly ash. (64 pp.) 2018
210. Siitonen, Juha: Synthetic Studies on 1-azabicyclo[5.3.0]decane Alkaloids. (140 pp.) 2018
211. Ullah, Saleem: Advanced Biorefinery Concepts Related to Non-wood Feedstocks. (57 pp.) 2018
212. Ghalibaf, Maryam: Analytical Pyrolysis of Wood and Non-Wood Materials from Integrated Biorefinery Concepts. (106 pp.) 2018

DEPARTMENT OF CHEMISTRY, UNIVERSITY OF JYVÄSKYLÄ
DISSERTATIONS PUBLISHED IN THE JYU DISSERTATIONS RESEARCH SERIES

1. Bulatov, Evgeny: Synthetic and structural studies of covalent and non-covalent interactions of ligands and metal center in platinum(II) complexes containing 2,2′-dipyridylamine or oxime ligands. (58 pp.) 2019. JYU Dissertations 70.
2. Annala, Riia: Conformational Properties and Anion Complexes of Aromatic Oligoamide Foldamers. (80 pp.) 2019. JYU Dissertations 84.
3. Isoaho, Jukka Pekka: Dithionite Bleaching of Thermomechanical Pulp - Chemistry and Optimal Conditions. (73 pp.) 2019. JYU Dissertations 85.
4. Nygrén, Enni: Recovery of rubidium from power plant fly ash. (98 pp.) 2019. JYU Dissertations 136.
5. Kiesilä, Anniina: Supramolecular chemistry of anion-binding receptors based on concave macromolecules. (68 pp.) 2019. JYU Dissertations 137.
6. Sokolowska, Karolina: Study of water-soluble p-MBA-protected gold nanoclusters and their superstructures. (60 pp.) 2019. JYU Dissertations 167.
7. Lahtinen, Elmeri: Chemically Functional 3D Printing: Selective Laser Sintering of Customizable Metal Scavengers. (71 pp.) 2019. JYU Dissertations 175.
8. Larijani, Amir: Oxidative reactions of cellulose under alkaline conditions. (102 pp.) 2020. JYU Dissertations 217.
9. Kolari, Kalle: Metal-metal contacts in late transition metal polymers. (60 pp.) 2020. JYU Dissertations 220.
10. Kauppinen, Minttu: Multiscale computational investigation of catalytic properties of zirconia supported noble metals. (87 pp.) 2020. JYU Dissertations 231.
11. Ding, Xin: Halogen Bond in Crystal Engineering: Structural Studies on Crystals with Ruthenium Centered Complexes and 1-(4-Pyridyl)-4-thiopyridine Zwitterion as Halogen Bond Acceptors. (59 pp.) 2020. JYU Dissertations 323.
12. Neuvonen, Antti: Toward an Understanding of Hydrogen-Bonding Bifunctional Organocatalyst Conformations and Their Activity in Asymmetric Mannich Reactions. (77 pp.) 2020. JYU Dissertations 336.
13. Kortet, Sami: 2,5-Diarylpyrrolidines and Pyroglutamic-Acid-Derived 2-Diarylmethyl-5-Aryl-Pyrrolidines: Their Synthesis and Use in Asymmetric Synthesis. (221 pp.) 2020. JYU Dissertations 337.
14. Saarnio, Ville: Fluorescent probes, noble metal nanoparticles and their nanocomposites: detection of nucleic acids and other biological targets. (80 pp.) 2021. JYU Dissertations 361.
15. Chernysheva, Maria: σ-hole interactions: the effect of the donors and acceptors nature in selenoureas, thioureas, halogenated species, substituted benzenes, and their adducts. (72 pp.) 2021. JYU Dissertations 370.
16. Bulatova, Margarita: Noncovalent interactions as a tool for supramolecular self-assembly of metallopolymers. (62 pp.) 2021. JYU Dissertations 377.

DEPARTMENT OF CHEMISTRY, UNIVERSITY OF JYVÄSKYLÄ
DISSERTATIONS PUBLISHED IN THE JYU DISSERTATIONS RESEARCH SERIES

17. Romppanen, Sari: Laser-spectroscopic studies of rare earth element- and lithium-bearing minerals and rocks. (66 pp.) 2021. JYU Dissertations 393.
18. Kukkonen, Esa: Nonlinear optical materials through weak interactions and their application in 3D printing. (58 pp.) 2021. JYU Dissertations 441.
19. Kuosmanen, Riikka: The Effect of Structure on the Gel Formation Ability and the Properties of Bile Acid Based Supramolecular Organogels. (68 pp.) 2021. JYU Dissertations 465.
20. Reuna, Sini: Development of a Method for Phosphorus Recovery from Wastewaters. (67 pp.) 2022. JYU Dissertations 486.
21. Taipale, Essi: Synthetic and Structural Studies on the Effect of Non-Covalent Interactions on N(*sp2*)-Heterocyclic Molecules. (67 pp.) 2022. JYU Dissertations 496.
22. Järvinen, Teemu: Molecular Dynamics View on Matrix Isolation. (143 pp.) 2022. JYU Dissertations 544.
23. Kumar, Parveen: Synthesis and Structural Studies on Halogen(I) Complexes. (160 pp.) 2022. JYU Dissertations 549.
24. Forsblom, Samu: Design and Construction of Metal-Organic Polyhedra. (212 pp.) 2022. JYU Dissertations 569.
25. Korpelin, Ville: Computational Studies of Catalytic Active Site Properties and Reactions at the Metal–Oxide Interface. (78 pp.) 2022. JYU Dissertations 578.
26. Vuori, Hannu: Extending Benson Group Increment Theory to Compounds of Phosphorus, Silicon, and Boron with Computational Chemistry. (59 pp.) 2022. JYU Dissertations 581.
27. Pallerla, Rajanish: Studies Towards Synthesis of Favipiravir & Humilisin E. (139 pp.) 2023. JYU Dissertations 611.
28. Taponen, Anni: Radical-Ion Salts based on Thiazyls and Tetracyanoquinodimethane: Hysteretic Magnetic Bistability in a Multicomponent System. (66 pp.) 2023. JYU Dissertations 613.
29. Aho, Noora: Molecular Dynamics Simulations of Acids and Bases in Biomolecular Environments. (78 pp.) 2023. JYU Dissertations 614.
30. Sabooni Asre Hazer, Maryam: Electronic and Optical Properties of Gold Clusters with Carbene Ligands using Density Functional Theory Calculations. (68 pp.) 2023. JYU Dissertations 650.
31. Kinnunen, Virva-Tuuli: Improving the Accuracy of Single Particle ICP-MS Analyses of Au and Ag Nanoparticles. (67 pp.) 2023. JYU Dissertations 689.
32. Kulomäki, Suvi: Preconcentration, Speciation, and Determination of Mercury in Natural Waters by Inductively Coupled Plasma Mass Spectrometry. (61 pp.) 2023. JYU Dissertations 725.
33. Schirmer, Johanna: Effects of Two-Photon Oxidation for the Development of Graphene-Bio Interfaces. (69 pp.) 2023. JYU Dissertations 726.
34. Halmemies, Eelis: Chemical Changes in the Industrial Extractive-Containing Sidestreams of Norway Spruce (*Picea abies*) during Storage. (84 pp.) 2024. JYU Dissertations 737.

DEPARTMENT OF CHEMISTRY, UNIVERSITY OF JYVÄSKYLÄ
DISSERTATIONS PUBLISHED IN THE JYU DISSERTATIONS RESEARCH SERIES

35. Alaranta, Johanna: Synthesis of Monomethine Cyanine Dyes and Gold Nanoclusters and their Applications as Fluorescent Probes. (67 pp.) 2024. JYU Dissertations 766.
36. Chevigny, Romain: Out-of-equilibrium and in-equilibrium amino acid-based supramolecular gels: Transient self-assembly and hybrid materials. (79 pp.) 2024. JYU Dissertations 768.